SCHRIFTEN DES INSTITUTS FÜR MIKROSTRUKTURTECHNIK
AM KARLSRUHER INSTITUT FÜR TECHNOLOGIE (KIT)

Band 52

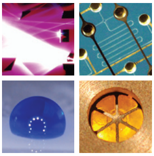

JULIE ROGER

Lamination and recrystallization of perovskite thin films for photovoltaics

KIT Scientific Publishing

Julie Roger

Lamination and recrystallization of perovskite thin films for photovoltaics

Schriften des Instituts für Mikrostrukturtechnik
am Karlsruher Institut für Technologie (KIT)
Band 52

Hrsg. Institut für Mikrostrukturtechnik

Eine Übersicht aller bisher in dieser Schriftenreihe
erschienenen Bände finden Sie am Ende des Buchs.

Lamination and recrystallization of perovskite thin films for photovoltaics

by
Julie Roger

KIT Scientific Publishing

Karlsruher Institut für Technologie
Institut für Mikrostrukturtechnik

Lamination and recrystallization of perovskite thin films for photovoltaics

Zur Erlangung des akademischen Grades einer Doktorin der Ingenieurwissenschaften (Dr.-Ing.) von der KIT-Fakultät für Maschinenbau des Karlsruher Instituts für Technologie (KIT) genehmigte Dissertation

von Julie Roger, M.Sc.

Tag der mündlichen Prüfung: 7. April 2025
Hauptreferent: Prof. Dr. Ulrich W. Paetzold
Korreferent: Prof. Dr. Hendrik Hölscher

Impressum

KIT Scientific Publishing

Karlsruher Institut für Technologie (KIT)
KIT Scientific Publishing
Straße am Forum 2
D-76131 Karlsruhe

www.bibliothek.kit.edu/ksp.php | E-Mail: info@ksp.kit.edu | Shop: www.ksp.kit.edu

Print on Demand 2025 – Gedruckt auf FSC-zertifiziertem Papier

ISSN 1869-5183
ISBN 978-3-7315-1450-3
DOI 10.5445/KSP/1000183611

Kurzfassung

Photovoltaik (PV) ermöglicht die Umwandlung der reichlich vorhandenen und unerschöpflichen Sonnenenergie in elektrische Energie. Diese Technologie geht sowohl den wachsenden globalen Energiebedarf als auch die Nachfrage, die Treibhausgasemissionen pro erzeugter Kilowattstunde zu verringern, strategisch an. Diese Versprechen treiben die Forschung an, um den Wirkungsgrad von Solarzellen zu erhöhen, ihre Produktion zu vereinfachen und die Anwendungsvielfalt zu steigern. Unter den aufstrebenden PV-Technologien haben sich Perowskit-Solarzellen (PSC) rasant entwickelt und erreichen bereits ähnliche Wirkungsgrade wie Silizium-PV. PSC profitieren von den Vorteilen der Dünnschicht-PV, u.a. minimale Materialanforderungen und die Möglichkeit leichte und flexible Module zu produzieren – ideal für integrierte PV. Aufgrund der niedrigen Prozesstemperaturen sinkt der Energieverbrauch bei der Herstellung, was die energetische Amortisationszeit verkürzt und ihr Potenzial zur Reduzierung von Treibhausgasen erhöht. PSC werden nicht nur als Konkurrenten von Silizium gesehen, sondern auch als Partner in Perowskit/Silizium-Tandemsolarzellen. Auf diese Weise können die grundlegenden Wirkungsgradeinschränkungen aufgrund der begrenzten Nutzung des Sonnenspektrums durch Einfachsolarzellen überwunden werden, wodurch Wirkungsgrade von über 34% ermöglicht werden.

Der größte Teil der derzeitigen Forschung für Einfach- und Tandemsolarzellen auf Perowskitbasis fokussiert sich auf Architekturen, die durch sequenzielle Abscheidung der Dünnschichten hergestellt werden. Die vorliegende Arbeit erforscht ein neuartiges Herstellungsverfahren durch Laminierung. Bei dieser Laminierungstechnik werden die PSC in zwei getrennten Schichtstapeln hergestellt, die anschließend unter Druck und Temperatur zusammengefügt werden. Die polykristalline Perowskitschicht rekristallisiert unter diese Bedingungen und an der Grenzfläche entsteht ein elektrischer Materialkontakt. Durch die entkoppelte Verarbeitung der unabhängigen Schichtstapel, bietet diese Methode hohe Flexibilität bei der Wahl der Materialien und der Abscheidetechniken der funktionellen Schichten. Zukünftig kann der Laminierungsprozess die Erforschung neuartiger Kombinationen von Materialschichten ermöglichen und den Übergang zu industriellen Herstellungsprozessen erleichtern. Dadurch trägt diese Technik dazu bei, die verbleibenden Herausforderungen Perowskit-basierter Solarzellen zu bewältigen. Besonderer Fokus liegt hierbei auf der Langzeitstabilität, sowie der Skalierung der aktiven Flächen auf industriell relevante Größen.

Diese Arbeit widmet sich dem praktischen Verständnis dieses Prozesses und seiner Anwendung in verschiedenen Konzeptnachweisen von Einfach- und Tandemsolarzellen auf Perowskitbasis. Experimentelle Studien heben zunächst den Einfluss des Heißprägens hervor, indem sie eine deutliche Verbesserung der Perowskit Morphologie und Kristallinität zeigen. Dieser Rekristallisationsprozess wird durch die Kernparameter des Heißprägens gesteuert: Temperatur, Druck und Laminierungszeit. Anschließend demonstrieren konkrete Beispielarchitekturen die neuen Freiheitsgrade für PSC, die mit Standardherstellungsmethoden normalerweise nicht zugänglich sind. Werden identische Architekturen konventionell und durch Laminierung hergestellt, weisen sie einen vergleichbaren Wirkungsgrad von bis zu 17.5% auf. Die verbesserte Qualität des Absorbers führt zu einer messbaren Erhöhung der Leerlaufspannung und einer erheblich längeren Lagerstabilität für laminierte Solarzellen von über einem Jahr. Zum Abschluss stellt diese Arbeit die allerersten Prototypen von monolithisch laminierten Perowskit/Silizium-Tandemsolarzellen mit stabilen Wirkungsgraden von über 20.0% vor.

Abstract

Photovoltaics (PVs) enable the conversion of abundant and inexhaustible solar energy into electrical energy. This technology strategically addresses both a growing global demand for energy and the necessity to reduce greenhouse gas emissions per produced kilowatt-hour. These promises drive research to advance solar cell efficiency, facilitate fabrication, and increase the range of applications. Among the emerging PV technologies, perovskite solar cells (PSCs) develop rapidly, achieving power conversion efficiencies (PCEs) close to the established silicon PV. PSCs share key advantages with thin-film devices, such as minimal material requirements and the possibility to produce lightweight and flexible modules – ideal for integrated PVs. Additionally, their low processing temperatures decrease energy consumption during fabrication, lowering energy payback time and increasing their potential for greenhouse gas reduction. PSCs are considered not only as competitors to silicon but also as partners in perovskite/silicon tandem solar cells. This technical concept overcomes fundamental efficiency constraints of single-junction devices due to limited use of the solar spectrum, allowing certified PCEs over 34% to date.

Most current research into perovskite-based single-junction and tandem devices focuses on architectures fabricated by sequential deposition of functional thin films. The present work explores a novel manufacturing method incorporating lamination. This technique involves fabricating PSCs in two separate layer stacks assembled at a final stage in a hot-pressing process. Lamination at high temperatures and pressures triggers perovskite recrystallization and creates an electrical contact at the interface between the half-stacks. Through a decoupled preparation of independent half-stacks, this methodology offers high flexibility in the choice of materials and deposition techniques of functional layers. Over the next few years, lamination can enable the exploration of novel combinations of materials and facilitate the transition to industrial manufacturing processes for PSCs. Thereby, this method contributes to overcoming remaining challenges of perovskite-based cells, in particular, stability over time and upscaling active areas to industrially relevant sizes.

This work is dedicated to the practical understanding of the lamination technique and its use in various proof-of-concept perovskite-based single-junction and tandem solar cells. Experimental studies first provide insights into the hot-pressing process by demonstrating a significant improvement in perovskite morphology and crystallinity. The temperature, pressure, and lamination duration control this recrystallization process. Subsequently, new degrees of freedom for PSC architectures are showcased via concrete example devices, which are usually inaccessible via standard fabrication methods. If identical architectures are produced conventionally and by lamination, the PSCs achieve a comparable PCE of up to 17.5%. The superior quality of hot-pressed absorbers results in a systematic increase in open-circuit voltage and enhanced shelf-life stability for laminated devices for more than a year. Finally, the first prototypes of laminated monolithic perovskite/silicon tandem solar cells with stable efficiencies exceeding 20.0% are presented.

Contents

Acronyms and symbols

Acronyms

AFM	atomic force microscopy
ALD	atomic layer deposition
CTL	charge transport layer
EQE	external quantum efficiency
ETL	electron transport layer
HTL	hole transport layer
PL	photoluminescence
PLQY	photoluminescence quantum yield
PSC	perovskite solar cell
PV	photovoltaic
RMS	root mean square
TCO	transparent conductive oxide
XRD	X-ray diffraction

Materials

BCP	bathocuproine
C_{60}	fullerene-C_{60}
CI(G)S	copper indium (gallium) selenide
FA	formamidium

IO:H	hydrogenated indium oxide
ITO	indium tin oxide
IZO	indium zinc oxide
LiF	lithium fluoride
MA	methylammonium
MgF_2	magnesium fluoride
NiO_x	nickel oxide
PEN	polyethylene naphthalate
PTAA	poly(triarylamine)
2PACz	[2-(9H-Carbazol-9-yl)ethyl]phosphonic acid
SHJ	heterojunction silicon solar cell
SnO_2-np	tin dioxide nanoparticles
Teflon (PTFE)	polytetrafluoroethylene

Symbols and variables

A	absorptance
E_γ	photon energy
E_g	bandgap energy
FF	fill factor
FWHM	full width at half maximum
I, J	current, current density
J_sc	short-circuit current density

λ (lambda)	wavelength
MPP	maximum power point
n_{id}	ideality factor
PCE	power conversion efficiency
R	reflectance
R_{series}	series resistance
R_{shunt}	shunt resistance
T	transmittance
θ (theta)	glancing angle
V	voltage
V_{oc}	open-circuit voltage
$V_{\mathrm{oc,imp}}$	implied open-circuit voltage

1 Introduction

The transition from fossil fuels to energy sources with reduced greenhouse gas emissions per Kilowatt-hour produced is a central measure in restructuring the global energy supply to combat climate change.[1,2] Photovoltaic (PV) is a mature technological solution that converts abundant solar energy into electrical energy at a steadily decreasing cost.[3] This versatile technology can be installed everywhere at small or large scales to support local energy production and is widely adopted for its noiseless operation and low maintenance requirements.[4–7] As a result, PV has become one of the pivotal technologies for climate neutrality. For instance, installed capacity in Germany increased from approximately 2 $\mathrm{GW_p}$ in 2005 to nearly 100 $\mathrm{GW_p}$ by the end of 2024.[8] The unit Watt-peak ($\mathrm{W_p}$) refers to the nominal power output of PV systems measured under standard test conditions (STC).[1] To exhaustively cover energy demand with renewables in Germany and achieve climate neutrality until 2045, around four times more PV capacity must be installed in the near future.[3] This requirement motivates the development of innovative systems for integrated PVs installed on existing surfaces, such as buildings and agricultural areas.[10,11] Meanwhile, current research aims to enhance the power conversion efficiency (PCE) of solar cells and facilitate their production.[12]

Among the new concepts being developed, perovskite solar cells (PSCs) have emerged as a promising PV technology, experiencing a remarkably rapid improvement in PCE over the last decade. The best research-cell PCE surpasses 26% today, comparable to established silicon PVs.[13] PSCs benefit from advantages of thin-film PV, including minimal material requirements and the possibility to fabricate bendable, lightweight, and semi-transparent solar cells and modules.[14–17] These attributes are

---

[1] STC include a standardized solar spectrum with an irradiance of 1000 $\mathrm{W/m^2}$, an air mass (AM) of 1.5, and a device temperature of 25 °C.[9]

essential for integrated PV systems, e.g., in windows and mobile applications. Additionally, low processing temperatures during fabrication limit required energy, shortening energy payback time and increasing their potential for reducing greenhouse gas emissions.[18] The high versatility of perovskite absorbers also allows engineering to achieve remarkable optoelectronic properties and adjust the bandgap over a wide range of energy.[19–23] Tunable bandgap energy is a promising feature for applications in tandem devices, a technology that overcomes fundamental physical limits of single-junction architectures.[24] This PV concept combines perovskite absorbers with established technologies such as silicon solar cells in so-called perovskite/silicon monolithic tandems, which recently exhibited PCEs above 34%.[25] Nevertheless, challenges remain for the perovskite PV technology, including i) long-term stability, ii) upscaling of PSCs, which are mainly investigated at laboratory scale with device sizes of less than a few squares centimeter, and iii) toxicity of materials like lead-containing compositions and solvents used during fabrication.[26–30] These challenges might be addressed with suitable material selections and advanced deposition processes.

Lamination is proposed as a novel fabrication method for perovskite-based PVs that offer increased degrees of freedom in the choice of materials, deposition techniques, and architectures. Devices are fabricated in two independently prepared half-stacks, subsequently united in a hot-pressing process. Lamination at high temperatures and pressures promotes the recrystallization of the polycrystalline perovskite thin film and creates an electrical contact at the interface between the half-stacks. While PSCs are conventionally produced via sequential layer deposition, lamination decouples the functional layer processing. Typical processing limitations, such as solvent incompatibilities and overheating, are thus overcome when depositing a material onto another. The possibility to explore novel material combinations and scalable deposition techniques that are otherwise incompatible, facilitates the transition to industrial-scale manufacturing processes. Moreover, the perovskite recrystallization triggered via hot-pressing can improve its morphology and crystallinity, enhancing device performance and stability over time. This method thus offers novel possibilities to address remaining challenges of perovskite PVs, especially long-term stability and upscaling of active surfaces to industrially relevant sizes. Extended flexibility in device architecture is also promising for fabricating perovskite-based tandem solar cells. Monolithic perovskite/silicon tandems are special in that regard, as they involve challenges such as multi-layer designs, light management, and current-matching requirements for high PCEs. In conclusion, lamination opens up new space for application and optimization in perovskite PVs. The following research questions are strategically selected:

1. **Recrystallization process**: How can the quality of perovskite absorbers, in terms of crystallinity and morphology, be enhanced by adjusting lamination pressure, temperature, and processing duration while preventing degradation?
2. **Device performance**: How do improved morphology and crystallinity of perovskite absorbers impact the performance and stability over time of laminated perovskite solar cells?
3. **Application versatility**: To what extent is the lamination technique relevant for supporting research of new materials, deposition processes, and device architectures in perovskite-based photovoltaics?
4. **Tandem technology**: How suitable is the presented lamination process for fabricating monolithic perovskite/silicon tandem solar cells, particularly in addressing multi-layer designs, light management, and current-matching requirements among subcells?

This work is dedicated to answering these questions in a detailed and structured way. **Chapter 2** presents fundamentals of perovskite semiconductors, PV principles, and technological concepts such as tandems. **Chapter 3** describes methods employed for fabricating and characterizing thin films and perovskite-based solar cells, with a focus on the lamination process. This chapter also outlines the procedure for assessing hot-pressed perovskite characteristics. **Chapter 4** targets Question 1 by qualitatively evaluating perovskite recrystallization as a function of applied pressure, temperature, and processing duration. Crystallinity and surface morphology are assessed to identify triggers for permanent recrystallization in polycrystalline thin films, such as grain growth and decreased surface roughness. Meanwhile, perovskite decomposition is monitored to define process windows preventing material degradation. By examining optoelectronic characteristics of hot-pressed perovskite films and interfaces with adjacent functional layers, this chapter also provides insights relevant to Question 2. **Chapter 5** addresses this question more directly by presenting fully laminated single-junction PSCs. The comparison with conventionally produced devices highlights intrinsic changes in light management and achieved performance. Long-term and thermal measurements under continuous illumination characterize the operational stability of laminated PSCs. Moreover, as described within the scope of Question 3, various proof-of-concept architectures are presented, such as semi-transparent devices, paving the way for fabricating tandem solar cells. In that regard, lamination is shown to offer numerous advantages in fabricating perovskite-based tandems through increased freedom in material combinations. **Chapter 6** explores this feature by demonstrating the first prototypes of laminated perovskite/silicon monolithic tandem solar cells as a proof of concept, responding to Question 4. This chapter also delves into the challenging light management of monolithic tandems. The focus is on improving the front layers transparency to enhance light transmission to the absorber and perovskite engineering to reach a current-matching condition among subcells. Finally, **Chapter 7** summarizes key findings of this work and evaluates the extent to which research questions have been answered. **Chapter 8** highlights perspectives for future developments in laminated perovskite PVs.

2 Fundamentals

Theoretical principles and concepts essential for this work are presented in the following. Crystallographic and optoelectronic characteristics of perovskite semiconductors are discussed in Section 2.1. The working principle of solar cells and photovoltaic characteristics are examined in Section 2.2, with an explicit reference to PSCs. Section 2.3 details the maximum theoretical efficiency of a single-junction solar cell – imposed notably by semiconductor physics – and describes a technological concept that can exceed this fundamental limit: multi-junction PVs.

2.1 Organometal halide perovskite absorbers

2.1.1 Crystallographic characteristics of perovskite materials

The term perovskite originates from the characteristic ionic crystal structure in ABX_3.[31] Usually described in a cubic unit cell shown in Figure 2.1, this crystal structure consists of BX_6 octahedrons with B cations

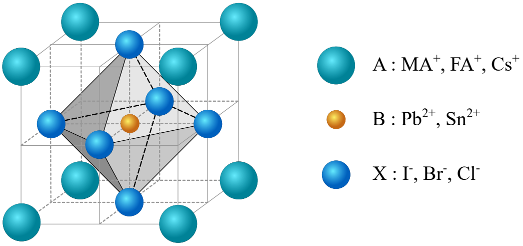

Figure 2.1: Perovskite crystal structure in ABX_3 represented in a cubic-unit cell. Common ions for A, B, and X sites used in absorbers for solar cell application are given. FA^+ and MA^+ stand for methylammonium ($CH_3NH_3{}^+$) and formamidinium ($HC(NH_2)_2{}^+$).

and X anions, forming a network with A cations in octahedral vacancies. Ions must fulfill size-ratio constraints to allow the perovskite structure formation, schematically indicated by different sphere sizes in Figure 2.1. Two factors determine whether an ion mixture of A, B, and X can form a perovskite structure depending on the ionic radius: the Gold-Schmidt tolerance factor (t_f) and the octahedral factor (μ), determined from equation (2.1).

$$\begin{cases} t_f = \frac{r_A + r_X}{\sqrt{2(r_B + r_X)}} \\ \mu = \frac{r_B}{r_X} \end{cases} \tag{2.1}$$

Where r_A, r_B, and r_X are ionic radii of ions A, B, and X, respectively. Perovskite crystal structures appear stable if t_f approximately ranges between 0.8 and 1.[31,32] There is also a lower size limit of the BX_6 octahedron with a $\mu > 0.4$ condition to ensure structural stability.

In perovskite semiconductors designed for PV applications, the A-site cation generally comprises organic molecules such as methylammonium ($CH_3NH_3^+$, denoted MA^+), formamidinium ($HC(NH_2)_2^+$, denoted FA^+), and inorganic cations, e.g., cesium (Cs^+) and rubidium (Rb^+). The B-site cations are typically occupied by lead (Pb^{2+}) and tin (Sn^{2+}). Common X anions are iodide (I^-), bromide (Br^-), and chloride (Cl^-). Perovskite compositions can combine several anions and cations with specific ratios to adjust optoelectronic characteristics. This tunability is one of the key advantages of the perovskite technology. Materials with more than one A-site cation are called multi-cation. Prominent examples are double-cation perovskites $Cs_{0.17}FA_{0.83}Pb(I_{0.92}Br_{0.08})_3$ and triple-cation $Cs_{0.05}MA_{0.22}FA_{0.73}Pb(I_{0.77}Br_{0.23})_3$. The term “perovskite” in this work is a simplified synonym for this material class of organometal halide perovskites.

Perovskite crystal structures depend on temperature and stoichiometry, and are determined by the arrangement of cations and anions, resulting in orthorhombic, tetragonal, and cubic phases. Single-cation perovskite materials usually suffer from thermal or structural instabilities. The archetypal methylammonium lead iodide ($MAPbI_3$) perovskite typically undergoes two phase transitions, one at around -113 °C from orthorhombic to tetragonal structure and a second to cubic at $\approx$55 °C .[33] $FAPbI_3$ and $CsPbI_3$ compositions also lack structural stability as they can crystallize in a photoactive phase at high temperatures but tend to revert into a photoinactive, non-perovskite phase at room temperatures.[33–35] In contrast, cation mixtures generally demonstrate stable structures over a wide range of temperatures.[34,36] This structural stability is crucial for applications in the PV field, as solar cells must sustain significant temperature variations in outdoor operation conditions. Triple-cation mixtures used in this work with Cs^+, MA^+, and FA^+, crystallizing in a stable cubic perovskite phase, are particularly promising, yielding a superior material with high thermal stability for PSCs.[34]

2.1.2 Optoelectronic characteristics of perovskite absorbers

The suitability of a semiconductor for application as an absorber in a solar cell depends on its optoelectronic characteristics. A longer diffusion length than the absorber thickness, implying that free charge carriers generated in the absorber can move towards contact layers before recombining, makes good PV materials. A high absorption coefficient is also advantageous so that a thin absorber layer is sufficient to efficiently absorb the incident light. In addition to reducing the amount of required material and device weight, thin-film absorbers enable the fabrication of bendable solar cells, facilitating the integration of PVs in buildings and mobile applications.[37] Among semiconductors, perovskite materials exhibit outstanding characteristics that are highly valuable for optoelectronic components, such as light-emitting diodes (LEDs), lasing, and solar cells.[38–40] In contrast to crystalline silicon (Si), which has an indirect bandgap requiring phonon mediation for the photon absorption process, perovskites are direct bandgap semiconductors.[41] A broad spectrum of bandgaps ranging from 1.1 to 2.3 eV are achieved through compositional engineering. Replacing the halide ion I^- by Br^- results in a wider bandgap,[19,20] and partially or entirely substituting Pb^{2+} with Sn^{2+} narrows it.[21–23] For instance, a bandgap of about 1.55 eV is reported for $MAPbI_3$ compositions, while $MAPbBr_3$ achieves approximately 2.3 eV.[38,42] This bandgap tunability over a wide energy range makes perovskites particularly interesting for applications in tandem solar cells.

As a direct bandgap suggests, perovskite absorbers exhibit a high absorption coefficient, with reported values similar to those in thin-film PV technologies with gallium arsenide (GaAs) and cadmium telluride (CdTe), and an order of magnitude higher than in crystalline silicon.[38,43] A 220 nm thin $MAPbI_3$ film demonstrated absorption coefficients exceeding 10^4 cm^{-1} in the visible wavelength range.[38] Through a high absorption coefficient, a thin perovskite layer of a few hundred nanometers is sufficient in PSCs, which is around three orders of magnitude thinner than standard silicon solar cells. PSCs with absorbers thinner than 800 nm can thus achieve PCEs exceeding 25%, which is unprecedented in the history of thin-film PVs.[44–49]

Perovskites are also described as materials with outstanding charge carrier diffusion lengths, which have been measured in the micrometer range, both in single crystals and polycrystalline films.[50] Remarkably, these optoelectronic characteristics are even retained in the presence of inhomogeneities such as ionic vacancies, which is interpreted as a high tolerance to intrinsic defects.[51,52] These superior optoelectronic characteristics, including tunable bandgap, high absorption coefficient, long diffusion length, and tolerance to intrinsic defects, make perovskite materials excellent absorbers for solar cells, either in single-junction or in tandem architectures.

2.2 Perovskite solar cells

2.2.1 Working principle of perovskite solar cells

Solar cells are a class of optoelectronic devices which utilize the photovoltaic effect to convert the energy of incident light into electrical energy.[53] The following discussion details the basic working principles of PSC operation. First, the absorption process of incident photons is described. The second part discusses how the voltage arises from a difference in the electrochemical potential of charge carriers between the two contacts. Next, this discussion outlines how the current originates from the selective extraction of charge carriers at the contact layers, leading to a directional flow of the charge carriers. The final section describes the current-voltage relation, including extreme conditions and the production of electrical power through the simultaneous generation of current and voltage under illumination and with a connection to an external load.

The energy conversion process in a PSC is illustrated in Figure 2.2a, where the perovskite is the intrinsic semiconductor sandwiched between an electron transport layer (ETL) and a hole transport layer (HTL), in contact with the respective electrodes. First, an electron from the valence band is energetically excited by an incident photon and lifted to the conduction band. This absorption process can only occur if the photon energy exceeds the semiconductor bandgap: $E_\gamma \geq E_\mathrm{g}$. Photons with lower energy are transmitted through the material.

The generated free charge carriers in the perovskite can be driven by two principal forces.[54] A gradient in the chemical potential (concentration gradient) leads to diffusion. A gradient in the electrical potential (electric field) leads to charge carrier drift. The sum of the chemical and electrical potential is the electrochemical potential. In a semiconductor at the thermodynamic equilibrium (in the dark), the electrochemical potential of electrons corresponds to the Fermi level, i.e. the energy level

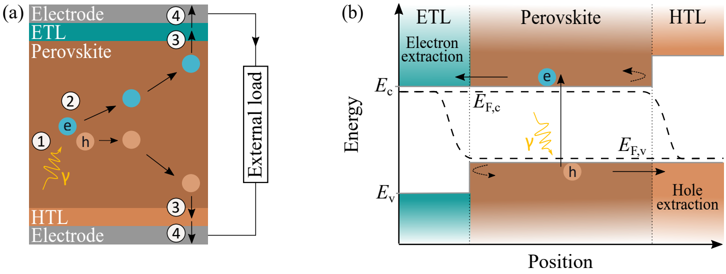

Figure 2.2: Incident light energy conversion into electrical energy in a perovskite solar cell. a) Device illustration with a perovskite absorber positioned between an electron transport layer (ETL) and a hole transport layer (HTL), both connected to respective electrodes. (1) The incident photons enter the absorber layer. (2) Creation of free charge carriers upon photon absorption. (3) Selective extraction of the electrons at ETL and holes at HTL interfaces. (4) Charge carriers transport to respective electrodes. b) Idealistic band diagram of a perovskite solar cell under illumination and at open-circuit condition, leading to quasi-Fermi level splitting into a quasi-Fermi level of electrons ($E_{\mathrm{F,c}}$) and holes ($E_{\mathrm{F,v}}$). Photon absorption results in the excitation of an electron from the valence band (E_{v}), lifted into the conduction band (E_{c}).

with a 50% occupation probability, according to the Fermi-Dirac distribution. In a solar cell under illumination, the semiconductor is brought out of this equilibrium due to the generation of free charge carriers, so that the state occupation can no longer be described by a single Fermi level. Nevertheless, each band can be considered in a steady state,[54] and the Fermi level splits into quasi-Fermi levels, corresponding to the electrochemical potential of the electrons in the conduction band (E_{c}), and the holes in the valence band (E_{v}). Figure 2.2b illustrates this quasi-Fermi level splitting. The quasi-Fermi level for electrons ($E_{\mathrm{F,c}}$) is closer to E_{c} than in the dark due to the increased electron density in the conduction band. Meanwhile, the quasi-Fermi level for holes ($E_{\mathrm{F,v}}$) nears E_{v} due to the increased hole density in the valence band. The difference between the quasi-Fermi levels is the maximum voltage that the solar cell can achieve.

The free charge carriers are selectively extracted at the ETL (electrons) and HTL (holes). The interfacial charge transport at the perovskite/ETL interface is optimum when the E_{c} of the ETL is similar or slightly lower than that of the perovskite layer. Meanwhile, the E_v of the ETL must be significantly different than that of the perovskite to hinder the extraction of holes on this side (dashed arrow in Figure 2.2b). Conversely, an ideal HTL has a similar E_v compared to that of the perovskite layer and a significant difference in E_c. A good energy alignment is important to reduce non-radiative recombination losses that would decrease the quasi-Fermi level splitting. It is noted that contact selectivity is key to device performance in all types of solar cells, and different technical solutions have been developed to improve the charge carrier extraction and prevent recombination losses, e.g., with surface treatments in PSCs,[55] and with tunnel oxide passivation layers in TOPCon silicon solar cells.[56]

Under illumination and open-circuit conditions, the difference between the two quasi-Fermi levels of electrons at the cathode (left) and holes at the anode (right) defines the external open-circuit voltage (V_oc).[57] It is noted that the V_oc is reduced by non-radiative recombination losses, as discussed in Section 3.2.2, and an imperfect selectivity of the contact layers. Under illumination and short-circuit conditions, the generated charge carriers are efficiently extracted at CTLs without accumulation at the conduction and valence bands. In these conditions, the Fermi level equilibrates across the heterojunction, and the photocurrent reaches its maximum value, the so-called short-circuit current density (J_sc). Under operational conditions, i.e. illumination and connected to an external load, the solar cell cell operates between these two extrema (short-circuit and open-circuit conditions). The product of the generated current and voltage under operating conditions is the power output of the solar cell. For an ideal solar cell, the current-voltage relation can be derived from equation (2.2), considering the generation and recombination rates.

$$J = e\int_0^d (R - G)dx \tag{2.2}$$

Where J is the current density, d is the absorber thickness, e is the elementary charge, and x is the position. The generation rate (G) is divided into G_0 in the dark, and ΔG, corresponding to the absorption of photons with $E_\gamma \geq E_\mathrm{g}$ under illumination. The recombination rate (R) is expressed in equation (2.3).

$$G = G_0 + \Delta G \;; \quad R = R_0 \left(e^{\frac{E_{F,c} - E_{F,v}}{k_B T}} \right) = R_0 \left(e^{\frac{e \cdot V}{k_B T}} \right) \tag{2.3}$$

Where R_0 is the recombination rate in the dark, e is the elementary charge, k_B is the Boltzmann constant, and T is the temperature. $E_\mathrm{F,c}$-$E_\mathrm{F,v}$ is the difference between the quasi-Fermi levels of charge carriers in the conduction and valence bands, which corresponds to the voltage V. In the dark, it becomes evident that $R_0 = G_0$, so the current density of equation (2.2) can be written:

$$J = e \int_0^d G_0 dx \cdot \left(e^{\frac{e \cdot V}{k_B T}} - 1 \right) - e \int_0^d \Delta G dx \tag{2.4}$$

Under short-circuit conditions (V=0), the term corresponding to the short-circuit current density (J_sc) can be identified, while the dark saturation current density (J_0) is identified in the dark. The resulting current density-voltage characteristics of an ideal solar cell thus becomes:

$$J = J_{sc} - J_0 \left(e^{\frac{e \cdot V}{k_B T}} - 1 \right) \tag{2.5}$$

2.2.2 Photovoltaic characteristics of solar cells

The current-voltage characteristics of an ideal solar cell was given in equation (2.5). A comparison with the Schockley equation for the electrical description of a diode shows that an ideal solar cell can be represented by an equivalent circuit consisting of a current source in parallel with a diode. In the dark, the voltage-dependent current (I-V) corresponds to the diode current (I_{diode}), following the Shockley diode equation:

$$I_{diode} = I_0 \left(e^{\frac{eV}{n_{id} k_B T}} - 1 \right) \tag{2.6}$$

Where I_0 is the diode saturation current, e is the elementary charge, V is the voltage, k_{B} is the Boltzmann constant, T is the temperature, and n_{id} is the ideality factor, which will discussed in Section 3.2.2.

Under illumination, the photocurrent (I_{ph}) generated by the solar cell is added to the dark current, flowing in the opposite direction:

$$I = I_{ph} - I_0 \left(e^{\frac{eV}{n_{id} k_B T}} - 1 \right) \tag{2.7}$$

The resulting I-V curve, which is exponentially related to the voltage, is graphically shifted by the superposition of the photocurrent. Figure 2.3a

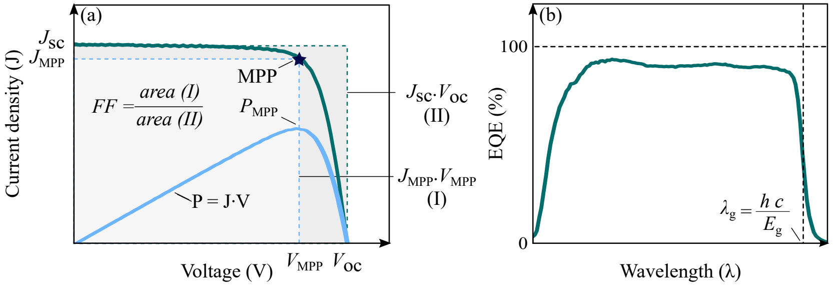

Figure 2.3: Photovoltaic characteristics of a solar cell. a) Current density - voltage curve. The output power (P) per area is the product of current density (J) and voltage (V). The J_{sc} and V_{oc} are defined at zero voltage and zero current, respectively. The maximum power point (MPP) is achieved when the product of current density and voltage is maximum. The corresponding current density is denoted J_{MPP} and voltage V_{MPP}, yielding a power output P_{MPP}. The fill factor (FF) is graphically described by the ratio of the area (I) – the product J_{MPP} and V_{MPP} – and area (II) – the product J_{sc} and V_{oc}. b) External quantum efficiency (EQE) of a typical perovskite solar cell. EQE exponentially decreases to zero for photon energy lower than absorber bandgap (E_{g}, corresponding to a wavelength λ_{g}). h and c stand for the Planck constant and the speed of light in a vacuum, respectively.

displays a typical PSC measurement. Short-circuit current density and open-circuit voltage are obtained when voltage and current are zero, respectively. Power output per area (P) is defined as the product of voltage and current density. The highest power is reached at the so-called maximum power point (MPP), where the product of current and voltage is the highest. The power conversion efficiency (PCE) of solar cells is determined using equation (2.8), the ratio of electrical output power at maximum power point (P_{MPP}) and incident light power (P_{in}) per area.

$$PCE = \frac{P_{MPP}}{P_{in}} = \frac{J_{MPP} \cdot V_{MPP}}{P_{in}} = \frac{FF \cdot J_{sc} \cdot V_{oc}}{P_{in}} \tag{2.8}$$

The fill factor (FF) is defined in equation (2.9), where J_{MPP} and V_{MPP} are the current and voltage at MPP, respectively. Graphically, the FF is described as the area ratio under the MPP to the product of V_{oc} and J_{sc}, as illustrated in Figure 2.3a. The FF is lowered by serial resistances and recombination losses and typically ranges from 70 to 85%.

$$FF = \frac{P_{MPP}}{J_{sc} \cdot V_{oc}} = \frac{J_{MPP} \cdot V_{MPP}}{J_{sc} \cdot V_{oc}} \tag{2.9}$$

Where P_{MPP} is the maximum power point at current density J_{MPP} and voltage V_{MPP}, J_{sc} is the short-circuit current density, and V_{oc} is the open-circuit voltage.

The external quantum efficiency (EQE), defined as the ratio of the number of collected electrons (N_{e}) to the number of incident photons (N_{γ}) in equation (2.10), characterizes the spectral response of a solar cell.

$$EQE = \frac{N_e}{N_\gamma} \tag{2.10}$$

A typical EQE measurement of a PSC is shown in Figure 2.3b. The difference between an ideal EQE reaching 100% and the real device is notably due to optical losses (e.g., reflected light at the front surface) and recombination losses. EQE characterization also enables the J_{sc} determination using equation (2.11).

$$J_{sc} = e \int EQE(\lambda) \cdot \Phi_{AM1.5}(\lambda)\, d\lambda \tag{2.11}$$

Where e is the elementary charge, $\phi_{\mathrm{AM1.5}}$ is the photon flux density at the standard AM1.5G solar spectrum, and λ is the wavelength.

The simplest equivalent circuit of a solar cell considering series and shunt resistances is the one-diode model, illustrated in Figure 2.4a. It is noted that more advanced models can be used, notably the two-diode model, which includes an additional diode to consider more complex recombination losses.[53] In the one-diode model, the current-voltage (I-V) characteristics are given by equation (2.12).

$$I = I_{ph} - I_0 \left(e^{\frac{e(V+I\cdot R_{series})}{n_{id} k_B T}} - 1 \right) - \frac{V + I \cdot R_{series}}{R_{shunt}} \tag{2.12}$$

Where I_{ph} is the photocurrent, I_0 is the diode saturation current, e is the elementary charge, n_{id} is the ideality factor, k_{B} is the Boltzmann constant, and T is the temperature. Parallel resistance (R_{shunt}) and series resistance (R_{series}) represent electrical losses in devices caused by shunt paths and ohmic resistances, respectively. An estimate for R_{series} and R_{shunt} can be determined from the slope of the I-V characteristics at V=0 (I_{sc}) and at $V = V_{\mathrm{oc}}$ (Figure 2.4b), corresponding to equation (2.13).[53]

$$\begin{cases} R_{series} = - \frac{\Delta V}{\Delta I}\Big|_{V=V_{oc}} \\ R_{shunt} = - \frac{\Delta V}{\Delta I}\Big|_{V=0} \end{cases} \tag{2.13}$$

Figure 2.4c shows the influence of an increased R_{series} on I-V characteristics. While V_{oc} and I_{sc} remain unchanged, the FF decreases significantly. In the case of a lower R_{shunt}, the FF is significantly reduced,

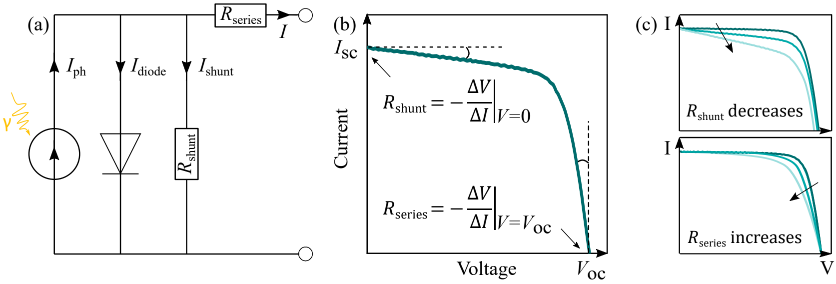

Figure 2.4: Consideration of series and shunt resistances in a solar cell. a) Equivalent circuit of a solar cell in the one-diode model. The current output (I) depends on the generated photocurrent (I_{ph}), diode current (I_{diode}), and parallel current (I_{shunt}). b) Estimation of the parallel resistance (R_{shunt}) and series resistance (R_{series}) from the slope of the current-voltage curve at $V{=}0$ (I_{sc}) and $V{=}V_{\mathrm{oc}}$, respectively. c) Current-voltage characteristics with increasing R_{series} and reducing R_{shunt}. Both decrease the FF and, thereby, the power output. When R_{shunt} is significantly reduced, the V_{oc} also decreases.

and the V_{oc} is also negatively affected. Low shunt resistances result, for instance, from short circuits through pinholes in the absorber, at grain boundaries, and defects in the bulk. High series resistances are due to limited layer conductivity (e.g., electrodes) and interfaces in the device architecture.

2.2.3 Device architectures and conventional fabrication techniques

Predominant architectures in current perovskite research are planar and mesoscopic PSCs, both demonstrating PCEs exceeding 25%.[45–49,58] This work focuses on planar PSCs, in which the absorber material is positioned between a HTL and ETL, in contact with respective electrodes. Two device architectures are distinguished depending on the illuminated side: Light enters from the ETL side in n-i-p structure (Figure 2.5a) and from the HTL in p-i-n (Figure 2.5b). The front electrode must be transparent and typically consists of a transparent conductive oxide (TCO). In opaque PSCs, the rear electrode is usually a metal layer of silver (Ag), gold (Au), or copper (Cu). A TCO can replace the rear opaque metal contact to obtain semi-transparent PSCs, as illustrated in Figure 2.5c. The electrode conductivity must be high for an efficient transport of the charge carriers.

The choice of CTL must consider numerous factors. For the selective extraction of electrons, a suitable ETL should have a conduction band aligned to that of the absorber layer, a significant difference in the valence band energy, a high electron conductivity, and a low hole conductivity, as discussed in Section 2.2.1. Conversely, a suitable HTL for the selective extraction of holes should have a valence band aligned with that of the perovskite, a significant difference in the conduction band energy, a high hole conductivity, and a low electron conductivity. Beyond their electrical characteristics, the optical transparency of functional layers is critical for device performance. Light transmission through the front layers must be high to prevent parasitic absorption and thus maximize photon absorption in the perovskite.[59–63] Moreover, the device architecture must demonstrate sufficient thermal and long-term stability to ensure that solar cells maintain a reliable power output under operating conditions. Indeed, light and temperature can trigger or accelerate degradation processes within PSCs. The degradation processes are notably related to chemical and structural instabilities of the absorber material, such as ion migration, chemical interactions with adjacent functional layers, or phase transitions in the temperature range relevant to PV operating

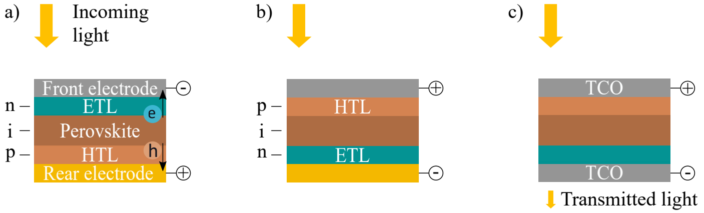

Figure 2.5: Established architectures for planar perovskite solar cells (PSCs). a) Illustration of the n-i-p structure, where light enters the electron transport layer (n) first, perovskite (i) and HTL (p). b) Light enters the HTL first in p-i-n architectures. c) In a semi-transparent PSC, the rear electrode is replaced by a transparent electrode, typically a transparent conductive oxide (TCO).

conditions.[64] In accordance with established protocols based on international summit on organic photovoltaic stability (ISOS) procedures, solar cells are hence subjected to testing under continuous illumination and at temperatures of up to 85 °C.[64]

Functional layers of a PSC are usually processed on top of each other, known as "sequential layer deposition" or "layer-by-layer deposition" techniques. Since these layers are particularly thin (CTLs: a few nanometers, electrodes: ≈100 nm, and perovskite absorbers: ≈500 nm), they are not self-supporting and must be deposited on a supporting substrate. The substrate is typically a rigid glass substrate. However, technological advancements enabled deposition onto flexible substrates such as polyethylene terephthalate (PET) foils, facilitating the creation of flexible and lightweight PVs.[37,65] Functional layers in PSCs are deposited using a variety of processes. Established methods are solution-based and physical vapor deposition, such as the sputtering technique (for TCOs and inorganic CTLs, e.g., nickel oxide, NiO_x) and thermal evaporation (for metal electrodes and CTLs, e.g. fullerene C_{60}). Most record PCEs for single-junction devices above 25% are based on spin-coated perovskites.[66] However, this solution-based coating technique can only produce perovskite films homogeneously over small areas, often restricted to a few square centimeters. Scalable deposition methods have, therefore, received sustained attention in recent research for perovskite-based PVs, and promising successes were achieved through thermal co-evaporation,[67,68] inkjet printing,[69,70] slot-die coating,[26,71,72] and blade coating.[73,74]

A wide variety of deposition methods for PSC fabrication broadens the range of applications compared to other established PV technologies. Nevertheless, the architecture-dependent process sequence of individual layers – either n-i-p or p-i-n – limits the choice of materials and deposition techniques compatible with device fabrication.[75] Some materials cannot be processed on the perovskite film, e.g., as the absorber or other sensitive underlying layers would be damaged due to incompatible solvents or excessive annealing temperatures. Thus, although both n-i-p and p-i-n architectures are considered equivalent and demonstrate high PCEs exceeding 25%,[45,46,49] different materials must be used, leading to distinct functional limitations.[75] Lamination is a promising – yet relatively underexplored – alternative for device fabrication that overcomes these processing incompatibilities. An overview of state-of-the-art techniques is outlined in Section 5.1. Unlike in standard sequential layer deposition, lamination involves processing PSCs in two independent half-stacks, which are subsequently assembled at a final stage. This work focuses on understanding and exploring the potential of this method, and corresponding advancements and challenges are discussed in the respective result sections.

2.3 Perovskite-based tandem solar cells

2.3.1 Theoretical efficiency limit of single-junction solar cells

A fundamental efficiency limit of single-junction solar cells is related to the band structure of semiconductors.[53] Only photons with sufficient energy ($E_\gamma \geq E_\mathrm{g}$) can interact with the semiconductor in an absorption process to create electron-hole pairs, as illustrated in Figure 2.6a. Photons with lower energy are primarily transmitted through the absorber and do not contribute to the energy conversion process. Although absorption of photons with higher energy than E_g can generate electron-hole pairs, the excess energy of charge carriers is dissipated as thermalization losses in the form of phonons, i.e. lattice vibrations.

For silicon solar cells (E_g=1.12 eV) under the AM1.5G solar spectrum, approximately 32% and 19% of incident solar radiation power is lost because of photon transmission and thermalization, respectively. Figure 2.6b displays the remaining part of the solar irradiance (49%) usable for electricity production. In the Shockley-Queisser model, quantifying

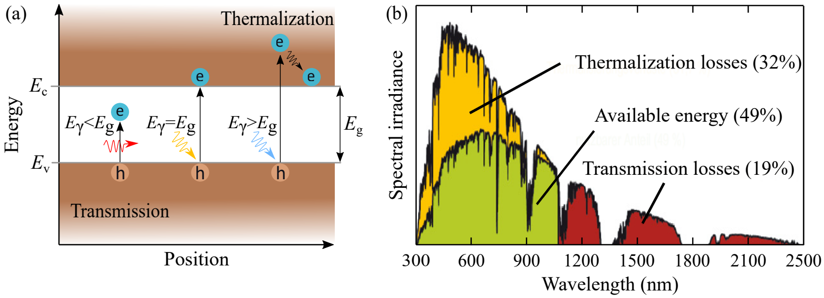

Figure 2.6: Photon interaction with a semiconductor absorber material depending on the photon energy (E_γ). a) Band diagram of a semiconductor with a bandgap energy (E_g). E_c and E_v stand for conduction and valence band, respectively. Photon transmission can occur when $E_\gamma < E_\mathrm{g}$. A photon absorption can create excitons if $E_\gamma \geq E_\mathrm{g}$. The excess energy when $E_\gamma > E_\mathrm{g}$ is released as thermalization losses in the form of phonons. b) Spectral irradiance utilization by a silicon solar cell at 1-Sun (AM1.5G). Photon transmission (red) and thermalization losses (yellow) represent 19% and 32% of the solar power that cannot be converted into electricity. The usable spectral irradiance for electricity production is colored green. Reproduced from reference[53].

the maximum theoretical efficiency of single-junction solar cells, this represents the so-called ultimate efficiency (υ),[76] which can be rationalized using the maximum current density (J_max), and maximum achievable voltage (V_max) in equation (2.14).

$$\upsilon = \frac{J_{max} \cdot V_{max}}{P_{in}} \tag{2.14}$$

Where P_in is the optical power of the incident light per area. The maximum current density (J_max) and voltage (V_max) are given in equation (2.15).

$$J_{max} = e \int_0^{\lambda_g} \Phi_{AM1.5}(\lambda) d\lambda \ ; \quad V_{max} = \frac{E_g}{e} \tag{2.15}$$

Where e is the elementary charge, $\Phi_\mathrm{AM1.5}$ is the photon flux density at the standard AM1.5G solar spectrum, and λ_g is the wavelength corresponding to the bandgap. For a silicon solar cell with E_g=1.12 eV, the

$J_{\max}$ is 44 mA/cm^2, and $V_{\max}$ 1.12 V, leading to an ultimate efficiency of 49% with an incident power of 100 W/cm^2. Similarly, for a PSC with E_{g}=1.63 eV, the $J_{\max}$ becomes 25 mA/cm^2, and $V_{\max}$ 1.63 V, yielding u=41%.

In their model, Shockley and Queisser also considered an impedance matching factor (a.k.a. the fill factor FF, defined in Section 2.2.2) and the fact that the voltage $V_{\max}$=E$_{\mathrm{g}}$/e cannot be reached in reality (temperature of the solar cell, $T_{\mathrm{c}}\neq 0$ K). The latter aspect is represented by the ratio $\nu = V_{\mathrm{oc}}/V_{\max}$. The maximum theoretical efficiency of a single-junction solar cell (η), which thus depends notably on E_{g} and T_{c}, can be written:[76]

$$\eta = t_s \cdot u \cdot FF \cdot \nu \tag{2.16}$$

Where t_{s} is the probability that a photon with $E_\gamma > E_{\mathrm{g}}$ produces an electron-hole pair (t_{s}=1 under the assumptions listed below). The detailed-balance limit of efficiency is 32.6% for silicon solar cells (E_{g}=1.12 eV) under test conditions (T_{c}=298 K, AM1.5G solar spectrum) and 29.6% for PSCs with a bandgap of 1.63 eV – used in this work.[77] It is noted that the Shockley-Queisser model builds on several assumptions: i) 100% absorption of photons with $E_\gamma \geq E_{\mathrm{g}}$, ii) 0% absorption of photons with $E_\gamma < E_{\mathrm{g}}$, iii) each photon absorption yields one electron-hole pair, iv) ideal selectivity of the contact layers with negligible ohmic resistance, and v) no non-radiative recombination losses. Introducing non-radiative recombination reduces the maximum achievable efficiency.[76,78] In this regard, models estimate an efficiency limit of 29.5% for 100 μm thick silicon solar cells when including, e.g., Auger recombination and parasitic free carrier absorption.[78,79] Additional effects, such as resistive, optical, and non-fundamental recombination losses, further restrain the practical efficiency of real devices.[80]

Numerous techniques have been explored to overcome the fundamental efficiency constraint of single-junction solar cells.[40,81–83] An established concept to overcome the detailed-balance limit consists of stacking solar cells with different bandgaps in so-called multi-junction devices. Today, this technology already achieved PCEs exceeding the single-junction limit with more than 34% in monolithic perovskite/silicon tandem solar cells.[25] Through reduced thermalization losses, the maximum theoretical limit increases with the number of absorber layers to 42% (for two), 49% (for three), and 68% (for an infinite number of absorber layers).[24] Combined with a light concentrator, the highest efficiency of a multi-junction architecture with an infinite number of layers theoretically improves to up to 86%.[24]

2.3.2 Principle and architectures of tandem solar cells

Multi-junction PV is an established concept for reducing fundamental loss mechanisms in single-junction devices, thereby exceeding the previously detailed Shockley-Queisser limit.[84,85] This technology combines two or more solar cells with different bandgaps.[53] In tandem devices, the top cell of bandgap $E_{\text{g-top}}$ can absorb photons with high energy ($E_{\gamma} \geq E_{\text{g-top}}$) for charge carrier generation and transmit the photons with longer wavelengths to the bottom cell, which has a narrower bandgap ($E_{\text{g-bottom}} < E_{\text{g-top}}$). The multi-junction device architecture allows for less i) transmission losses in the top cell through the additional absorption of photons with an energy below $E_{\text{g-top}}$ in the bottom cell, and ii) thermalization losses in the bottom cell due to the absorption of high-energy photons in the top cell. Solar irradiance is more efficiently used than in a single-junction architecture, increasing available solar energy for conversion into electrical energy.[86]

Two types of devices currently dominate research in tandem PVs: the four-terminal architecture and two-terminals, also referred to as monolithic devices.[87] While subcells in the first case are only optically coupled (e.g., superposed) and individually operated, they are optically and electrically connected in series in monolithic tandems. Both architectures are illustrated in Figure 2.7. The total PCE of four-terminals corresponds to the sum of individual subcell PCEs. In a monolithic

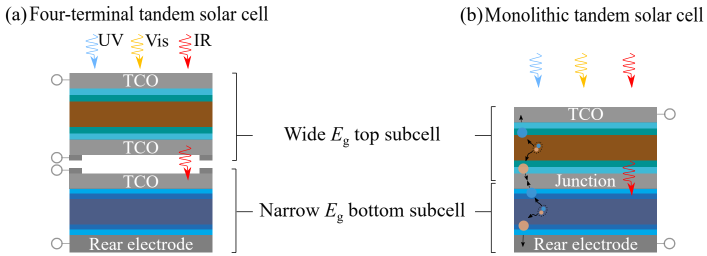

Figure 2.7: Typical tandem architectures, combining two subcells of wide and narrow bandgap (E_g). a) Four-terminal architecture, where subcells are superposed for optical connection and individually operated. Front electrodes of both subcells are usually made of transparent conductive oxide (TCO). b) Monolithic tandem architecture consisting of two subcells optically and electrically connected in series via a junction layer. In both architectures, ultraviolet (UV) and visible light (Vis) are efficiently absorbed in the top cell, while infrared photons (IR) are primarily absorbed in the bottom cell. Charge carriers are represented with colored circles (e.g., electrons in blue and holes in pink).

tandem solar cell, since subcells are connected in series, the current flowing in the device is limited by the lowest current of both subcells, and subcell voltages add up. Subcells are connected through a junction layer, where charge carriers from the top cell (e.g., electrons) recombine with the other type (holes) from the bottom cell. This junction layer is typically a 10 to 20 nm thin TCO electrode or a tunnel diode for reduced parasitic absorption losses.[88–92]

Each technology presents advantages and disadvantages in fabrication and operation.[93] On the one hand side, four-terminals benefit from the independent optimization and manufacture of both subcells. In monolithic devices, where the front cell is directly grown atop the bottom one, challenges remain in the subcell fabrication to preserve the already deposited layer stack, resulting in limitations in device architectures.[94] Current-matching requirements for optimal operation also restrict suitable bandgap combinations in monolithic devices compared to four-terminal architectures.[95] In addition, since each subcell is efficiently operated with individual MPP tracking systems, four-terminal devices are less sensitive to spectral variations of outdoor illumination compared to monolithic tandems.[96] On the other hand, despite the simplicity in manufacturing and operation, four-terminals require doubling electronic components, increasing the associated installation costs compared to monolithic tandems.[93,97] As a result, balance-of-system costs increase, negatively impacting the levelized cost of energy (LCOE) of the final installation. Moreover, optical coupling in four-terminal tandems involves more layers than monolithic devices, including an air gap or filling materials between subcells and an additional TCO film.[98] The transparent electrodes between subcells must be thicker or necessitate the introduction of metal grids for efficient charge carrier transport.[99] These requirements reduce the transmitted light to the bottom cell, highlighting challenges in achieving optimal optical coupling.

The tunability of the perovskite bandgap over a wide energy range from 1.1 to 2.3 eV through compositional engineering allows for numerous material combinations.[19–23] A bandgap above 1.5 eV is suitable for the top PSC in a tandem device with crystalline silicon and copper indium (gallium) selenide ($CuIn(Ga)Se_2$, denoted CI(G)S) bottom cells.[97] With a lower perovskite bandgap, the PSC can function as a low-bandgap bottom cell. All-perovskite tandems can thus be fabricated using pure Pb (wide $E_{\text{g-top}}$) and mixed Sn-Pb (narrow $E_{\text{g-bottom}}$) compositions in the top and bottom cells.[100] Calculation of the theoretical tandem efficiency as a function of top and bottom bandgap shows that optima can be found in the bandgap combination.[97] Generally, a top perovskite bandgap near 1.7 eV appears ideal for silicon and CI(G)S bottom cells.[87,96,97,101,102] Certified PCEs of 23.1% and 25% were achieved in monolithic and four-terminal tandems, respectively.[103] Both monolithic and four-terminal perovskite/silicon tandem solar cells recently demonstrated PCEs of over 30%, exceeding the highest certified efficiency of 27% for single-junction silicon solar cells.[104] Monolithic devices even overcome the maximum theoretical efficiency limit for single-junction devices with PCEs exceeding 34%.[13] Ultimately, monolithic perovskite/CI(G)S tandem solar cells were investigated, enabling high efficiencies, and flexible and lightweight PV.[105] Perovskite/CIS tandems notably exhibited PCEs approaching 25% and 30% in monolithic and four-terminal architectures, respectively.[106,107]

3 Experimental methods

This chapter details methods and processes involved in producing and characterizing perovskite-based solar cells in this work. Section 3.1.1 outlines device architectures with a particular focus on laminated PSCs and tandems. Functional layer materials, thicknesses, and deposition techniques are described in Section 3.1.2. Methodologies for hot-pressed perovskite investigation and device fabrication are presented in Section 3.1.3. Finally, characterization methods for thin films (Section 3.2.1) and solar cells (Section 3.2.2) are discussed, notably the measurement of current density-voltage characteristics of PSCs.

3.1 Fabrication methods

3.1.1 Device architectures of laminated perovskite-based solar cells

Single-junction perovskite solar cells

Reference PSCs consist of front and rear electrodes, CTLs, and a perovskite absorber. Functional layers are deposited on a 1 mm thick and (16x16) mm large glass substrate coated with a front TCO of indium tin oxide (ITO). The HTL comprises NiO_x and a self-assembled monolayer of [2-(9H-Carbazol-9-yl)ethyl]phosphonic acid (2PACz). The absorber layer deposited on the HTL has a triple-cation composition: $Cs_{0.1}(MA_{0.17}FA_{0.83})_{0.9}Pb(I_{0.83}Br_{0.17})_3$. After perovskite processing, a double ETL of C_{60} (C_{60}) and bathocuproine (BCP) is deposited. Edges of the front ITO electrode are exposed by swiping the perovskite using γ-butyrolactone (GBL, Merck). An Au electrode is deposited on the layer stack to complete the device. Figure 3.1a illustrates the device layout. Front and rear electrode overlap defines four active areas with a p-i-n architecture of approximately 10.5 mm^2.

Functional layers in laminated PSCs are deposited in two independent half-stacks, as displayed in Figure 3.1b-c. The front half-stack comprises the glass/ITO substrate, front CTL, and perovskite absorber. After exposing ITO edges by swiping the perovskite, Au stripes (denoted “metal contacts” in Figure 3.1b) are deposited. The rear electrode and CTL are deposited on (16x16) mm large polyethylene naphthalate (PEN) foils, which are subsequently cut into (16x14) mm superstrates. The half-stack overlap defines four active areas of about 10.5 mm^2 on each substrate. Cutting PEN foils smaller than glass substrates creates access to both front and rear electrodes, enabling laminated devices to be measured as conventional PSCs. Table 3.1 summarizes materials and architectures employed in this work. Laminated opaque PSCs have the same p-i-n architecture as the reference PSCs described above, except for

Table 3.1: Material selection and architectures of laminated perovskite solar cells. Triple-cation perovskites are employed as absorbers for all devices, except in Section 5.3.1, where a double-cation perovskite is used. ST stands for semi-transparent.

	Section 5.2.1	Section 5.2.2	Section 5.2.3	Section 5.3.3 to Section 5.5
Architecture	Opaque	ST	ST	Opaque
Orientation	n-i-p	p-i-n	n-i-p	p-i-n
Substrate	Glass	Glass	Glass	Glass
Front electrode	ITO	ITO	ITO	ITO
Front CTL	SnO_2-np	NiO_x, 2PACz	SnO_x, C_{60}	NiO_x, 2PACz
Absorber	Perovskite	Perovskite	Perovskite	Perovskite
Rear CTL	PTAA, NiO_x	C_{60}, SnO_x	2PACz, NiO_x	C_{60}, BCP
Rear electrode	Au	ITO	ITO	Au
Superstrate	PEN foil	PEN foil	PEN foil	PEN foil

the additional PEN foil that remains atop the device, offering a possible encapsulation function.

The $Cs_{0.1}(MA_{0.17}FA_{0.83})_{0.9}Pb(I_{0.83}Br_{0.17})_3$ triple-cation perovskite is used in laminated and reference PSCs. A $Cs_{0.17}FA_{0.83}Pb(I_{0.92}Br_{0.08})_3$ double-cation absorber is also employed in Section 5.3.1. Section 5.2.1 presents an n-i-p architecture combining inorganic CTLs. Tin dioxide nanoparticles (SnO_2-np) are used as ETL, and the HTL comprises NiO_x and poly(triarylamine) (PTAA). In semi-transparent PSCs, ITO transparent electrodes replace Au rear contacts. NiO_x and 2PACz are employed as double HTL. C_{60} and tin oxide (SnO_x) are used as double ETL.

Monolithic perovskite/silicon tandem solar cells

Laminated monolithic perovskite/silicon tandems are composed of a top PSC and a double-side polished heterojunction silicon (SHJ) solar cell provided by Forschungszentrum Jülich GmbH. The silicon solar cell has the following architecture: ITO (30 nm) / a-Si: H <n> layer ($\approx$4 nm) / a-Si: H <i> ($\approx$4 nm) / c-Si wafer <n> (280 μm) / a-Si: H<i> ($\approx$6 nm) / a-Si: H <p> ($\approx$12 nm) / ITO (70 nm). Device layouts are illustrated in Figure 3.1c. After lamination, the rear ITO electrode is manually covered with silver paste (Acheson 1415, Plano GmbH). The front stack is prepared on a superstrate (PEN foil or ultra-thin glass), where TCO and CTL are deposited. Three TCO types are investigated in this work: ITO, indium zinc oxide (IZO), and hydrogenated indium oxide (IO:H). Orientations of tandem devices in p-i-n or n-i-p depend on whether light enters first the HTL or ETL of the PSC, respectively. This convention implies that a p-i-n single-junction PSC becomes an n-i-p subcell in monolithic tandems. In both cases, a double HTL of NiO_x and a self-assembled monolayer of 2PACz is employed as HTL, and a double layer of C_{60} and SnO_x is used as ETL. In Sections 6.3.3 and 6.3.4, a passivation layer of lithium fluoride (LiF) is thermally evaporated on the C_{60} to reduce interfacial recombination. The triple-cation perovskite is either deposited on the front or rear half-

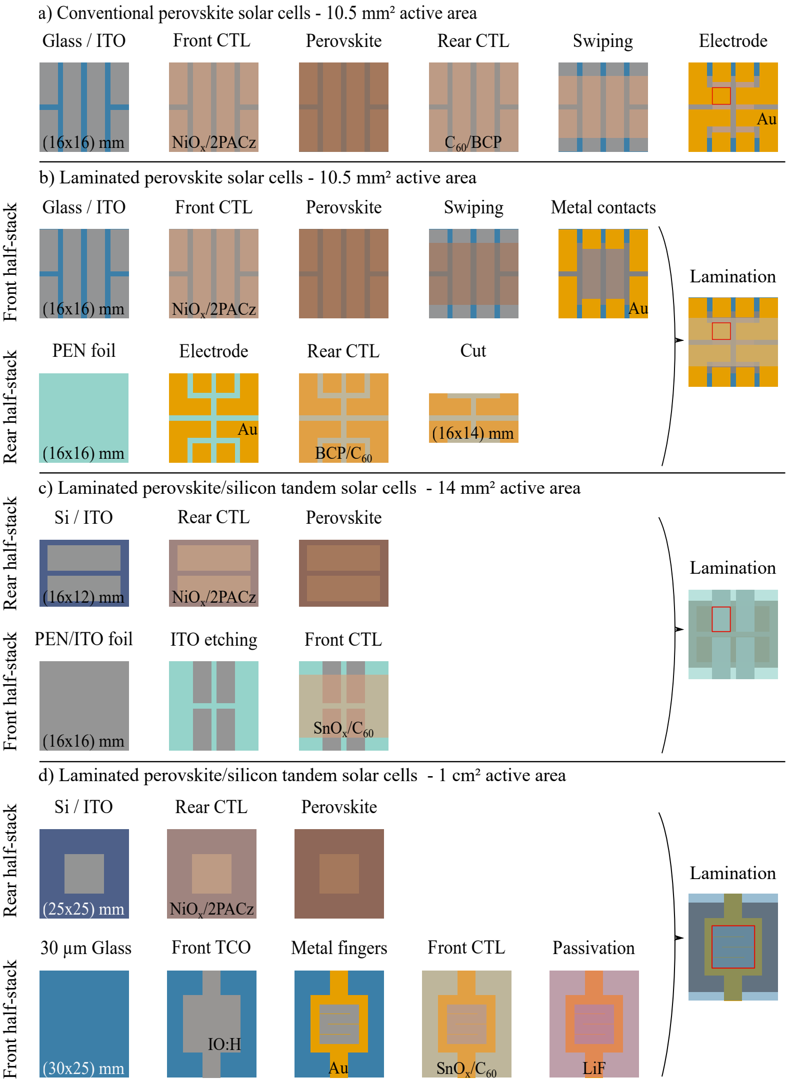

Figure 3.1: Architectures and layouts of perovskite-based solar cells. a) Conventionally fabricated, and b) laminated perovskite solar cells. c) Laminated monolithic perovskite/silicon tandems with an active area of 14 mm², and d) 1 cm². The red frame highlights the active area of a solar cell. Exemplary materials are indicated.

stack. Its composition is either $Cs_{0.1}(MA_{0.17}FA_{0.83})_{0.9}Pb(I_{0.83}Br_{0.17})_3$ or $Cs_{0.05}(MA_{0.23}FA_{0.77})_{0.95}Pb(I_{0.77}Br_{0.23})_3$ depending on the target bandgap: 1.63 and 1.68 eV, respectively. Table 3.2 summarizes materials and architectures used for laminated monolithic perovskite/silicon tandem solar cells. For the first proof-of-concept experiment in Section 6.2.1, di[2-chloro-*p*-xylylene] (Parylene C dimer) is additionally deposited on superstrate edges (not on the active area) to reinforce half-stack adhesion and prevent delamination after fabrication. Two layouts for laminated monolithic tandem devices were developed. The first type consists of four 14 mm² small active areas per SHJ substrate (Figure 3.1c). The second type exhibits a single, 1 cm² large active area on each substrate (Figure 3.1d). An additional Au metal grid (three fingers, each 150 μm wide and 200 nm thick) is evaporated on the front TCO in large tandems to improve conductivity. In both layouts, superstrates are larger than the SHJ solar cell to enable contacting the front TCO after lamination for measurement.

Table 3.2: Material selection and device architectures for laminated perovskite/heterojunction silicon (SHJ) monolithic tandem solar cells. In Section 6.3.2, IO:H, ITO, and IZO are used as transparent conductive oxide (TCO).

	Section 6.2	Section 6.3.2	Section 6.3.3 and 6.3.4	Section 6.3.4
Active area	14 mm²	14 mm²	1 cm²	1 cm²
Architecture	n-i-p	n-i-p	n-i-p	p-i-n
Superstrate	PEN foil	30 µm glass	30 µm glass	30 µm glass
Front electrode	ITO	TCO	IO:H, Au grid	IO:H, Au grid
Front CTL	SnO_x, C_{60}	SnO_x, C_{60}	SnO_x, C_{60}	2PACz, NiO_x
Passivation	Ø	LiF	LiF	LiF
Perovksite	1.63 eV	1.63 eV	1.63/1.68 eV	1.68 eV
Rear CTL	2PACz, NiO_x	2PACz, NiO_x	2PACz, NiO_x	SnOx, C_{60}
Junction layer	ITO	ITO	ITO	ITO
SHJ subcell	n-side up	n-side up	n-side up	p-side up

3.1.2 Thin-films deposition methods

Deposition techniques, material providers, and resulting thin-film thicknesses of functional layers are presented in this section. Processing conditions are maintained unchanged independently of the underlying layer stack and are, therefore, the same for conventional and laminated perovskite-based solar cells.

Super- and substrate preparation

Substrates used for hot-pressed perovskite investigation and PSC fabrication are 1 mm thick glasses coated with 140 nm ITO. The ITO layer of 15 Ω/sq sheet resistance is patterned via photolithography by the manufacturer Luminescence Technology Corp. (Lumtec), ensuring a precise electrode layout. For opaque laminated PSCs, a PEN foil of type TEONEX Q65HA provided by DuPont Teijin Films is used as a superstrate. Superstrates of 125 μm thick PEN foils with a 300 nm thick ITO coating from Peccell Technologies Inc. are used for semi-transparent laminated PSCs and tandem devices. The sheet resistance is similar to glass/ITO substrates with 15 Ω/sq. ITO etching is performed by defining the desired ITO pattern with protective masks and immersing PEN/ITO foils for 7 min in hydrochloric acid (HCl, 37% concentration in water, VWR). The 30 μm ultra-thin glass superstrates of type AF32 eco in laminated tandems are provided by Schott AG. All superstrates and silicon solar cells are thoroughly cleaned after cutting in ultrasonic baths of acetone (VWR) and isopropanol (VWR) for 10 min each. Additionally, glass and PEN/ITO substrates are treated immediately before the deposition of subsequent functional layers in oxygen (O_2) plasma at a power of 100 W for 3 min in a Femto plasma cleaner (Diener Electronics).

Opaque and transparent electrode deposition

In conventionally processed and laminated perovskite-based solar cells, Au (Junker Edelmetalle) opaque electrodes (75 nm), contacts (50 nm), and fingers (200 nm) are thermally evaporated through 150 μm thick shadow masks in a Vactec B.V. vacuum system. Depositions are performed at a rate of 1 Å/s and a process pressure of about $2{\cdot}10^{-6}$ mbar. Front TCO electrodes in laminated tandems are sputtered with a Pro Line PVD 75 from Kurt J. Lesker company. Three TCO types are investigated in this work: ITO, IZO, and IO:H (Kurt J. Lesker company). Substrates are neither actively cooled nor heated during sputtering. Shadow masks of 150 μm thickness are used to define the electrode layout. Table 3.3 summarizes deposition parameters for each TCO. The resulting ITO layers are about 150 nm thick with 19 Ω/sq sheet resistance after annealing for 15 min in an ambient atmosphere at 250 °C (initially 53 Ω/sq). The IZO thickness is approximately 150 nm, and the as-deposited sheet resistance of 66 Ω/sq is reduced to 48 Ω/sq after annealing for 30 min at 200 °C in nitrogen (N_2) atmosphere. IO:H layers exhibit a thickness of about 220 nm and sheet resistance of 25 Ω/sq. An annealing step was unnecessary to improve the IO:H conductivity or optical characteristics. Optical characterizations of the three TCOs are provided in Figure 3.4 as exemplary transmittance and reflectance measurements.

Table 3.3: Sputtering conditions of ITO, IZO, and IO:H materials. All depositions are performed in constant current mode.

	Deposition time	Source voltage	Source power	O_2 flow	Ar/H_2 flow	Pressure
ITO	2200 s	325 V	50 W	0.3 sccm	13 sccm	0.8 mTorr
IZO	682 s	130 V	190 W	0.2 sccm	17 sccm	1.1 mTorr
IO:H	4850 s	320 V	50 W	1.6 sccm	28 sccm	1.6 mTorr

Charge transport layers and passivation layer deposition

For the ETL of SnO_2-np, a 15% aqueous colloidal SnO_2 dispersion solution (Alpha Aesar) is diluted with deionized water to a final concentration of 2%. The solution-based deposition onto ITO substrates is conducted by spin-coating at a rotation speed of 4000 rpm for 30 s. Samples are subsequently annealed at 250 °C for 30 min in an ambient atmosphere. The resulting SnO_2-np layers are approximately 20 nm thick. C_{60} (Sigma Aldrich), BCP (Lumtec), and LiF (Sigma Aldrich) materials are thermally evaporated in a Vactec Coat 320 (Angstrom Engineering) at a chamber pressure of about $2 \cdot 10^{-6}$mbar. The deposition rate is 0.2 Å/s to achieve final layer thicknesses of approximately 20 nm C_{60} and 5 nm BCP. The 1 nm LiF passivation layer is deposited at a rate of 1 Å/s. Rotating substrates are neither actively cooled nor heated. The SnO_x deposition is performed via atomic layer deposition (ALD) in a Picosun R-200 Advanced (Picosun) with tetrakis(dimethylamido)tin(IV) (TDMASn, Strem) precursors and H_2O as a reactant. Depositions are conducted at 80 °C and count 300 cycles of 1.6 s TDMASn exposure, followed by a mixed Argon (Ar) and N_2 gas purging for 12 s, and 0.1 s H_2O exposure, followed by Ar/ N_2 purging for 16 s. Samples are then annealed in an N_2 atmosphere for 60 min at 100 °C. The deposited SnO_x layer thickness is approximately 35 nm, as measured on a silicon wafer.

For the HTL of PTAA (EM ex Korea Index), 0.8 mg is dissolved in 1 mL toluene (Sigma-Aldrich). Thin films of PTAA are deposited by spin-coating at a rotation speed of 5000 rpm for 30 s and subsequently annealed at 100 °C for 10 min in an N_2 atmosphere. NiO_x layers ($\approx$20 nm) are deposited via sputtering using Pro Line PVD75 from Kurt J. Lesker Company under radio frequency (RF) conditions at a power of 100 W with a 17 sccm Ar flow and at a process pressure of 1 mTorr. Substrates are neither actively cooled nor heated during deposition. Self-assembled monolayers of 2PACz (TCI) are deposited via solution-based processing. The precursor solution is prepared by dissolving 4 mg of 2PACz in 8 mL ethanol absolute (VWR). A thin layer of 2PACz is deposited by spin-coating at 3000 rpm rotation speed for 30 s with 1000 rpm/s acceleration rate, followed by an annealing step at 100 °C for 10 min in an N_2 atmosphere. Before 2PACz deposition on NiO_x, substrates are pretreated in an O_2 plasma for 30 s at 30 W using a Femto plasma cleaner (Diener Electronics).

Solution-based perovskite processing

The triple-cation perovskite $Cs_{0.1}(MA_{0.17}FA_{0.83})_{0.9}Pb(I_{0.83}Br_{0.17})_3$ is prepared according to Saliba et al.,[34] with following precursors: cesium iodide (CsI, Alfa Aesar), methylammonium bromide (MABr, GreatCell Solar), formamidinium iodide (FAI, GreatCell Solar), lead iodide (PbI_2, TCI) and lead bromide ($PbBr_2$, TCI). Two precursor solutions are prepared: i) 390 mg CsI is dissolved in 1 mL of dimethyl sulfoxide (DMSO, Sigma Aldrich), and ii) 172 mg FAI, 22.4 mg MABr, 507 mg PbI_2 and 73.4 mg $PbBr_2$ are dissolved in 1 mL solvent mixture of dimethylformamide (DMF, Sigma Aldrich) and DMSO in a 4:1 volume ratio. After complete dissolution, 88.9 μL of solution (i) is transferred into solution (ii). The final precursor solution is deposited on substrates using a two-step spin-coating method: first 1000 rpm for 10 s, then 6000 rpm for 20 s. The acceleration rate is 5000 rpm/s for both steps. After 13 s of the second step, 100 μL or 400 μL of chlorobenzene antisolvent (CB, Sigma Aldrich) is released on the rotating (16x16) or (25x25) mm substrate, respectively. Samples are subsequently annealed at 100 °C for 1 h in an N_2 atmosphere. The achieved perovskite film demonstrates a thickness of about 370 nm and a bandgap of 1.63 eV.

$Cs_{0.05}(MA_{0.23}FA_{0.77})_{0.95}Pb(I_{0.77}Br_{0.23})_3$ triple-cation perovskites exhibit a thickness of approximately 550 nm and a 1.68 eV bandgap. Two precursor solutions are prepared for a 1.53 mol/L molarity: i) 390 mg CsI is dissolved in 1 mL of DMSO, and ii) 558 mg PbI_2 is dissolved in 1 mL solvent mixture of DMF/DMSO in a 4:1 volume ratio. Solution (ii) is heated at 130 °C for 30 min. After complete dissolution, 50 μL of solution (i), 191 mg FAI, 38 mg MABr, and 137 mg $PbBr_2$ are added to solution (ii). The final precursor solution is deposited on substrates using a two-step spin-coating method: first 1000 rpm for 10 s with an acceleration rate of 2000 rpm/s, then 5000 rpm for 30 s with 2000 rpm/s. After 17 s of the second step, 150 μL or 450 μL of ethyl acetate antisolvent (AE, Sigma Aldrich) is released on the rotating (16x16) or (25x25) mm substrate, respectively. Samples are then annealed at 100 °C for 30 min in an N_2 atmosphere.

The double-cation perovskite $Cs_{0.17}FA_{0.83}Pb(I_{0.92}Br_{0.08})_3$ exhibits a film thickness of about 800 nm and a bandgap of 1.58 eV. A precursor solution is prepared with 622 mg PbI_2 and 64 mg $PbBr_2$ dissolved in 1 mL DMF/DMSO solvent mixture with a 4:1 volume ratio and heated at 130 °C for 30 min. After complete dissolution, 200 mg FAI, 62 mg CsI, and 8 mg urea (Sigma Aldrich) are added. The final precursor solution is deposited on substrates using a two-step spin-coating method: first 200 rpm for 2 s, then 2000 rpm for 30 s. The acceleration rate is 2000 rpm/s for both steps. After 12 s of the second step, 150 μL of AE antisolvent is released on the rotating (16x16) mm substrate. Samples are then annealed at 100 °C for 25 min in an N_2 atmosphere.

Additional functional layer deposition

In the proof-of-concept laminated monolithic perovskite/silicon tandem solar cells (Section 6.2.1), the device front side is coated with a magnesium fluoride (MgF_2, Sigma Aldrich) layer. This 125 nm thick antireflective coating is deposited via thermal evaporation in a Vactec Coat 320 (Angstrom Engineering) with a deposition rate of 0.2 Å/s and at a chamber pressure of about $5 \cdot 10^{-6}$ mbar. Parylene C dimer (Specialty Coating Systems) is deposited via vapor deposition polymerization in a Labcoter1, PDS 2010 system (Specialty Coating Systems). The dimer is sublimated, and pyrolytic cleavage is triggered at 690 °C. The resulting monomer polymerizes in an approximately 30 nm thin layer at room temperature in the vacuum chamber.

3.1.3 Lamination and hot-pressing processes

In this work, the lamination technique refers to uniting two individually prepared layer stacks by applying high pressures and temperatures. The hot-pressing process promotes perovskite recrystallization and creates an electrical contact at the interface between the half-stacks. This method is introduced to fabricate single-junction PSCs and monolithic perovskite/silicon tandem solar cells. The hot-pressing technique is also used to investigate perovskite recrystallization, providing insights into achieved material quality – morphology, crystallinity, and optoelectronic characteristics. For both applications, the machine and process sequence detailed in the following are identical.

Hot-pressing setup

Hot-pressing processes are conducted in an in-house developed hydraulic press named “Wum 2” and build in cooperation with Jenoptik Mikrotechnik (Figure 3.2a). The system is equipped with an oil heater and water cooling system. Although both plates (116 mm in diameter) are heated and cooled down during the process, only the bottom plate temperature is recorded and regulated within a ±2 °C range around the target value. Although the machine is located in ambient air, the sample and plates are enclosed in a vacuum chamber, which is evacuated to about $1{\cdot}10^{-3}$ mbar and filled with N_2 several times. These purge cycles remove oxygen and moisture from the chamber atmosphere, thereby preventing perovskite degradation during the hot-pressing process. Pressure is applied on the sample by moving the lower plate until contact with the fixed upper plate. The set pressure is calculated as measured force divided by the smallest surface in the layer stack.

Hot-pressing process

Figure 3.2b illustrates two exemplary hot-pressing processes at 80 °C and 120 °C. The heating rate is 10 °C/min, independent of the target temperature. In contrast, the cooling rate increases with temperature: -10 °C/min when cooling from 80 °C and -12 °C/min from 120 °C. These machine-specific rates imply that hot-pressed samples at 120 °C stay 5 min longer in the machine than at 80 °C. For consistency, processing duration refers to the period when pressure and temperature are applied simultaneously. Height process steps are distinguished for the exemplary lamination at 120 °C. After placing half-stacks and stamp on the bottom plate, the chamber closes. Pressure augments because the chamber springs are compressed (1). Heating starts in step (2) while the lower plate is lifted at 2 mm/min to a few millimeters away from the sample. Contact with the sample is made at a slower speed of 0.5 mm/min, yielding a sudden pressure increase (3). In step (4), the vacuum chamber is pumped down and flushed with N_2 several times (three cycles) to

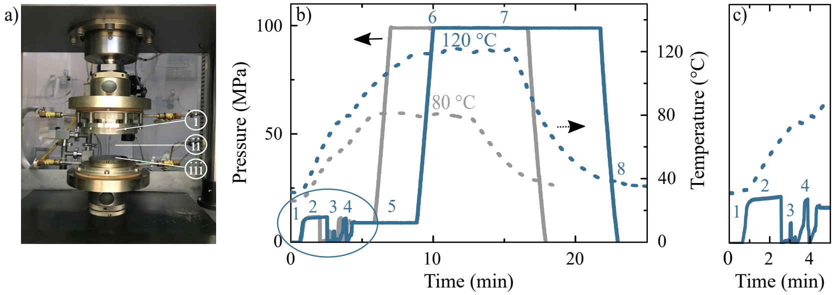

Figure 3.2: Insights into the hot-pressing process. a) Photograph of the hydraulic press used for hot-pressing and lamination: i) indicates the upper plate position, ii) vacuum chamber (currently open), and iii) lower plate. b) Typical hot-pressing processes at 80 °C (in grey) and 120 °C (in blue) under 100 MPa for 5 min. Applied pressure is shown in solid lines, while the temperature is displayed in dashed lines. Height steps are distinguished for the process at 120 °C. c) Detail of the first four steps, which correspond to closing and cleaning the chamber atmosphere. Step 5 is the heating phase. Steps 6 to 7 denote the effective hot-pressing duration, where temperature and pressure are simultaneously applied. The process is completed after releasing pressure and cooling to 40 °C (step 8).

remove moisture and oxygen. The pressure is kept constant until the target temperature is reached (5). Afterward, the lower plate is driven to apply 100 MPa for a given time, here 5 min (from steps 6 to 7). After cooling the sample to 40 °C (8), the lower plate is moved downwards, releasing pressure, and the chamber opens. A complete process from the heating to the cooling phase is performed in 20 to 25 min, depending on the target temperature. The corresponding lamination program is detailed in Table 9.1, Appendix. All hot-pressing and lamination processes performed in this work follow this procedure, and only the three parameters of pressure, temperature, and duration are adjusted.

Sample and stamp position during hot-pressing processes

The stamp position and half-stacks on the lower plate must be adjusted for each hot-pressing application, including the fabrication of laminated PSCs and tandems. Positioning half-stacks upwards or downwards must be considered to facilitate their alignment, although pressure distribution is identical in both cases. Therefore, the largest half-stack is typically placed on the lower plate. Figure 3.3 summarizes the configurations for hot-pressed perovskite, laminated PSCs, and tandems. A (14x14) mm

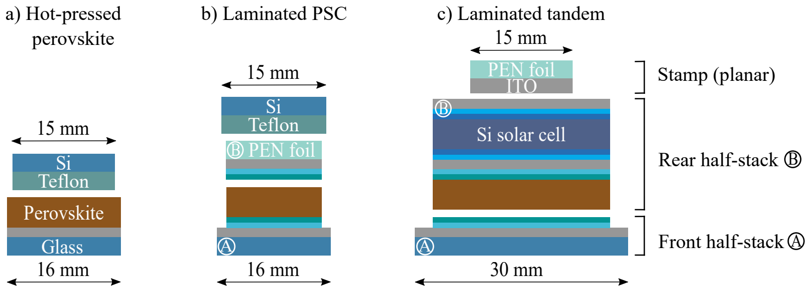

Figure 3.3: Sample positioning between the lower and upper plates of the hydraulic press. a) For hot-pressed perovskites on glass substrates, a Teflon-coated silicon stamp is positioned atop the absorber layer. b) For laminated perovskite solar cells (PSCs), the stamp is placed atop the PEN foil superstrate. c) For laminated perovskite/silicon tandems, the modified silicon solar cell and a stamp of PEN/ITO foil are placed atop the glass superstrate.

piece of silicon wafer with an anti-adhesive coating of polytetrafluoroethylene (PTFE, referred to as Teflon) is used and removed afterward to investigate hot-pressed perovskites. This silicon stamp offers a clean, perfectly flat surface, enabling homogeneous pressure distribution. It must be smaller than the (16x16) mm glass substrate. Otherwise, the stamp bends, and pressure cannot be applied to the sample center. The Teflon anti-adhesive coating layer prevents perovskite from sticking to the silicon stamp. For laminated PSCs, half-stacks building on a (14x15) mm PEN foil and the (16x16) mm glass substrate are first positioned atop each other, then a (15x16) mm Teflon-coated silicon wafer is placed atop the PEN foil. The stamp must be slightly larger than the flexible PEN foil to avoid inhomogeneous pressure distribution. For laminating perovskite/silicon monolithic tandem solar cells, the half-stack building on a (25x30) mm glass superstrate is placed on the lower plate, followed by the (25x25) mm modified silicon solar cell and (15x15) mm PEN/ITO stamp, covering the (10x10) mm active area in the sample center.

3.2 Characterization methods

3.2.1 Characterization of thin films

Atomic force microscopy

Atomic force microscopy (AFM) is performed with a NanoWizard II from JPK Instruments AG to visualize the as-deposited and hot-pressed perovskite surface morphology. Measurements are performed in an intermittent contact mode, where the cantilever oscillates close to its resonance frequency. The tip deflection related to the surface topology is monitored through reflection on a photodetector of a laser beam pointed at the cantilever. Piezoelectric elements regulate the cantilever height over the sample surface to maintain a constant oscillation amplitude.

The spatially resolved measurement with a resolution of a few nanometers thus allows the root mean square (RMS) roughness and grain size of perovskite surfaces to be determined. Images, typically (5x5) μm large with a resolution of (1024x1024) pixels, are processed with Gwyddion software. All RMS roughness values given in this work are calculated on an (3x3) μm area. Statistical grain size analysis is conducted using ImageJ software. The Feret diameter approximates grain size as the longest distance between two points along the selected boundary. The measurement uncertainty related to sample-to-sample variations is ±10 nm, as determined according to ISO/IEC 98-3:2008-09 guidelines.[108] For instance, pristine perovskites (as-deposited) exhibit a mean grain size of (270±10) nm.

Ultraviolet-visible spectroscopy

Optical characterization of thin films and solar cells is conducted in a PerkinElmer LAMBDA 1050 spectrophotometer equipped with an integrating sphere of 150 mm diameter and a dual light source of deuterium and tungsten halogen lamps. The studied spectral range extends from ultraviolet and visible wavelengths to near-infrared. PSCs are typically characterized from 300 to 850 nm, and perovskite/silicon tandem solar cells from 300 to 1250 nm, with a 5 nm step size. For transmittance or reflectance measurements, the device under test is placed in front of the integrating sphere on the optical path or rear side, respectively. Transmitted or reflected light from the sample is collected inside the integrating sphere and monitored by a Si/InGaAs photodiode detector. Figure 3.4 displays typical optical characterizations of in-house sputtered TCOs before and after a post-deposition annealing step. High temperatures of 250 °C trigger ITO recrystallization, yielding decreased parasitic absorption at short wavelengths. The absorptance (A) is indirectly determined from reflectance (R) and transmittance (T) measurements at each wavelength λ using equation (3.1).

$$A(\lambda) = 1 - R(\lambda) - T(\lambda) \tag{3.1}$$

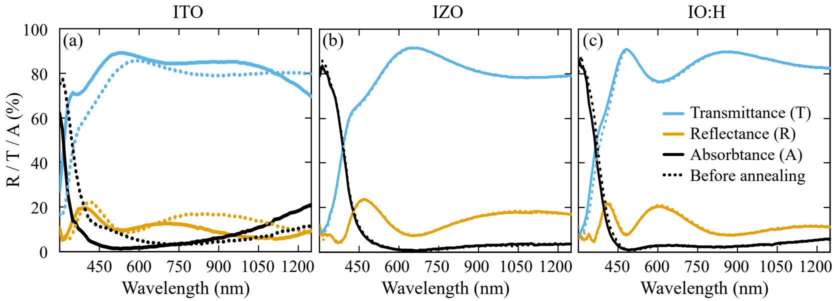

Figure 3.4: Optical characterization of transparent conductive oxides deposited on glass. a) Characterization of ITO, b) IZO, and c) IO:H. R, T, and A stand for reflectance (orange), transmittance (blue), and absorptance (black), respectively. Measurements before and after annealing are depicted in dashed and solid lines. This method highlights that an annealing step significantly improves the optical characteristics of the ITO layer.

X-ray diffraction

X-ray diffraction (XRD) measurements are conducted in a Bruker system (D2Phaser) with a copper K-α source. X-rays with a wavelength of 1.5405 Å are directed onto the sample, and an adjustable detector measures the angle-dependent diffraction with a 0.01° step size within a 2θ range from 10 to 35°. In materials with a periodic lattice, constructive interference – and thus reflection of the X-ray – occurs if the Bragg condition given by equation (3.2) is fulfilled.

$$n\lambda = 2d\sin(\theta) \tag{3.2}$$

Where n is a diffraction order, λ is the wavelength, d is the distance between two parallel diffraction planes, and θ is the glancing angle. A typical measurement of a triple-cation perovskite thin-film coated on a glass/ITO substrate is shown in Figure 3.5. Peaks corresponding to the ITO layer at 21.4° and 30.4° are identified from an XRD measurement on a bare glass/ITO substrate and are consistent with the literature.[109] The predominant perovskite peak at 14.2° is attributed to the

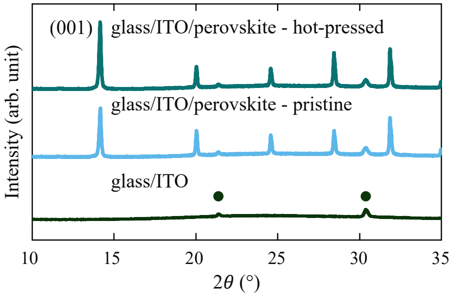

Figure 3.5: X-ray diffraction pattern of glass/ITO and glass/ITO/perovskite substrates before and after hot-pressing in the 2θ range from 10 to 35°. The predominant peak at 14.2° is attributed to the preferred crystallographic plane orientation (001) of the perovskite material. Circles highlight the peaks corresponding to the ITO layer.

preferred crystallographic plane orientation (001), indexed in the cubic space group (Pm-3m).[33,110,111] XRD measurements are performed to detect perovskite decomposition after the hot-pressing process, which would be indicated by the emergence of additional peaks not present initially. Furthermore, the material crystallinity is investigated by analyzing the dominant peak intensity and full width at half maximum (FWHM). An increased peak area (e.g., higher intensity and narrower peak) is interpreted as enhanced perovskite crystallinity.[112–115] Section 4.2 investigates these aspects, comparing XRD measurements performed on pristine and hot-pressed perovskites. Measurement uncertainties related to sample-to-sample variations are ±0.012° in the peak position, and ±0.168 in the peak area (arb. unit), as determined according to ISO/IEC guidelines.[108] Variations within these intervals are not further interpreted.

3.2.2 Characterization of solar cells

External quantum efficiency

The external quantum efficiency (EQE) provides insights into the spectral current generation in a solar cell. EQE measurements are performed with a Bentham PVE300 photovoltaic characterization system. The monochromatic light is assembled from a dual xenon/quartz halogen light source and is modulated by an optical chopper at a 575 Hz frequency. This chopping frequency is filtered in a lock-in-amplifier to distinguish the signal to be measured from background noises (e.g., ambient light). Measurements are performed with an integration time of 750 ms and a 5 nm step size. The aperture size, defining the light spot size, is (0.74x0.74) mm for solar cells with a small active area of around 10 mm^2 and (1.5x1.5) mm for laminated tandems with a 1 cm^2 large active area. For monolithic perovskite/silicon tandem measurements, subcells are individually measured with an adapted bias light: The PSC signal is measured with an 800 nm LED, while the silicon solar cell is measured with a 450 nm LED and a white light source. When the bottom cell EQE signal is noisy, measurement data are smoothed using the Savitzky-Golay method. Integrated J_{sc} values remain unaffected.

A typical EQE measurement of a single-junction PSC from 300 to 850 nm is illustrated in Figure 3.6a. EQE exponentially decreases for longer wavelengths than 750 nm, as the photon energy is insufficient for absorption in the perovskite to create excitons. This feature allows for determining the absorber bandgap from the EQE inflection point.[116] Figure 3.6b shows the EQE first derivative. The perovskite bandgap is taken as the Gauss fit center, here 1.63 eV. Measurement uncertainties due to sample-to-sample variations are estimated at ±0.004 eV according to ISO/IEC guidelines,[108] and variations in this range are not further interpreted. EQE characterizations also enable the J_{sc} determination using equation (2.11). Integrated J_{sc} over the wavelength range is displayed in Figure 3.6a.

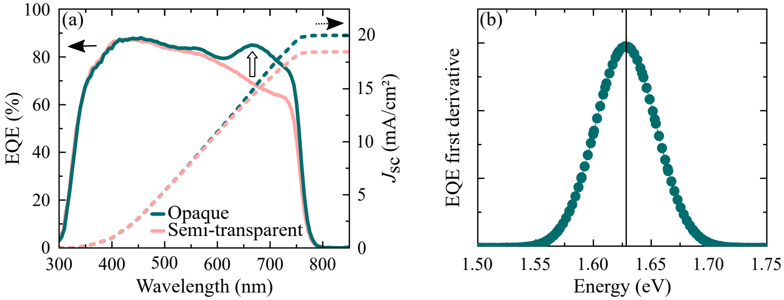

Figure 3.6: External quantum efficiency (EQE) of perovskite solar cells. a) Typical EQE characterization performed on opaque (green) and semi-transparent (pink) devices. The EQE signal increases from 600 to 750 nm in opaque solar cells due to photon recycling through reflection on the opaque rear electrode. Integrated J_{sc} (dashed lines) reaches 20.1 and 18.7 $\mathrm{mA/cm^2}$ in opaque and semi-transparent architectures. b) First derivative of EQE plotted over photon energy. The perovskite bandgap (1.63 eV) is taken as the Gauss fit center.

In addition, EQE spectral measurements support the analysis current losses in laminated monolithic perovskite/silicon tandem solar cells. Wavelength-dependent EQE characterizations allow a certain depth resolution through the layer stack. Because the absorption coefficient in a semiconductor increases with photon energy, short wavelengths are predominantly absorbed in the perovskite front surface. In contrast, longer wavelengths penetrate to the solar cell rear side. EQE, ideally as close as possible to 100%, is reduced by optical losses such as reflected light on the device front side or transmitted light. In semi-transparent PSCs, photons are partially transmitted through the device, decreasing the EQE. In opaque devices, photons are reflected at the rear metal electrode, acting as a mirror. These recycled photons are predominantly absorbed deep in the perovskite film, enhancing EQE in the infrared spectral range compared to semi-transparent devices, as highlighted in Figure 3.6a. Additional factors reducing EQE are discussed in this work related to the absorber thickness and parasitic absorption in functional layers, e.g., in front electrodes and CTLs.

Current density-voltage characteristics

Current density-voltage (J-V) characteristics measurement enables the determination of solar cell characteristics: PCE, FF, J_{sc}, and V_{oc}. Measurements are performed in a Newport 91194-1000 solar simulator equipped with a xenon lamp (Osram Licht AG). Solar cells are characterized in an N_2 atmosphere, at room temperature (≈25 °C) and under 1-Sun, corresponding to the global standard AM1.5G spectrum with an integrated power density of 1000 W/m². Measurement conditions correspond to the protocol IEC 60904. The light output is calibrated using a certified KG5 filtered and non-filtered silicon reference solar cell from Newport Company for PSCs for single-junction and tandem devices, respectively. All J-V characteristics are obtained in both backward (bw: $V_{\mathrm{oc}} \rightarrow J_{\mathrm{sc}}$) and forward (fw: $J_{\mathrm{sc}} \rightarrow V_{\mathrm{oc}}$) in the voltage range from -0.2 to 1.2 V at a scan rate of 300 mV/s for PSC and from -0.2 to 2 V at 600 mV/s for tandems, respectively. PCE, FF, J_{sc}, and V_{oc} are extracted from J-V characteristics in the backward scan direction. For clarity, only backward measurements are shown when several J-V

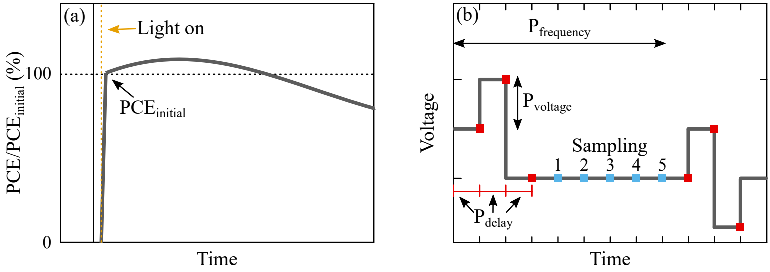

Figure 3.7: Maximum power point (MPP) tracking of perovskite solar cells. a) Figure-of-merit for characterizing long-term stability. The initial PCE value ($\mathrm{PCE}_{\mathrm{initial}}$) is taken after turning the light on. b) Applied voltage during MPP tracking. The voltage is varied by ±0.01 V ($\mathrm{P}_{\mathrm{voltage}}$) in 0.1 s intervals ($\mathrm{P}_{\mathrm{delay}}$). The software calculates the corresponding power for all three points and sets the voltage with the highest power. The current is then measured at this position five times (sampling), and the average value is retained. These steps are repeated every second ($\mathrm{P}_{\mathrm{frequency}}$) during the MPP tracking.

characteristics are compared in a figure. Masks are used for J-V measurements to reduce uncertainties in the active area of laminated devices resulting from, e.g., a minute change in the half-stack overlap during the hot-pressing step. When PSCs are compared with different architecture in Section 5.2.3, a 7.07 mm^2 mask is used, and in Sections 5.2.2 and 5.4, when laminated PSCs are compared with references, a 5.6 mm^2 mask is employed. Large tandems presented in Section 6.3 are measured through a 1 cm^2 mask. In this work, solar cell characteristics are displayed in box-whisker diagrams. In these graphs, the standard deviation (SD) of data points is represented by a box, in which the median is shown as a solid line and the mean value as a circle. Whiskers indicate minimum and maximum values.

MPP tracking measurements are conducted using the same setup as J-V characterizations, in an N_2 atmosphere, at room temperature ($\approx$25 °C) and under 1-Sun. MPP tracking is performed for at least 5 min to determine the stabilized power output of solar cells. Extended measurements of up to 100 hours are also conducted to investigate the long-term stability of laminated PSCs under continuous illumination. For MPP measurements over several hours, the device temperature is regulated in an in-house developed sample holder equipped with a microcontroller and a Peltier element for cooling and heating. This sample holder is also used for measurements at 80 °C. The figure-of-merit for characterizing the long-term stability of solar cells in this work is shown in Figure 3.7a. During MPP tracking, the applied voltage is regularly varied by ±0.01 V for 0.3 s each, and the best achieved PCE every second is retained, as illustrated in Figure 3.7b.

Photoluminescence quantum yield

Photoluminescence quantum yield (PLQY) measurements are conducted to determine implied open-circuit voltage ($V_{\mathrm{oc,imp}}$) of perovskite thin films and PSCs. Measurements are performed in an integrating sphere (LabSphere) of 15 cm diameter with an LD-515-10MG green laser from

Roithner Lasertechnik as a light source. The transmitted, reflected, or remitted light collected within the sphere is guided with an optical fiber into an AvaSpec-ULS2048 × 64TEC spectrophotometer (Avantes Compagny). The spectral response is calibrated using a HL-3plus-INT-Cal calibration lamp from Ocean Optics. Three measurements are performed,[117] starting with quantifying the excitation intensity collected in the empty integrating sphere. A second measurement is conducted with the sample under direct illumination, positioned at 15° relative to the excitation beam to prevent specular reflectance toward the entrance port. A third measurement is performed with indirect illumination of the sample to consider repetitive sample excitation from diffuse reflected light in the integrating sphere. All measurements are performed in ambient air with a maximum of 30% relative humidity.

PLQY measurements allow intensity-dependent calculations of the $V_{\mathrm{oc,imp}}$ according to procedures outlined by Krueckemeier et al.[116] and Stolterfoht et al.[118] PLQY is the ratio of emitted photon flux ϕ_{emitted} and the absorbed photon flux ϕ_{absorbed}. Equation (3.3) can also be formulated as the ratio of integrated current densities J_{rad} (radiative current density) and J_{ph} (photogenerated current density at 1-Sun).

$$PLQY = \frac{\Phi_{emitted}}{\Phi_{absorbed}} = \frac{J_{rad}}{J_{ph}} \tag{3.3}$$

J_{ph} depends on the number of absorbed photons and typically corresponds to the J_{sc} (around 20 mA/cm$^{\mathbf{2}}$ for standard PSCs).[119] J_{rad} is calculated from equation (3.4).

$$J_{rad} = J_{0,\mathrm{rad}}\ e^{\frac{eV_{oc,\mathrm{imp}}}{k_B T}} \tag{3.4}$$

Where e is the elementary charge, k_{B} is the Boltzmann constant, and T is the temperature of the solar cell. The radiative saturation current density $J_{0,\mathrm{rad}}$ is calculated with equation (3.5), integrating the photon flux density emitted by a blackbody (ϕ_{BB}) at the temperature T and the external quantum efficiency (EQE) over the wavelength (λ).

$$J_{0,\mathrm{rad}} = e \int EQE(\lambda) \cdot \Phi_{BB}(\lambda)\, d\lambda \tag{3.5}$$

The resulting equation (3.6) for $V_{\mathrm{oc,imp}}$ calculation finally distinguishes the radiative open-circuit voltage limit ($V_{\mathrm{oc,rad}}$) from the non-radiative recombination loss term.

$$V_{oc,\mathrm{imp}} = \frac{k_B T}{e} \cdot \ln\left(\frac{PLQY\, J_{ph}}{J_{0,\mathrm{rad}}}\right) = V_{oc,\mathrm{rad}} + \frac{k_B T}{e} \cdot \ln(PLQY) \tag{3.6}$$

$V_{\mathrm{oc,rad}}$, given in equation (3.7), corresponds to the maximum voltage achievable, assuming that all recombination processes are radiative and that every luminescent photon escapes the solar cell (PLQY=100%).

$$V_{oc,\mathrm{rad}} = \frac{k_B T}{e} \cdot \ln\left(\frac{J_{ph}}{J_{0,\mathrm{rad}}}\right) \tag{3.7}$$

Intensity-dependent PLQY measurements also enable n_{id} determination, indicating the dominant recombination mechanism within the solar cell. The n_{id} is derived from the slope of a logarithmic fit of $V_{\mathrm{oc,imp}}$ as a function of light intensity. Previous reports highlighted the dependency of n_{id} and recombination mechanisms in perovskite bulk and at interfaces.[55] A n_{id} reduction towards 1 generally correlates with the dominance of radiative recombination, while an increase to 2 indicates the dominance of non-radiative recombination.

Photoluminescence imaging

Photoluminescence (PL) images are acquired using an in-house setup developed by Ternes et al. to visualize device degradation over time.[26] This work compares PL images of PSCs measured after preparation (t=0) and after 130 days of storage to identify signs of degradation – notably the emergence of inhomogeneous areas. The complete stability study is detailed in Section 5.5. For PL measurements, PSCs are exposed from the glass side to an LED of 467 nm wavelength (DL2 by CCS Inc.) for 5 s. Measurements are performed in ambient air. A Quantalux sCMOS camera (Thorlabs), equipped with a 780 nm long-pass filter (FGL780S, Thorlabs) to filter the excitation light out, monitors the PL signal. This setup allows measurements of 100 cm^2 large areas with a high spatial resolution of (1000x800) pixels in a few seconds. An exemplary PL image of a PSC is displayed in Figure 3.8. The images illustrates how the overlap of Au and ITO electrodes defines four active areas (10.5 mm^2) on the glass substrate.

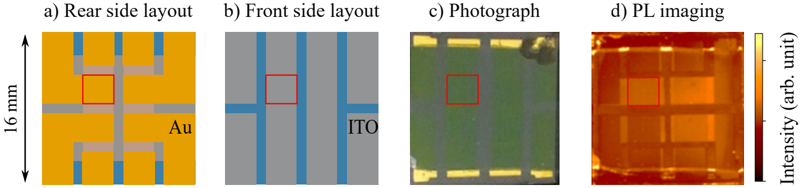

Figure 3.8: Photoluminescence (PL) imaging on perovskite solar cells (PSCs). a) Illustration of the rear side layout, and b) the front side. Au and ITO layers are colored yellow and grey, respectively. c) Photograph, and d) PL imaging of a PSC. The red frame highlights one of the four active areas on the substrate. The solar cell in the bottom left is shunted (low intensity), and defects (dots) appear visible on the right side from the PL imaging.

4 Hot-pressed perovskites

The perovskite absorber quality plays a pivotal role in device performance. Accurate knowledge of the film thickness, surface roughness, grain size, crystallinity, and optoelectronic properties is thus essential to design efficient PSCs. This chapter aims to quantify the improved quality of hot-pressed absorbers as a function of applied temperatures and pressures, and to determine the suitable process window for preventing material degradation. In this context, physical (crystallinity, film thickness, and surface morphology) and optoelectronic (bandgap, implied open-circuit voltage, and ideality factor) characteristics of hot-pressed perovskites are compared with as-deposited thin films. Experimental results provide insights into absorber recrystallization, enabling future optimization of highly efficient laminated PSCs.

Acknowledgments and contributions

Outlined sections with † and ‡ review the first author publications *"Laminated perovskite photovoltaics: Enabling novel layer combinations and device architectures"* in Advanced Functional Materials,[14] and *"Laminated monolithic perovskite/silicon tandem photovoltaics"* in Advanced Energy Materials,[120] respectively. This chapter also refers to co-author publications *"Lasing from laminated quasi 2D/3D perovskite planar heterostructures"* in Advanced Functional Materials,[121] and *"A self-assembly method for tunable and scalable nano-stamps: A versatile approach for imprinting nanostructures"* in Advanced Materials Technologies.[122] In addition, content produced during supervised master's theses of M. Heydarian,[123] and L. K. Schorn are included.[124]

Julie Roger and Prof. Dr. Ulrich W. Paetzold conceived the idea and developed research plans. Julie Roger designed experiments and supervised their execution. Julie Roger, Minasadat Heydarian, and Luisa K. Schorn *fabricated the thin films and performed hot-pressing processes. Dr. Somayeh Moghadamzadeh and Dr. Mahdi Malekshahi Byranvand optimized the triple-cation perovskite recipe. Dr. Ahmed Farag optimized the double-cation perovskite recipe. Marc Schneider provided technical assistance for the hot-pressing process. Heike Fornasier provided the Teflon-coated silicon stamps. Minasat Heydarian and Luisa K. Schorn performed AFM measurements. Julie Roger and Minasat Heydarian performed XRD measurements. Dr. Paul Faßl performed PLQY characterizations and supported the corresponding data analysis. Julie Roger performed the rest of characterizations and data analysis. Prof. Dr. Ulrich W. Paetzold supervised the project.*

4.1 Introduction

This chapter focuses on determining to what extent applying elevated temperatures and pressures improves perovskite quality in terms of crystallinity and morphology. Thresholds are highlighted to trigger recrystallization, and a suitable process window is determined by identifying parameter limits (e.g., in temperature) that should not be exceeded to prevent degradation. Section 4.2 provides insights into the perovskite structure via XRD. These measurements enable both assessing absorber crystallinity and detecting possible material decomposition. Section 4.3 quantifies grain growth and roughness reduction observed in hot-pressed polycrystalline absorbers. Since the layer thickness is also susceptible to change due to the high pressure, this hypothesis is examined through a sequential lamination of perovskite films in Section 4.4. Ultimately, Section 4.5 evidences enhancements in optoelectronic characteristics of the hot-pressed perovskite and its interface with subsequently deposited functional layers.

State-of-the-art hot-pressing techniques for perovskite absorbers

The hot-embossing technique is an established technology for microstructuring thermoplastic materials by replication,[125–127] and finds applications in optoelectronic fields.[39,122,128] Some fabricate self-cleaning covers with imprinted microcones, providing a hydrophobic surface that prevents soiling of solar modules.[129] Others produce textured solar cell covers, e.g., to advance light harvesting by using surface microstructures imitating petal surfaces (biomimetic).[130] During the past few years, (hot-)pressing also attracted particular attention in the perovskite technology. Figure 4.1 illustrates three post-deposition techniques for perovskite materials.

Thermal nanoimprint lithography (NIL) consists of patterning a polycrystalline perovskite material with nanostructures (Figure 4.1a). The absorber recrystallizes due to the applied heat and pressure, yielding

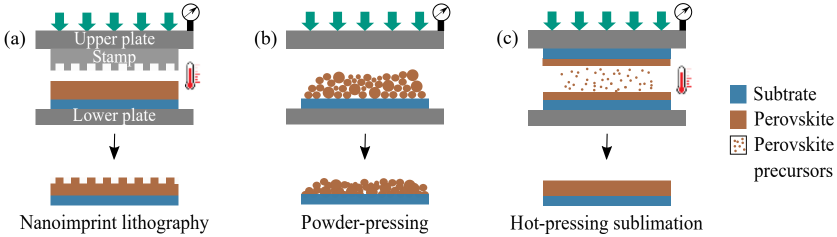

Figure 4.1: Three exemplary post-deposition treatments for perovskite materials using (hot-)pressing techniques. a) Thermal nanoimprint lithography process. The thin-film absorber is patterned with a textured stamp during a hot-embossing step. b) Perovskite powder pressed into pellets. A pressure-induced sintering can occur between grains, yielding a compact film. c) Hot-pressing of two perovskite layers. Material sublimation is triggered at high temperatures, allowing for anion exchange in an enclosed space. This sublimation process results in a newly recrystallized absorber after cooling.

an improved crystal structure with fewer surface defects. Such nanopatterned layers were reported in optically-pumped lasing,[39,131–134] PSCs,[135] LEDs,[136] and photodetectors.[137] In addition, PSCs containing nanoimprinted perovskite film demonstrated enhanced light trapping by incident light diffraction at the textured interface, resulting in reduced reflectance losses.[114,135,138] Another utilization of pressing techniques involves compacting perovskite powder into pellets (Figure 4.1b). The formation of sinter necks between grains evidenced a pressure-induced sintering process, allowing the fabrication of millimeter-thick absorber layers (also called wafers).[139] These wafers were used as active layers for efficient X-ray detectors in optoelectronic devices,[140] and as targets for physical-vapor-based perovskite depositions, e.g., in sputtering techniques.[141,142] Figure 4.1c shows a third application where two perovskite layers are hot-pressed together. Material sublimation was triggered at temperatures of about 150 °C, allowing anion exchange in a confined space, leading to a newly recrystallized thin film after cooling.[143,144] High-quality absorbers were thus achieved, resulting in highly efficient PSCs with PCEs exceeding 22%.[144] Lower temperatures were also investigated ($\leq$120 °C), and the laminated perovskite/perovskite interface was improved in this case by partially dissolving the perovskite surfaces with chlorobenzene or acetonitrile preliminarily.[112,145,146] This solvent-assisted hot-pressing process significantly reduced void defects at the interface, yielding PSCs with up to 22.5% of PCE.[145]

Determining perovskite recrystallization during hot-pressing processes

This work aims to provide insight into a hot-pressing technique that mimics lamination conditions. The process initiates recrystallization in a conventionally deposited perovskite thin film by simultaneously applying high pressures and temperatures in an in-house developed hydraulic press. Three main phases are outlined in Figure 4.2a:

I. Samples undergo heating via machine plates;

II. Pressure is applied when the target temperature is reached;

III. Once the target duration has elapsed, samples are cooled, and pressure is released.

The process follows a typical hot-embossing sequence for thermoplastics,[125–127] and NIL.[39,122,133–135] This sequence is also compatible with roll-to-roll or roll-to-plate applications, where heating occurs before applying pressure, followed by a nearly instantaneous pressure release and cooling.[147] The three key parameters – temperature, pressure and duration – regulate the perovskite recrystallization. It is noted that an increase (or decrease) in the target temperature results in a longer (or shorter) treatment due to machine-specific heating and cooling rates, as detailed in Section 3.1.3. For consistency, hot-pressing duration refers to the period when target temperature and pressure are simultaneously applied (phase II). In contrast to state-of-the-art sublimation techniques, temperatures investigated here are lower than 150 °C, which broadens

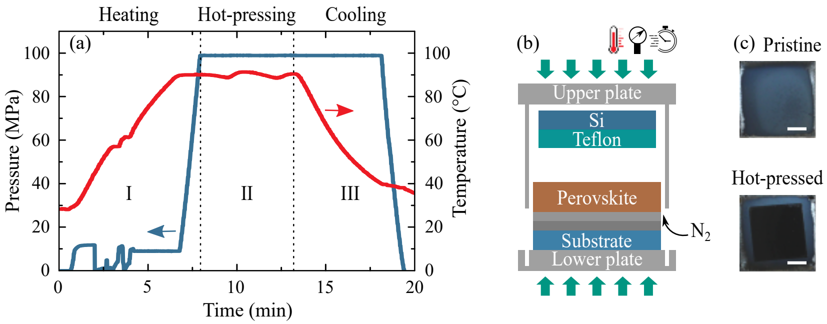

Figure 4.2: Illustration of the hot-pressing process as conducted in this work. a) Typical hot-pressing procedure showing pressure (blue) and temperature (red) over time. Three phases are distinguished: heating (I), hot-pressing (II), and cooling phase (III). In this example, a pressure of 100 MPa is applied for 5 min on a 90 °C heated thin-film perovskite absorber. b) Perovskite substrates are hot-pressed with a flat silicon (Si) stamp between the lower and upper plates of the hydraulic press. The anti-adhesive Teflon coating facilitates the stamp separation from the absorber surface. The machine is equipped with a vacuum chamber and N_2 flushing system to perform the process in an inert atmosphere, thereby preventing perovskite degradation. c) Exemplary photographs of pristine and hot-pressed perovskites. The (11x11) mm area under the stamp appears darker after hot-pressing the (16x16) mm sample, indicating perovskite recrystallization. The white scale bar corresponds to 4 mm.

the range of compatible materials and facilitates the process, primarily relying on solid-state layers. Hot-pressing of perovskite films is typically performed in this work at 90 °C, under 80 MPa for 5 min.

Insights into the absorber recrystallization process are essential to understand and optimize laminated PSCs. Perovskite thin films are hot-pressed with a flat silicon stamp (contrary to NIL techniques using textured stamps), as illustrated in Figure 4.2b. Subsequent stamp removal exposes the recrystallized absorber surface, which appears darker (Figure 4.2c), and allows for further characterizations. Using a flat silicon stamp offers several advantages. First, no complete device stack is required for perovskite thin film investigations. Second, since the stamp is removed after treatment, the recrystallized surface is directly accessible without contamination from other functional layers (e.g., CTLs). Third, a flat stamp enables a homogeneous distribution of applied pressure despite the unevenness and imperfect surface of machine tools, e.g., high roughness, scratches, or other defects. Silicon stamps are coated with a Teflon layer to facilitate stamp separation from the absorber. This technique contrasts with the procedure described in our first report, in which PSCs were delaminated to assess hot-pressed perovskite properties and retroactively adjust the process.[14]

This work focuses on the material $Cs_{0.1}(MA_{0.17}FA_{0.83})_{0.9}Pb(I_{0.83}Br_{0.17})_3$. Initially developed by Saliba et al., this triple-cation composition allows for highly efficient and stable PSCs over time.[34] Our research also shows that other compositions are conceivable, notably double-cation perovskites and different film thicknesses from hundreds of nanometers to up to micrometer thick layers. The following sections systematically characterize pristine and hot-pressed perovskites, highlighting a recrystallization process at high temperatures and pressures. A suitable process window is defined to enhance absorber morphology and crystallinity while preventing its degradation. These results will support the lamination of high-quality perovskite-based PVs in single-junction (Chapter 5) and tandem (Chapter 6) device architectures.

4.2 Process window definition via crystallinity analysis†

Defining the suitable process window for perovskite materials is critical to prevent degradation under high pressure and temperature. Recent reports suggested that a tight contact between the hot-pressed stamp and sample could inhibit decomposition.[143,148,149] Keeping volatile decomposition products in an enclosed space allows them to reintegrate the absorber during recrystallization while cooling. This principle was fundamental when perovskite sublimation was triggered at particularly high temperatures ($\geq$150 °C).[150] In that regard, Ding et al. hot-pressed triple-cation absorbers at 150 °C, while Dunlap-shohl et al. employed 250 °C for $MAPbI_3$.[143,144] In both cases, recrystallized thin films exhibited outstanding quality after cooling. As each composition seems to react differently depending on applied temperatures,[151] the suitable process window must be specified for triple-cation absorbers in the focus of this work.

Perovskite crystallinity is studied by XRD characterization, i.e., analyzing peak positions and area as described in Section 3.2.1. Overall, pristine and hot-pressed perovskites at 85 to 105 °C present a similar diffraction pattern (Figure 4.3). Figure 4.4 shows a detailed analysis of the dominant peak at 14.2°, assigned to the (001) crystallographic plane and identified as preferential orientation. While the peak position and FWHM remain the same, the peak height systematically increases after hot-pressing at all investigated pressures, temperatures, and durations compared to pristine absorbers. This improvement is accentuated for longer treatments ($>$5 min) and higher pressures ($>$20 MPa). The resulting larger peak area suggests an enhanced crystallinity of hot-pressed perovskites, in consistency with existing literature.[112–115]

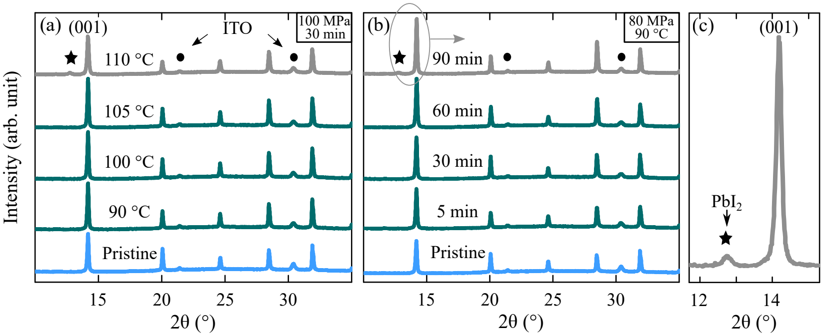

Figure 4.3: X-ray diffraction (XRD) characterization of hot-pressed perovskites. a) XRD patterns of pristine (blue) and hot-pressed perovskites (green) for different temperatures, and b) processing durations. Layer stacks are glass/ITO/perovskite. Circles highlight ITO peaks at 21.4 and 30.4°. The peak at 14.2° is attributed to the (001) crystallographic plane of the perovskite. Pristine and hot-pressed perovskites at 85 to 105 °C present a similar diffraction pattern. It is only for temperatures and times exceeding 110 °C and 90 min (in grey) that an additional PbI_2 peak at 12.6° emerges, as highlighted with a star, indicating perovskite decomposition. c) Zoomed-in view of the region highlighted in (b), showing the additional PbI_2 peak. Further XRD data are available in reference[123].

XRD patterns of hot-pressed triple-cation perovskites indicate no sign of degradation for temperatures up to 105 °C, in agreement with our previous findings.[14] An additional diffraction peak appears at 12.6° for a temperature of 110 °C, revealing the presence of unreacted PbI_2 (Figure 4.3a). The emergence of a PbI_2 peak, which was not visible at lower temperatures, suggests a perovskite decomposition, usually detrimental to material quality and device intrinsic stability.[152] This result indicates that perovskites can degrade from overheating despite tight contact with the stamp.[14,143,150] A perovskite decomposition also occurs during excessively long hot-pressing durations, as a PbI_2 peak emerges after 90 min (Figure 4.3b). Consistent degradation trends were confirmed across different pressure levels and durations.[14,123] Regarding pressure, the general perovskite crystal structure remains unaffected even when increased up to 150 MPa, as shown in Figure 9.2, Appendix. These findings are consistent with recent literature on a similar triple-cation composition, demonstrating good thermal stability for short annealing at temperatures up to 100 °C (without applying pressure) while highlighting immediate decomposition at 120 °C or after 50 min at lower temperatures.[151] In conclusion, this study identified upper parameter

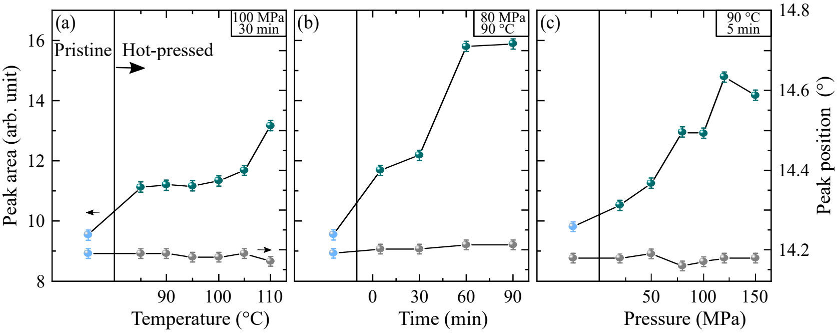

Figure 4.4: Systematic area increase of the 14.2° peak assigned to the (001) crystallographic plane of hot-pressed perovskites, indicating enhanced crystallinity. a) Peak area (green) and position (grey) of hot-pressed perovskites for various temperatures, b) processing durations, and c) pressures. Peak areas and positions for reference films are shown in blue. Error bars represent measurement uncertainties, as discussed in Section 3.2.1.

limits preventing perovskite degradation: While the pressure can be increased up to 150 MPa, temperature and duration should not exceed 105 °C and 60 min, respectively. This process window constitutes the starting range for the following studies.

4.3 Surface morphology of hot-pressed perovskites

4.3.1 Perovskite grain growth‡

Although the role of perovskite grain boundaries in PSCs is still under debate in the literature, recent research showed possible benefits of large-grain absorbers.[153–156] Larger grains and/or passivated grain boundaries could reduce trap-state density, thus mitigating recombination mechanisms, especially non-radiative recombination losses.[114,157–161] Fewer grain boundaries could also enhance steric effects by hindering the movement of uncoordinated iodide species and the penetration of water and oxygen molecules through the absorber, thereby preventing decomposition.[115,155,162,163] Grain size is conventionally controlled during or after perovskite deposition, e.g., through additives engineering,[158,164] thermal annealing under an inert atmosphere,[165] or using solvent-based post-deposition treatments.[145,159] However, hot-pressing techniques also demonstrated promising results in inducing grain growth in perovskite layers.[114,148,149,166] According to the literature, temperature, and duration are interlinked in crystal growth. In the model developed by Mayer et al. for $MAPbBr_3$ materials, two significant observations were stated: "(i) Growth is fast initially but slows down with time; [. . .] (ii) Treatment temperature accelerates growth substantially."[148] The pivotal role of temperature was further underlined by Wang et al., showing that applying pressures of up to 34 GPa without heating might be insufficient to induce grain growth and plastic deformations in $MAPbBr_3$ perovskites.[167] As each composition might recrystallize differently – especially depending on the temperature –,[151] grain growth must be studied for triple-cation perovskites in the focus of this work. Duration, pressure and temperature are systematically varied to characterize the interlinked influence of hot-pressing parameters:

1) Duration variations from 5 to 90 min at 90 °C under 100 MPa;
2) Pressure variations from 5 to 150 MPa at 90 °C for 5 min;
3) Temperature variations from 85 to 120 °C for 30 min under 100 MPa.

Selected ranges build on insights provided in Section 4.2: To prevent perovskite degradation caused by overheating, the highest temperature is limited to 120 °C, and duration is not extended beyond 90 min. Temperatures below 80 °C are neglected for grain growth, as some level of heat is required, according to Mayer et al.[148]

First, the grain size is studied for various durations, and respective values are summarized in Table 4.1. A hot-pressing step results in a significant increase in average grain size to 320 nm (+14$\%_{\mathrm{rel}}$) for 5 min and 350 nm (+25$\%_{\mathrm{rel}}$) for 30 min, as compared to pristine perovskites exhibiting 280 nm large grains. Longer times do not lead to significant further improvements, suggesting a saturation effect. Therefore, a duration of 30 min maximum is considered sufficient to promote grain growth. Regarding pressure, a complementary study presented in

Table 4.1: Measured grain size in nanometers of pristine and hot-pressed perovskites for a duration of 5 to 90 min. The temperature and pressure are fixed at 90 °C and 100 MPa. SD stands for standard deviation. A similar trend is found at different pressure levels.[123]

	Pristine	5 min	30 min	60 min	90 min
Mean	280	320	350	350	370
SD	65	81	85	92	76
Minimum	130	180	130	150	190
Maximum	420	550	570	550	660

Figure 9.2, Appendix, does not provide conclusive evidence of the primary role of pressure in controlling grain growth. Nevertheless, the results confirmed that a 5 min short treatment can induce grain growth in the triple-cation perovskite.

When studying grain growth as a function of temperature, considering that heating and cooling phases take longer as the set temperature rises is crucial. A sample hot-pressed at 90 °C for 5 min spend in total 5 min less in the machine compared to a sample at 120 °C, which is as long as the hot-pressing itself. This difference is illustrated in Figure 3.2 (Section 3.1.3). To reduce the dominance of heating and cooling phases with varying temperatures, the hot-pressing duration is extended to 30 min in the following study. The relative time difference of the complete process is thus decreased to below $10\%_{\mathrm{rel}}$ between samples treated at 90 and 120 °C for a more equitable comparison. Measured grain sizes as a function of temperatures are displayed in Figure 4.5. As temperature rises, grains significantly enlarge from 350 nm at 90 °C ($+30\%_{\mathrm{rel}}$, compared to pristine perovskite with 270 nm) to 400 nm at 100 °C ($+48\%_{\mathrm{rel}}$) and 470 nm at 120 °C ($+74\%_{\mathrm{rel}}$), on average. The mean grain size increases approximately by 50 nm for every 10 °C step. Remarkably, grains as large as 780 nm are observed at 120 °C, compared to a maximum size of 420 nm in pristine films. This enhancement aligns with recent literature reporting on additives, such as trimethylammonium chloride (TACl) incorporation in $MAPbI_3$ materials exhibiting a comparable initial grain size,[157] and the $+73\%_{\mathrm{rel}}$ larger grains obtained with a similar triple-cation composition enriched with methylammonium chloride (MACl).[164] Whether improved absorber morphology benefits its optoelectronic properties will be discussed in Section 4.5 by PLQY analysis.

The present study demonstrates that hot-pressing is suitable for tuning the grain size of triple-cation perovskites and that temperature is the primary parameter to achieve larger grains. Even if the processing duration also increases the grain size, the rate slows over time, aligning with the growth law introduced by Mayer et al.[148] This saturation effect implies that compensating for reduced temperatures by longer

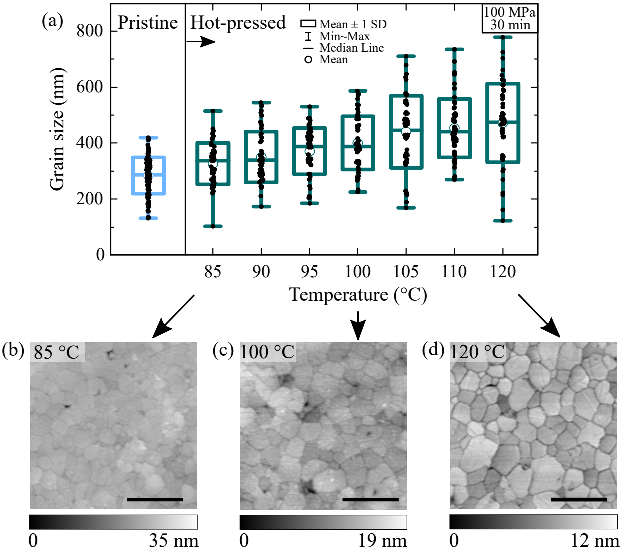

Figure 4.5: Grain growth in hot-pressed perovskites with increasing processing temperature. a) Measured grain size on pristine (as deposited, blue) and hot-pressed films (green) at different temperatures. SD stands for standard deviation. b) Representative atomic force microscopy (AFM) images of hot-pressed perovskite surfaces at 85 °C, c) 100 °C and d) 120 °C. The layer stack is glass/ITO/perovskite. The scale bar corresponds to 1 μm. Adapted from reference[120] with the permission of Wiley. Further AFM images are available in reference[123].

treatments is not a practical strategy. These findings are favorable outcomes in the context of upscaling and roll-to-roll applications, where time is a constrained parameter. In addition, differences are noticed in growing rates compared to values obtained for $MAPbBr_3$ materials,[148] confirming that each perovskite composition requires individual optimization of hot-pressing conditions. In summary, applying the highest possible temperature is beneficial for maximizing grain growth, while a duration of 30 min appears already sufficient. As it remains uncertain if larger grains improve device performance despite perovskite decomposition (starting at 110 °C), complete laminated PSCs will be investigated in Section 5.3 to conclude the suitable parameter window yielding solar cells with high PCEs.

4.3.2 Perovskite surface roughness decrease[‡]

Smooth perovskite surfaces in PSCs can reduce the interface resistance to enhance charge carrier extraction, facilitate subsequent CTL deposition, and possibly increase steric hindrance and structural bulk stability.[113,145,168] To obtain smooth perovskite films, several methods have been proposed, focusing either on the layer deposition or on post-treatments, e.g., using solvents to dissolve the perovskite surface partially.[145,169] Promising results were achieved by hot-pressing treatments: Pourdavoud et al. reported a remarkable RMS roughness reduction from 23.8 nm to 0.5 nm by applying only 10 MPa at 150 °C on $CsPbBr_3$ perovskites,[132] and from 46 to 0.6 nm in $MAPbBr_3$ under 10 MPa at 90 °C.[133] Moreover, Witt et al. underlined that $MAPbI_3$ films were substantially smoother after a tempered pressing while applying the same pressure of 100 MPa at room temperature only reduced roughness to a certain degree (70 nm compared to 24 nm at 100 °C).[139] These reports highlight two essential aspects of the hot-pressing technique: i) There is an interlinked influence of heat and pressure on the achieved perovskite surface roughness, and ii) the suitable parameter ranges depend on the material composition. The following study systematically investigates the roughness of triple-cation perovskite films depending on hot-pressing conditions.

The hot-pressed perovskite surface roughness is investigated by AFM measurements. Three types of experiments are conducted and subsequently discussed in the following:

1) Duration variations from 5 to 90 min at 90 °C under 100 MPa;
2) Pressure variations from 5 to 150 MPa at 90 °C for 5 min;
3) Temperature variations from 85 to 120 °C for 30 min under 100 MPa.

These parameter variations mirror those conducted in Section 4.3.1, with a focus on RMS roughness values obtained from the same AFM measurements. 1) A substantial reduction in the RMS roughness is observed

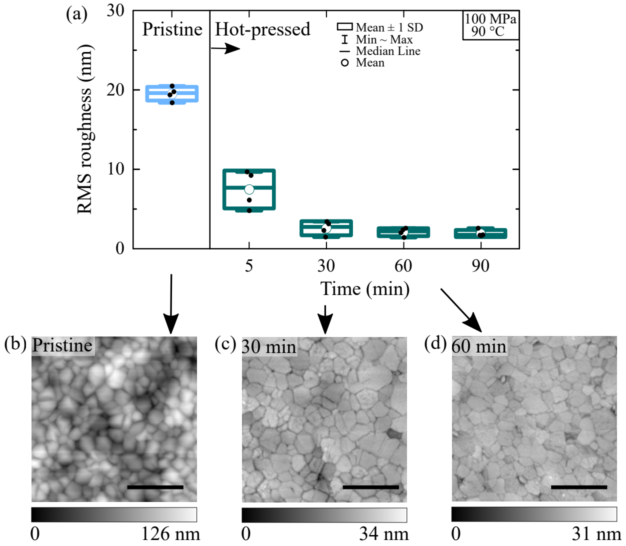

Figure 4.6: Reduced surface roughness of hot-pressed perovskites with increasing processing duration. a) Root mean square (RMS) roughness of pristine (as deposited) and hot-pressed perovskites for 5 to 90 min. All RMS roughness values are calculated on an (3x3) μm area. SD stands for standard deviation. b) Representative atomic force microscopy (AFM) images of perovskite surfaces as-deposited, c) treated for 30 min, and d) 60 min. The layer stack is glass/ITO/perovskite. The scale bar corresponds to 1 μm. Adapted from reference[120] with the permission of Wiley. Further AFM images are available in reference[123].

over time from about 20 nm in pristine perovskites to less than 10 nm after a 5 min treatment and further decreases to below 3 nm at 30 min (Figure 4.6). As longer hot-pressing durations do not further reduce the roughness, a maximum of 30 min appeared sufficient. The repetition of this duration-dependent study under 80 to 120 Mpa confirms a saturation effect, as summarized in Table 4.2. 2) The pressure variation study, detailed in Figure 9.2, Appendix, highlights a minimum threshold of 20 MPa that must be exceeded to induce recrystallization and a minimum of 50 MPa for a significantly reduced surface roughness under 10 nm. Below 20 MPa, no plastic deformation is induced in the perovskite. The smoothest absorber layers (about 3 nm RMS) are achieved

Table 4.2: Root mean square (RMS) surface roughness measured on perovskites hot-pressed under pressures from 80 to 120 MPa and durations from 5 to 90 min. Temperature is kept constant at 90 °C. RMS values are given in nanometers and are calculated on an (3x3) μm area. The data can be visualized in reference[123].

	5 min	30 min	60 min	90 min
80 MPa	8.6	3.0	1.3	1.5
100 MPa	5.3	1.5	1.4	1.3
120 MPa	5.2	1.7	1.3	1.2

when exceeding 100 MPa. 3) All hot-pressed perovskites exhibit remarkably low RMS roughness of less than 2 nm, independently of the temperature (Table 4.3). Even if the temperature is increased from 85 to 120 °C, the surface roughness cannot be further reduced.

Overall, the perovskite RMS surface roughness of a few nanometers aligns with that achieved using other hot-pressing treatments, with similar reported values calculated over comparable surface areas.[115,132,133] Interestingly, the minimum pressure threshold of 50 MPa for smooth perovskite layers is substantially higher than in the literature, reporting typically 10 MPa.[112,115,132,133,148,149] Furthermore, even if the hot-pressing duration also plays a role in the triple-cation perovskite recrystallization, similarly low RMS values of only a few nanometers are obtained either by using high pressure or long times. That higher pressures can compensate for a shorter duration is particularly interesting for future roll-to-roll

Table 4.3: Root mean square (RMS) surface roughness measured on hot-pressed perovskites at 85 to 120 °C. Pressure and duration are fixed at 100 MPa and 30 min. All RMS roughness values are calculated on an (3x3) μm area. The data can be visualized in reference[123].

	85 °C	90 °C	95 °C	100 °C	105 °C	120 °C
RMS (nm)	2.0	1.6	1.3	1.5	1.2	1.5

applications where time is constrained. In summary, this study demonstrated that hot-pressing can enhance perovskite surface morphology, which is expected to improve the interface with adjacent functional layers in PSCs and possibly enhance the long-term device stability. These aspects will be investigated in Sections 4.5 and 5.5, respectively.

4.4 Film thickness of hot-pressed perovskites

Applying pressure on perovskite absorbers was reported as a promising post-treatment technique when the deposition method led to incomplete substrate coverage, e.g., via spray-coating.[170,171] High pressures closed gaps and pinholes in the absorber – possible shunt paths –, resulting in continuous and smoother layers. The compacted films were significantly thinner, with an as-deposited thickness of 850 nm reduced to 520 nm after pressing.[171] However, the compaction process seems to depend on the initial absorber porosity. For example, Gong et al. did not observe significantly thinner layers after hot-pressing conventionally spin-coated perovskite films.[145] Scanning electron microscopy measurements revealed only a 20 nm reduction in total thickness when laminating two 520 nm thick perovskite layers. An interesting question arises in the light of the literature: To what extent does our hot-pressing procedure affect the thickness of conventionally spin-coated perovskite absorbers?

Two arrangements are implemented to accentuate an eventual thickness reduction and decrease measurement uncertainty. First, a 720 nm thick perovskite layer is used, of composition $Cs_{0.17}FA_{0.83}Pb(I_{0.92}Br_{0.08})_3$. For comparison, the triple-cation absorber employed elsewhere is only half as thick (about 370 nm). Second, several perovskite thin films are deposited atop each other by successive lamination steps, as illustrated in Figure 4.7a. This sequential process consists of hot-pressing two half-stacks prepared in parallel. The half-stacks comprise a perovskite film deposited on PEN/ITO foil or glass/ITO substrates. After hot-pressing, peeling off the PEN foil results in a double absorber layer on the glass

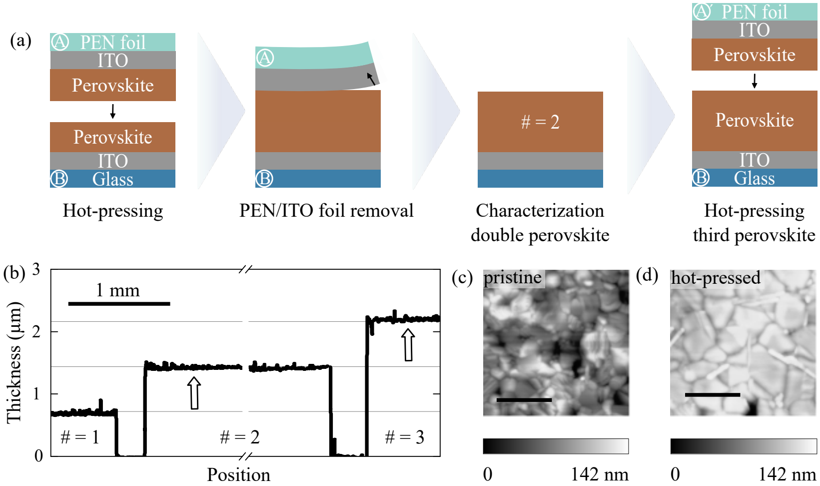

Figure 4.7: Characterization of the perovskite film thickness after hot-pressing. a) Illustration of the sequential lamination of independent half-stacks comprising: (A) PEN foil/ITO/perovskite, and (B) glass/ITO/perovskite. A stack of two perovskite layers (# = 2) is obtained after peeling off the PEN/ITO foil. This process is repeated with a third film, resulting in a triple perovskite layer (# = 3). b) Profilometry measurement of pristine, double-, and triple-perovskite layers, which are approximately 720, 1440, and 2160 nm thick, respectively, suggesting that the absorber thickness remains relatively unaffected by the hot-pressing process. c) Representative atomic force microscopy (AFM) images of the pristine perovskite surface, and d) after laminating a second perovskite layer. AFM scale bar corresponds to 1 μm.

substrate. Half-stack adhesion occurs through recrystallizing the two perovskite films at high temperature and pressure (90 °C, 80 MPa, for 5 min). This procedure is repeated with a third absorber layer deposited on a PEN/ITO foil substrate. The thickness measurement of three hot-pressed perovskite films is expected to accentuate a potential thickness reduction by three times.

Profilometry measurements reveal a linear increase in thickness with the number of stacked perovskite layers (Figure 4.7b). Laminating two perovskite films doubles the initial thickness from about 720 to 1440 nm. Repeating the procedure with a third film triples the initial single-layer thickness to approximately 2160 nm. A slight variation in thickness in the range of a few nanometers may not be detectable and, therefore, cannot be entirely excluded. However, the fact that perovskite films can be sequentially laminated without substantial loss in thickness suggests that the absorber thickness remains relatively unaffected. These findings are key for analyzing light management in PSCs containing hot-pressed perovskites, as absorber thicknesses severely affect light absorption near its bandgap.[172] Sequential lamination is also promising to produce ultra-thick perovskite films exceeding 2 μm, which is challenging to achieve conventionally.[74,173] Further applications in tandem PVs are particularly interesting, where the complete coverage of perovskite on rough substrates, such as textured silicon and CI(G)S solar cells remains challenging.[174] The feasibility of using the hot-pressing process to produce sufficiently thick absorber layers for covering textures is investigated as part of Chapter 8. An additional benefit of thicker perovskite films is a possible enhancement of the PSC fabrication yield, notably by preventing the formation of shunt paths through more continuous absorber layers.[159] Sequential lamination also has a significant potential for producing perovskite heterostructures by combining different materials that cannot be deposited on each other otherwise, e.g., due to solvent incompatibilities. Thus, advanced energy level alignment can be achieved, as demonstrated in our report on laminated semiconductor lasers,[121] and surface defects could be efficiently passivated for improved PSC performance.[55]

4.5 Optoelectronic properties of hot-pressed perovskites‡

Optoelectronic properties of hot-pressed perovskites are expected to improve through the enhanced morphology – larger grain size and smoother surface – and crystallinity achieved under high temperatures and pressures.[144] Properties of particular interest for optoelectronic performance can often be rationalized through a detailed understanding of a material band structure. The bandgap energy of pristine triple-cation absorbers employed in this work is 1.63 eV, as determined from the EQE inflection point of PSCs.[116] Figure 4.8 shows the bandgap determination for representative pristine and hot-pressed perovskites in different conditions. These measurements reveal no significant bandgap shift. For all temperatures, pressures, and durations, bandgaps remain within the sample-to-sample variation range of (1.63±0.004) eV, indicating that the perovskite composition remains unaffected. The bandgap preservation aligns with existing literature that employs similar temperatures (≤100 °C).[112] In contrast, exceeding 150 °C to trigger sublimation was associated with a bandgap shift toward shorter wavelengths, highlighting a possible change in perovskite composition due to the escape of volatile chemical components.[115,150] These results are in good agreement with XRD measurements presented in Section 4.2, indicating no evident perovskite decomposition at temperatures under 100 °C. Therefore, the previously outlined process window to preserve absorber quality is confirmed with a maximum of 100 °C, 100 MPa, and 30 min.

Further optoelectronic characteristics of hot-pressed perovskites are investigated via PLQY measurements, enabling the determination of the implied V_{oc} and n_{id}, an indicator of the dominant recombination type. Device half-stacks comprising a glass/ITO substrate, a HTL of 2PACz, and a perovskite film are characterized as-deposited and hot-pressed and compared to identify enhancements related to the absorber recrystallization. The process is conducted within the aforementioned range at 90 °C under 80 MPa for 5 min. In addition, the interface between the smooth perovskite layer and adjoining CTL is investigated by evaporating an ETL of C_{60} on the half-stacks. The systematic comparison between hot-pressed and pristine layer stacks provides insights into the improved quality of the perovskite and its interface with adjacent CTLs.

Figure 4.9 displays the implied V_{oc} of pristine and hot-pressed perovskites. After treatment, the layer stack retains a similar implied V_{oc} of 1.21 V on average, confirming that the absorber remains preserved. The benefits of hot-pressed perovskite surface morphology are revealed by applying on the absorber an ETL of C_{60}, widely used in PSCs.[67,175–177] Here, a reference stack (I), where the C_{60} is directly

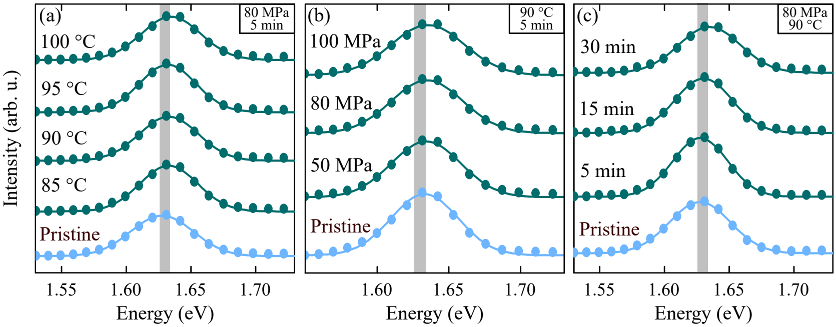

Figure 4.8: Analysis of the perovskite bandgap as a function of hot-pressing conditions. a) Bandgap determination of hot-pressed perovskites for different temperatures, b) pressures, and c) processing durations. The plotted intensity is derived from the external quantum efficiency inflection point (Section 3.2.2). The bandgap is taken as the Gauss fit center. The band gap of hot-pressed perovskites remains similar to that of pristine films at (1.63±0.004) eV, within the range of measurement uncertainties (in grey).

evaporated on the pristine perovskite, is compared to an identical, hot-pressed stack (II), subsequently completed with a C_{60} layer. The implied V_{oc} drop to 1.08 V in references (I) due to increased recombination losses at the perovskite/C_{60} interface, as previously reported.[178,179] The hot-pressed layer stack (II) demonstrates a slight enhancement in implied V_{oc} and lower n_{id} (Figure 4.9b), indicating a reduced contribution of non-radiative recombination.[55] This improvement is attributed to the recrystallized perovskite exhibiting larger grains and a smoother surface, thereby limiting primary trap-assisted recombination channels.[180,181] The results align with recent findings on hot-pressed perovskites, consistently reporting reduced non-radiative recombination losses.[112,114,144]

Comparing layer stacks I and III – where C_{60} is deposited on hot-pressed perovskites – highlights a substantial improvement in the C_{60}/perovskite interface. In the latter configuration, C_{60} is applied on a recrystallized absorber surface resulting in an enhanced implied V_{oc} of 1.11 V and a lower n_{id} of 1.59 (Figure 4.9c). PLQY measurements thereby confirm that the perovskite morphology plays a pivotal role in the interface quality with adjacent CTLs. While the C_{60}/perovskite interface area

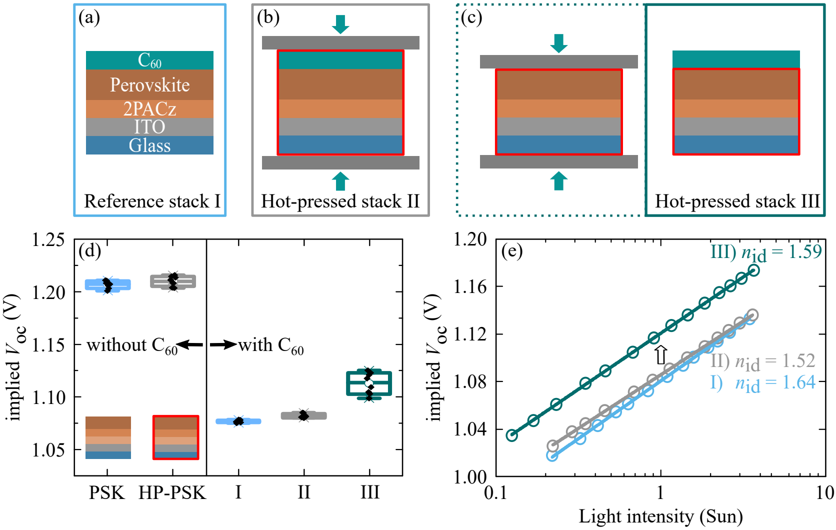

Figure 4.9: Photoluminescence quantum yield (PLQY) characterization of hot-pressed perovskites. Three layer stacks are compared: a) Reference layer stack (I), conventionally prepared, b) Layer stack (II), consisting of a hot-pressed reference stack, and c) layer stack (III), containing a hot-pressed perovskite stack, subsequently completed with C_{60}. Red frames indicate hot-pressed stacks at 90 °C and 80 MPa for 5 min. d) Implied V_{oc} measured via PLQY at 1-Sun. Reference measurements for pristine (PSK) and hot-pressed layer stacks (HP-PSK) comprising glass/ITO/2PACz/perovskite are displayed. e) Intensity-dependent measurement of implied V_{oc}. n_{id} stands for ideality factor. An outlined arrow highlights an enhancement in implied V_{oc} in stack (III), attributed to the improved absorber morphology and perovskite/C_{60} interface. Adapted from reference[120] with the permission of Wiley.

is extensive when C_{60} is deposited on the pristine perovskite, the surface contact of these materials is assumed to be significantly reduced when C_{60} is processed on smooth layers, which is beneficial to device performance. Therefore, reduced non-radiative recombination losses in the hot-pressed perovskite are attributed to its enhanced morphology and interface with the adjoining CTL.

4.6 Summary

Insights into the recrystallization process of polycrystalline perovskite thin films during hot-pressing are provided by monitoring the crystallinity and morphology achieved. Experimental results indicate that 50 MPa is a minimum pressure threshold that must be exceeded to induce plastic deformation and significantly reduce the perovskite RMS surface roughness to a few nanometers. Grain growth can be triggered by increasing the temperature, which is consistent with existing literature. In the 85 to 120 °C range, the mean grain size increases by approximately 50 nm for each 10 °C step. To a lesser extent, hot-pressing duration can also increase grain size. However, a 5 min process seems sufficient to significantly improve the perovskite morphology and crystallinity.

Despite the harsh hot-pressing conditions, no evidence of material decomposition is noticed as long as the temperature and duration do not exceed about 100 °C and 60 min. These findings outline a process window in which hot-pressed perovskites exhibit larger grains, smoother surfaces, and enhanced crystallinity compared to pristine films while preventing material degradation. The process parameters – temperature, pressure, and time – can be controlled according to the targeted outcome. Therefore, this technique can be envisioned as a post-treatment method to decouple the deposition process from the final absorber quality required for efficient optoelectronic devices. Interestingly, the process window appears compatible with roll-to-roll applications, allowing the application of high pressure and temperature in a short time. A roll-to-roll process would be particularly interesting for future upscaling of the lamination technique, allowing higher throughput and rapid treatment of large areas.

Improved perovskite morphology and crystallinity of perovskite absorbers are intrinsically linked to the performance of PSCs. PLQY measurements show that a recrystallized perovskite film provides an improved interface with the subsequently deposited CTL of C_{60}. Higher implied V_{oc} and lower n_{id} are achieved in hot-pressed layer stacks, indicating a reduced dominance of non-radiative recombinations. Mitigating these losses – known to be particularly severe at the perovskite/C_{60} interface – may benefit device performance. These results suggest that PSCs can be improved by integrating a hot-pressing step on the perovskite layer in the device fabrication sequence. This work on hot-pressed perovskites also contributes to understanding the behavior of fully laminated PSCs presented in the following chapters. In particular, the improved absorber morphology is expected to enhance device stability over time, a hypothesis tested in Section 5.5.

An additional feature of the lamination technique was explored when investigating possible changes in the thickness of hot-pressed perovskites. Sequential lamination of multiple perovskite layers evidenced that the initial perovskite thickness is not reduced by hot pressing. For instance, the total thickness triples when three perovskite layers are laminated. Nonetheless, these results also demonstrated that sequential lamination enables the processing of ultra-thick perovskite films exceeding 2 μm, which might have several advantages in the PV field. Stacked perovskite films could increase the yield in PSC fabrication by preventing the formation of shunt paths through more continuous absorber layers. Sequential lamination could also be used to produce perovskite heterostructures, e.g., for advanced energy level alignment and surface passivation, by combining materials that cannot be conventionally deposited atop each other. Finally, this method could provide an alternative solution to facilitate the usually challenging coverage of rough and textured substrates, such as silicon solar cells in the context of tandem PV, as highlighted in Chapter 8.

5 Laminated perovskite solar cells

An innovative lamination technique is introduced as an alternative fabrication method for PSCs, overcoming standard sequential layer deposition limitations. Different proof-of-concept architectures explore the increased degree of freedom in the choice of materials and deposition techniques. Notably, semi-transparent PSCs are successfully laminated, which is a milestone for applications of this technology in the tandem PV field. Through variations in temperature, duration, and pressure, a suitable process window that maximizes the PCE is identified. The resulting laminated PSCs exhibit PCEs of up to 17.5%, comparable to conventionally produced references. This direct comparison also reveals additional features of the lamination technique attributed to the improved perovskite morphology achieved by recrystallization during the hot-pressing process.

Acknowledgments and contributions

Sections outlined with † and ‡ review first author publications *"Laminated perovskite photovoltaics: Enabling novel layer combinations and device architectures"* in Advanced Functional Materials,[14] and *"Laminated monolithic perovskite/silicon tandem photovoltaics"* in Advanced Energy Materials,[120] respectively. This chapter also includes content produced during supervised master's theses of M. Heydarian,[123] L. K. Schorn,[124] and D. O. Baumann.[182]

Julie Roger, Dr. Raphael Schmager, and Prof. Dr. Ulrich W. Paetzold conceived the idea and developed research plans. Julie Roger designed experiments and supervised their execution. Julie Roger, Minasadat Heydarian, Luisa K. Schorn and Daniel O. Baumann fabricated the laminated perovskite solar cells and performed characterization under solar simulator and external quantum efficiency measurements. Fabian

Schackmar conceived the sample holder for long-term and temperature-regulated MPP tracking. Dr. Somayeh Moghadamzadeh and Dr. Mahdi Malekshahi Byranvand optimized the triple-cation perovskite recipe. Dr. Bahram Abdollahi Nejand introduced the PTAA recipe, which Julie Roger has then optimized for application in laminated devices. Marc Schneider provided technical assistance for the hot-pressing process. Heike Fornasier provided the Teflon-coated silicon stamps. Thomas Feeney optimized and performed SnO_x *depositions via ALD. Dr. Paul Faßl performed PLQY characterizations and supported corresponding data analysis. Julie Roger performed the rest of the characterizations and data analysis. Prof. Dr. Ulrich W. Paetzold supervised the project.*

5.1 Introduction

The lamination technique emerged as a promising fabrication method for perovskite PVs, that can offer new opportunities for research into innovative materials and deposition processes. The following overview outlines a range of state-of-the-art techniques. A novel lamination method is then introduced, allowing enhanced freedom in PSC architectures. Section 5.2 illustrates the application versatility, notably by manufacturing semi-transparent devices, which are particularly interesting for integrated PVs and the tandem technology. Section 5.3 provides insights into suitable hot-pressing temperatures and pressures for high device performance. Section 5.4 demonstrates through a direct comparison that laminated PSCs can be on par with conventionally produced devices and reveals additional features of this fabrication technique. Ultimately, to test the hypothesis that enhanced perovskite morphology achieved after recrystallization should advance device stability, long-term measurements under continuous illumination are performed and discussed in Section 5.5.

State-of-the-art lamination techniques for perovskite solar cells

Recent developments in perovskite PVs focused mainly on novel materials, layer combinations, and deposition techniques to advance the performance and stability of PSCs. While absorbers were optimized by tuning composition,[183,184] morphology,[185] and bulk passivation,[186] device architectures were improved through optimization of CTLs,[187,188] electrodes, and interfacial passivation techniques,[189,190] for maximizing charge carrier extraction. Most PSCs are produced by sequential layer deposition. This procedure must consider that some deposition techniques can damage the preceding layer stack, e.g., if the required temperature exceeds the thermal tolerance of underlying films or if particles

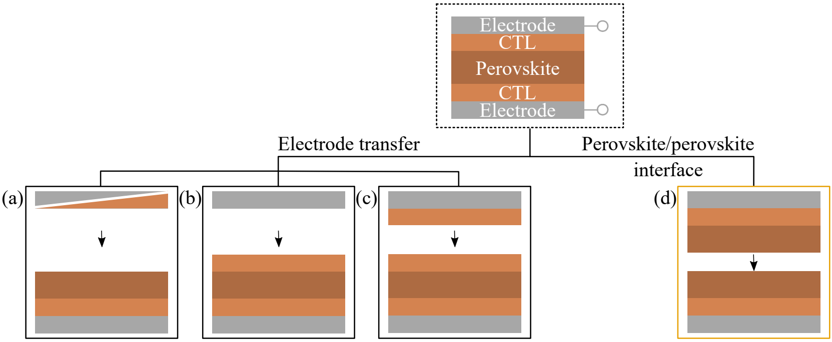

Figure 5.1: Overview of state-of-the-art lamination techniques. Two main categories are distinguished based on the lamination interface. a) The first consists of transferring an electrode on a pre-fabricated half-stack using at least one adhesive material at the interface between the perovskite and electrode, b) between the charge transport layer (CTL) and electrode, and c) between two CTLs. The adhesives might be an additional buffer layer, a CTL, and an self-adhesive electrode. d) The second technique focuses on a recrystallization process at a perovskite/perovskite interface.

of high kinetic energy are involved, as in the case of sputtering deposition.[191] Other techniques can be hindered in practice, such as solution-based processing on thin-film surfaces causing dewetting.[192–194] Consequently, conventional methods severely restrict the choice of materials and processing techniques as each deposition must preserve the already prepared layer stack.[150] These constraints restrict accessible device architectures despite the development of numerous innovative materials for PSCs in recent years.

Fabrication techniques via lamination – also known as stacking – were proposed to overcome standard method limitations. The fundamental principle is to decouple the deposition of functional layers by preparing two individual half-stacks assembled in a final step.[195] Figure 5.1 shows that this technique was primarily employed to transfer an electrode onto a pre-fabricated half-stack. A carbon-based layer, which could serve a double function of HTL and rear electrode, was directly laminated onto the perovskite absorber and generally conferred enhanced stability to the PSC.[196–198] Alternatively, lamination was performed at the

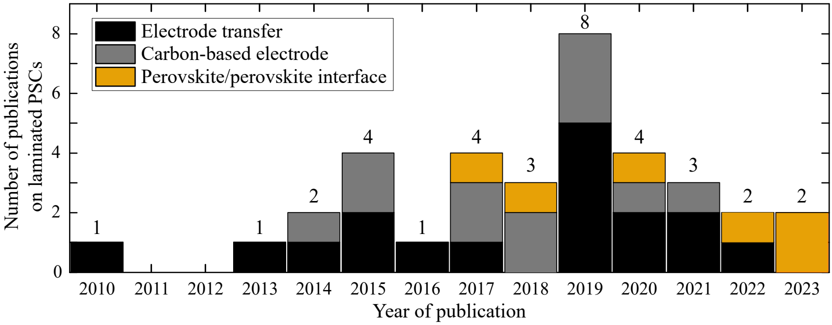

Figure 5.2: Number of publications on perovskite solar cells fabricated via lamination since 2010. The electrode transfer technique is used in a total of 29 publications. Almost half of them focused on a carbon-based electrode. Six publications reported on a lamination process at the perovskite/perovskite interface. Corresponding references are summarized in Table 9.2, Appendix.

CTL/electrode or CTL/CTL interface. Adhesive materials were introduced between the half-stacks, such as transparent conductive adhesives (also called e-glue),[199,200] wet thin films,[201] or self-adhesive materials.[202,203] Only a few research groups, as depicted in Figure 5.2, used the recrystallization of two hot-pressed perovskite layers.[115,204–206] Applying pressures and high temperatures ($\geq$120 °C) triggered a diffusion process or even the sublimation of perovskite materials in a confined space. This technique resulted in a newly recrystallized thin film, uniting the device half-stacks. In response to the limited knowledge about this underappreciated method, this work demonstrates the feasibility of manufacturing high-performance PSCs via lamination (proof-of-concept) and conducts an in-depth analysis of involved parameters. Hot-pressing processes are also shown to offer additional features compared to the mainly employed electrode transfer through the improved perovskite absorber quality.

Novel methodology: laminated perovskite single-junction devices

This work introduces a novel lamination process for single-junction PSC fabrication. The method consists of preparing the device in two individual layer stacks subsequently hot-pressed together, as illustrated in Figure 5.3. In the depicted example, front half-stack A builds on a superstrate (so-called as it remains atop the device after lamination), on which the front transparent electrode, CTL, and absorber are successively deposited. The rear CTL and electrode are processed on an independent substrate in half-stack B. The combination of heat (≈90 °C) and high pressure (≈80 MPa) promotes perovskite recrystallization and creates an electrical contact between materials at the half-stacks interface. This hot-pressing process unites the half-stacks, thus completing the PSC. Other configurations are possible, as explored in this work, e.g., the perovskite can be deposited on either or both sides,[14] a CTL can be a combination of several selective materials, and incident light might come from the super- or substrate side. Similar to other lamination methods, this technique overcomes conventional method limitations, allowing the manufacture of novel architectures for PSCs that are otherwise challenging to produce. Nonetheless, this unique process offers additional features discussed below.

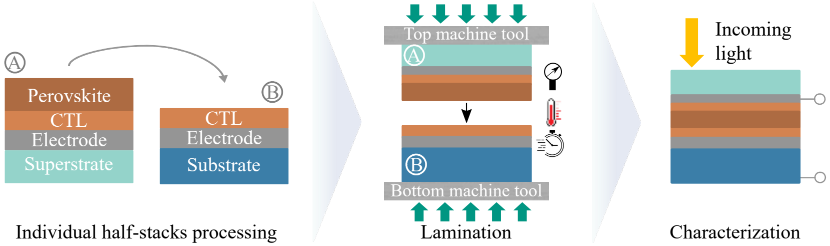

Figure 5.3: Lamination technique proposed in this work for fabricating single-junction perovskite solar cells (PSCs). Device half-stacks A and B are prepared independently on top of a super- and substrate, respectively. High temperatures and pressures are then applied to induce perovskite recrystallization. This hot-pressing process unites the half-stacks, completing the PSC. Other configurations are possible, e.g., the absorber can be deposited on top of either or both half-stacks, and a CTL can combine several layers.

The hot-pressing technique developed in this work combines and enhances advantages of state-of-the-art lamination methods. As with the electrode transfer, this technique provides substantial flexibility in the choice of electrodes, optimally deposited on an independent substrate.[200,203] Typical processing damage, such as metal diffusion through pinholes during thermal evaporation of the electrode, is thereby prevented.[207] Nevertheless, adhesives – which may introduce optical and resistive losses – are not required.[199] Laminated PSCs presented in this work have the same number of functional layers as conventionally processed devices, except for the superstrate that remains on top, providing a possible encapsulation function. Lamination also substantially increases the degree of freedom in the choice of materials, architectures, and deposition techniques for PSCs through the decoupled processing of the functional layers, including the perovskite absorber and CTLs. In addition, laminated PSCs benefit from the improved perovskite quality achieved at elevated temperatures and pressures. However, distinctively from other state-of-the-art techniques using hot-pressed perovskite/perovskite interfaces, only a single perovskite layer is sufficient to unite half-stacks, which broadens the range of accessible architectures.[14] Moreover, this work focuses on a hot-pressing process at lower temperatures ($\leq$100 °C), which has two significant advantages: it firstly prevents perovskite decomposition and simplifies fabrication by reducing the risk of escape of volatile chemical components. Secondly, lower temperatures broaden the material options, especially for substrates. Since 100 °C aligns with the thermal tolerance of specific polymer foils, e.g., PEN foils with T_g of around 120 °C, this technique enables the creation of flexible laminated PSCs and paves the way for roll-to-roll processes, as demonstrated in our previous report.[14] Finally, the parallel half-stack preparation and possible direct device encapsulation render this original fabrication process particularly promising for the future industrialization of perovskite-based solar cells.

5.2 Proof-of-concept solar cells in single-junction architectures

This section presents three proof-of-concept laminated architectures overcoming typical constraints of standard fabrication methods. The focus is set on innovative material combinations and layer deposition sequences. Other factors, such as triple-cation perovskite composition $Cs_{0.1}(MA_{0.17}FA_{0.83})_{0.9}Pb(I_{0.83}Br_{0.17})_3$ and lamination conditions, remain constant throughout, demonstrating the process versatility. Section 5.2.1 focuses on a combination of inorganic CTLs, which is expected to improve the thermal stability of the device but is difficult to produce conventionally. Section 5.2.2 explores the increased degree of freedom in the choice of electrode by replacing the opaque rear contact with a transparent electrode, resulting in semi-transparent laminated PSCs. Finally, Section 5.2.3 illustrates variations in the thin-film deposition order enabled by lamination, bridging the gap between the development of n-i-p and p-i-n PSC architectures. These proof-of-concept studies not only find applications for the fabrication of PSCs targeting, for instance, thermal stability but also demonstrate interesting features of the lamination technique for future perovskite-based tandem PVs.

5.2.1 Enabling pairing of inorganic charge transport layers for enhanced thermal stability†

Thermal stability is a cornerstone in the development of perovskite-based PVs and their future industrial applications. Thermal stability studies aim to ensure that solar cells maintain a reliable power output under outdoor operation conditions. Endurance to thermal cycling is particularly important, as solar panels installed outdoors experience significant temperature variations during the day.[208,209] Exposure to constant elevated temperatures beyond standard operational levels is also a key stressor for solar cells as it significantly influences degradation mechanisms, accelerating physical and chemical reactions, particularly in organic materials.[210] Operating solar cells at consistent high temperatures thereby accelerates aging, which can allow for predicting device operational lifetime, e.g., by identifying Arrhenius temperature-dependent degradation in solar cells.[211,212] Measurements at elevated temperatures of up to 85 °C are hence part of IEC standards for commercial PVs and established protocols for assessing and reporting the stability of perovskite PVs based on ISOS procedures.[64,210] The following thermal stability study is based on the ISOS-L-2-I protocol, which involves testing solar cells at 85 °C under continuous illumination with electrical bias (here, MPP tracking).[64] It is noted that the device temperature is limited in this work to 80 °C to prevent damaging the in-house fabricated sample holder. However, this minor difference is not expected to significantly influence the trend observed. Testing conditions are summarized in Table 5.1.

Table 5.1: Measurement conditions based on the ISOS-L-2-I protocol for testing device thermal stability.[64] The temperature is limited to 80 °C, instead of the 85 °C stipulated in the protocol, to prevent damage to the in-house fabricated sample holder.

ISOS protocol (adapted)	L-2-I
Atmosphere	Inert atmosphere, N_2 (O_2<1 ppm; H_2O< 1ppm)
Temperature	80 °C
Light	ON
Bias voltage	ON (MPP tracking)

New materials and architectures have been investigated to achieve thermally stable PSCs. Several studies reported on inorganic CTLs such as copper iodide (CuI),[213] copper thiocyanate (CuSNC),[214] and NiO_x,[215,216] demonstrating enhanced device stability over time compared to those with organic materials (notably, 2,2´,7,7´-tetrakis[*N*,*N*-di(4-methoxyphenyl) amino]-9,9´-spirobifluorene, a.k.a. Spiro-OMeTAD).

Among the inorganic materials, NiO_x and SnO_2-np are particularly promising HTL and ETL, respectively.[187,217] However, it remains challenging to process NiO_x and SnO_2-np within the same device conventionally. The NiO_x deposition can lead to either sputtering damage of the underlying perovskite layer or overheating in the case of solution-based processing, due to high annealing temperatures (approximately 300 °C).[218–220] Meanwhile, polar solvents involved in solution-based SnO_2-np deposition, in particular water, would dissolve an underlying perovskite film.[221] The lamination technique overcomes these limitations via the decoupled CTL processing, as NiO_x and SnO_2-np must not be directly deposited on top of the sensitive absorber. This novel material combination, which is challenging to fabricate conventionally, is particularly interesting to target PSCs with enhanced thermal stability.

PSCs are prepared in two independent half-stacks (Figure 5.4a). The front layer stack builds on a glass substrate, on which a transparent ITO, ETL of SnO_2-np, and the perovskite absorber are deposited. The rear stack comprises a PEN foil, an Au electrode, and a double HTL of NiO_x and PTAA. Both half-stacks are subsequently laminated at 90 °C, 80 MPa for 5 min. Figure 5.4b displays the champion device performance, which exhibits a PCE of 14.0%, a FF of 64.6%, a V_{oc} of 1.08 V, and a J_{sc} of 20.0 mA/cm². The laminated PSC presents a stabilized PCE of 13.5% after 5 min MPP tracking. Even at high temperatures as high as 80 °C, the device shows good thermal stability by retaining 96.8% of its initial PCE during 10 h of continuous illumination at 80 °C (Figure 5.4c). The enhanced stability over time and device performance achieved are consistent with our previous report using the same architecture, where for the first time a laminated PSC equipped with two inorganic CTLs maintained a stable power output under continuous illumination at high temperatures.[14] These results demonstrate the process reproducibility and confirm the enhanced thermal stability of this material combination, which also appears robust against temperature variations.[14]

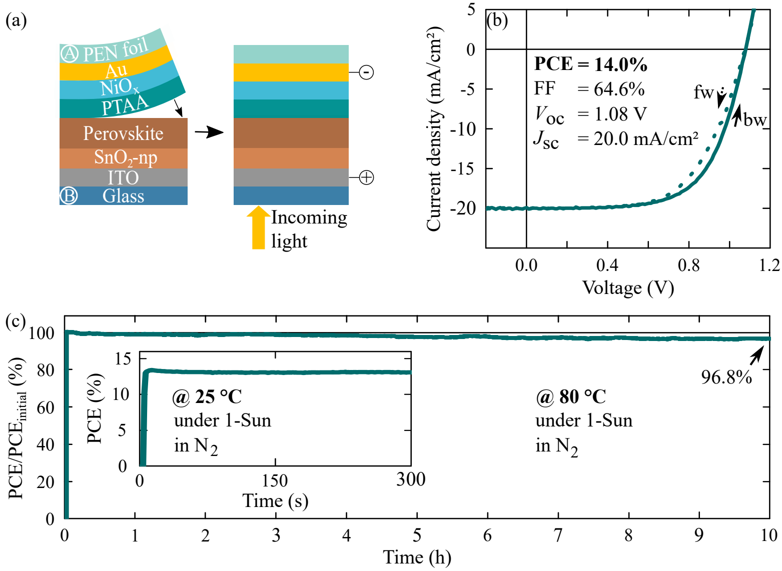

Figure 5.4: Proof-of-concept architecture combining SnO_2-np and NiO_x inorganic charge transport layers in a laminated perovskite solar cell (PSC). a) Illustration of the device architecture and lamination process. b) Current density-voltage characteristics of the champion laminated PSC, scaled to the integrated J_{sc} from external quantum efficiency measurement. c) Maximum power point (MPP) tracking of the champion device under illumination for 10 h at 80 °C to test operational stability based on the ISOS-L-2-I protocol.[64] Initial stabilized power output (PCE$_{initial}$) is determined by MPP tracking for 5 min, shown in the inset.

The champion device is competitive with state-of-the-art laminated PSCs with similar materials.[115,150,222] Nevertheless, this prototype exhibits a lower PCE than conventional opaque architectures, reaching up to 26% today.[13] The major limiting factor is the FF, which is about 20%$_{rel}$ behind record PSCs. A possible explanation is a poor interface quality between the laminated half-stacks. This hypothesis is supported by findings from Jung et al., quantifying the interfacial adhesion strength of laminated perovskite/NiO_x, perovskite/SnO_2-np, and perovskite/perovskite layers.[115] The former interface was the weakest, causing the highest electrical losses. We significantly improved this interface by adding a PTAA buffer layer between the perovskite and

Table 5.2: Fabrication yield of the lamination process for perovskite solar cells with and without a PTAA layer at the perovskite/NiO_x interface. The yield is calculated as the total number of functional devices divided by the number of produced devices.

	Without PTAA	With PTAA
Total number of fabricated devices	76	72
Total number of functional devices	32	56
Number of batches	2	3
Fabrication yield	42%	78%

NiO_x, increasing i) the fabrication yield by $36\%_{abs}$, with a total of 78% functional devices (Table 5.2), and ii) the average PCE of up to $4.6\%_{abs}$ (Figure 9.3, Appendix).[14] This amelioration is accentuated with thicker PTAA films, resulting in significantly higher FF (to a certain limit). The thin PTAA layer is presumed to fill remaining gaps at the interface, thereby enhancing mechanical and electrical contact between the recrystallized absorber and NiO_x. Replacing the buffer layer, e.g., with a SAM – widely used to date in high-efficiency and operationally stable PSCs –,[223] or changing the lamination interface to perovskite/ETL could further boost the PCE. Both options are explored later in this work, resulting in laminated PSCs with a FF reaching up to 75%. Apart from the potential for higher PCE, these proof-of-concept devices showcase new possibilities that lamination offers. This process might support optimizations in existing architectures of PSCs or investigations of new materials to target enhanced long-term device stability.

5.2.2 Laminated semi-transparent perovskite solar cells‡

Semi-transparent PSCs might find applications in future architectural concepts such as window- and building-integrated PV, and play a pivotal role in the tandem technology as top solar cells.[224] The standard opaque rear electrode – typically thermally evaporated Au or Ag – must be substituted with a transparent conductive material. Transparent conductive oxides such as sputtered ITO, IZO, or IO:H are widely used as they provide low sheet resistance and low parasitic absorption.[59] However, TCO sputtering on top of a device layer stack is challenging. Perovskite films and CTLs, e.g., BCP, are soft and would be irreversibly damaged when exposed to particle bombardment during the sputtering deposition.[191] A prevailing strategy to address this incompatibility issue is incorporating buffer layers. These layers act as protective shields for sensitive layer stacks, permitting the deposition of transparent conductive materials on top. Common buffer layers include molybdenum oxide (MoO_x),[225] zinc oxide (ZnO),[226] and most prominently, ALD-deposited SnO_x.[218,227,228] The lamination technique proposes an alternative solution, as the rear electrode is independently deposited on a separate substrate. Decoupling the deposition of perovskite and TCO layers eliminates the risk of sputter damage, thereby broadening the range of compatible processing techniques and materials to advance the device performance of semi-transparent PSCs and tandem PVs.

This work applies the lamination process to PSCs in a semi-transparent architecture. A 300 nm thick ITO electrode optimally sputtered onto a PEN foil replaces the standard metal contact. This electrode demonstrates a low sheet resistance of 15 Ω/sq, equivalent to commercial glass/ITO substrates. The device comprises a front layer stack prepared on a glass substrate with an ITO electrode, a double HTL of NiO_x and 2PACz, and the perovskite absorber. The rear ITO electrode and double HTL of SnO_x and C_{60} are deposited on a separate PEN foil. The independently processed half-stacks are subsequently laminated at 90 °C, 80 MPa for 5 min, as illustrated in Figure 5.5a. This device architecture, established for the first time in this work, enables comparisons with existing literature using standard fabrication techniques.[120]

The lamination process results in functional semi-transparent PSCs with a remarkable fabrication yield of 88% functional devices – with PCEs exceeding 12 % criterion – in a single batch. Corresponding statistical data are provided in Figure 9.4, Appendix. The champion device exhibits a

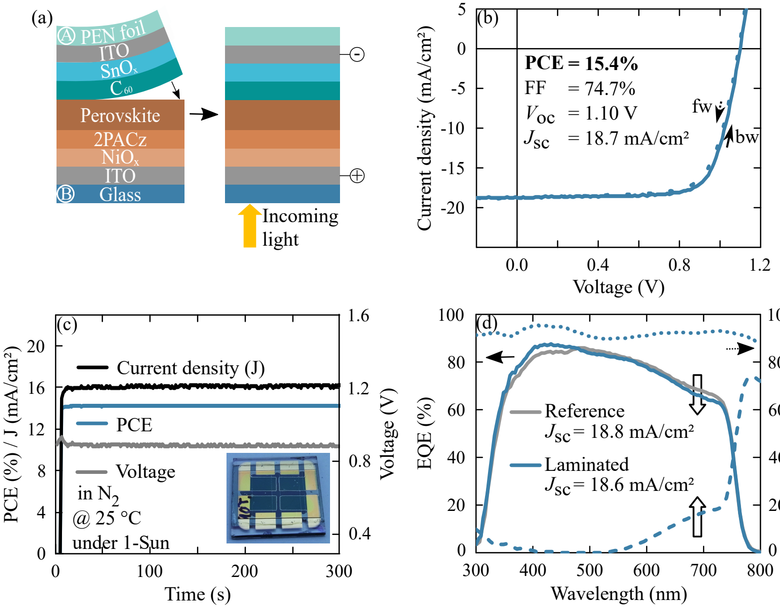

Figure 5.5: Lamination of semi-transparent perovskite solar cells (PSCs) by replacing the Au opaque contact with an ITO transparent electrode. a) Illustration of the solar cell architecture and lamination process. Devices are illuminated from the glass side. b) Current density-voltage characteristics, and c) maximum power point tracking of the champion PSC. The photograph shows a representative laminated semi-transparent PSC from the PEN foil side.[124] d) External quantum efficiency (EQE, solid line), reflectance (R, dots line), and transmittance (T, dashed line) characterization of the champion device. EQE of a representative semi-transparent device conventionally produced is shown in grey for comparison. Outlined arrows highlight decreased EQE near the perovskite bandgap, correlating with enhanced transmittance. Adapted from reference[120] with the permission of Wiley.

PCE of 15.4% with minor hysteresis and a stable power output displayed in Figure 5.5. This device outperforms our previously reported laminated semi-transparent PSCs by 4.1%$_{\text{abs}}$,[14] which is primarily attributed to the improved FF through reduced R_{series} and increased R_{shunt}. Compared to laminated opaque PSCs presented later in Section 5.3, the semi-transparent device demonstrates a similar V_{oc} of 1.1 V and FF of 74.7%. The J_{sc} of 18.7 mA/cm$^{\mathbf{2}}$, confirmed by EQE measurement (Figure 5.5d), is lower than in opaque laminated PSCs (about 20 mA/cm^2) due to imperfect light absorption near the perovskite bandgap from 600 to 750 nm. Indeed, the standard metal rear electrode in opaque devices acts as a reflective surface, enhancing light absorption via photon recycling within the solar cell.[229] Compared with conventional semi-transparent references, laminated PSCs show equivalent light management without specific absorption losses caused by the hot-pressing process (Figure 5.5c). Moreover, the device performance fully aligns with previously reported conventional references of a comparable layer stack – including the same triple-cation perovskite composition.[230] These results demonstrate that the high pressure and temperature applied do not lead to evident degradation of materials and interfaces.

This versatile fabrication technique paves the route for future investigations of novel types of transparent electrodes, which are usually restricted by the challenging sputtering deposition. Lamination allows the use of new electrodes with an optimized balance between conductivity and transparency, which could further improve the performance of semi-transparent PSCs.[231] These new electrodes could even be integrated directly into the superstrate.[200,203] Introducing anti-reflective coatings,[232] and textured layers are additional optimization strategies for increasing J_{sc} through reduced reflectance losses – typical for planar architectures.[128,233] To conclude, this study demonstrates the suitability of the lamination method to produce semi-transparent PSCs with high PCE. The presented architecture is a milestone in the development of the perovskite-based tandem technology. The PSC front layer stack might be hot-pressed atop the bottom solar cell to process future monolithic tandem devices with more degrees of freedom in the choice of materials and architectures. The feasibility of this novel fabrication concept is examined in Chapter 6 with the first prototypes of laminated perovskite/silicon monolithic tandems solar cells.

5.2.3 Bridging the gap between regular and inverted architectures

There are two common architectures for PSCs: regular (n-i-p) and inverted (p-i-n). Both architectures employ different CTLs due to compatibility constraints of standard fabrication methods. In p-i-n devices, thermally-evaporated materials such as C_{60} or its solution-processed fullerene derivative phenyl-C_{61}-butyric-acid-methyl-ester (PCBM) are used as ETL,[178,234,235] while NiO_x and 2PACz serve as HTL.[176,187] The n-i-p type architecture typically employs titanium dioxide (TiO_2) or SnO_2-np as ETL,[236,237] and Spiro-OMeTAD or PTAA as HTL.[238,239] Although some materials, such as PTAA, can be deposited on both sides

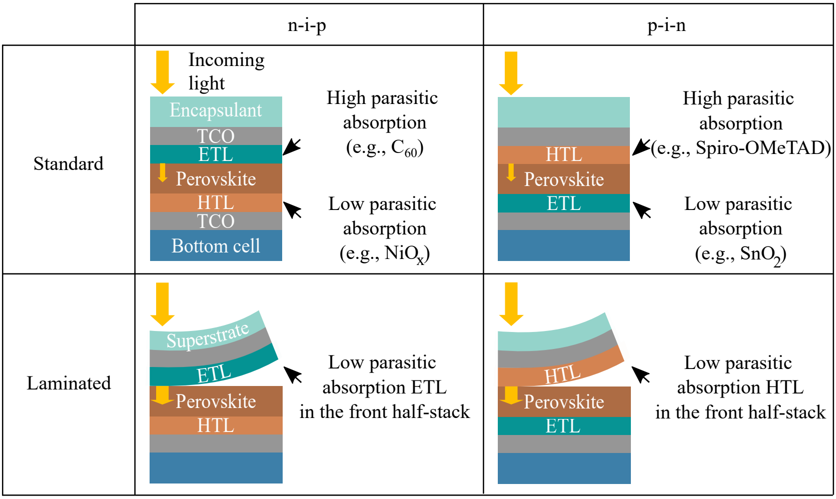

Figure 5.6: Concept illustration of the architecture inversion of a top perovskite solar cell via lamination in a monolithic tandem. Standard n-i-p (left) and p-i-n (right) orientations are compared. Both architectures are commonly limited by parasitic absorption at short wavelengths from about 300 to 550 nm caused by the front CTLs, typically C_{60} or Spiro-OMeTAD. In contrast, the rear CTLs usually exhibit high transparency (e.g., NiO_x and SnO_2). The CTLs causing parasitic absorption should be placed behind the perovskite film in the optical path to increase the amount of light reaching the absorber layer.

of the perovskite layer, most structures offer only one practical deposition order. For instance, NiO_x is conventionally deposited before the absorber to prevent sputtering damage.[219] Conversely, C_{60} is preferably deposited on top of the perovskite film due to its hydrophobic nature, complicating subsequent solution-based layer depositions.[192,193] Advances in materials and deposition techniques in n-i-p and p-i-n are thus difficult to conciliate, resulting in a gap between the development of the two architectures.[240] In the context of tandem PVs, the architecture type has important implications for device light management. Front-side CTLs must exhibit high transmission at short wavelengths to maximize the current in the top PSC. As illustrated in Figure 5.6, tandem solar cells in both architectures face problems of high parasitic absorptions caused in front CTLs, such as C_{60} in n-i-p and Spiro-OMeTAD in p-i-n structure.[60–63] Lamination suggests a solution to this challenge, as it allows variations in the deposition order of functional layers. The problematic layer can be placed behind the absorber in the PSC, enhancing the amount of absorbed light for charge carrier generation. The following proof-of-concept experiment demonstrates the feasibility of this innovative concept in single-junction devices.

Lamination can be used to invert the architecture of single-junction PSCs by varying the thin-film deposition order. Devices are fabricated in an n-i-p orientation with a layer stack developed for p-i-n PSCs. The resulting n-i-p architecture could not be conventionally produced due to the incompatibility issues mentioned above. CTL and perovskite processing remain the same for both architectures, with only the deposition order on the glass substrate differing. A semi-transparent architecture using a PEN/ITO superstrate allows a fair comparison with similar CTL/electrode interfaces, as shown in Figure 5.7. A double HTL consisting of NiO_x and 2PACz, and the perovskite absorber are either deposited on glass/ITO substrates in p-i-n structure or PEN/ITO foils in n-i-p. The double CTL of C_{60} and SnO_x is processed on the corresponding substrate or superstrate. The independently prepared half-stacks are subsequently laminated under the same conditions at 90 °C, 50 MPa for 5 min. By

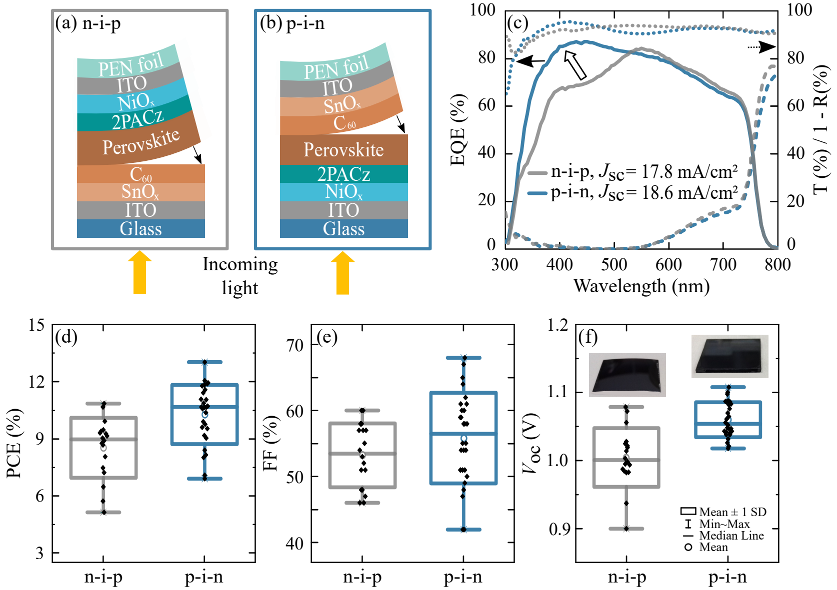

Figure 5.7: Proof of concept for varying the order of deposition of materials by lamination. a) Illustration of the n-i-p, and b) p-i-n architecture. The C_{60} charge transport layer (CTL) causing parasitic absorption is either placed before the perovskite film in the optical path (n-i-p) or behind (p-i-n). Devices are illuminated from the glass side. c) External quantum efficiency (EQE, solid lines), reflectance (R, dots), and transmittance (T, dashed lines) characterization of champion devices. The increase in EQE in p-i-n devices, highlighted by an outlined arrow, is attributed to reduced parasitic absorption losses in the front layers. d) PCE, e) FF, and f) V_{oc} laminated perovskite solar cells in both p-i-n and n-i-p architectures. Current density-voltage characteristics are available in reference[182]. Photographs in the inset show a perovskite film deposited on a PEN/ITO foil (left), which is slightly bent due to high residual strains, and a glass/ITO substrate (right).

doing so, the CTL causing parasitic absorption (C_{60}) is either placed before the absorber in the optical path (n-i-p) or behind (p-i-n). Therefore, this experiment allows the investigation of improving light management by inverting the layer stack of PSCs using the lamination technique.

Laminated PSCs demonstrate PCEs of 10.3% and 8.5% on average for p-i-n and n-i-p architectures, as displayed in Figure 5.7d. EQE and optical characterizations indicate that the improved J_{sc} in p-i-n devices is due to an increased absorption in the wavelength range from 300 to 530 nm (Figure 5.7c). Conversely, diminished absorption in the n-i-p structure is attributed to parasitic absorption caused by the front C_{60} layer, reducing the J_{sc} by 0.8 mA/cm². This finding highlights the crucial role of the architecture type in light management in PSCs, underscoring careful consideration when selecting appropriate architecture for optical optimization. Furthermore, while the FF remains unchanged, V_{oc} decreases by approximately 40 mV on average in n-i-p. An additional experiment is conducted to investigate this reduction, which compares conventional PSCs of the same architecture prepared on PEN/ITO foils or glass/ITO substrates. Replacing glass with PEN foil results in a similar decrease in V_{oc} (Table 5.3), suggesting that factors beyond the lamination process are involved. H. Lai et al. made similar observations and concluded that the relatively rough PEN/ITO surface affects the uniformity of the 2PACz deposition.[241] A possible additional factor is the higher residual strain in PEN foils, shown in Figure 5.7f, which could alter the device performance due to the different coating qualities of both solution-processed 2PACz and perovskite thin films. Nevertheless, comparably high PCE between the two architectures underlines the potential of lamination in bridging the gap in the development of n-i-p and p-i-n PSCs. By allowing for variations in the material deposition order,

Table 5.3: PCE, FF, V_{oc}, and J_{sc} of single-junction perovskite solar cells using glass (11 devices) or PEN foil (13) as substrates. Devices are conventionally fabricated and comprise ITO/$\mathrm{NiO_x}$/2PACz/perovskite/BCP/C_{60}/Au. SD stands for standard deviation.

	PCE (%)		FF (%)		V_{oc} (V)		J_{sc} (mA/cm²)	
	Glass	PEN	Glass	PEN	Glass	PEN	Glass	PEN
Mean	16.7	13.6	72.0	71.0	1.13	1.08	20.7	17.8
SD	0.4	0.2	1.6	0.7	0.01	0.01	0.2	0.2
Minimum	15.9	13.3	69.0	70.0	1.12	1.07	20.3	17.6
Maximum	17.3	14.1	74.0	72.0	1.13	1.09	21.0	18.0

lamination overcomes severe parasitic absorption in functional layers, substantially improving the J_{sc}. The feasibility of this technique, which has now been demonstrated in single-junction solar cells, is investigated in Section 6.3.4 in perovskite-based tandem devices.

5.3 Hot-pressing conditions for solar cell lamination

The improved perovskite morphology and crystallinity achieved by applying high pressures and temperatures are expected to enhance the performance of laminated PSCs. While Section 5.3.1 highlights the critical role of the temperature for successful device half-stack adhesion, Section 5.3.2 investigates the influence of key hot-pressing parameters on device performance. The hot-pressed perovskite surface also affects light management in PSCs, which is the focus of Section 5.3.3. Conventional references are systematically prepared in parallel with laminated devices. Functional layers are the same in both cases, as illustrated in Figure 5.8. The front layer stack comprises a glass substrate, an ITO front electrode, and a double HTL of NiO$_x$ and 2PACz. The absorber is a triple-cation

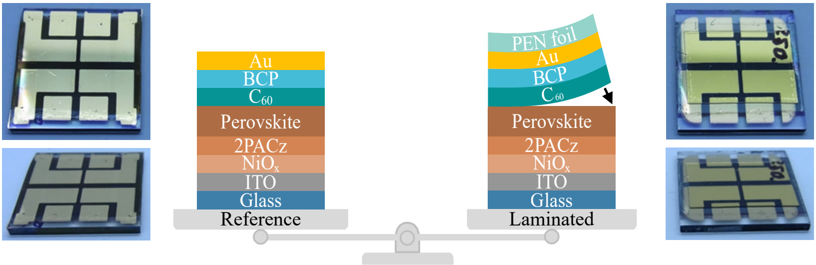

Figure 5.8: Architecture of conventionally processed references and laminated perovskite solar cells (PSCs). Photographs show representative devices from the Au electrode from different angles. All functional layers are the same. PEN foils are used as superstrates to fabricate the rear half-stack in laminated PSCs. Each (16x16) mm substrate comprises four independent 10.5 mm^2 active areas.

perovskite of composition $Cs_{0.1}(MA_{0.17}FA_{0.83})_{0.9}Pb(I_{0.83}Br_{0.17})_3$ unless otherwise specified. In laminated PSCs, a PEN foil is used as a superstrate to deposit the Au electrode and a double CTL of BCP and C_{60}. In references, these functional layers are deposited directly on the absorber. For clarity, the direct comparison between laminated and reference PSCs is detailed in a dedicated Section 5.4, highlighting intrinsic characteristics of the lamination process on materials and interfaces.

5.3.1 Evidence of a temperature threshold for successful lamination

The hot-pressing temperature plays a pivotal role in the perovskite recrystallization process.[148] In state-of-the-art lamination techniques for PSCs at the perovskite/perovskite interface, high temperatures exceeding 120 °C are employed,[115,150,222] suggesting an implicit minimum threshold to induce recrystallization. The present study examines lower temperatures, ranging from 60 to 100 °C, on half-cell adhesion and device performance of laminated PSCs. Other parameters, such as pressure and duration, are fixed at 80 MPa and 5 min, respectively. A 720 nm double-cation absorber is employed with the composition $Cs_{0.17}FA_{0.83}Pb(I_{0.92}Br_{0.08})_3$. This material slightly differs from the triple-cation perovskite used in following sections, showcasing the lamination versatility with different thicknesses and compositions.

Figure 5.9 displays the performance of laminated devices depending on hot-pressing conditions and corresponding fabrication yields based on a decision criterion of 10% PCE. At temperatures as low as 60 and 75 °C, adhesion between half-stacks is insufficient, resulting in non-functional devices (yield = 0%). Starting at 90 °C, half-stacks adhere together, leading to laminated PSCs with PCEs of up to 12.6%. Nevertheless, the fabrication yield remains below 20%. The wide statistical data variation primarily stems from J_{sc} variations, averaging (6.6±5.2) mA/cm²

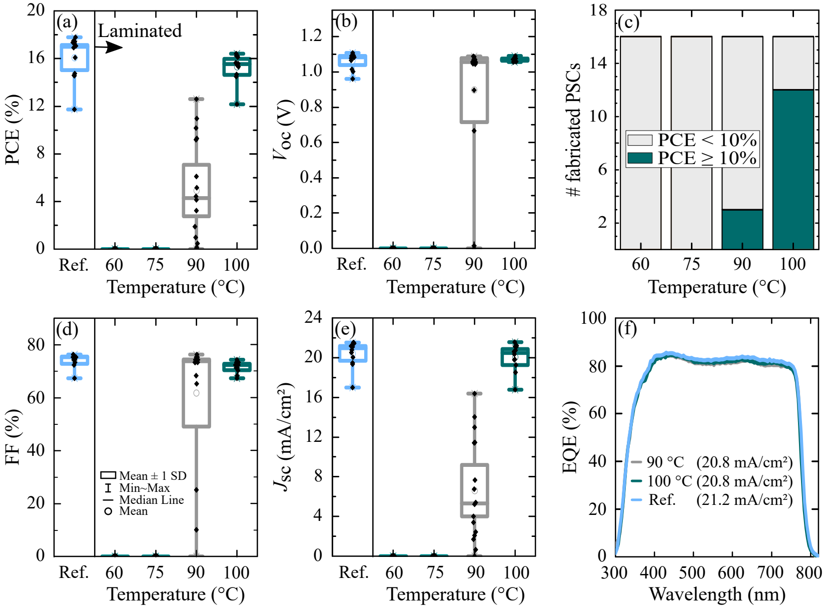

Figure 5.9: Evidence of a minimum temperature threshold for successful lamination. a) PCE, b) V_{OC}, d) FF, and e) J_{SC} of conventional references (Ref.) and perovskite solar cells (PSCs) laminated at different temperatures from 60 to 100 °C. c) Total number of fabricated PSCs and functional devices (green). The corresponding yields are 0% at 60 and 75 °C and increase to 19% and 75% at 90 and 100 °C, respectively. f) External quantum efficiency (EQE) measurements of a representative reference (blue), and laminated PSCs at 90 (grey) and 100 °C (green). Corresponding J_{SC} are given in the inset. Current density-voltage characteristics are available in reference[124].

in J-V characteristics. Interestingly, integrated J_{SC} from EQE measurements reach similar values to references with about 20.8 mA/cm^2 (Figure 5.9f). This substantial inconsistency – which disappears at higher temperatures – is attributed to an inhomogeneous lamination quality across the active area (≈10.5 mm^2), as EQE measurements are conducted on small spots only (0.74 mm x 0.74 mm aperture size). At 100 °C, 75% of the devices are functional with a mean PCE of 15.3%, on par with conventionally produced references (16.1%).

This temperature variation study highlights numerous critical insights concerning the lamination process. More than a high pressure of 80 MPa alone is necessary to unite the two half-stacks. A minimum threshold in temperature must be exceeded for successful lamination. Heat provides the required energy to trigger the perovskite recrystallization, enabling device half-stack adhesion. These findings are consistent with existing literature emphasizing the essential role of elevated temperatures in recrystallization processes and laminating PSCs at the perovskite/perovskite interface.[115,204–206] For instance, the roughness reduction of a hot-pressed perovskite surface was significantly more pronounced than when the same pressure was applied without heat.[139] This study also underscores the lamination compatibility with different perovskite compositions and thicknesses, although the suitable process window may vary: while this double-cation absorber is successfully laminated at 100 °C, the triple-cation perovskite investigated in the following shows promising outcomes already at 85 °C. Recent publications reinforced this observation by adjusting hot-pressing temperature depending on the absorber composition: e.g., 150 °C for $CsPbBr_3$,[132] and 90 °C for $MAPbBr_3$,[133] with the same applied pressure of 10 MPa in both cases. Even multi-cation perovskites exhibit different thermal sensitivity between 80 and 120 °C, depending notably on the presence of MA.[151] Therefore, identifying appropriate hot-pressing conditions in accordance with the absorber composition is essential to achieve efficient laminated PSCs.

5.3.2 Suitable process window for enhanced device performance

Laminating PSCs in a suitable process window, i.e. taking into account the three key hot-pressing parameters, is critical to maximize the device performance. Two key findings emerged from previous results regarding the temperature: While a perovskite-specific minimum threshold must be overcome to allow successful lamination (Section 5.3.1), exceeding 100 °C initiates triple-cation perovskite decomposition (Section 4.2). These insights have delimited a primary range from 85 to 100 °C for characterizing PSCs as a function of the applied temperature. Duration and pressure are fixed at 5 min and 80 MPa, respectively. Results displayed in Figure 5.10a show that the investigated range yields high-efficiency PSCs of up to 17.1%. An analysis of variance (ANOVA) indicates no statistical significance at the 0.05 α-level in a PCE improvement with increasing lamination temperatures. The FF, V_{oc}, and J_{sc}, summarized in Table 5.4, appear independent of temperature variations in this range. In particular, outstanding FFs of about 77% are achieved at both range limits of 85 and 100 °C. These FF values are significantly higher than those attained with state-of-the-art lamination techniques for PSCs, with only a few reports overcoming the 70% milestone.[115,166,204,205,242,243] An open question remains regarding the lamination of PSCs at temperatures exceeding 100 °C, where larger perovskite grains are obtained (Section 4.3.1), possibly enhancing device performance. Hence, an additional study is conducted within an extended range to 120 °C, as presented in Figure 9.5, Appendix. Laminated PSCs at 105 °C and above encounter a severe decline in V_{oc} from 1.08 V at 90 °C to 1.03 and 1.01 V at temperatures of 105 and 120 °C, respectively. Reduced V_{oc} is attributed to the perovskite decomposition above 100 °C, as defects in the crystal lattice constitute one of the predominant pathways for non-radiative recombination.[244,245] Overall, the average V_{oc} of 1.09 V for temperatures under 100 °C (Table 5.4) exceeds those obtained in PSCs laminated at the perovskite/perovskite interface (around 1.02 V).[115,146,150,204–206,222] This improvement might be explained by the lower temperatures than those used elsewhere ($\geq$120 °C). Lower temperatures effectively prevent degradation while yielding efficient PSCs and expanding the range of compatible materials for functional layers.

Insights evidenced in Chapter 4 delimited an initial interval for investigating lamination time on PSC performance. Increasing duration significantly reduces the perovskite RMS surface roughness, predominantly

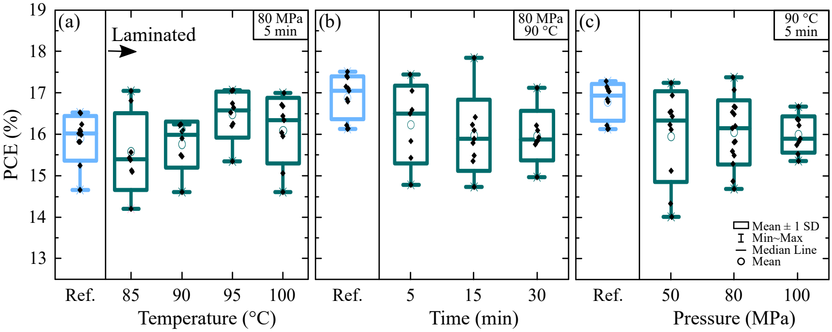

Figure 5.10: Performance of laminated perovskite solar cells depending on hot-pressing conditions. Each parameter is varied separately in a batch. a) PCE of devices as a function of applied temperature, b) process duration, and c) pressure. The performance of references (Ref.), conventionally fabricated in parallel to enable comparison, highlight some inevitable batch-to-batch variations. Current density-voltage characteristics are available in reference [123].

between 5 and 30 min, and exceeding an hour leads to material decomposition. Figure 5.10b displays the PCE of PSCs laminated for 5 to 30 min in comparison with conventional references. Pressure and temperature are fixed at 80 MPa and 90 °C, respectively. Laminated PSCs demonstrate outstandingly high PCEs for a short time of 5 min, averaging at 16.6%. Although the J_{sc} and FF remain approximately constant for 5 and 15 min, longer durations appear detrimental to device performance (Table 5.4), in consistency with existing literature. [243] ANOVA test indicates that exceeding 5 min results in a statistically significant V_{oc} reduction at the 0.05 α-level. A short duration of 5 min, therefore, not only accelerates device fabrication but also benefits the PSC performance. Compared to an average hot-pressing of 20 min, [115,144,150,204–206] 5 min is substantially faster than other state-of-the-art lamination techniques for PSCs using perovskite recrystallization.

Another key lamination parameter is the pressure applied. In that regard, this work previously highlighted that a minimum of 50 MPa is required to improve perovskite surface morphology, and pressures of more than 100 MPa are unnecessarily high (Section 4.3.2). The substantially higher pressure level compared to other laminated PSCs using perovskite recrystallization (<10 MPa),[115,150,222] raises the question of whether such elevated pressures might cause damage within the device layer stack. To answer this question, a study within the range from 50 to 100 MPa is performed at a fixed temperature and duration of 90 °C and 5 min, respectively. Figure 5.10c shows the achieved PCE of PSCs. Remarkably, high PCEs are demonstrated, averaging at 16.1%, with an excellent V_{oc} of 1.11 V. The champion device, laminated at 80 MPa, exhibits an outstanding PCE of 17.4%. It is noted that the standard deviation in all J-V characteristics is progressively reduced by increasing

Table 5.4: FF, V_{oc}, and J_{sc} of conventional references (Ref.) and laminated perovskite solar cells under different hot-pressing conditions. Temperature (33 devices), duration (26), and pressure (34) are investigated in separate batches. The performance of conventionally fabricated references is a concatenation of three batches prepared in parallel (35 devices in total). SD, min., Max. stand for standard deviation, minimum, and maximum value, respectively. Unless otherwise specified, temperature, pressure, and processing duration are fixed at 90 °C, 80 MPa, and 5 min. The data can be visualized in reference[123].

	FF (%)		V_{oc} (V)		J_{sc} (mA/cm^2)	
	Mean (SD)	Min/Max	Mean (SD)	Min/Max	Mean (SD)	Min/Max
Ref.	74.9 (2.0)	68.3/78.2	1.06 (0.02)	1.04/1.1	20.8 (0.4)	20.3/21.6
85 °C	71.1 (3.4)	66.0/76.7	1.08 (0.01)	1.06/1.10	20.2 (0.5)	19.6/21.0
90 °C	71.5 (2.6)	66.3/73.9	1.07 (0.01)	1.06/1.08	20.6 (0.4)	19.7/21.0
95 °C	73.8 (1.3)	71.7/75.2	1.08 (0.01)	1.06/1.10	20.7 (0.5)	19.7/21.1
100 °C	72.7 (3.2)	66.6/76.5	1.07 (0.01)	1.05/1.08	20.7 (0.2)	20.4/20.9
5 min	73.2 (4.0)	66.3/77.0	1.09 (0.01)	1.08/1.10	20.8 (0.3)	20.5/21.2
15 min	73.2 (3.9)	64.4/76.7	1.08 (0.01)	1.06/1.09	20.3 (0.8)	19.0/21.3
30 min	71.6 (3.0)	66.1/76.7	1.08 (0.01)	1.07/1.10	20.6 (0.2)	20.4/20.9
50 MPa	69.7 (3.7)	63.4/73.7	1.11 (0.02)	1.07/1.12	20.6 (0.2)	20.3/21.1
80 MPa	72.6 (2.9)	68.0/77.5	1.11 (0.01)	1.10/1.12	20.2 (0.5)	19.3/21.0
100 MPa	70.3 (1.8)	67.8/72.2	1.10 (0.01)	1.10/1.12	20.6 (0.2)	20.4/20.8

pressure. This improvement might indicate an enhanced homogeneity in the lamination quality and supports the hypothesis that higher pressures lead to more uniform hot-pressed perovskite surfaces.

In summary, these results demonstrate the repeatability of the lamination process, indicate a certain degree of batch-to-batch variations, and outline an appropriate process window. Temperatures between 85 and 100 °C and pressures from 50 to 100 MPa applied for 5 min are suitable for fabricating high-efficiency PSCs using this triple-cation perovskite absorber. With PCEs above 17%, this technique is one of the most performant among state-of-the-art methods (Table 9.2, Appendix). Furthermore, three critical findings were underscored: i) Limiting the temperature to 100 °C enhances device performance while broadening the range of compatible materials, facilitating future research in novel architectures; ii) Higher pressures (80-100 MPa) might be favorable to reduce the output variability; iii) An extended lamination negatively affects the V_{oc}. Hot-pressing duration is limited to 5 min, enabling outstanding FF and V_{oc} compared to state-of-the-art techniques while accelerating the fabrication throughput. Further studies could explore even shorter durations and target instant lamination. It is also noted that laminated PSCs exhibit similar performance to conventional references, with a systematically higher V_{oc} (Table 5.4), highlighting that they not only withstand hot-pressing without evident signs of degradation but might benefit from it. The substantial V_{oc} enhancement is one of the additional advantages of this fabrication process and merits a dedicated discussion in Section 5.4.

5.3.3 Lamination process implications in device light management

A smoother perovskite surface after recrystallization is likely to change its reflectivity and, consequently, the light management of the solar cell.[242,246–248] The recrystallization is dependent on the temperature, pressure, and duration applied during the hot-pressing process. EQE measurements are conducted on laminated PSCs under different conditions to characterize their spectral responses. These measurements also confirm previous J_{sc} values extracted from J-V characteristics (Table 5.4). Integrated J_{sc} from EQE are, indeed, less sensitive to uncertainties in the exact active area arising, e.g., from a half-stack misalignment. Figure 5.11 indicates that J_{sc} values might fluctuate from batch to batch but are generally unaffected by temperature variations. Increasing pressure and time, however, progressively decreases the J_{sc}. At 5 min, the J_{sc} is 20.6 mA/cm² and decreases to 20.2 mA/cm² for a 30 min long lamination. This reduction is consistent with the statistical data provided in Table 5.4. Overall, J_{sc} values are comparable to those obtained with state-of-the-art lamination techniques for fabricating opaque PSCs.[206,242,249] Reported semi-transparent laminated solar cells usually achieve higher J_{sc} exceeding 22 mA/cm², which is primarily attributed to significantly thicker double perovskite layers from 600 to 800 nm.[115,150] Using thicker films is an established strategy for enhancing the current in single-junction PSCs. However, this approach may not be suitable for tandem applications. With a current thickness of 370 nm,

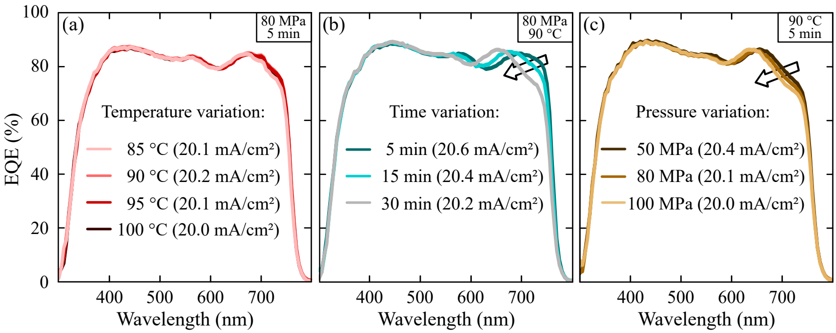

Figure 5.11: External quantum efficiency (EQE) of laminated perovskite solar cells depending on hot-pressing conditions. a) EQE of representative devices as a function of the applied temperature, b) processing duration, and c) pressure. Each parameter is independently varied. Insets show the integrated J_{sc}. Outlined arrows highlight a shift in EQE signal at wavelengths from 600 to 750 nm, which becomes more pronounced with a longer lamination and higher pressures. These shifts are attributed to a progressive reduction of the perovskite roughness triggered by the hot-pressing process. Adapted from reference[120] with the permission of Wiley.

perovskite/silicon tandem solar cells can already attain current-matching conditions, as discussed in Section 6.3.3.

Reduced J_{sc} observed in PSCs laminated for long times and elevated pressures are caused by a shift in the spectral response near the perovskite bandgap from 600 to 750 nm, as illustrated in Figure 5.11. Such interference patterns suggest a variation in absorber thickness.[172] However, no change in thickness was evidenced even after several hot-pressing steps in Section 4.4. The amplitude of the EQE signal shift seems to correlate with the degree of reduction in perovskite surface roughness. Indeed, the shift is accentuated as lamination duration increases, which perfectly mirrors changes in reflectance (Figure 9.6, Appendix), while a progressive decrease in RMS roughness is noticed from about 10 to 2 nm for 5 and 30 min, respectively (Section 4.3.2). The EQE signal shift is less pronounced when pressure varies from 50 to 100 MPa, which aligns with expectations as the RMS roughness only decreases from about 6 to 4 nm in this range. Temperature variations, which did not affect perovskite roughness, also show no influence on light management in laminated PSCs, in consistency with existing literature using a similar hot-pressing process.[143] These results underscore a correlation between the interference patterns at long wavelengths and the smoother perovskite surface. Diffuse reflectance measurements provided in the following further reinforced this hypothesis.

5.4 Laminated perovskite solar cells on par with conventional references‡

Laminated PSCs are here systematically compared with conventional references of identical architecture, highlighting the influence of hot-pressing processes on materials and interfaces. Functional layers are kept the same to allow a direct comparison. Still, three fundamental aspects that might affect the comparison, regardless of the architecture, must be acknowledged, as outlined in the following.

1. Laminated devices are covered by a PEN foil, which is used as a superstrate for depositing the rear electrode and CTLs. An indirect access to the rear electrode beneath the PEN foil requires a more intricate contacting technique, which can result in higher resistive losses.
2. Laminated PSCs exhibit some uncertainty in their active area, arising from i) minute alignment shifts, modifying the half-stack overlap, and ii) edges that may not be precisely defined due to minor processing variations, such as shadow-mask effects during metal evaporation.
3. Although lamination is conducted under an isolated, N_2-filled chamber, the machine is outside a glove box in an ambient atmosphere. As a result, the samples are assembled in an environment that exposes them to particles, oxygen, and humidity, which are known triggers of perovskite degradation.

While these factors may lead to higher statistical data variability in laminated PSCs, this comparison is a first step in determining whether this manufacturing process can compete with standard methods in terms of device performance.

The following comparison between references and laminated PSCs is based on the concatenation of three previous parameter studies from Section 5.3 and totalizes 40 laminated devices and 34 references. All laminated devices considered in this analysis are fabricated using identical temperature (90 °C), pressure (80 MPa), and duration (5 min). Both champion PSCs achieve outstanding PCEs of 17.5% (Figure 5.12a), with stable power output.[120] The laminated PSC exhibits a V_{oc} of 1.10 V, a FF of 76.6%, and a J_{sc} of 20.7 mA/cm^2. While the remarkable overlap of J-V characteristics indicates equivalent device performance, two aspects should be underlined: The laminated device exhibits a higher V_{oc} (+20 mV) compared to the reference, which compensates for a slight FF reduction (-1.2%$_{\mathrm{abs}}$). The J_{sc} remains the same in both cases. This observation is consistent with a previous report showing

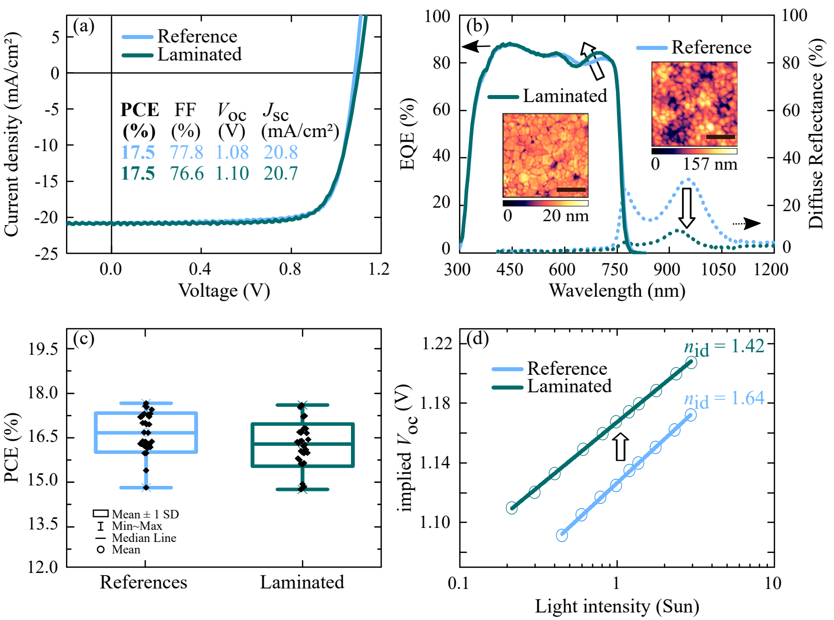

Figure 5.12: Conventionally processed references and laminated perovskite solar cells (PSCs) in comparison. a) Current density-voltage characteristics, and b) external quantum efficiency (EQE) of the champion perovskite solar cells (PSCs). Diffuse reflectance is measured on an identical layer stack. Outlined arrows highlight an EQE signal shift and reduced diffuse reflectance, attributed to the smoother perovskite surface after lamination. The inset shows atomic force microscopy images of hot-pressed and pristine perovskite films. The scale bar corresponds to 1 μm. c) PCE of laminated PSCs on par with conventional references. d) Intensity-dependent characterization of implied V_{oc} of representative devices. The V_{oc} enhancement in laminated devices aligns with the increased implied V_{oc}, indicated by an outlined arrow. n_{id} stands for ideality factor. Adapted from reference[120] with the permission of Wiley.

that PSCs with pristine and hot-pressed perovskites demonstrate similar J_{sc} despite harsh processing conditions (up to 250 °C).[143] EQE measurements of champion devices, displayed in Figure 5.12b, reveal a peak shift discernible at long wavelengths from 600 to 750 nm near the perovskite bandgap. At first, such interference patterns suggest a variation in absorber thickness.[172] However, we did not find evidence of changes in thickness after hot-pressing. The EQE signal shift is reminiscent of findings presented in Section 5.3.3, where a correlation with reduced perovskite roughness in laminated PSCs is emphasized. That a smoother surface with larger grains modifies the EQE characteristics aligns with existing literature.[247,248] This hypothesis is further substantiated by optical characterization, which reveals less diffuse reflectance, dropping from $31\%_{\mathrm{abs}}$ in references to $8\%_{\mathrm{abs}}$ in laminated devices at the 950 nm wavelength. Reduced diffuse reflectance is characteristic of planar surfaces, which inherently reduce light scattering. These results demonstrate that despite comparable device performance, the impact of lamination on the perovskite absorber and its enhanced surface morphology can still be discerned.

The two champion devices are representative of a broader statistical data set depicted in Figure 5.12c. Laminated PSCs achieve comparable PCEs to references, averaging 16.2%. Furthermore, a total fabrication yield of about 80% functional devices – with PCEs exceeding the 14% criterion – is obtained across three batches, reaching up to 94% within a single batch. A high yield indicates the reliability and homogeneity of the hot-pressing process, emphasizing its potential to match the performance of conventional methods. Furthermore, from an apparent reduced FF in laminated PSCs (Table 5.5), two features must be distinguished: On the one hand, R_{series} are significantly higher, and the statistical data variation is noticeable, which are both attributed to the more intricate contacting procedure. On the other hand, laminated devices demonstrate a substantially higher R_{shunt}, in consistency with observations from Li et al.[207] A possible explanation is the prevention of metal diffusion through pinholes during the thermal evaporation of the metal electrode – typical for standard fabrication methods. The formation of possible shunt paths is limited as the Au electrode is not directly deposited on the layer stack. Higher R_{shunt} might also be related to more continuous CTLs through a facilitated deposition on smooth superstrates compared to sequential processing on rough perovskite surfaces, as suggested in a previous report.[206] Indeed, we measured an RMS roughness of only

Table 5.5: FF, V_{oc}, J_{sc} of references (34 devices) and laminated perovskite solar cells (40) presented in Figure 5.12. SD, Min. and Max. stand for standard deviation, minimum, and maximum values, respectively.

	FF (%)		V_{oc} (V)		J_{sc} (mA/cm²)		R_{series} (Ω)		R_{shunt} (kΩ)	
	Ref.	Lam.	Ref.	Lam.	Ref.	Lam.	Ref.	Lam.	Ref.	Lam.
Mean	74.9	72.1	1.06	1.09	20.8	20.4	68	115	66	147
SD	2.0	3.0	0.02	0.02	0.4	0.5	7	30	52	203
Min.	68.3	66.3	1.04	1.06	20.3	19.3	56	69	9	14
Max.	78.0	77.5	1.09	1.12	21.6	21.0	85	181	231	935

2 nm on Au layers evaporated on PEN foils, significantly smoother compared to about 20 nm of pristine perovskite films. The current device active area aligns with the 0.1 cm² average size for state-of-the-art lamination techniques.[115,166,197,200,204–206,242,249] Nonetheless, Yadavalli et al. recently reported that high R_{shunt} of laminated devices is retained even over larger areas, increased from 0.1 to 1.15 cm².[206] Wu et al. also demonstrated the ability to produce a 25 cm² large module with a lamination process using perovskite recrystallization.[205] Improved perovskite/CTL interface and reduced typical shunt paths in the PSC make this technique particularly interesting for upscaling. As pinholes and inhomogeneities in the absorber are usually challenging on large substrates, lamination addresses one critical aspect of upscaling the perovskite-based PV technology.[250]

Laminated PSCs also demonstrate a 30 mV higher V_{oc} on average than references, as Table 5.5 summarizes. PLQY measurements, displayed in Figure 5.12d, reveal that the V_{oc} improvement closely aligns with a higher implied V_{oc}. Reduced n_{id} indicates less contribution of non-radiative recombination losses in laminated PSCs.[55] These results are in line with PLQY measurements conducted on hot-pressed perovskites (Section 4.5), suggesting that the increased V_{oc} can be attributed to i) the enhanced surface morphology exhibiting larger grains and a smoother surface, and ii) the superior perovskite/C_{60} interface quality through a decreased surface area. In conclusion, the lamination technique can perform equivalently to standard methods with promising additional advantages, such as a significant V_{oc} and R_{shunt} enhancement. Despite the harsh hot-pressing conditions, functional layers and interfaces remain of high quality. This is particularly interesting, as we use significantly higher pressure, lower temperatures, and shorter times than state-of-the-art lamination techniques, reporting <10 MPa, ≥ 120 °C, and a 20 min hot-pressing duration on average.[115,146,150,204–206,222] Increasing the duration or temperature for our process thus appears unnecessary, facilitating the device fabrication and accelerating the throughput. Under such hot-pressing conditions, the enhanced perovskite morphology veritably benefits the overall device performance.

5.5 Shelf-life stability of laminated solar cells‡

The stability of PSCs over time remains a critical challenge that must be addressed for future industrial applications. Stress factors are classified as either i) intrinsic, triggered by light exposure, temperature variations, and electrical bias, or ii) extrinsic, governed by interactions with ambient species such as oxygen and moisture.[64] While encapsulation targets solar cell protection from extrinsic factors,[251] recent research emphasized a significant influence on device intrinsic stability of the perovskite composition,[252] morphology,[253] and device architecture, including passivation techniques.[55] Here, long-term measurements are performed on laminated PSCs to test the hypothesis that a hot-pressed absorber improves the device intrinsic stability. Devices are compared to conventional references with the same architecture to distinguish the contribution of the lamination technique from the material selection. In this comparison, the possible direct encapsulation of devices must be considered. Because functional layers are sandwiched between the sub- and superstrates, sensitive materials are possibly protected from extrinsic degradation factors. However, the sides of solar cells remain exposed (lateral permeation). Given the unknown barrier properties of this partial encapsulation, all stability studies in this work are conducted in an inert atmosphere.

The consensus statement based on ISOS procedures for stability assessment and reporting for perovskite-based PVs proposes different levels of sophistication.[64] The simplest standardized ISOS-D-1-I protocol refers to the shelf-life stability of devices stored in the dark, in an inert atmosphere, at room temperature, and in open-circuit conditions, as summarized in Table 5.6. This protocol is often a starting point for stability assessment in the literature, as it provides insights into the intrinsic stability of solar cells subject to time only, enables testing an unlimited number of devices, and because storage conditions can be carefully controlled and reproduced in any laboratory.[254–258] The primary focus of this work is a comparative stability study of references and laminated PSCs using this ISOS-D-1-I protocol. A more robust test of the high operational stability for laminated devices is also presented, testing the combined effects of light and heat during MPP tracking, corresponding to the established ISOS-L-2-I protocol introduced in Section 5.2.1. Further comparative studies to fully assess the device stability over time, including exposure to temperature, light, and electrical bias, can be undertaken to demonstrate devices withstand operating conditions in real-world applications.

The first shelf-life stability study is performed on laminated and references PSCs over 100 days. Figure 5.13a displays the device performance evolution over time. Remarkably, laminated PSCs maintain their initial PCEs throughout 100 days without any sign of degradation. In contrast, references experience a rapid deterioration, with a PCE decrease of $20\%_{\mathrm{rel}}$ within the first 40 days. J-V characteristics of references in Figure 9.7, Appendix, reveal an evident S-shape, systematically emerging over time and impacting all J-V characteristics: The FF and J_{sc} decline by approximately $30\%_{\mathrm{rel}}$ at $\mathrm{t} = 100$ days compared to their initial values. Additional photoluminescence measurements are provided in Figure 5.14 to illustrate the degradation process. Here, the stability study is reproduced with laminated and reference PSCs characterized before and after an aging period of 130 days under identical ISOS-D-1-I storage conditions. The most prominent observation is the emergence of inhomogeneous areas in reference PSCs, which were initially uniform. This degradation pattern is not reflected in laminated devices. Similar results were reported by Li et al.,[207] demonstrating that PSCs with a transferred Au electrode are more stable than conventionally prepared devices of the same architectures stored over 100 days in N_2 and in the dark. The different layer quality and growth of the Au rear electrode and ETLs could be contributing factors. In the lamination technique, these thin films are thermally evaporated on the PEN foil and not directly onto the absorber, as in standard methods. This fundamental difference might prevent critical proximity between the perovskite and Au through more continuous layers, limiting Au migration and providing enhanced intrinsic stability to devices.[259–263]

Table 5.6: Storage conditions of perovskite solar cells according to the ISOS-D-1-I protocol for testing shelf-life device stability.[64]

ISOS protocol	D-1-I
Atmosphere	Inert atmosphere, N_2 (O_2<1 ppm; H_2O<1 ppm)
Temperature	Ambient (25 °C)
Light	OFF
Bias voltage	OFF (open-circuit condition)

Considering the outstanding shelf-life stability of laminated PSCs, the study is prolonged to one year. Ten previously studied devices (Section 5.4) are re-measured after a storage compliant with the ISOS-D-1-I protocol. All PSCs retain their initial efficiency, with an average PCE of 16.6%, a FF of 76%, a V_{oc} of 1.10 V, and a J_{sc} of 20.5 mA/cm² at t = 1 year. In particular, the champion device maintains its initial PCE of 17.6%, as shown in Figure 5.13c. One year is an unprecedented period of time for examining the stability of laminated PSCs,

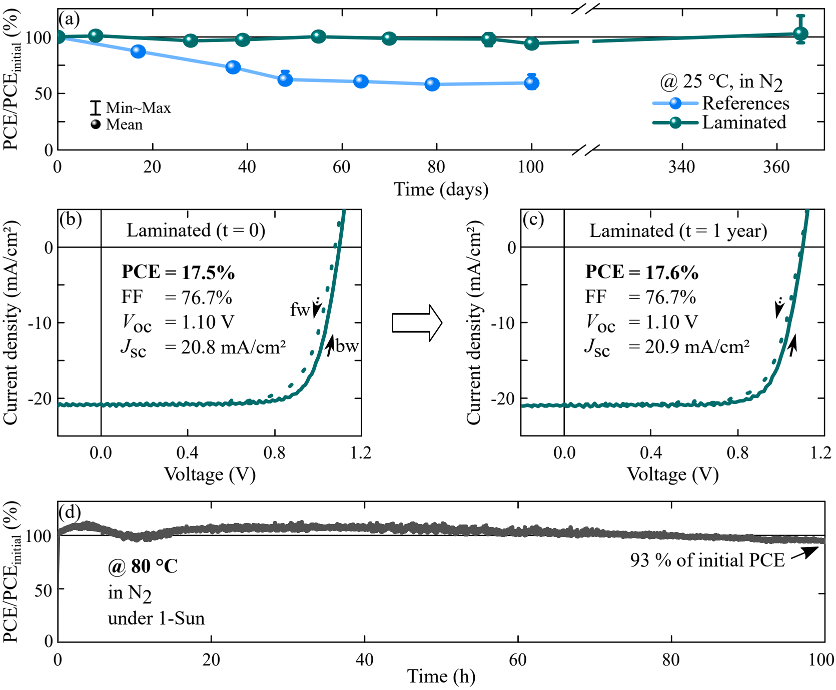

Figure 5.13: Thermal and long-term stability studies of laminated perovskite solar cells (PSCs). a) PCE evolution over 100 days of laminated devices (3 devices) and references (3) stored according to the ISOS-D-1-I protocol and measured with a bi-weekly interval. These devices are representative of the complete study – available in[124] – based on a total of 24 solar cells, measured after preparation (t = 0), at mid-term, and after 100 days. Initial PCEs (PCE$_{\text{initial}}$) of laminated and reference PSCs are (16.0±0.8)% and (17.4±0.3)%, respectively. b) J-V characteristics of the champion PSC measured before (t = 0), and c) after a year. d) Maximum power point tracking of a representative laminated PSC at 80 °C under continuous illumination over 100 h. These measurement conditions are based on the ISOS-L-2-I protocol introduced in Section 5.2.1. Adapted from reference[120] with the permission of Wiley.

with studies limited to a few days or a month in the literature.[115,146,166,196,203–207,264–270] This period also corresponds to one of the longest stability reported for conventional PSCs (10 000 h).[271] The electrode transfer technique does not systematically yield devices more stable over time than conventional references,[267] which implies that another factor probably contributes to the improved shelf-life stability of laminated PSCs in addition to the less critical proximity between the electrode and absorber. Improved perovskite morphology after the hot-pressing step can also play a role. As previously reported, enlarged grains and a smoother surface likely contributed to enhanced long-term device stability,[253,272–274] including when this absorber quality was achieved via hot-pressing.[144] This explanation complies with observations from Wu et al., showing that smaller grains resulted in a faster degradation compared to larger grain absorbers obtained with a similar lamination procedure.[205]

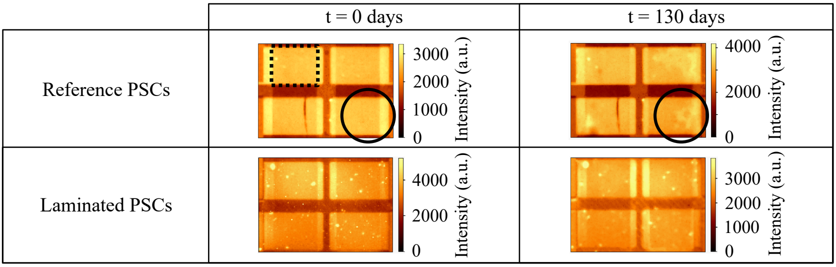

Figure 5.14: Photoluminescence (PL) images of representative references and laminated perovskite solar cells (PSCs) before and after 130 days of storage in ISOS-D-1-I conditions. Four solar cells are located on each substrate. The active area of one PSC (10.5 mm^2) is underlined with a dashed rectangle. Inhomogeneous areas emerge in references over time, as highlighted by circles. This pattern is not reflected in laminated PSCs. PL intensity is measured through the glass side. Adapted from reference[120] with the permission of Wiley.

Temperature and light can induce or accelerate harmful chemical reactions, leading to perovskite decomposition and defect formation.[64] Recent studies established that prolonged illumination can cause ion diffusion, degradation of organic CTLs, and material interaction with adjacent functional layers.[268,275,276] Figure 5.13d displays a long-term measurement combining continuous light and heat exposure. A representative laminated PSC demonstrates robust thermal stability at 80 °C during 100 h under constant illumination, maintaining 93% of its initial PCE. This thermal stability study is successfully reproduced with an eight-month-aged device, which retains 98% of its initial PCE after MPP tracking over 70 h at 80 °C under continuous illumination (Figure 9.8, Appendix). Self-encapsulation of laminated PSCs is expected to prevent the outgassing of volatile chemical components from the hot-pressed perovskite absorber at high temperatures.[206] Even when PSCs are exposed to moisture,[146] the self-encapsulation also provided an additional protection barrier. Therefore, the possible direct encapsulation feature should not be underestimated in the enhancement of laminated device stability over time. Nevertheless, further investigations are required to fully assess the encapsulation properties of PEN foils. Overall, given that elevated temperatures are crucial aspects of real-world outdoor conditions and accelerated degradation tests, the promising thermal stability of laminated PSCs at 80 °C is particularly encouraging.

Although the studies were conducted under inert conditions, the remarkable shelf-life and thermal stability of laminated PSCs represent a significant step toward understanding perovskite stability and underscore the potential for further advancements in the field. In summary, enhanced stability over time compared to conventional references using the same architecture is attributed to i) the improved morphology of the hot-pressed perovskite absorber, ii) the prevention of critical proximity between the absorber and Au through more continuous layers, and iii) the potential barrier function of the PEN foil superstrate, preventing volatile chemical components from escaping under device operation conditions, as observed in encapsulated devices.[251,277] In addition to intrinsic characteristics of the lamination process, increased freedom in the choice of materials can also benefit the stability of perovskite-based PV over time. In that regard, numerous reports focused on replacing Au and Ag metal electrodes – susceptible to diffuse and react with functional layers – with carbon-based materials, decreasing fabrication costs and improving operational device stability.[278–281] The choice of CTLs is also critical, with all-inorganic architectures typically conferring superior stability to laminated PSCs over time,[14,206] as discussed in Section 5.2.1. These features render lamination promising to produce intrinsically stable devices with enhanced freedom in the material combination.

5.6 Summary

Lamination offers additional degrees of freedom in the fabrication of PSCs through decoupled processing in two independent half-stacks. As device architecture is known to play a pivotal role in PSC operational stability and upscaling feasibility, this technique may be relevant to support research in addressing remaining challenges of this technology. This work presents several proof-of-concept laminated devices that showcase the application versatility, enabling architectures that would be difficult or impossible to fabricate conventionally. Various materials for CTLs, electrodes, and the perovskite composition and thickness in PSCs were explored. The first study illustrates that lamination can specifically target the thermal stability of the devices. Established inorganic CTLs are effectively combined, resulting in a unique architecture. With this combination of inorganic CTLs, the champion device retained 97% of its initial PCE after 10 h at 80 °C under continuous illumination. This result is consistent with our previously reported findings, which demonstrated for the first time that laminated PSCs can maintain their power output under these conditions.[14] In addition, by replacing the opaque rear electrode with a transparent contact, semi-transparent PSCs are successfully laminated, a cornerstone for tandem applications. A final proof-of-concept device demonstrates that the thin-film deposition sequence – severely restricted by standard techniques – can be varied with lamination. The same device architecture is produced in either p-i-n or n-i-p deposition order while achieving comparable PCEs, bridging the gap between two distinct development routes for single-junction PSCs. These prototypes demonstrate that lamination can readily support research in the perovskite-based PV field. Numerous architectures become accessible, facilitating the choice of i) materials that provide enhanced operational stability, ii) scalable processing techniques, and iii) deposition order that eases the device fabrication.

The successful fabrication of these unique laminated PSCs builds on a fundamental understanding of the hot-pressing process acquired in this work. Empirical studies outlined a suitable parameter range for laminating efficient PSCs. One key finding is a perovskite-specific minimum temperature threshold to trigger half-stack adhesion. Applying high pressure alone is insufficient. The final process window spans from 85 to 100 °C and 50 to 100 MPa for a short treatment time of 5 min. The effects of hot-pressing on the perovskite morphology are visible in laminated PSCs. Optical characterizations reveal reduced diffuse reflectance, indicating less light scattering inherent to a smoother absorber layer. The smoother perovskite surface also changes the spectral device light management with a slight shift in the EQE signal. However, no particular absorption losses are noticed, and the integrated J_{sc} remains unchanged compared to the references. Moreover, laminated PSCs consistently demonstrate higher implied V_{oc} and lower n_{id}, indicating reduced dominance of non-radiative recombination. Mitigation of these losses is attributed to the improved perovskite morphology and interface with the adjacent CTL of C_{60}. Laminated PSCs also exhibit outstanding shelf-life stability, retaining their initial PCE after one year of aging, while references of the same architecture rapidly degrade. Stability over a year is a milestone in perovskite technology and aligns with the longest studies reported for PSCs. Even at high temperatures of 80 °C and under continuous illumination, devices demonstrated good thermal stability for up to 100 h. The enhanced intrinsic stability is attributed to the recrystallized perovskite morphology and limited critical proximity with functional layers susceptible to reacting with the absorber over time, e.g., gold diffusion mechanisms. Additionally, the PEN foil used as a superstrate during processing can be seen as a possible PSC encapsulant, preventing volatile chemical components from escaping. This possible direct device encapsulation is an additional feature of the lamination technique, an advantage for future integration in production lines. Therefore, lamination by hot-pressing benefits PSC performance and stability over time while remaining an industry-relevant process.

Laminated PSCs achieve high PCEs of up to 17.5%, on par with the conventional references prepared in parallel. For the first time, an absorber

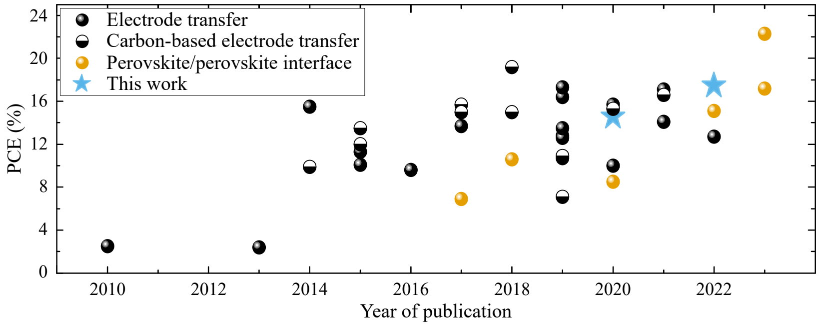

Figure 5.15: PCE chart of laminated perovskite solar cells since 2010. The most common technique is the electrode transfer, often used to deposit a carbon-based electrode on a pre-fabricated layer stack. Only a few research groups focused on the recrystallization of two hot-pressed perovskite layers to unite the device half-stacks. Reported PCE in publications derived from this work are highlighted with blue stars.[14,120]

material suitable for tandem application is used, compared to state-of-the-art lamination techniques via perovskite recrystallization, typically employing the archetypal $MAPbI_3$ composition. The achieved PCE was one of the highest for laminated perovskite solar cells at publication, as illustrated in Figure 5.15. Now exceeding 20% of PCE, recent advancements highlight the growing interest in this technique and justify further investments in closing the efficiency gap towards record-breaking, conventionally-produced PSCs. Hence, lamination provides unique opportunities to address the remaining challenges of perovskite technology, especially the insufficient long-term device stability, by facilitating the exploration of new materials and layer combinations for PSCs. The potential of this technique in the future development of perovskite-based PVs, including tandems, is further discussed in the following.

6 Laminated perovskite/silicon tandem solar cells

Enhancing solar cell performance for high power output can lower the LCOE of PVs. A strategy to advance the PCE of the established silicon technology consists of stacking a complementary solar cell atop to reduce thermalization losses. Although significant milestones have recently been achieved in this field, research in new materials and layer deposition techniques is still required to enhance the PCE and stability while facilitating fabrication of tandem devices. Lamination can offer higher flexibility in the choice of materials and individual subcell processing, addressing typical challenges of multi-layer designs. This chapter explores the potential of this technology to manufacture monolithic perovskite/silicon tandem PVs.

Acknowledgments and contributions

Sections outlined with ‡ review first author publication *"Laminated monolithic perovskite/silicon tandem photovoltaics"* in Advanced Energy Materials.[120] A patent *"Perowskit-basierte Mehrfachsolarzelle und Verfahren zu ihrer Herstellung"* was field as part of this work, Europäische Patentanmeldung EP 22712309.8.[282]

Julie Roger and Prof. Dr. Ulrich W. Paetzold conceived the idea and developed research plans. Julie Roger designed experiments, fabricated the laminated perovskite/silicon tandem solar cells and performed characterizations and data analysis. Weiyuan Duan, Sun Nan, Kaining Ding, and Andreas Lambertz from Forschungszentrum Jülich developed and provided the SHJ solar cells. Dr. Somayeh Moghadamzadeh optimized the triple-cation perovskite recipe and supported the optimization of the solution molarity. Marc Schneider provided technical assistance for the hot-pressing process. Heike Fornasier provided the Teflon-coated silicon stamps. Thomas Feeney optimized and performed SnO_x *depositions via ALD. Prof. Dr. Ulrich W. Paetzold supervised the project.*

6.1 Introduction

This work investigates the suitability of the lamination technique for manufacturing monolithic perovskite/silicon tandem solar cells. First prototypes are presented in Section 6.2, demonstrating the concept feasibility. Following this achievement, a thorough performance analysis is conducted to evaluate the proof-of-concept solar cells compared to conventional devices. Main areas of improvement are identified, paving the way for further refinement. Two major challenges in multi-layer designs of perovskite/silicon tandems are achieving a current-matching condition, and reducing parasitic absorption losses. Beyond established strategies of tuning perovskite bandgap and thickness to reach a current-matching condition, lamination offers new possibilities introduced in Section 6.3. Notably, the increased freedom in the choice of material and deposition order of functional layers allows for a substantial reduction in parasitic absorption losses and enhancement in the photocurrent.

State-of-the-art mechanical stacking techniques for perovskite-based tandem solar cells

Monolithic tandem solar cells are particularly attractive for decreasing LCOE compared to the current market leader silicon-based PVs, and numerous reports intend to optimize the PCE and operational stability of perovskite/silicon tandems.[102,233,283–285] As in single-junction PSCs, the selection of functional layers – perovskite absorber, CTLs, and electrodes – is crucial for tandem performance. Device architectures require fine-tuning to achieve current-matching requirements,[102,286] reduce parasitic absorption losses,[60,101] and enhance charge carrier extraction.[287–289] However, standard methods restricts the choice of materials and processing techniques for the top PSC, as each deposition must preserve the underlying layer stack, including the bottom cell. Several factors determine the compatibility of materials and deposition conditions for PSC fabrication. In tandem PVs, TCO sputtering processes

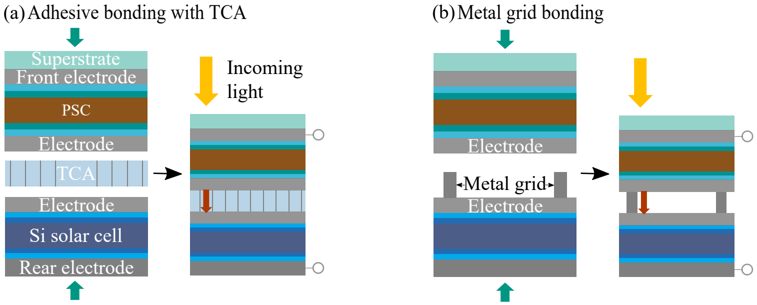

Figure 6.1: Mechanical stacking techniques for fabricating monolithic perovskite/silicon tandem. a) Adhesive bonding uses a transparent conductive adhesive (TCA) to connect two subcells in series. b) The metal grid bonding technique involves superposing the subcells to connect the silicon solar cell front electrode with the perovskite solar cell (PSC) rear contact. A metal grid (optional) is introduced to improve junction conductivity. The light that is not absorbed by the top PSC (in infrared wavelengths) is transmitted through the TCA or air gap to the silicon subcell, respectively, as illustrated by red arrows.

are particularly challenging and cannot be directly performed on the perovskite absorber, requiring additional buffer layers.[191] Furthermore, typical post-deposition treatments to enhance the optoelectronic characteristics of TCO electrodes require elevated temperatures ($\geq$250 °C for ITO) exceeding the thermal tolerance of functional layers, e.g., about 200 °C for SHJ solar cells.[290]

Alternative technologies to the previously discussed hot-pressing process include mechanical stacking for monolithic perovskite-based tandems. These so-called bonding techniques have been investigated to increase the degree of freedom in solar cell architectures, uniting two independent subcells in a final fabrication step. Some methods use transparent conductive adhesives (TCA) to connect subcells in series, while the transparency of the adhesives allows the transmission of infrared wavelengths for absorption in the bottom cell (Figure 6.1a).[147,164,291–293] Such adhesives allow for PCEs exceeding 30% in monolithic perovskite/silicon tandem solar cells.[164] Others connect the two subcells by directly contacting the PSC rear electrode with the bottom cell front electrode.[94,294–297] The junction conductivity can be improved with metal grids, as depicted in Figure 6.1b, enabling PCEs of more than 32%.[297] Mechanical stacking techniques combine advantages of monolithic architectures through the simplicity of device operation, and the flexibility in individual subcell processing as in four-terminal tandem solar cells.

Lamination via hot-pressing for perovskite-based tandems

This work proposes to manufacture monolithic perovskite/silicon tandem solar cells via lamination, as illustrated in Figure 6.2.[120] Devices comprise two independently produced half-stacks, united in a hot-pressing process. Lamination at high temperatures and pressures trigger perovskite recrystallization and results in an electrical contact at the half-stacks interface. Thereby, subcells are optically and electrically connected in series. Lamination provides numerous advantages for applications in tandem PVs, in particular the flexibility in PSC processing. Decoupling the subcell fabrication enables architectures that would be otherwise challenging or impossible to produce using standard methods. Different combinations of subcells can be envisaged, such as all-perovskite,[103], perovskite/CI(G)S,[105] and perovskite/silicon tandem solar cells – the focus of this work. Optical and electrical systems remain comparable to conventional tandems, as no conductive adhesives

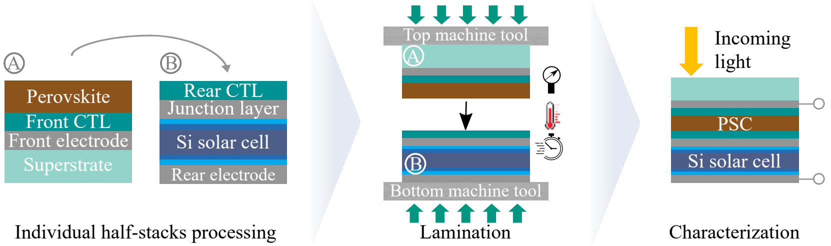

Figure 6.2: Lamination technique for fabricating monolithic perovskite/silicon tandems. Half-stacks are prepared independently on superstrates (A) and rigid silicon solar cells (B). Applying high temperatures and pressures induces perovskite recrystallization and creates a close contact at the lamination interface, completing the tandem. Other configurations are possible, e.g., perovskite absorber can be deposited on either or both half-stacks, and each CTL can combine several materials.

or air gaps between subcells are introduced. These additional layers can cause optical losses, either by parasitic absorption or light reflection, negatively impacting device performance.[147] In addition to facilitating research into novel materials and architectures, lamination offers promising features for future industrial applications through the parallel half-stack preparation and possible direct encapsulation for faster throughput. This technique also resembles the established encapsulation method for silicon solar panels and, therefore, appears compatible with integration in large-scale production lines.[298]

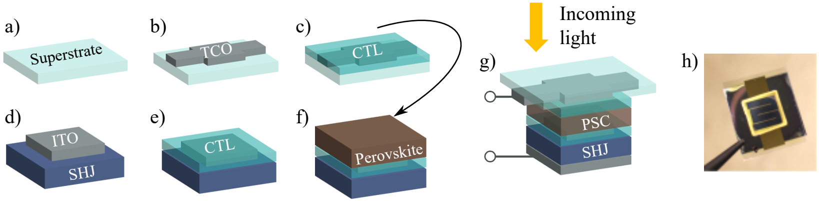

Figure 6.3: Detailed design of laminated monolithic perovskite/silicon tandems. a) The front half-stack comprises a superstrate, b) front transparent conductive oxide (TCO), and c) charge transport layer (CTL). d) The bottom stack includes the heterojunction silicon (SHJ) solar cell, ITO junction layer, e) CTL, and f) perovskite absorber. The overlap of the front electrode, junction layer, and rear electrode defines an active area of around 1 cm^2. g) Illustration of the completed laminated device. The (25x30) mm superstrates are slightly larger than the (25x25) mm silicon subcells to enable accessing the front TCO (b) after hot-pressing. Solar cells are contacted from the rear side, one probe on the front TCO and the other on the rear electrode of the silicon subcell. h) Photograph of a laminated tandem device from the front side. An Au frame and fingers were deposited at step b) on the front TCO to improve conductivity.

Tandem half-stacks are individually prepared by depositing functional layers on the rigid bottom cell (silicon solar cell) and superstrate (PEN foil or glass), as illustrated in Figure 6.2. The possibility of depositing the perovskite absorber on top of either one or both half-stacks provides flexibility in the layer sequence and material combinations. The overlap of the front electrode, junction layer, and rear electrode defines the active area. Figure 6.3 details the half-stack layouts of laminated monolithic perovskite/silicon tandem solar cell with a 1 cm^2 active area. Devices are probed from the rear side: One probe contacts the silicon subcell rear electrode, and the second contacts the overstanding part of the front TCO on the superstrate of the PSC. As shown in Figure 6.3h, metal grids can be deposited on the front TCO to increase conductivity, a technique used by numerous research groups for conventionally produced tandems.[233,285,299]

Perovskites used in the following studies have a triple-cation composition whose compatibility with lamination has been previously verified. Suitable hot-pressing conditions for perovskite recrystallization and efficient single-junction PSCs include a temperature range from 90 to 100 °C, a minimum pressure of 50 MPa, and a duration of 5 min. This process window – specific to this triple-cation material – enhances morphology and crystallinity while preventing material degradation. The previously demonstrated improved perovskite quality, its interface with adjacent CTL, and the advanced device stability over time are further motivations for applying lamination to the tandem PV field.

6.2 Proof-of-concept solar cells in tandem architectures

6.2.1 Prototypes of laminated monolithic perovskite/silicon tandems‡

This work realizes the first prototypes of laminated perovskite/silicon tandem solar cells. As previously described, the method involves preparing devices in two independent half-stacks, which are subsequently united in a hot-pressing process. Here, the front layers of an n-i-p PSC (stack A) are hot-pressed on a modified heterojunction silicon (SHJ) subcell (stack B), resulting in a monolithic perovskite/silicon tandem, as illustrated in Figure 6.4a. Stack A comprises a flexible PEN foil superstrate, an ITO electrode, and a double ETL of SnO_x and C_{60}. Stack B denotes a double-side-polished SHJ bottom solar cell, a thin ITO junction layer on its n-side, a double HTL of sputtered NiO_x and 2PACz, and the triple-cation perovskite. The hot-pressing step at high temperature (90 °C) and high pressure (80 MPa) promotes perovskite recrystallization and creates an electrical contact between materials at the interface.

The champion device in Figure 6.4b achieves up to 20.0% PCE, comparable to most mechanically stacked tandems.[147,291,294,295] This PCE is $30\%_{\mathrm{rel}}$ higher than laminated semi-transparent PSCs presented in Section 5.2.2. The solar cell exhibits a V_{oc} of 1.75 V, a FF of 73.6%, and a J_{sc} of 15.5 mA/cm², with minor hysteresis and a stable power output, stabilized at 19.3% (Figure 6.4c). As expected in a monolithic tandem device, the V_{oc} nears the sum of both subcell voltages. Table 6.1 summarizes J-V characteristics of the five best solar cells. The repeatability of the lamination technique is demonstrated by a similar performance to the champion device with an average J_{sc} and V_{oc} of 15.5 mA/cm² and 1.76 V, respectively. Due to uncertainties in the exact active area, J_{sc} values are integrated from EQE measurements. These prototypes of simple optical and electrical designs already reach V_{oc} values comparable to reported monolithic perovskite/silicon tandems manufactured via mechanical stacking.[94,147,291,294] Contribution of both subcells is also highlighted by EQE measurements (Figure 6.4d), revealing a J_{sc} of 16.8 mA/cm² in the PSC and 15.5 mA/cm² in SHJ subcell. Thereby, the first prototypes surpass the J_{sc} observed in planar mechanically stacked

Table 6.1: PCE, FF, V_{oc}, and J_{sc} of the five best laminated monolithic perovskite/silicon tandem solar cells with integrated J_{sc} from external quantum efficiency measurement. SD stands for standard deviation. Device architecture is displayed in Figure 6.4. In total, 8 tandems were successfully fabricated.

	PCE (%)	FF (%)	V_{oc} (V)	J_{sc} (mA/cm²)
Mean	19.0	70.2	1.75	15.4
SD	1.2	3.8	0.01	0.2
Minimum	17.6	66.1	1.75	15.2
Maximum	20.1	73.7	1.76	15.6

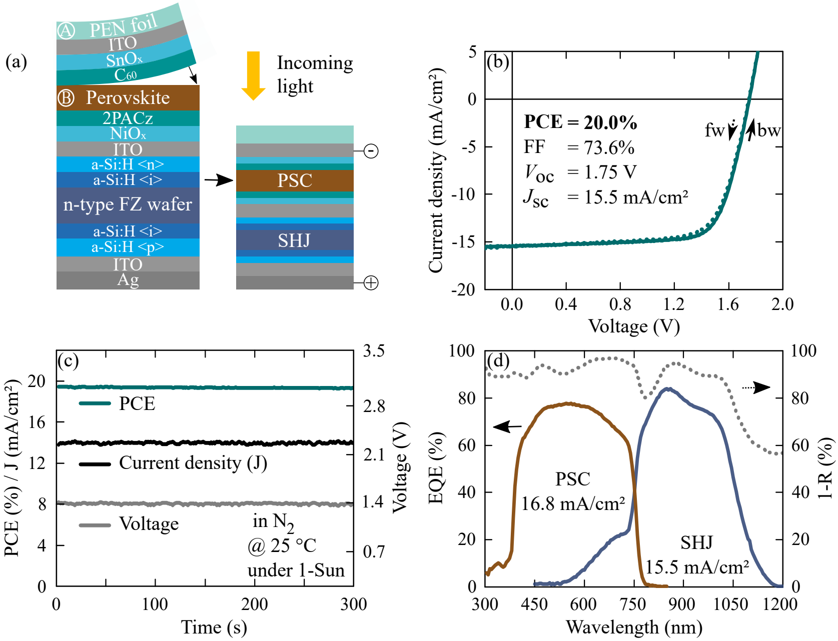

Figure 6.4: Proof-of-concept device of a monolithic perovskite/silicon tandem fabricated via lamination. a) Illustration of solar cell architecture and lamination process. The front stack of an n-i-p perovskite solar cell (PSC, A) is hot-pressed on a modified heterojunction silicon subcell (SHJ, B). b) Current density-voltage (J-V) characteristics of the champion device. Due to uncertainties in the exact active area, J-V characteristics are scaled to integrated J_{sc} from external quantum efficiency (EQE) measurement. c) Maximum power point tracking, and d) EQE of the champion device and reflectance (R, dashed line) measurement of an identical layer stack. Current densities generated in PSC and SHJ subcells are displayed in the respective areas. Adapted from reference[120] with the permission of Wiley.

solar cells of around 14 mA/cm².[194–196] These results indicate that perovskite absorbers and SHJ solar cells remain preserved despite high temperatures and pressures applied during lamination. Nevertheless, the process must be improved to achieve PCEs that are more competitive with conventional devices. For this reason, a detailed performance analysis is conducted in the following section, and the most important loss channel is addressed accordingly. To date, no comparable techniques for perovskite/silicon tandems have been reported in the literature.[120] The first prototypes of laminated monolithic perovskite/silicon tandems already demonstrate the potential of this alternative fabrication technique in this field.

6.2.2 Performance analysis of first laminated tandem prototypes‡

The previous proof-of-concept experiment demonstrated that lamination is a suitable fabrication technique for monolithic perovskite/silicon tandem solar cells. However, a PCE of 20.0% is behind records for conventionally processed devices, which was around 31% then and has since steadily progressed.[13] Simulation results for a similar architecture suggest that laminated perovskite/silicon tandems can reach PCEs beyond 33%.[300] Figure 6.5a illustrates the contribution of the FF, V_{oc}, and J_{sc} to the PCE improvement. Although the V_{oc} and FF should be increased by 15%$_{\mathrm{rel}}$ and 11%$_{\mathrm{rel}}$, respectively, the limiting factor in the current proof-of-concept devices is the J_{sc}, which could theoretically achieve ≈20 mA/cm². By comparing the EQE of a laminated tandem solar cell and an optical optimization study using a similar architecture,[301] four main areas of improvement (I to IV) are distinguished in Figure 6.5b to augment the J_{sc}.

Optical characterizations of PEN/ITO foils reveal significant optical losses in Figure 9.9, Appendix, through parasitic absorption at short wavelengths and high reflectance. At 300 to 380 nm wavelengths, PEN/ITO foils decrease transmittance to below 20% and, at longer wavelengths, to below 85%. Reflectance losses at the interface with air were significantly reduced by applying an anti-reflective MgF_2 coating on the PEN foil front side to enhance in-coupling light, as shown in Figure 9.10, Appendix. Nevertheless, the current in region I (Figure 6.5b) remains low due to severe parasitic absorption losses. Future strategies to lower optical losses in the front half-stack include i) replacing the 125 μm thick PEN foil with a more transparent superstrate such as

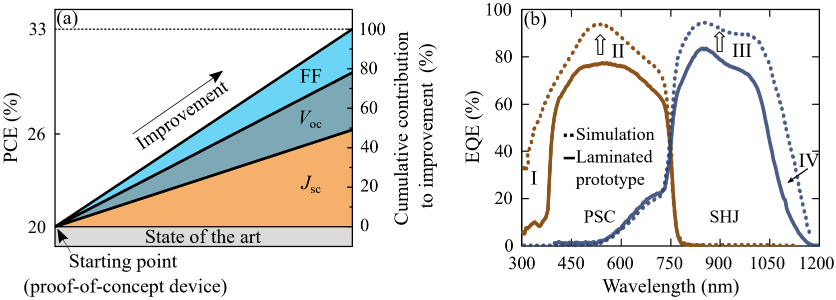

Figure 6.5: Performance analysis of the first prototypes of laminated monolithic perovskite/heterojunction silicon (SHJ) tandems. a) Illustration of the cumulative contribution to improvement in J_{sc}, V_{oc}, and FF. The prototype with up to 20% of PCE is compared with existing literature, suggesting optimization strategies to exceed 33% PCE.[300] The J_{sc} requires particular attention for significantly improving the PCE. b) External quantum efficiency (EQE) measurements of the prototype and a simulation with a similar architecture achieving around 20 mA/cm². [301] This comparison highlights four main areas of improvement in EQE (I-IV), currently reduced by optical losses such as parasitic absorption and light reflection.

glass, ii) reducing the 300 nm front ITO thickness, which is significantly thicker than typically reported for high-efficiency devices,[233,285,299,302] and iii) using a more transparent front TCO, e.g., IZO or IO:H.[59] Indeed, as ITO causes parasitic absorption at infrared wavelengths, using thinner films or replacing the TCO material is expected to enhance the current in region III. The ETL of C_{60} also causes substantial parasitic absorption losses at short wavelengths from 300 to 550 nm, limiting the PSC current.[62] Thinner C_{60} layers (currently 20 nm) or more transparent materials as front CTLs are further strategies to increase the EQE response in regions I and II. In addition, the SHJ solar cells are double-side polished, which leads to incomplete in-coupling light. Reflectance losses on planar front and rear sides of silicon subcells, evident in Figure 6.5b at about 790 nm and beyond 1000 nm, limit the EQE in infrared wavelength regions III and IV. Incorporating textured silicon solar cells – standard for silicon-based PVs – could significantly reduce these reflection losses and improve light trapping.[227,287,303,304] Laminated prototypes also suffer from a mismatch between subcells, with a subcurrent difference of more than 1 mA/cm². The laminated tandem devices would benefit from a slightly wider bandgap of approximately 1.68 eV in the top cell.[305,306] This adjustment might require optimizing absorber thickness according to its bandgap, an established method to increase the J_{sc} of monolithic devices and the energy yield.[286,307–309] This performance analysis highlights that laminated perovskite/silicon tandem solar cells are expected to achieve a J_{sc} comparable to conventionally processed devices using established optimization strategies. This work also emphasizes the importance of effective light management in tandems to achieve high PCEs and that designing multi-layer perovskite/silicon tandems is challenging due to the interrelated influence of functional layers. Beyond the standard improvement strategies outlined here, the lamination process offers further opportunities, which are discussed in Section 6.3.

It is noted that the electrical system of laminated tandem prototypes is intentionally kept simple in this work and primarily relies on two factors reducing non-radiative recombination losses: i) perovskite recrystallization, and ii) an enhanced interface with C_{60}, as previously discussed. To further improve the V_{oc}, promising passivation techniques proposed in the literature yielding significantly higher V_{oc} by efficiently minimizing charge-carrier recombination losses could be introduced.[55,178,310] In a complementary study presented in Figure 9.11, adding a 1 nm thin LiF layer at the interface between perovskite and C_{60} consistently results in a comparable V_{oc} increase in standard single-junction PSCs and laminated tandems. The respective average improvement by 50 and 64 V is consistent with existing literature on LiF as surface passivation.[311] This result suggests that passivation techniques commonly employed in conventionally produced PSCs can be successfully applied in laminated devices, indicating a potential for achieving similar efficiencies with both fabrication methods. In forthcoming research, the architecture could be enriched with elaborate optimization strategies, such as incorporating 2D materials for perovskite surface passivation and additives into the absorber for bulk passivation. Promising materials are transition metal carbides and nitrides (MXene), and phenethylammonium iodide (PEAI).[55,164,296,312] Furthermore, silicon subcells used in the first prototypes (14 mm^2) are smaller than the typical size for perovskite-based tandem PV research (1 cm^2).[233,285,305] In small silicon solar cells, edge recombination becomes significant, contributing to lower efficiencies through reduced V_{oc}.[284] Therefore, an active area enlargement to 1 cm^2 of laminated perovskite/silicon tandems is also investigated in the following.

6.3 Optical improvement of perovskite-based tandems via lamination

Designing multi-layer perovskite/silicon tandems presents significant challenges, particularly in achieving a current-matching condition and minimizing parasitic absorption losses. The preceding performance analysis identified J_{sc} as a primary limiting factor of laminated tandems, emphasizing the importance of effective light management. Lamination offers a wide range of strategies to optimize these complex architectures. Section 6.3.1 explores the use of highly transparent ultra-thin glass superstrates to improve light transmission. The increased freedom in the choice of front electrodes is showcased in Section 6.3.2, comparing three highly transparent and conductive TCOs. Section 6.3.3 examines how lamination enables perovskite engineering to achieve a current-matching condition through thickness and bandgap variations, an established technique readily applicable in laminated tandems. Finally, flexibility in layer deposition order allowed through the decoupled half-stack processing facilitates the development of a novel architecture with significantly reduced parasitic absorption losses, presented for the first time in Section 6.3.4.

6.3.1 Highly transparent and flexible superstrates

The superstrate is an essential component of laminated tandem architectures. As the first layer in the optical light path, high transparency over a wide wavelength range is essential. Apart from serving as a superstrate for depositing functional materials, this layer can also be seen as a possible encapsulant, protecting the underlying stack from oxygen and humidity, which are detrimental to the long-term stability of PSCs.[64] PEN foil is a promising superstrate material for lamination, as it allows for fabricating flexible PSCs and is compatible with large-scale production technology such as roll-to-roll processes.[14] However, optical characterizations reveal severe parasitic absorption losses at short wavelengths in the polymer (Figure 9.9, Appendix). To overcome this issue, PEN foils are replaced with thin-glass superstrates, providing higher transparency for enhanced light management in laminated tandem solar cells.

First, lamination with thin-glass superstrates is experimentally demonstrated to produce 14 mm^2 small tandems, as large as the first prototypes presented in Section 6.2.1. The active area is then enlarged to 1 cm^2, in line with the standard size of conventional perovskite-based tandem devices.[233,285,305] Photographs of tandems with PEN foil and glass superstrates can be seen in Figure 6.6. The successful replacement of the PEN foil with hard glass represents a milestone, providing evidence that the mechanical characteristics of the polymer, such as thermal deformation and softness, are not essential for half-stack adhesion in this hot-pressing technique. Nevertheless, the transition to glass presented

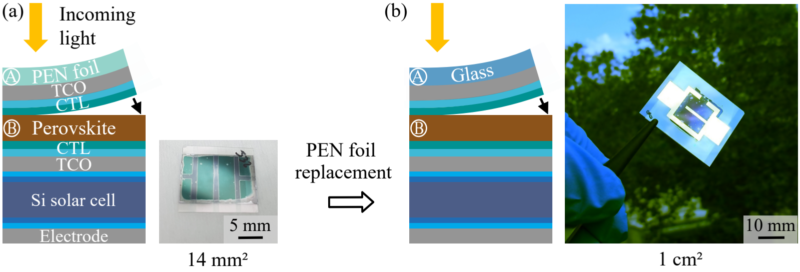

Figure 6.6: Laminated monolithic perovskite/heterojunction silicon (SHJ) tandems using a 125 μm thick PEN foil (left) and a highly transparent 30 μm thin-glass superstrate (right). a) Architecture and photograph of a device from the front side, with four active areas of 14 mm^2. b) Solar cell architecture after superstrate replacement and updated design for an enlarged active area. The photograph shows a large device from the front side with an active area of approximately 1 cm^2.

challenges. Laminated samples incorporating 150 μm thick glass were inhomogeneously laminated, as shown in Figure 6.7a. Typical interference patterns visible through the glass revealed an air gap at the perovskite/CTL lamination interface, indicating that these materials were not in close contact. Three principal adjustments were implemented to obtain a successful adhesion: i) The applied pressure was increased, ii) the machine plate quality was enhanced with a surface treatment, and iii) thinner glass superstrates were employed.

The problem-solving approach is illustrated in Figure 6.7. At first, pressure distribution during the hot-pressing process was examined using Fujifilm Prescale HS foils positioned between the layer stack and machine plate.[313] Integrated micro-color capsules break inside the Prescale foil during pressing, leaving a visible trace of applied forces. When exceeding 50 MPa, the foil displays a magenta-colored imprint, contrasting with a white appearance below this threshold. As a minimum of 50 MPa is required to improve perovskite morphology (Section 4.3), this foil indicates whether sufficient pressure is applied during lamination. Magenta-colored imprint images (Figure 6.7b) demonstrated that less than 50 MPa is applied in the sample center, where the active area of the tandem solar cell is located. Increasing pressure to 200 MPa overcame this issue. However, the additional stress applied to machine tools deformed their surfaces, as shown in Figure 6.7c. A surface treatment of machine plates was employed to prevent tool deterioration under such high pressure, which would otherwise affect the subsequent lamination. The tool surface quality in contact with samples was improved by lapping, yielding a smooth and robust surface capable of withstanding the high pressure without deformation.

The glass superstrate thickness also played a pivotal role in the lamination quality of perovskite/silicon tandem solar cells. The crucial influence of the thickness has already been pointed out in research on wafer-bounding techniques.[315,316] Defects created by particles at the lamination interface enlarge with particle size and substrate thickness. A typical particle-related defect is displayed in Figure 6.7d. If the glass is

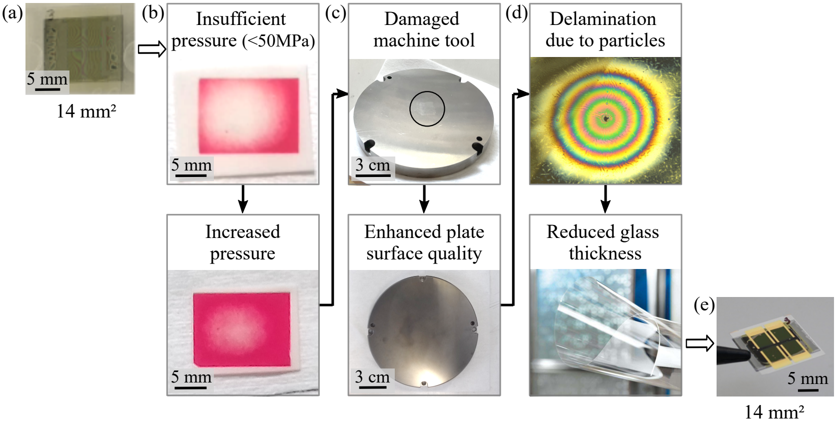

Figure 6.7: Problem-solving approach for laminating monolithic perovskite/silicon tandems with glass superstrates. a) Photograph of a representative device with a 150 μm glass superstrate showing poor half-stack adhesion. Interference patterns indicate an air gap at the lamination interface. b) Fujifilm prescale foil, which displays a magenta color when a minimum of 50 MPa is applied, reveals an uneven pressure distribution. The set pressure is thus increased to 200 MPa. c) Photographs of machine tools. A lapping surface treatment improved the surface quality, allowing the machine tools to withstand the high pressure without deforming. The black circle highlights the imprint left by a sample after hot-pressing. d) Optical microscopy image of a delamination defect around a particle. The defect size can be reduced by using a more flexible superstrate. Photograph of the bendable AF 32® ecotype thin glass, copyright Schott AG.[314] e) Photograph of a tandem successfully laminated with a 30 μm thin-glass superstrate.

insufficiently thin, particles cause larger defects, which might yield complete delamination of half-stacks. Ultra-thin glasses, such as AF 32® ecotype from Schott AG with a thickness of 30 μm,[314] are bendable, which allows the glass to bend around particles and promote half-stack adhesion. A successfully laminated device is shown in Figure 6.7e.

Remaining particle-related defects might be detrimental to device performance and additionally result in uncertainties in the active area of laminated tandems. A recent study emphasized that inhomogeneities, depending on their size, can negatively affect J-V characteristics of perovskite solar modules.[317] In particular, these defects may contribute to a reduced interface conductivity, decreasing the FF. The number of particle-related defects could be limited by strict cleaning procedures, e.g., sample handling in cleanrooms and filtered glove box atmosphere, and using anti-electrostatic tapes next to samples to release static electricity and catch potential particles. Automatization, rapid processing, and continuous vacuum systems should further reduce particle-related defects in future industrial production lines. Alternatively, transparent buffer layers, either conductive such as poly(3,4-ethylenedioxythiophene) polystyrene sulfonate (PEDOT:PSS),[200] or insulating, e.g., poly (methyl methacrylate) (PMMA), polydimethylsiloxan (PDMS), ethyl vinyl acetate (EVA), and silane-grafted polyolefin elastomers (POEs).[291,318–320] could be introduced to fill cavities or cushion particles, lowering the defect size.

Replacing PEN foil with glass represents a significant advancement toward the durability of laminated tandems, as glass is more resistant to long-term sunlight exposure. This substitution also broadens the range of compatible materials and deposition techniques in future front PSCs, facilitating the use of inorganic functional layers that contribute to improved device stability over time, as discussed in Section 5.2.1. In addition, using thin glass opens up new opportunities for large-scale production. The bendability of ultra-thin glass is particularly advantageous for roll-to-roll processing, a method with augmented production capacity that could partially compensate for the higher cost of thin glasses compared to standard thicknesses.[321] From an optical perspective, glass offers advantages to enhance light management, e.g., by applying textured layers on the glass front side to improve in-coupling light.[128,130] The glass superstrate also offers attractive features for optical optimization research through its high transparency, high thermal tolerance, and robustness against harsh processing conditions, such as in sputtering depositions. This increased degree of freedom – particularly for the choice of front TCO – is explored in the following section to enhance light management in perovskite-based tandems.

6.3.2 Highly transparent conductive oxides as front electrodes

Optimal optoelectronic characteristics of front electrodes are essential for highly efficient tandem solar cells. Parasitic absorption should be minimized to enhance charge carrier generation in the perovskite absorber and augment the J_{sc}.[299] Meanwhile, high conductivity is required for efficient charge-carrier transport with reduced resistive losses.[299] Standard materials include sputtered ITO, IZO, and IO:H, with the latter attracting particular attention due to its nearly optimal optoelectronic characteristics.[59] For highly conductive TCOs, sputtering processes should preferably be performed at high power, yielding dense films, and on a heated substrate at elevated temperatures.[322] Post-deposition treatments are also beneficial for most TCOs and usually consist of a simple annealing step. However, these processing conditions are not necessarily compatible with fabricating perovskite-based solar cells. Reports showed that increased sputtering power and duration are detrimental to device performance.[225,323] The front electrode sputtering deposition on PSCs must, therefore, be mitigated to prevent damage from high-kinetic energy particles in the underlying layer stack,[324] and additional protective buffer layers such as ALD-deposited $\mathrm{SnO_x}$ are commonly introduced in the device architecture.[218,227,228] Also, the required post-treatment temperatures (e.g., ≥250 °C for ITO) exceed the thermal tolerance of sensitive functional layers, including the perovskite absorber.[59,325] Lamination overcomes these typical processing limitations since the front electrode can be optimally deposited on an independent superstrate. In this context, a glass superstrate has significant advantages, such as robustness against demanding sputtering conditions and high thermal tolerance, enabling subsequent electrode annealing for optimum optoelectronic properties. Using this enhanced flexibility in TCO materials, deposition, and post-treatment conditions enabled by lamination, this work targets highly transparent and conductive oxides as front electrodes for tandem solar cells.

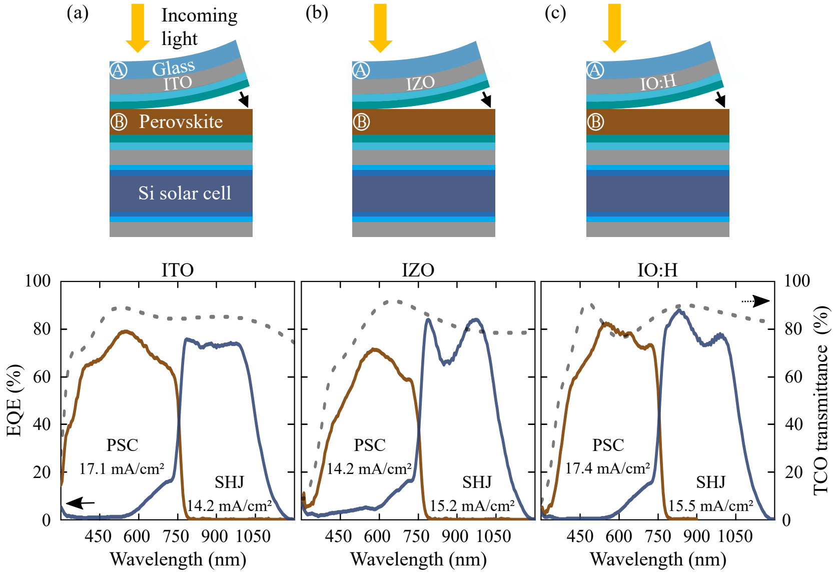

Figure 6.8: External quantum efficiency (EQE) of laminated monolithic perovskite/heterojunction silicon (SHJ) tandems with different front electrodes. a) Illustration of the architecture and corresponding EQE characterization of solar cells with a transparent conductive oxide (TCO) of 145 nm ITO, b) 150 nm IZO, and c) 220 nm IO:H, sputtered on 30 μm thin-glass superstrates. Current densities generated in perovskite and silicon subcells are shown in the respective areas. The transmittance of different TCOs on glass is displayed in dashed lines.

Three in-house sputtered TCO materials in monolithic perovskite/silicon laminated tandems are compared: ITO, IZO, and IO:H. TCOs are directly deposited on 30 μm thick glass superstrates, followed by a double ETL of SnO_x and C_{60}. This front layer stack is hot-pressed on a modified SHJ solar cell, comprising a double HTL of NiO_x and 2PACz and the perovskite. Successful device lamination indicates that all TCO materials appear compatible with the hot-pressing process. TCO transparency directly influences generated current in subcells, as highlighted by EQE measurements in Figure 6.8. With ITO, the tandem J_{sc} is limited by the silicon cell with 14.2 mA/cm^2 due to low transmittance at

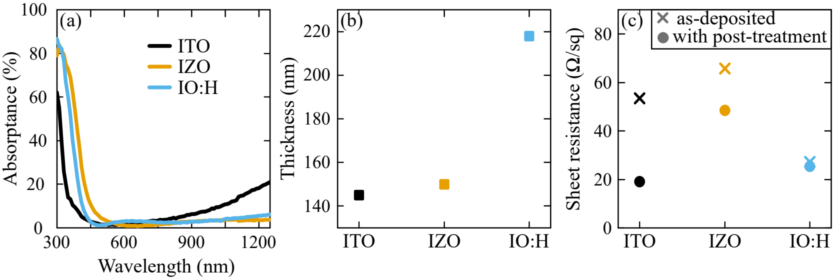

Figure 6.9: Optoelectronic characteristics of sputtered ITO, IZO, and IO:H electrodes. a) Absorptance, b) film thickness, and c) sheet resistance of the three TCOs sputtered on glass substrates as-deposited (crosses) and after post-treatment (circles). Absorptance is calculated from transmittance and reflectance measurements shown in Figure 3-5. Post-deposition treatments include annealing at 250 °C for 15 min in air for ITO (black), and annealing at 200 °C for 30 min in N_2 for IZO (orange) and IO:H (blue).

long wavelengths. Conversely, IZO demonstrates higher parasitic absorption at short wavelengths, reducing J_{sc} in top PSC with 14.2 mA/cm². The IO:H appears as a compromise solution with enhanced transparency over the entire spectrum and simultaneously provides the highest current for top PSCs and SHJ cells with 17.5 and 15.5 mA/cm², respectively.

These results build on experimental improvements of IO:H sputtering conditions, as detailed in Figure 9.1. Two main insights are highlighted: i) Longer deposition times increase layer thickness linearly while decreasing sheet resistance, and ii) doubling O_2 flow suppresses parasitic absorption at wavelengths from 400 nm. Optimized deposition conditions yields an IO:H electrode as transparent as IZO with less than 6% absorption at long wavelengths from 500 nm (Figure 6.9a). In comparison, ITO causes severe parasitic absorption in infrared wavelengths, linearly increasing from 750 nm to 20% at 1250 nm. Additionally, IO:H demonstrates a slightly higher transmittance at short wavelengths, with 16% absorptance at 400 nm compared to 37% in IZO. Given this enhanced transparency, IO:H is deposited in relatively thick layers (around 220 nm, Figure 6.9b) to target low sheet resistance of approximately 25 Ω/sq, comparable to ITO and significantly more conductive than

IZO, exhibiting 48 Ω/sq (Figure 6.9c). Before characterizations, ITO was annealed at 250 °C for 15 min in air. IZO and IO:H were annealed at 200 °C for 30 min in a N_2 atmosphere.

The present study demonstrates that front electrode materials, deposition conditions, and post-treatments can be readily optimized in laminated tandems. High transmission in the relevant wavelength range and high conductivity are achieved by selectively adjusting sputtering parameters and film thicknesses. These outcomes align with recent literature on outstanding optoelectronic characteristics of IO:H materials.[59,326,327] Furthermore, as the front electrode deposition is performed independently of other functional layers, new types of contacts can be envisioned, such as efficient mesh-liked electrodes.[328–330] Decoupled TCO processing from the sensitive perovskite film also implies that a buffer layer of SnO_x is possibly no longer required in the device architecture. Nevertheless, this layer is deliberately retained in laminated tandems to ensure comparability with established architectures.

6.3.3 Perovskite engineering to achieve a current-matching condition

Integrating a highly transparent superstrate and front TCO in laminated architectures immediately affects current-matching requirements, which are critical for maximizing power output in monolithic tandem devices. The bottom cell current can be adjusted by regulating transmitted light from the top PSC. Two established strategies for enhancing the bottom cell current through perovskite engineering include bandgap increase or thickness reduction. In solution-based processing, the band gap is adjusted by compositional engineering, primarily by augmenting bromide fraction, while thickness tuning involves changing the solution molarity and spin-coating speed.[92,102,102,331] This section explores current-matching conditions in laminated monolithic tandem solar cells with variations in front absorber bandgap and thickness.

Table 6.2: PCE, FF, V_{oc}, and J_{sc} of conventional single-junction perovskite solar cells using a triple-cation perovskite with a bandgap of 1.63 eV (31 devices) and 1.68 eV (31). SD, Min., and Max. stand for standard deviation, minimum, and maximum, respectively. Solar cell architectures comprise glass/ITO/NiO_x/2PACz/perovskite/C_{60}/BCP/Au.

	PCE (%)		FF (%)		V_{oc} (V)		J_{sc} (mA/cm^2)	
	1.63 eV	1.68 eV	1.63 eV	1.68 eV	1.63 eV	1.68 eV	1.63 eV	1.68 eV
Mean	17.3	16.0	79.3	74.7	1.08	1.09	20.1	19.7
SD	0.4	0.3	1.7	1.2	0.00	0.02	0.7	0.3
Min.	16.1	15.0	76.0	72.0	1.08	1.07	18.3	19.2
Max.	17.8	16.6	82.0	77.0	1.10	1.11	21.3	20.4

Two triple-cation perovskites developed in our research group are compared in this study. One has a 1.63 eV bandgap, is approximately 370 nm thick, and has been successfully used in single-junction PSCs. The second has a 1.68 eV bandgap, is thicker with 720 nm, and was optimized for tandem applications. This 1.68 eV bandgap energy was highlighted in numerous reports as the optimal value for monolithic perovskite/silicon tandem devices.[56,285,302,305,306] Conventional single-junction PSCs are successfully fabricated with both perovskite compositions as references, resulting in average PCEs of 17.3% and 16.0% with 1.63 and 1.68 eV bandgaps, respectively (Table 6.2). As expected, PSCs with a 1.68 eV bandgap exhibit a lower J_{sc} due to a narrower wavelength absorption range. Comparing both absorbers in laminated tandem solar cells provides insights into the influence of bandgap and thickness adjustments on light management.

First, the influence of the absorber thickness is examined by tuning the solution molarity of 1.68 eV perovskites. The precursor solution, initially at 1.53 M, is diluted to a new molarity estimated at 0.84 M. In Figure 6.10a, transmittance measurements with molarities ranging from 0.84 to 1.53 M confirm that a thickness decrease leads to an increased light transmission near the perovskite bandgap. Figure 6.10b displays

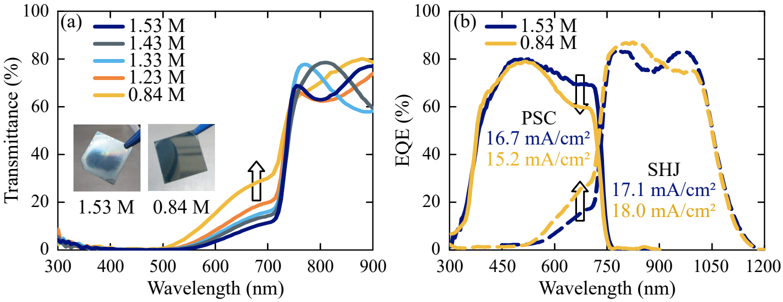

Figure 6.10: Current-matching conditions in laminated monolithic perovskite/heterojunction silicon (SHJ) tandems depending on perovskite thickness. The perovskite film thickness is adjusted by changing the solution molarity (M). a) Transmittance measurements on glass/ITO/perovskite with molarity varying from 0.84 to 1.53 M. An outlined arrow highlights an increase in transmission as molarity decreases. The inset shows photographs of 1.53 and 0.84 M perovskite layers spin-coated on (25x25) mm silicon substrates. b) External quantum efficiency (EQE) of laminated tandems depending on the perovskite molarity. Current densities generated in perovskite and silicon subcells are displayed in the respective areas. Outlined arrows indicate a reduced EQE signal in the perovskite solar cell (PSC) with lower molarity, correlating with an improved EQE of the SHJ subcell in the same wavelength range.

EQE measurements of laminated tandems. A thinner absorber enhances the EQE by $10\%_{\mathrm{abs}}$ at 700 nm in the top PSC. As in communicating vessels, the EQE in the SHJ solar cell simultaneously improves by $10\%_{\mathrm{abs}}$ at the same wavelength. Consequently, the SHJ subcell current with a 0.84 M perovskite molarity achieves 18 mA/cm^2, which is 1 mA/cm^2 higher than initially. Although this particularly thin perovskite layer is unsuitable for high-efficiency devices due to a significant current mismatch, this result emphasizes the correlation between the top absorber thickness and the generated bottom cell current. Overall, thicker perovskite with a 1.68 eV bandgap and a molarity of 1.53 M molarity allows current-matching conditions to be achieved, with around 17 mA/cm^2 J_{sc} in both subcells.

Laminated tandem solar cells with perovskite bandgaps of 1.63 and 1.68 eV are now compared within the same batch. Perovskite layers are conventionally processed with their respective thickness of 370 and

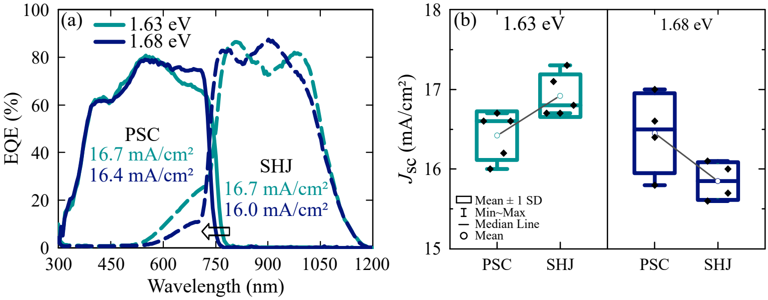

Figure 6.11: Influence of the perovskite bandgap on achieving a current-matching condition in laminated monolithic perovskite/heterojunction silicon (SHJ) tandems. a) External quantum efficiency (EQE) characterizations of laminated devices approaching a current-matching condition with a bandgap of 1.63 and 1.67 eV. Current densities generated in perovskite and silicon subcells are shown in the respective areas. The outlined arrow highlights an EQE signal shift related to a wider bandgap. b) Statistical data of integrated J_{sc} from EQE measurements in each subcell. SD stands for standard deviation.

720 nm. Hot-pressing conditions (90 °C, 200 MPa, 5 min) did not require adjustment based on the absorber material to enable successful half-stack adhesion. In this experiment, SnO_x film is deposited significantly thinner than usual (≈35 nm), implying that EQE and integrated J_{sc} values from subcells cannot be directly compared with previously shown results. Figure 6.11a displays EQE measurements of laminated devices with the smallest current mismatch. Both bandgaps enable good current matching. Remarkably, using a 1.63 eV bandgap resulted in a 16.7 mA/cm^2 current in both subcells, representing a significant improvement compared to the first prototypes, severely limited by a current mismatch. The EQE characterization of the 1.68 eV perovskite-based tandem solar cell in Figure 6.11a is representative of a trend in statistical data presented in Figure 6.11b. The bottom cell current is slightly lower, averaging 16.0 mA/cm^2, while top PSCs exhibit 16.5 mA/cm^2. Increased bandgap correlates with an EQE signal shift toward shorter wavelengths near the perovskite bandgap. Meanwhile, a thicker perovskite layer enhances light absorption in the top cell between 500 and 700 nm.

The choice of bandgap and film thickness appears as essential as in conventional tandems to reach a current-matching condition since these factors determine how much light is absorbed in the top and bottom cells. These results suggest that adjusting perovskite bandgap and thickness in laminated solar cells does not require systematically re-optimizing process conditions. Nevertheless, designing future laminated tandems to achieve a high J_{sc} is complex. Even minor architecture modifications (e.g., CTL thickness) can shift optimum conditions, as shown in this study: devices with a 1.68 eV perovskite absorber achieved a current-matching condition with standard $\mathrm{SnO_x}$ thickness, whereas the 1.63 eV material enabled similar results with a thinner $\mathrm{SnO_x}$ layer. Further improvement strategies include adding an anti-reflective or coupling coating, such as $\mathrm{MgF_2}$, LiF, or silicon dioxide ($\mathrm{SiO_2}$), texturing front and rear sides of the subcells, and adjusting the refractive index gradient within the device to minimize reflection losses.[332–334] Given the range of possible strategies and the multitude of material combinations enabled by lamination, computational modeling constitutes a key resource in future optimization processes. This computer-assisted approach, increasingly employed in recent literature for conventionally fabricated tandems, can facilitate identifying an optimum bandgap and film thickness.[101,102] It should be noted that the influence of encapsulation materials on light management is immediately considered in laminated devices. As an inherent part of commercial solar cells, including this encapsulation layer in optimization calculations is crucial. This fundamental consideration is often overlooked in reports on record devices.[56,102,285]

6.3.4 Reduced parasitic absorption losses in inverted architectures

Lamination provides additional options compared to standard fabrication techniques for optically improving monolithic tandems through the decoupled deposition of functional layers. The material combination in laminated solar cells presented until now was based on an established architecture compatible with conventional processing methods.[102,285,305,335] As displayed in Figure 6.12a, light enters the device through an n-i-p top PSC. However, the front CTL of C_{60} is known to cause substantial parasitic absorption at short wavelengths, limiting the J_{sc}.[62,63] The following study demonstrates that lamination can overcome this issue by enabling an architecture inversion to place the problematic CTL of C_{60} behind perovskite on the optical path. In this inverted layer stack, the highly transparent double HTL of NiO_x and 2PACz is located in the front, allowing for increased light transmission to the absorber. Consequently, charge carrier generation in the top PSC should be enhanced without changing materials or key interfaces, such as the nearly optimal perovskite/2PACz interface.[176,336] The feasibility of this original idea was demonstrated in a pre-experiment for single-junction PSCs, Section 5.2.3, and is now investigated in tandems with an architecture established for the first time in this work.

Laminated tandems with inverted architecture are prepared by hot-pressing a front layer stack of a p-i-n PSC on a modified SHJ solar cell, as displayed in Figure 6.12b. The front stack builds on a 30 μm thin-glass superstrate coated with a front TCO of IO:H, and a double HTL of NiO_x and 2PACz. It is noted that a NiO_x layer is optional, as previous reports demonstrated that 2PACz could be in direct contact with IO:H and yield highly efficient devices.[337,338] However, an underlying sputtered NiO_x film results in a more uniform and conformal coverage of solution-based self-assembled monolayers and was, therefore, retained in the architecture.[176] The 70 nm ITO junction layer and double ETL of SnO_x and C_{60} are processed on the p-side of the bifacial SHJ solar cell. A 1.68 eV triple-cation perovskite film is deposited on the front stack. Solution molarity is 1.33 M, slightly lower than in the n-i-p layer stack (1.53 M). This thinner perovskite absorber in p-i-n architecture aims to compensate for an anticipated PSC current enhancement related to reduced parasitic absorption losses at short wavelengths. This p-i-n architecture is challenging to produce conventionally using the same deposition techniques as the n-i-p. Lamination overcomes here several limitations: i) The C_{60} surface causes dewetting, which complicates the subsequent

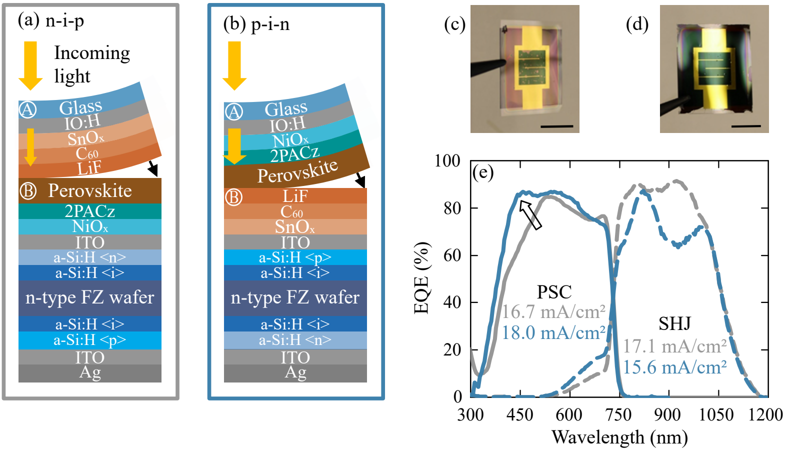

Figure 6.12: Proof of concept for architecture inversion of monolithic perovskite/silicon tandems by lamination. This inversion is expected to enhance current in the top perovskite solar cell (PSC) by reducing parasitic absorption in front functional layers. a) Device illustration with a front PSC in n-i-p (grey) and b) p-i-n (blue) architecture using identical processing techniques. c) Photographs of laminated solar cells from the glass front side in n-i-p, and d) p-i-n. The scale bar corresponds to 10 mm. e) External quantum efficiency (EQE) characterization of representative devices. Current densities generated in perovskite and silicon subcells are shown in the respective areas. The outlined arrow highlights an EQE improvement attributed to decreased parasitic absorption.

solution-based perovskite deposition,[192,193] ii) solvent incompatibility as ethanol used for 2PACz would dissolve the perovskite,[339,340] and iii) the challenging sputtering process of IO:H and NiO_x on perovskites, due to the absence of buffer layers.[219,341]

EQE characterizations of p-i-n laminated tandems indicate a 1.9 mA/cm^2 higher J_{sc} in PSCs on average compared to the n-i-p architecture, as outlined in Figure 6.12e. Light absorption enhancement at short wavelengths from 300 to 550 nm yields a subcurrent of up to 18 mA/cm^2 in the PSC. This improvement is consistent with pre-experiments on single-junction devices, demonstrating that architecture inversion enables overcoming C_{60} parasitic absorption losses. Despite precautions taken with the adjusted perovskite solution molarity, current mismatch in p-i-n laminated tandems is significant, and subcurrent in SHJ solar cells averages only 15.5 mA/cm^2 (Table 6.3). Different factors might reduce the bottom cell current in this p-i-n architecture, initially optimized for n-i-p devices. The non-optimized light management is underlined by severe interference patterns in the infrared wavelength range, suggesting that appropriate functional layer thicknesses and refractive index gradients must be investigated. Moreover, a thicker ITO layer on the p-side of the SHJ subcell (70 nm), compared to 30 nm on the n-side, contributes to parasitic absorption at long wavelengths. A thinner junction layer of 20-30 nm should enable to minimize these optical losses and enhance current in the SHJ subcell.[192]

Table 6.3: PCE, FF, V_{oc}, and J_{sc} of laminated monolithic perovskite/heterojunction silicon (SHJ) tandem solar cells with n-i-p (6 devices) and p-i-n (3) architectures. SD, Min., and Max. stand for standard deviation, minimum, and maximum, respectively.

	PCE (%)		FF (%)		V_{oc} (V)		J_{sc} (mA/cm^2) PSC		J_{sc} (mA/cm^2) SHJ	
	n-i-p	p-i-n	n-i-p	p-i-n	n-i-p	p-i-n	n-i-p	p-i-n	n-i-p	p-i-n
Mean	16.2	15.3	58.0	60.3	1.75	1.63	15.9	17.8	17.1	15.5
SD	1.8	1.7	2.8	4.6	0.03	0.05	0.9	0.3	0.2	0.1
Min.	13.9	13.9	54.0	55.8	1.70	1.59	14.7	17.5	16.8	15.4
Max.	18.0	17.1	60.0	65.0	1.80	1.69	16.7	18.0	17.3	15.6

By introducing flexibility in material deposition sequence, lamination effectively overcomes severe parasitic absorption in the PSC, substantially enhancing its subcurrent. The successful inversion of an established tandem architecture, with no precedent reported to date, underlines the potential of this fabrication process in bridging the gap in the development of n-i-p and p-i-n devices. Moreover, n-i-p laminated tandems, which serve as references in this study, also show remarkable improvements compared to the first prototypes presented in Section 6.2.1, such as an increased J_{sc} in the top cell through highly transparent IO:H and glass superstrate. The V_{oc} of up to 1.8 V (Table 6.3) is comparable to conventionally processed tandems,[56] and higher than most mechanically stacked solar cells.[94,147,164,291,294–296] This could be linked to the improved quality of recrystallized perovskite absorber and the larger active area of 1 $\mathrm{cm^2}$, twice as large as mechanically stacked devices with 0.5 $\mathrm{cm^2}$ on average. Indeed, a larger active area might explain a higher V_{oc} augmentation through reduced recombination losses in silicon solar cells due to less edge effects.[284] These photovoltaic characteristics are representative of the different fabricated batches, irrespective of the lamination parameters or the materials used. The overall device performance is now limited by the FF, remaining below 70%, which is not fully understood at the moment. It is suspected that the particle-related defects may play a role, as previously discussed, as well as the exposure to oxygen and moisture related to the sample handling that is not always conducted in a protective atmosphere. Nevertheless, laminated PSCs demonstrated FFs of up to 77% in single-junction architectures (Section 5.3), so the FF is not expected to be intrinsically limited by the lamination process.

6.4 Summary

Monolithic perovskite/silicon tandem solar cells were manufactured via lamination for the first time in this work. This technique involves hot-pressing the PSC front layer stack onto a modified SHJ bottom cell. During the process, perovskite recrystallizes at the interface between the subcells, connecting them electrically and optically in series. Hence, monolithic tandems are obtained without conventionally depositing layers sequentially atop each other. First prototypes exhibit up to 20% PCE, representing a $30\%_{\mathrm{rel}}$ increase in efficiency compared to laminated semi-transparent PSCs in single-junction. While the current efficiencies remain modest compared to more mature monolithic tandem technologies, the laminated technique introduces unique advantages compared to conventional fabrication methods. For instance, a major challenge in designing multi-layer perovskite/silicon tandems is achieving a current-matching condition and minimizing parasitic absorption losses. Through the decoupled preparation of both subcells, lamination offers a wide range of strategies to optimize these complex architectures.

Lamination enables perovskite engineering, an established technique for optimizing device performance, such as bandgap and thickness tuning. Adjusting the absorber composition led to the fabrication of current-matched devices. The J_{sc} of laminated tandems increases to about 17 mA/cm^2 in both subcells, compared to 15.5 mA/cm^2 in the first prototypes. These results built on a successful PEN foil replacement with a more transparent glass superstrate. The front electrode was optimally deposited on individual glass superstrates, allowing for flexibility in the architecture by varying front TCO materials, deposition parameters, and post-treatment conditions. In-house sputtered IO:H achieves high transparency and conductivity, which is essential for enhanced charge-carrier generation and extraction. The outstanding application versatility provided by the lamination technique was further explored in a final proof-of-concept architecture that would be difficult or impossible to process conventionally. By inverting the device layer stack, typical issues of conventional monolithic perovskite/silicon tandems, such as parasitic absorption losses in front CTLs, are overcome.

Improvement strategies presented in this work provide new opportunities for enhancing tandem architectures and innovation beyond conventional designs. Further advancements include the incorporation of textured surfaces in the device architecture, particularly textured silicon subcells, which are standard and cost-effective in the PV industry. In this regard, preliminary experiments investigating the perovskite lamination on textured silicon substrates have shown promising results, as presented in Chapter 8. Future research will focus on integrating these industry-relevant silicon solar cells with the lamination process, which represents a decisive step toward the industrialization of perovskite-based tandem technology. Overall, the successful fabrication of monolithic perovskite/silicon tandems suggests that lamination readily applies in this field, offering a wider range of materials and facilitating research into new architectures. Combinations of different technologies can be envisioned, as demonstrated by novel prototypes of perovskite/CI(G)S tandem solar cells in Chapter 8.

7 Conclusion

With record PCEs exceeding 26%, PSCs are now one of the most efficient and rapidly developing PV technology. The fast development was facilitated by fabrication steps realizable with standard laboratory techniques for lab-scale devices, low-temperature processing, and the high tunability of perovskite absorber characteristics. These attributes enable a wide range of applications, from single-junction to integration in tandem solar cells. An alternative fabrication technique for perovskite-based PV proposed in this work overcomes limitations of standard deposition methods and offers additional strategies to address remaining challenges of this highly promising technology. Research questions guiding experimental studies aimed to: 1) Assess the hot-pressed perovskite recrystallization, improving its morphology and crystallinity; 2) Determine the influence of a hot-pressed absorber quality on device performance and stability of laminated PSCs over time; 3) Explore the vast range of application of the lamination technique; 4) Evaluate the role of the lamination process in supporting research on tandem PVs. Answers to these questions are now detailed, referring to results presented in the main Chapters 4 to 6.

1. Recrystallization process: How can the quality of perovskite absorbers, in terms of crystallinity and morphology, be enhanced by adjusting lamination pressure, temperature, and processing duration while preventing degradation?

Compared to standard advancement strategies for perovskite PVs, including tuning absorber composition, morphology, and bulk passivation, this work provides insights into an alternative and complementary method. The hot-pressing technique involves a simultaneous application of high pressures and temperatures to enhance perovskite quality. Our research demonstrates that hot-pressed polycrystalline films exhibit larger grains, reduced surface roughness, and improved crystallinity. While previous studies explored recrystallization via hot-pressing, the process window varied widely depending on perovskite compositions. For the first time, we conducted thorough investigations on a hot-pressed triple-cation absorber designed for efficient and long-term stable PSCs with a suitable bandgap for tandem applications. This perovskite composition remains preserved when the temperature and duration do not exceed 100 °C and 60 min, defining an initial process window. Consistent with existing literature, grain growth is primarily driven by higher hot-pressing temperatures, achieving $43\%_{\mathrm{rel}}$ larger grains at 100 °C than pristine layers. Although longer treatments can further increase grain size, 5 min appears sufficient to improve perovskite morphology and crystallinity. After the hot-pressing step, the initial $\approx$20 nm RMS surface roughness decreases to a few nanometers when a pressure of at least 50 MPa is applied. The final process window, validated through the successful lamination of efficient PSCs, includes a maximum treatment duration of 30 min, a minimum pressure of 50 MPa, and a temperature between 85 and 100 °C. The findings of this work demonstrate that hot-pressing is an effective post-treatment process, decoupling the deposition method from the final layer quality required for efficient optoelectronic devices. As it enables the production of perovskite absorbers with improved morphology and crystallinity in a controllable process, hot-pressing treatments contribute to addressing the upscaling challenge of the perovskite technology. In addition, this solvent-free technique uses relatively low temperatures, broadening the range of compatible materials and facilitating the process – primarily relying on solid-state layers – on a future industrial scale. The subsequent research question explores the impact of this hot-pressed perovskite quality on device performance and stability over time.

2. Device performance: How do improved morphology and crystallinity of perovskite absorbers impact the performance and stability over time of laminated perovskite solar cells?

A comparison between laminated PSCs with conventionally produced references of identical architecture reveals intrinsic characteristics unique to the lamination process via hot-pressing. The smoother perovskite surface is recognized by optical characterizations, notably showing reduced diffuse reflectance. Remarkably, laminated PSCs exhibit an enhanced V_{oc} and lower n_{id}, indicating reduced non-radiative recombination losses. These outcomes are consistent with the smoother surface and larger grains of the perovskite absorber, which typically benefit device performance by decreasing trap-state density and enhancing charge carrier extraction. Furthermore, laminated PSCs demonstrate exceptional shelf-life stability over a year while references degrade rapidly. Even under continuous illumination, laminated devices maintain stable power outputs both at room temperature and at 80 °C over 100 h. These experimental results highlight that lamination contributes to achieving operational stability, addressing one of the remaining challenges of perovskite-based PVs. The outstanding thermal and long-term device stability is attributed to i) the improved absorber morphology after the hot-pressing step, ii) the prevention of critical proximity between the perovskite and electrode, limiting Au migration, and iii) the potential barrier function of the superstrate, underscoring a possible direct encapsulation feature of the lamination technique. Moreover, PCEs of up to 17.5% with both lamination and conventional methods are demonstrated at a consistent yield of functional devices over 80% across several batches. The achieved PCE was one of the highest worldwide for laminated perovskite PVs using a comparable manufacturing process at the publication date. Exceeding 20% of PCE today, recent advancements highlight the growing interest in this technique and justify further investments in closing the efficiency gap towards record-breaking, conventionally-produced PSCs. Beyond performance and long-term stability considerations, the hot-pressing process offers a wider range of accessible material combinations compared to standard PSC fabrication methods. Various applications were explored in this work, which will be detailed when addressing the following research questions.

3. Application versatility: To what extent is the lamination technique relevant for supporting research of new materials, deposition processes, and device architectures in perovskite-based photovoltaics?

Lamination overcomes restrictions of standard sequential layer depositions. Through the device preparation in independent half-stacks, high flexibility is achieved in the choice of materials, deposition order, and processing techniques. The fabrication of otherwise inaccessible architectures is facilitated to target enhanced device performance and long-term operational stability while supporting the transition to scalable manufacturing processes. An emblematic material combination in this work pairs SnO_2 on the ETL side and NiO_x as HTL atop the perovskite, resulting in laminated PSCs with good thermal stability over 100 h at 80 °C under continuous illumination. Conventionally manufacturing this architecture is challenging due to processes that can damage the perovskite absorber: the water solvent and high annealing temperatures of 250 °C used for SnO_2 deposition, and the NiO_x sputtering process involving high-kinetic energy particles. The selected device architecture showcases the applicability expansion of scalable deposition processes for functional layers enabled by lamination. Techniques such as sputtering, usually restricted to layers below the perovskite absorber or requiring additional buffer layers, are used more flexibly through lamination. This feature also facilitates the integration of inorganic CTLs, advancing the long-term stability of perovskite-based PVs. Another application of lamination is the sequential deposition of independently processed absorber layers to overcome solvent incompatibility issues. With a final thickness exceeding 2 µm of three combined perovskite layers, this technique can address challenges in covering textured silicon solar cells for tandem applications, as discussed in Chapter 8. Sequential lamination can also be used to fabricate heterojunctions with various absorbers, including 2D and 3D materials, for enhanced device performance. Ultimately, the application versatility of the lamination process is demonstrated by successfully varying the thin-film deposition order, which is severely restricted in standard techniques. The distinct development routes for single-junction PSCs in n-i-p and p-i-n structures are effectively bridged by producing identical device architectures in conventional and reversed deposition order while achieving comparable PCEs. Lamination thus introduces novel improvement strategies, including for tandem PVs, which will be further explored in the following research question.

4. Tandem technology: How suitable is the presented lamination process for fabricating monolithic perovskite/silicon tandem solar cells, particularly in addressing multi-layer designs, light management, and current-matching requirements among subcells?

Tandem PV is an established technology that enables high PCEs by overcoming fundamental losses in single-junction devices. With the advancement of perovskite-based PV, novel material combinations have rapidly emerged. A promising concept consists of depositing a PSC directly atop a silicon solar cell to create a monolithic tandem. This architecture, involving more layers than a single-junction device, requires increased flexibility in material combinations and processing methods. The first prototypes of laminated monolithic perovskite/silicon tandems demonstrate the potential of this alternative fabrication technique in that field. These prototypes build on the successful lamination of semi-transparent PSCs by replacing the opaque rear contact with transparent conductive oxides. However, designing multi-layer tandems remains challenging due to optical interdependencies and current-matching requirements. High transparency in front layers is essential to prevent parasitic absorption and improve charge carrier generation in absorbers.

Lamination addresses these constraints through several aspects. First, it allows for the individual optimization of front electrodes on separate superstrates, preserving sensitive device layer stacks. In that regard, ultra-thin glass superstrates contribute to optical optimization through enhanced transparency, high thermal tolerance, and robustness against harsh processes such as sputtering techniques. Lamination also allows adjusting the layer stack orientation in the optical path to position the more transparent layers in front of the absorber and thus reduce parasitic absorption. This work finally demonstrates the lamination of perovskite materials with various thicknesses and bandgap energies to achieve a current-matching condition essential for high-efficiency devices. Overall, these insights reveal numerous advantages of the lamination process, offering a promising route for developing novel perovskite-based PVs.

8 Outlook

This work has established lamination as a promising fabrication method for perovskite-based solar cells. Further development of this technique must address three essential pillars of the perovskite technology: scalability, efficiency, and operational stability. Four key aspects for future research are discussed in the following: 1) Scaling up the lamination technique first necessitates transitioning to large area deposition processes and mastering device fabrication in half-stacks; 2) Upscaling of laminated perovskite/silicon tandems also requires the use of industrially relevant, typically textured, silicon solar cells; 3) Enriching the laminated architectures with recently proven advanced materials is expected to improve device performance; 4) One particular technology where lamination could be particularly valuable is perovskite/CIGS tandem PVs, which combine high efficiency, stability over time and benefits of all thin-film PVs.

1. Transition to industrial scale processes

While the current size of laminated PSCs (10.5 mm^2) and tandems (1 cm^2) is in line with the latest laboratory standards for perovskite-based solar cells, a critical research objective is the upscaling of this technology to industrially relevant module sizes. The spin-coating technique currently used for perovskite processing is the most widely adopted, yielding the highest PCEs.[66] The perovskite research field benefits from this relatively simple, compact, time and cost-efficient technique. However, spin-coating techniques are not suitable for homogeneously processing large areas. Therefore, the transition to scalable deposition methods, such as thermal co-evaporation,[67,68] inkjet printing,[69,70] slot-die coating,[26,71,72] and blade coating,[73,74] is inevitable. Furthermore, future PV production lines can take advantage of the rapid device fabrication through parallel half-stack preparation and possible direct encapsulation. However, the fabrication of laminated devices in two half-stacks presents challenges that need to be addressed to increase the reproducibility and manufacturing yield. Currently, lamination requires more manual handling and transport than the standard fabrication method, and the process is not fully performed in a protective atmosphere. As a result, laminated samples are exposed to more particles, oxygen, and moisture than references, reducing reproducibility and fabrication yield. The number of particle-related defects and exposure to the ambient atmosphere is expected to be limited by automation, rapid processing, and continuous vacuum systems in future industrial production lines. Alternatively, transparent buffer layers, such as EVA and POEs, established thermoplastic PV encapsulants,[319,320] could be introduced into the layer stack to fill voids or cushion particles, possibly reducing defect size while completing the device encapsulation.

2. Incorporating textured silicon subcells in laminated tandems

Upscaling perovskite-based laminated tandem devices will also involve overcoming challenges such as covering commercially available, typically textured, silicon solar cells in future research. Standard processing techniques face difficulties coating micrometer-high textures with perovskite films that are only hundreds of nanometers thick.[342] Uncovered pyramidal tips of the silicon texture, outlined in Figure 8.1a, can create shunt paths detrimental to device performance. Laminating perovskite absorbers onto textured surfaces could outperform standard sequential deposition methods. A preliminary experiment, illustrated in Figure 8.1, demonstrates that laminated perovskite layers on micrometer-sized textured surfaces achieve uniform coverage and large grain sizes, showcasing the feasibility of the concept. Alternatively, recent studies indicated that nanotextured silicon substrates are already sufficient to significantly improve light management in tandems while facilitating the deposition of

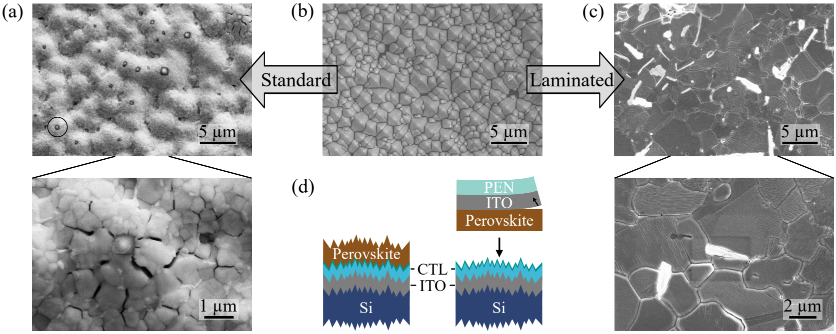

Figure 8.1: Prospective study of laminated perovskite films on micrometer-sized textured silicon substrates. a) Scanning electron microscopy (SEM) image after depositing the absorber via standard spin-coating processing, yielding a rough perovskite surface with incomplete coverage of the silicon textures. The detailed view displays an emerging pyramid silicon tip through the perovskite layer. b) SEM image of a textured silicon substrate, and c) after laminating the absorber layer, resulting in a smooth and outstanding coverage of the silicon textures. The detailed view shows the hot-pressed perovskite morphology exhibiting larger grains. d) Illustration of the layer stack when the perovskite is conventionally deposited (left) and laminated (right). The independently processed perovskite film on an ITO/PEN foil is laminated at 80 MPa, 100 °C for 5 min on the textured silicon substrate. The PEN/ITO foil is subsequently removed. Further SEM images and configurations are available in reference [124].

homogeneous perovskite films.[74,173,302,306] Using such strategies, lamination is expected to be readily compatible with textured silicon bottom solar cells. Overall, introducing textures can reduce the reflectance losses inherent to planar layer stacks, as observed in our first prototypes.[227,287,303,304] Strategies to enhance in-coupling light include introducing textured foils as anti-reflective coatings on the superstrate front side,[130,343] and combining lamination with nanoimprint lithography.[39,122,135] The latter technique would allow for texturing the perovskite layer and assembling the device half-stacks in a single step. These innovative methodologies open new perspectives for improving the competitiveness of laminated PSCs.

3. Advancing laminated architectures

This work presents prototypes showcasing how lamination expands the range of accessible architectures for perovskite-based solar cells. Future research can prioritize materials that enhance operational stability, scalable processing techniques, and deposition orders that ease device fabrication. It is also noted that the architectures presented in this work remain relatively simple. The proof-of-concept devices were primarily intended to underscore the intrinsic characteristics of the lamination process. However, future architecture can benefit from recent achievements reported in the literature, notably regarding passivation techniques. The current architecture could be enriched with advanced optimization strategies to improve device performance, such as incorporating 2D materials for surface passivation and additives for perovskite bulk passivation.[55,121] In this context, sequential lamination also has significant potential to produce perovskite heterostructures with advanced energy level alignment by combining different materials that cannot be deposited atop each other otherwise, e.g., due to solvent incompatibilities. Given the vast variety of possible material combinations enabled by lamination, machine learning is expected to be a key resource in future optimization processes.

4. Laminated perovskite/CIGS tandem solar cells

Beyond the lamination of monolithic perovskite/silicon tandem solar cells, future work could explore other subcells, such as CI(G)S, which pairs well with wide bandgap perovskites. Perovskite/CI(G)S tandem solar cells already achieve PSCs exceeding 24% and share the advantages of thin-film PVs, enabling the fabrication of flexible, lightweight devices, with a possible reduction in LCOE.[13,106,344] These device architectures benefit from research on perovskite/silicon tandems, including efficient passivation techniques and front electrodes.[174] However, challenges remain, such as imperfect perovskite deposition on the rough

CI(G)S surfaces and damage to the bottom cell during fabrication. Lamination could overcome these processing hurdles, facilitating the fabrication of perovskite/CI(G)S tandems.[292] A preliminary experiment in Figure 9.12, Appendix, demonstrates the feasibility of laminating a PSC onto a CI(G)S bottom cell via hot-pressing. The very first prototype achieves 9.7% of PCE, with evident contributions from both subcells as indicated by EQE characterizations and a V_{oc} adding up to 1.45 V. This proof-of-concept device demonstrates that lamination readily applies to various tandem PV architectures, paving the way for further advances in the field.

9 Appendix

Lamination program

The lamination program in Table 9.1 is specifically written for the in-house developed machine Wum2 at IMT (KIT). The tree critical parameters are temperature (here 90 °C), pressure (100 MPa), and duration (5 min). The bottom plate position controls the applied pressure, while the top plate remains fixed. After the chamber closes (step 1), machine plates are heated (2), and contact between the top plate and sample is made (3). The chamber atmosphere is cleaned by successive cycles of pumping down and N_2 flushing (4). When the temperature reaches 90 °C (5), hot-pressing starts by applying a pressure of 20 000 N (6) for 5 min. This force corresponds to a pressure of 100 MPa for a (14x14) mm large hot-pressed area. Samples are then cooled to 45°C (7), pressure is released, and the chamber opens (8). All hot-pressing and lamination processes performed in this work follow this procedure, and only pressure, temperature, and duration are adjusted. The eight steps are illustrated in Figure 3.2 (Section 3.1.3), displaying pressure and temperature over time.

Table 9.1: Program used for hot-pressing thin films and laminating perovskite-based solar cells.

Phase	Step	Command
Heating	1	Initialize ForceControl(true/false=0)
		Open File Measure( )
		Close Chamber( )
	2	Start Heating( )
		Position relative(Pos:4mm, Vel:2mm/min, MaxForce:2kN)
	3	SetMeasureForce0()
		Touch Force(Force=100N)
		Position relative(Pos:1µm, Vel:0.05mm/min, MaxForce:5kN)
	4	Evacuate Chamber( )
		Wait Time(Time=10.00s)
		Venting Chamber( )
		Wait Time(Time=5.00s)
		Evacuate Chamber( )
		Wait Time(Time=10.00s)
		Venting Chamber( )
		Wait Time(Time=5.00s)
		Force - Force controlled(Force:1.5kN, Vel:0.5mm/min)
		IF Test Temperature >=(Temperature=88.0deg, Channel=8)
		Start Cooling( )
		Temperarture <=(Temperature=90.0deg, Channel=8)
		ENDIF
		Temperature >=(Temperature=87.0deg, Channel=8)
		Stop Heating( )
	5	Wait Time(Time=25.00s)

Continued on next page

Phase	Step	Command
Hot-pressing	6	Force - Force controlled(Force:20kN, Vel:0.5mm/min)
		Heating(Temp=90.0deg,>limit=90.0deg,<limit=89.0deg)
	6	Wait Time(Time=300.00s)
Cooling	7	Start Cooling( )
		Temperature <=(Temperature=45.0deg, Channel=8)
	8	Position relative(Pos:-0.5mm,Vel:0.05mm/min, MaxForce:2kN)
		Close File Measure( )
		Venting Chamber( )
		Wait Time(Time=5.00s)
		Stop Cooling( )
		Open Chamber( )
		Unlock door( )

Deposition study of sputtered IO:H electrodes

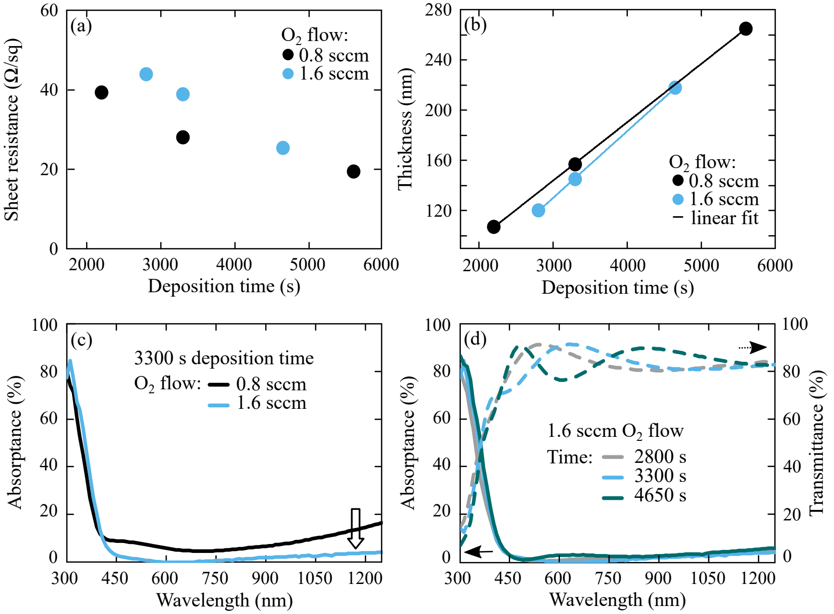

Figure 9.1: Electrical and optical characterizations of IO:H transparent conductive oxides. The deposition time and O_2 flow are varied during sputtering deposition on glass substrates, impacting sheet resistance, thickness, and transparency. a) Sheet resistance of IO:H films for a deposition time from 2000 to 5850 s. The sheet resistance decreases with a longer deposition time and a 0.8 sccm O_2 flow (black) compared to 1.6 sccm (blue). b) IO:H thickness, linearly increasing with deposition time. c) Absorptance measurement of IO:H layers with different O_2 flow while deposition time is fixed at 3300 s. The outlined arrow highlights less parasitic absorption at longer wavelengths than 400 nm with an O_2 flow of 1.6 sccm compared to 0.8 sccm. d) Absorptance (solid line) and transmittance (dashed line) of IO:H films for different deposition times, while O_2 flow is fixed at 1.6 sccm. Low parasitic absorption losses are observed for all deposition times. Transmittance measurements reveal a shift in interference patterns, attributed to different layer thicknesses. In conclusion, a 1.6 sccm O_2 flow and a deposition time of 4850 s are retained to sputter the IO:H front electrode with enhanced conductivity and transparency on glass superstrates for laminated tandems in Section 6.3.

State-of-the-art lamination techniques for perovskite solar cells

Table 9.2: Overview of state-of-the-art lamination techniques for perovskite solar cells with corresponding reference, publication date, and achieved PCE. Two approaches are distinguished: the electrode transfer technique, including carbon-based electrodes, and hot-pressing at the perovskite/perovskite interface.

Reference	Publication date	PCE (%)	Electrode transfer	Carbon-based	Perovskite/ Perovskite
[265]	2010	2.5	X	–	–
[266]	2013	2.4	X	–	–
[200]	2014	15.5	X	–	–
[201]	2014	9.9	X	X	–
[345]	2015	11.3	X	–	–
[346]	2015	12.0	X	X	–
[196]	2015	13.5	X	X	–
[347]	2015	10.1	X	–	–
[348]	2016	9.6	X	–	–
[268]	2017	15.7	X	X	–
[281]	2017	15.0	X	X	–
[207]	2017	13.7	X	–	–
[146]	2017	6.9	–	–	X
[150]	2018	10.6	–	–	X
[349]	2018	15.0	X	X	–
[202]	2018	19.2	X	X	–
[350]	2019	12.8	X	–	–
[199]	2019	16.4	X	–	–
[246]	2019	10.7	X	X	–
[269]	2019	10.9	X	X	–

Continued on next page

Reference	Publication date	PCE (%)	Electrode transfer	Carbon-based	Perovskite/ Perovskite
[143]	2019	12.6	X	–	–
[351]	2019	13.5	X	–	–
[270]	2019	17.3	X	–	–
[197]	2019	7.1	X	X	–
[222]	2020	8.5	–	–	X
[267]	2020	10.0	X	–	–
[14]	2020	14.6	–	–	–
[166]	2020	15.7	X	–	–
[249]	2020	15.3	X	X	–
[198]	2021	16.6	X	X	–
[242]	2021	17.1	X	–	–
[203]	2022	14.1	X	–	–
[243]	2022	12.7	X	–	–
[120]	2022	17.5	–	–	–
[204]	2022	15.1	–	–	X
[115]	2023	17.2	–	–	X
[205]	2023	22.3	–	–	X
[206]	2024	21.0	–	–	X
[352]	2024	20.8	X	–	–
[353]	2024	20.3	X	X	–

Hot-pressed perovskites and lamination interface

This study investigates to what extent the pressure is involved in improving perovskite crystallinity and morphology during a hot-pressing process. The applied pressure varies from 5 to 150 MPa, while temperature and time are fixed at 90 °C and 5 min, as illustrated in Figure 9.2. X-ray diffraction characterizations of hot-pressed perovskites demonstrate a similar pattern as in pristine films. This result indicates that the absorber composition is preserved even under pressures as high as 150 MPa. Increased intensity of the dominant peak at 14.2° in hot-pressed films also suggests an enhanced crystallinity, as discussed in Section 4.2. The perovskite surface morphology is examined using AFM images. Perovskite grains are slightly larger after treatment (290 nm) than in as-deposited films (270 nm). However, no evident pattern implies that higher pressure consistently induces grain growth. 5 MPa appears insufficient to modify the absorber surface (Figure 9.2e), and RMS values remain similar to as-deposited perovskites (20 nm). Visible recrystallization of the absorber surface starts at 20 MPa. Beyond 50 MPa, the RMS roughness is significantly reduced to under 10 nm. Therefore, 50 MPa constitutes a minimum pressure threshold for fabricating perovskite-based solar cells.

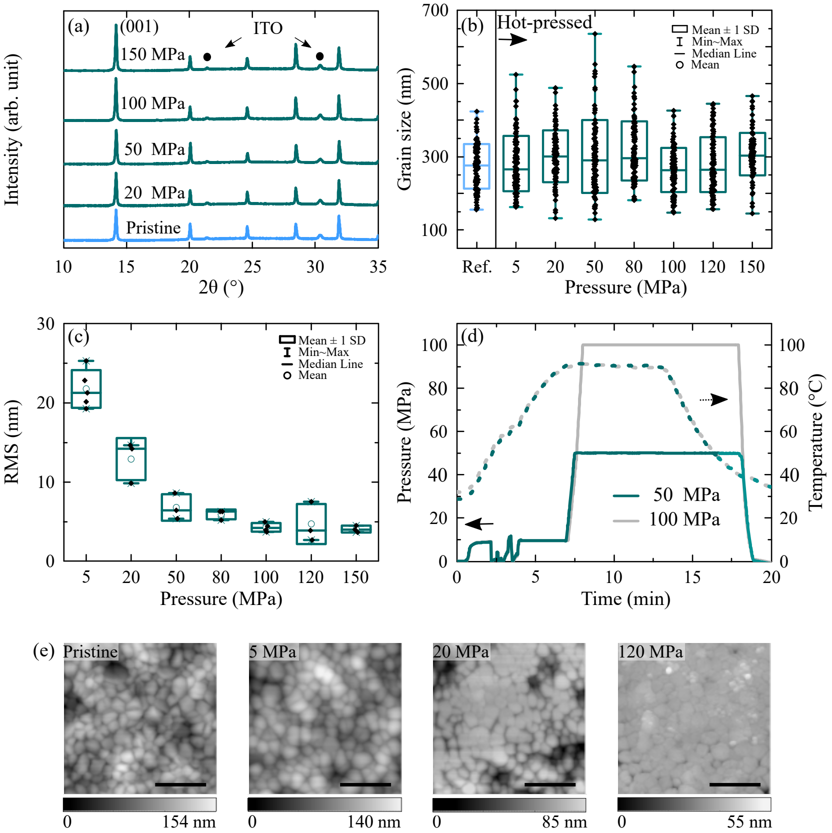

Figure 9.2: Crystallinity and morphological characteristics of pristine and hot-pressed perovskites depending on the applied pressure. The investigated layer stack is glass/ITO/perovskite hot-pressed at 90 °C for 5 min under 5 to 150 MPa. a) X-ray diffraction measurements showing the characteristic signature of the triple-cation absorber. Circles highlight ITO peaks at 21.4° and 30.4°. b) Grain size measurement of hot-pressed and pristine perovskites. SD stands for standard deviation. c) Root mean scare (RMS) surface roughness for different applied pressures. d) Exemplary process performed at 50 and 100 MPa. e) Representative atomic force microscopy (AFM) images of perovskite surface as-deposited and hot-pressed under 5, 20, and 120 MPa, respectively. AFM scale bar corresponds to 1 µm. Further AFM images are available in reference[123].

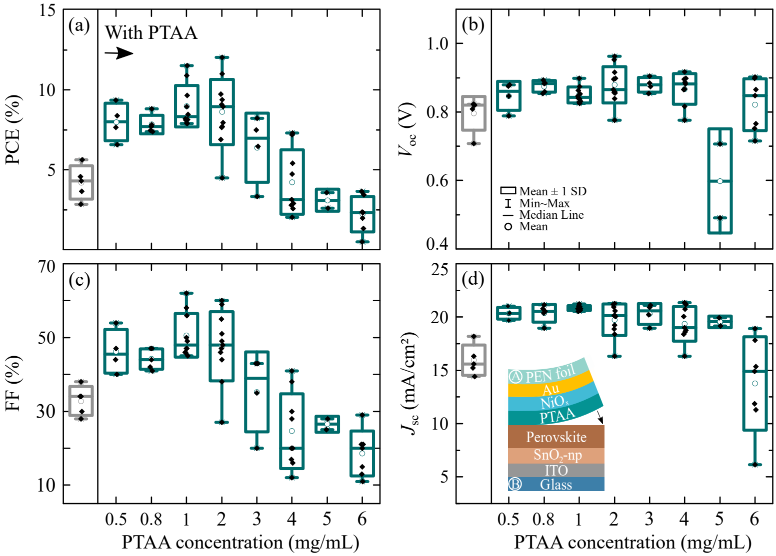

Figure 9.3: Performance of laminated perovskite solar cells (PSCs) with a PTAA layer at the lamination interface between the NiO$_x$ and perovskite layer. a) PCE, b) V_{oc}, c) FF, and d) J_{sc} of laminated PSCs without (grey) and with PTAA (green). The concentration of PTAA dissolved in toluene – related to the film thickness – varies from 0.5 to 6.0 mg/mL. Device architecture is illustrated in d). The thin PTAA layer is presumed to enhance the mechanical and electrical contact between the recrystallized perovskite and NiO$_x$. Improved PCE principally results from higher FF and V_{oc} for PTAA concentrations of up to 2 mg/mL. Decreased performance at higher concentrations suggests that PTAA is too thick and becomes insulating.

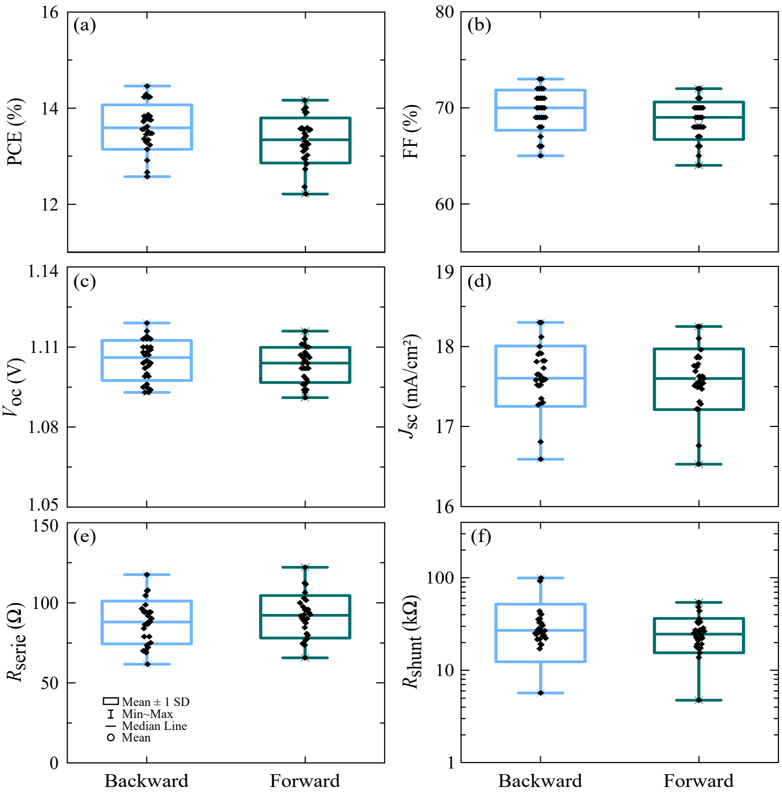

Figure 9.4: Performance statistics of laminated semi-transparent perovskite solar cells. a) PCE, b) FF, c) V_{oc}, d) J_{sc}, e) series resistance (R_{series}) and f) shunt resistance (R_{shunt}) extracted from J-V characteristics of laminated devices in backward and forward scanning directions, respectively. Measurements performed without masks. Min., Max., and SD stand for minimum, maximum, and standard deviation, respectively. The corresponding fabrication yield is 88%, with 28 functional devices out of 32 fabricated (decision criterion: PCE>12%). Experimental details on the optimization of SnO_x deposition via ALD are available in reference[124].

Lamination parameters and device performance

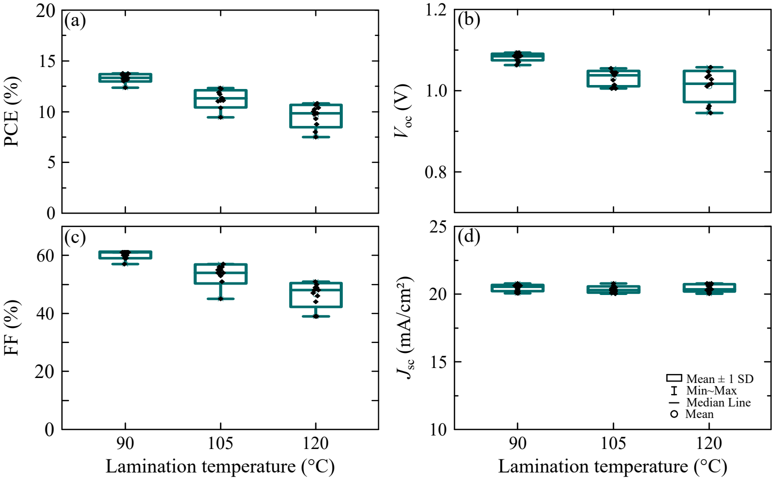

Figure 9.5: Investigation of the lamination temperature upper limit for fabricating perovskite solar cells (PSCs). Device architecture is shown in Figure 9.6a. a) PCE, b) V_{oc}, c) FF, and d) J_{sc} of laminated PSCs fabricated at temperatures from 90 to 110 °C, 80 MPa for 5 min. While the J_{sc} remains constant, increased temperature results in decreased V_{oc} and FF. This degradation is attributed to a perovskite decomposition occurring at high temperatures, as indicated by X-ray diffraction measurements in Section 4.2. The process window for laminating efficient PSCs is thus limited to a maximum temperature of 100 °C.

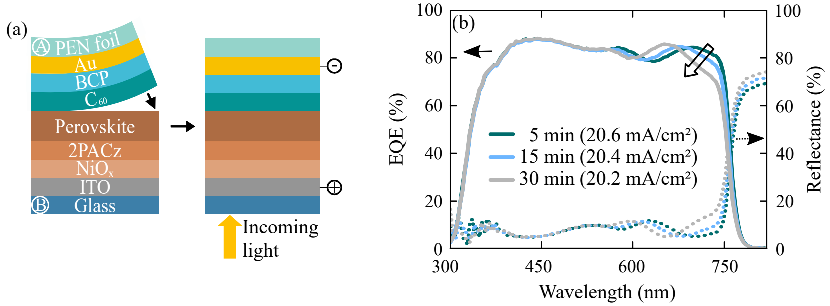

Figure 9.6: Light management in laminated perovskite solar cells (PSCs) depending on the lamination duration. a) Illustration of the device architecture. b) External quantum efficiency (EQE) and reflectance measurements of laminated PSCs for 5 to 30 min lamination times. The pressure and temperature are fixed at 80 MPa and 90 °C. Values in parenthesis correspond to integrated J_{sc}. The outlined arrow highlights an EQE signal shift between 600 and 750 nm, mirroring the reflectance measurement. This shift is attributed to a progressive reduction of the perovskite surface roughness for longer lamination times, as demonstrated in Section 4.3.2. Adapted from reference [120] with the permission of Wiley.

Stability study on laminated perovskite solar cells

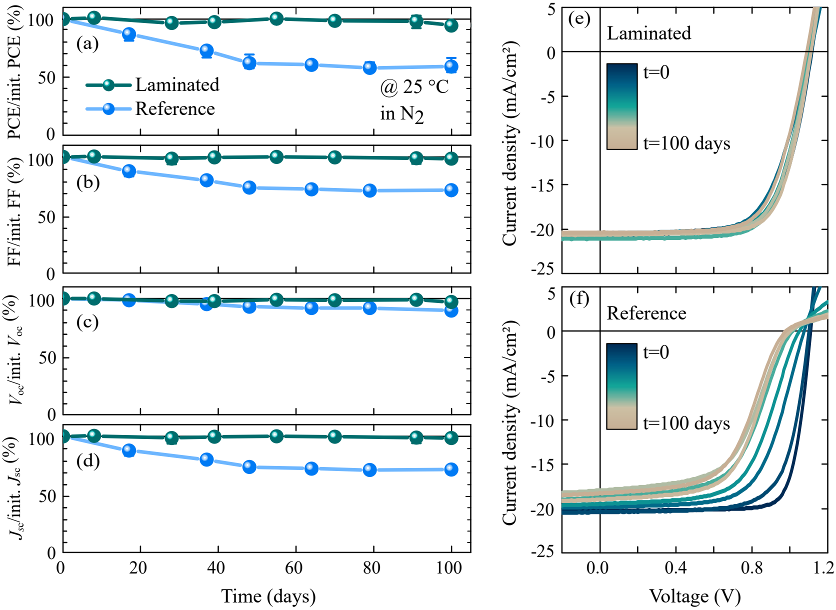

Figure 9.7: Shelf-life stability study of laminated perovskite solar cells (PSCs, 3 devices), in comparison with conventionally produced references (3) with the same architecture. Device architecture is shown in Figure 9.6. a) Evolution of the PCE, b) FF, c) V_{oc}, and d) J_{sc} over 100 days compared to initial values. PSCs were stored according to the ISOS-D-1-I protocol and bi-weekly characterized under 1-Sun.[64] Laminated devices remarkably maintained a stable power output over 100 days. Meanwhile, references degraded rapidly with a PCE decreasing by 20%rel in the first month. e) Evolution of current density-voltage characteristics of a representative laminated PSC, and f) reference. The reference degradation correlates with the emergence of an S-shape over time. Reproduced from reference[120] with the permission of Wiley.

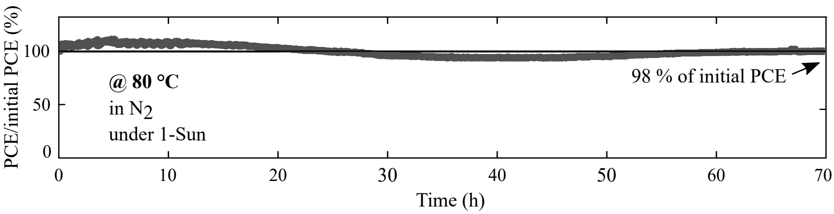

Figure 9.8: Thermal stability study of an eight-month-old laminated perovskite solar cell stored according to the ISOS-D-1-I protocol.[64] The maximum power point tracking is performed at 80 °C under continuous illumination over 70 h in an N_2 atmosphere. The PCE is maintained at 98% of its initial value, demonstrating the good thermal stability of the laminated device. Reproduced from reference[120] with the permission of Wiley.

Laminated perovskite/silicon tandem solar cells

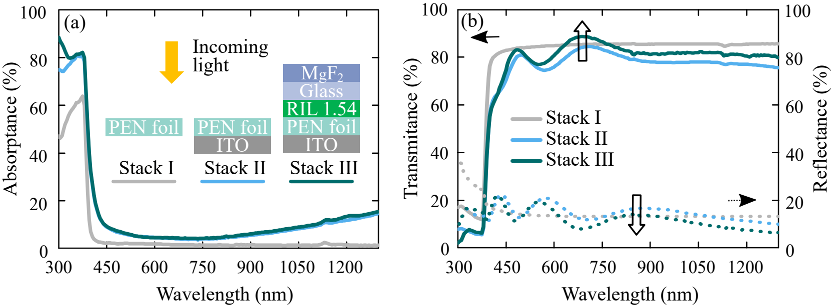

Figure 9.9: Optical characterization of PEN foils with an ITO layer and an MgF_2 anti-reflective coating. a) Absorptance of the layer stack from left to right: PEN foil (stack I), PEN/ITO foil (stack II), and MgF_2/Glass/RIL/PEN/ITO foil (stack III). RIL stands for refractive index liquid, which fills the gap between the PEN foil and glass substrate. PEN foils cause substantial parasitic absorption losses from 300 to 400 nm. The ITO layer additionally causes optical losses at longer wavelengths. b) Transmittance (solid lines) and reflectance (dashed) are displayed for the three layer stacks. The MgF_2 reduces reflective losses caused by the PEN foil at wavelengths from 450 nm. Adapted from reference [120] with the permission of Wiley.

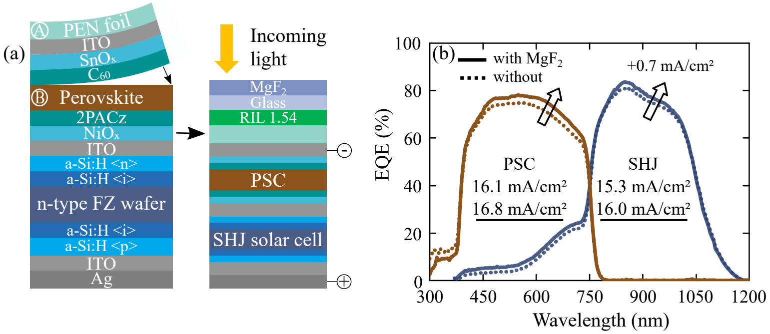

Figure 9.10: Integration of a MgF_2 anti-reflective coating on a laminated perovskite/silicon tandem solar cell. a) Illustration of the device architecture. The glass is used as a substrate to prevent delamination of the PEN foil when contacting probes during characterization. The 1.54 refractive index liquid (RIL) fills the gap between the PEN foil and glass substrate to improve light coupling. b) External quantum efficiency (EQE) measurement indicating an increase of 0.7 mA/cm² in each subcell after deposition of 125 nm MgF_2 on the device front side (solid line). The J_{sc} is given in respective areas for top perovskite (brown) and silicon subcells (blue). Underscored values correspond to the J_{sc} after MgF_2 deposition. Adapted from reference[120] with the permission of Wiley.

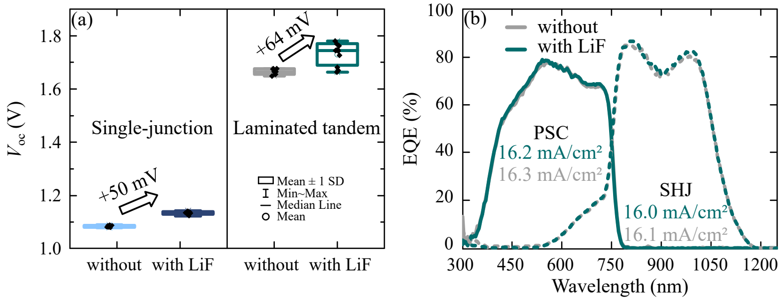

Figure 9.11: Introduction of a LiF passivation layer in laminated monolithic perovskite/silicon tandems. The tandem device architecture comprises IO:H/C_{60}/(LiF) deposited on 30 µm ultra-thin glass superstrates, and NiO_x/2PACz/perovskite deposited on heterojunction silicon (SHJ) subcells. Half-stacks are subsequently laminated at 200 MPa, 90 °C for 5 min. Single-junction devices are conventionally produced as references and comprise glass/ITO/NiO_x/2PACz/perovskite/(LiF)/C_{60}/BCP/Au. a) V_{oc} of single-junction perovskite solar cells (PSCs) and laminated tandems with and without a 1 nm thick LiF layer at the perovskite/C_{60} interface. SD stands for standard deviation. Outlined arrows highlight a V_{oc} improvement of 50 and 64 mV on average in single-junction and laminated tandem devices with surface passivation. b) External quantum efficiency (EQE) characterization of laminated tandems. Integrated J_{sc} values are displayed in respective areas with LiF (green) and without (grey). This additional layer does not impact other J-V characteristics, especially the J_{sc} remaining constant at 16 mA/cm² in both subcells.

Laminated perovskite/CIGS monolithic tandem solar cells

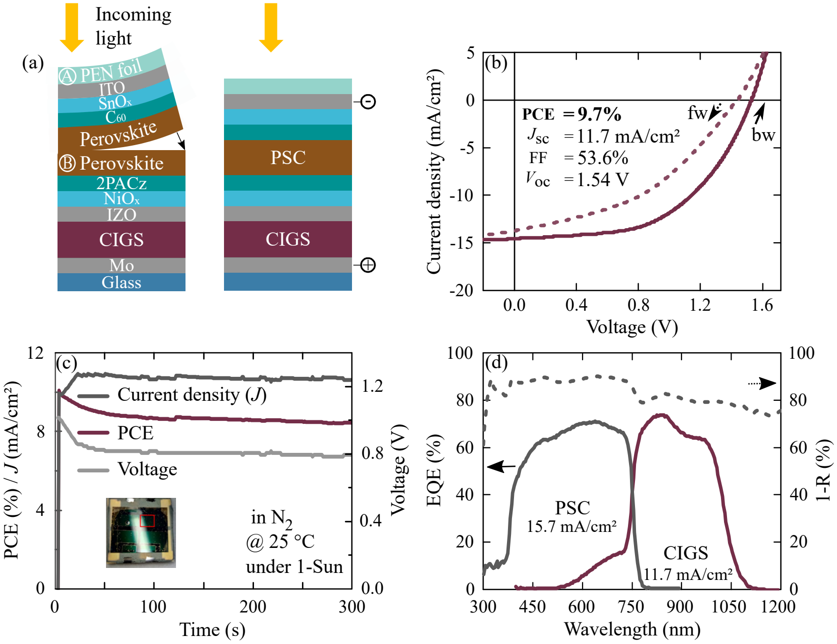

Figure 9.12: Proof-of-concept experiment of a monolithic perovskite/CIGS tandem device fabricated via lamination. a) Illustration of the device architecture and lamination process. The front stack of a n-i-p perovskite solar cell (PSC, A) is hot-pressed on a modified copper indium gallium selenide solar cell (CIGS, b) at 90 °C, 80 MPa for 5 min. b) Current density-voltage (J-V) characteristics of the champion laminated device. Due to uncertainty in the exact active area, J-V characteristics are scaled to integrated J_{sc} from external quantum efficiency (EQE) measurement. c) Maximum power point tracking showing the PCE, current density (J), and voltage over time. A photograph of the laminated tandem is provided in the inset. A red scare highlights the corresponding active area. d) EQE of the champion device and reflectance (R) measurement of an identical layer stack (dashed line). Current densities generated in PSC (grey) and CIGS (purple) solar cells are displayed in respective areas. Experimental details on the device fabrication are available in reference[182].

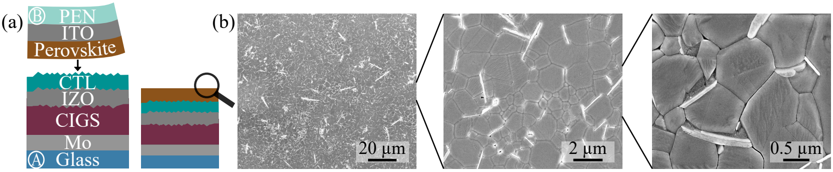

Figure 9.13: Lamination of a perovskite film on a rough copper indium gallium selenide (CIGS) solar cell. a) Illustration of the perovskite layer lamination on a modified CIGS solar cell. The perovskite surface is investigated after peeling off the PEN/ITO foil. b) Scanning electron microscopy (SEM) of the perovskite surface at different scales. The CIGS surface is successfully covered with a recrystallized perovskite absorber, exhibiting large grains. Further SEM images are available in reference[124].

Resources and tools

This work was conducted at the Karlsruhe Institute of Technology (KIT) as part of a collaboration between the Institute of Microstructure Technology (IMT),[1] and the Light Technology Institute (LTI).[2] Thin-films processing and characterizations of perovskite-based solar cells were primarily conducted in the LTI laboratories. Thin-film characterizations were predominantly performed at IMT. Hot-pressing perovskite absorbers and laminating single-junction and tandem solar cells were conducted using the hydraulic press Wum2 at IMT. Further details on the experimental methods employed are provided in Chapter 3. Experimental data presented in this work were processed using the data analysis software Origin. Image J was used to process images, notably AFM and PL images. The technical illustrations in this work were created using the vector graphics editor Inkscape. This dissertation was written using the LaTeX editor Overleaf. Language models were used in the preparation of this work exclusively to correct syntax errors and obtain suggestions for improving text readability, without providing any scientific contribution or supporting the data analysis. References cited in the Bibliography were managed using Citavi and Mendeley.

The financial support was provided by the Helmholtz Young Investigator Group (HYIG) of Prof. Dr. Ulrich W. Paetzold (FKZ VH-NG-1148), POF IV 38.01.04, the Helmholtz Energy Materials Foundry (HEMF), the Federal Ministry for Economic Affairs and Climate Actions (27Plus6 (Grant: 03EE1056B) and TOUCH (Grant: 0324351) projects). The research was supported by the Karlsruhe School of Optics and Photonics (KSOP). The European Union co-funded the study (ERC, Lami-Pero, 101087673). Views and opinions expressed are, however, those of the authors only and do not necessarily reflect those of the European Union or the European Research Council. Neither the European Union nor the granting authority can be held responsible.

---

[1] IMT, Forschungszentrum 240, 76344 Eggenstein-Leopoldshafen, Germany

[2] LTI, Engesserstraße 13, 76131 Karlsruhe, Germany

List of Figures

List of Tables

List of Publications

Peer-reviewed publications

Raphael Schmager, Julie Roger, Jonas A. Schwenzer, Fabian Schackmar, Tobias Abzieher, Mahdi Malekshahi Byranvand, Bahram Abdollahi Nejand, Matthias Worgull, Bryce S. Richards, Ulrich W. Paetzold, *"Laminated perovskite photovoltaics: Enabling novel layer combinations and device architectures"*, in Advanced Functional Materials, 2020, Volume 30, Issue 9, 1907481. R. S. and J. R. contributed equally to this work.

Yang Li, Julie Roger, Isabel Allegro, Jan C. Fischer, Qihao Jin, Ulrich Lemmer, Ian A. Howard, Ulrich W. Paetzold, *"Lasing from laminated quasi 2D/3D perovskite planar heterostructures"*, in Advanced Functional Materials, 2022, Volume 32, Issue 27, 2200772.

Yidenekachew J. Donie, Yingxuan Yuan, Isabel Allegro, Fabian Schackmar, Ihteaz M. Hossain, Robert Huber, Julie Roger, Ulrich W. Paetzold, Guillaume Gomard, Ulrich Lemmer, *"A self-assembly method for tunable and scalable nano-stamps: A versatile approach for imprinting nanostructures"*, in Advanced Materials Technologies, 2022, Volume 7, Issue 6, 2101008.

Julie Roger, Luisa K. Schorn, Minasadat Heydarian, Ahmed Farag, Thomas Feeney, Daniel O. Baumann, Hang Hu, Felix Laufer, Weiyuan Duan, Kaining Ding, Andreas Lambertz, Paul Fassl, Matthias Worgull, Ulrich W. Paetzold, *"Laminated monolithic perovskite/silicon tandem photovoltaics"*, in Advanced Energy Materials, 2022, Volume 12, Issue 27, 2200961.

Daniel O. Baumann, Felix Laufer, Julie Roger, Roja Singh, Mohammad Gholipoor, Ulrich W. Paetzold, *"Repeatable perovskite solar cells through fully automated spin-coating and quenching"*, in ACS Applied Materials and Interfaces, 2024, 16, 54007-54016.

Benjamin Hacene, Nils W. Rosemann, Julie Roger, Xuzheng Liu, Daniel O. Baumann, Ronja Pappenberger, Mohammad Gholipoor, Hannah Racky, Paul Fassl, Ian A. Howard, Ulrich W. Paetzold, *"Imaging of recombination rates and lifetime in perovskite thin film processing"*, in Small Methods, 2025, 2402119.

Yang Li, Shangpu Liu, Thomas Feeney, Julie Roger, Mohammad Gholipoor, Hang Hu, Dewei Zhao, Ian A. Howard, Felix Deschler, Ulrich Lemmer, Ulrich W. Paetzold, *"Electrically-switchable gain in optically pumped* $CsPbBr_3$ *lasers with low threshold at nanosecond pumping"*, in Small, 2025, 2411935.

Patent

Raphael Schmager, Ulrich W. Paetzold, Julie Roger, Paul Fassl, Tobias Abzieher, *"Perowskit-basierte Mehrfachsolarzelle und Verfahren zu ihrer Herstellung"*, Europäische Patentanmeldung EP 22712309.8, international filing date: 24.02.2022.

Conference contributions

Raphael Schmager, Julie Roger (speaker), Jonas Schwenzer, Mahdi Malekshahi Byranvand, Tobias Abzieher, Bryce S. Richards, Ulrich W. Paetzold, *"Flexible and stable perovskite solar cells"*, PSCO conference, 2019, Lausanne (Switzerland). Oral presentation.

Julie Roger (speaker), Luisa K. Schorn, Thomas Feeney, Ahmed Farag, Paul Fassl, Matthias Worgull, Ulrich W. Paetzold, *"Lamination: A novel fabrication route for monolithic perovskite/silicon tandem solar cells"*, Tandem PV workshop, 2020, Freiburg (Germany). Oral presentation.

Julie Roger (speaker), Raphael Schmager, Jonas A. Schwenzer, Fabian Schackmar, Tobias Abzieher, Mahdi Malekshahi Byranvand, Bahram

Abdollahi Nejand, Paul Faßl, Matthias Worgull, Bryce S. Richards, Ulrich W. Paetzold, *“Lamination of perovksite solar cells: A novel route to stable and flexible devices”*, EMRS Spring conference, 2020, online. Oral presentation.

Julie Roger (poster presenter), Raphael Schmager, Jonas A. Schwenzer, Fabian Schackmar, Tobias Abzieher, Mahdi Malekshahi Byranvand, Bahram Abdollahi Nejand, Paul Faßl, Matthias Worgull, Bryce S. Richards, Ulrich W. Paetzold, *“Lamination: A versatile route for stable perovskite photovoltaics”*, EUPVSEC conference, 2020, online. Poster presentation.

Julie Roger (speaker), Luisa K. Schorn, Minasadat Heydarian, Ahmed Farag, Thomas Feeney, Daniel Baumann, Hang Hu, Felix Laufer, Weiyuan Duan, Kaining Ding, Andreas Lambertz, Paul Fassl, Matthias Worgull, Ulrich W. Paetzold, *“Novel lamination approach for fabrication of monolithic perovskite/silicon tandem photovoltaics”*, PVSEC-33 conference, 2022, Nagoya (Japan). Oral presentation.

Julie Roger (poster presenter), Ahmed Farag, Thomas Feeney, Daniel O. Baumann, Hang Hu, Somayeh Moghadamzadeh, Paul Fassl, Matthias Worgull, Ulrich W. Paetzold, *“Monolithic perovskite/silicon tandems fabricated via lamination”*, Tandem PV workshop, 2023, Chambéry (France). Poster presentation.

Julie Roger (speaker), Ahmed Farag, Thomas Feeney, Daniel O. Baumann, Hang Hu, Paul Fassl, Matthias Worgull, Ulrich W. Paetzold, *“Lamination: Alternative fabrication method for monolithic perovskite/ silicon tandem solar cells”*, EUPVSEC conference, 2023, Lissabon (Portugal). Oral presentation.

Supervised master theses

Minasadat Heydarian, *“Laminated perovskite photovoltaics”*, conducted at KIT at the Light Technology Institute (LTI) and Institute of Microstructure Technology (IMT), in cooperation with Freiburg University, January 2021. Examiners: Prof. Dr. Stefan Glunz, and Prof. Dr. Ulrich Lemmer. Supervisors: Prof. Dr. Ulrich W. Paetzold, and Julie Roger.

Luisa K. Schorn, *“Development of a novel lamination process for stable perovskite solar cells and future applications in the field of tandem photovoltaics”*, conducted at LTI and IMT, KIT, January 2022. Examiners: PD Dr. Matthias Worgull, and Prof. Dr. Andreas E. Guber. Supervisors: Prof. Dr. Ulrich W. Paetzold, Julie Roger, and Dr. Ahmed Farag.

Daniel O. Baumann, *“Laminating semi-transparent perovskite solar cells for textured tandem cells”*, conducted at LTI and IMT, KIT, August 2022. Examiners: Prof. Dr. Ulrich W. Paetzold and Prof. Dr. Ulrich Lemmer. Supervisors: Prof. Dr. Ulrich W. Paetzold, and Julie Roger.

Amer Alhomaidi, *“Lamination of perovskite planar heterojunction for lasing application”*, conducted at LTI and IMT, KIT, February 2023. Examiners: Prof. Dr. Ulrich W. Paetzold, and Prof. Dr. Ulrich Lemmer. Supervisors: Prof. Dr. Ulrich W. Paetzold, Dr. Yang Li, and Julie Roger.

Hannah Racky, *“In-situ photoluminescence of hot-pressed perovskite thin films”*, conducted at LTI and IMT, KIT, March 2024. Examiners: Prof. Dr. Ulrich W. Paetzold, and Prof. Dr. Carsten Rockstuhl. Supervisors: Prof. Dr. Ulrich W. Paetzold, Julie Roger, and Benjamin Hacene.

Bibliography

[1] International Energy Agency (IEA), “Net zero by 2050 - roadmap for the global energy sector,” https://www.iea.org/reports/net-zero-by-2050, 2021 (Accessed: 1/17/2025).

[2] K. Keramidas et al., “Global energy and climate outlook 2019: Electrification for the low-carbon transition,” *JRC Publications*, 2020.

[3] Fraunhofer Institute for Solar Energy Systems ISE, “Recent facts about photovoltaics in Germany,” https://www.ise.fraunhofer.de/en/publications/studies/recent-facts-about-pv-in-germany.html, 2024 (Accessed: 1/17/2025).

[4] N. Haegel et al., “Terawatt-scale photovoltaics: Transform global energy,” *Science*, vol. 364, no. 6443, pp. 836–838, 2019.

[5] L. Hernández-Callejo et al., “A review of photovoltaic systems: Design, operation and maintenance,” *Solar Energy*, vol. 188, pp. 426–440, 2019.

[6] Panasonic Newsroom Global, “Panasonic showcases the world’s first manufacturing facility capable of being powered entirely by renewable energy,” https://news.panasonic.com/global/de/stories/1003, 2022 (Accessed: 1/17/2025).

[7] A. Alshahrani et al., “The technical challenges facing the integration of small-scale and large-scale PV systems into the grid: A Critical review,” *Electronics*, vol. 8, no. 12, p. 1443, 2019.

[8] Energy-Charts, “Net installed electricity generation capacity in Germany in 2024,” https://www.energy-charts.info/charts/installed_power/chart.htm?l=en&c=DE&year=2024&expansion=installed_power (Accessed: 1/17/2025).

[9] International Energy Agency, “Climatic rating of photovoltaic modules,” https://iea-pvps.org/key-topics/climatic-rating-of-photovoltaic-modules/ (Accessed: 30/04/2025).

[10] A. Chatzipanagi et al., “Overview of the potential and challenges for agri-photovoltaics in the european union,” *JRC Publications*, 2023.

[11] C. Ballif et al., “Integrated thinking for photovoltaics in buildings,” *Nature Energy*, vol. 3, no. 6, pp. 438–442, 2018.

[12] A. C. Lazaroiu et al., “A comprehensive overview of photovoltaic technologies and their efficiency for climate neutrality,” *Sustainability*, vol. 15, no. 23, p. 16297, 2023.

[13] National Renewable Energy Laboratory (NREL), “Best research-cell efficiency chart,” https://www.nrel.gov/pv/cell-efficiency.html (Accessed: 1/17/2025).

[14] R. Schmager et al., “Laminated perovskite photovoltaics: Enabling novel layer combinations and device architectures,” *Advanced Functional Materials*, p. 1907481, 2020.

[15] D. B. Ritzer et al., “Translucent perovskite photovoltaics for building integration,” *Energy & Environmental Science*, vol. 16, no. 5, pp. 2212–2225, 2023.

[16] H. Eggers et al., “Perovskite solar cells with vivid, angle-invariant, and customizable inkjet-printed colorization for building-integrated photovoltaics,” *Solar RRL*, vol. 6, no. 4, p. 2100897, 2022.

[17] C. Zhou et al., “Flexible perovskite solar cells on ultra-thin stainless-steel with a power-to-weight ratio over 3000 Wkg^{-1},” *Solar RRL*, vol. 8, no. 5, 2024.

[18] T. Ibn-Mohammed et al., “Perovskite solar cells: An integrated hybrid lifecycle assessment and review in comparison with other photovoltaic technologies,” *Renewable and Sustainable Energy Reviews*, vol. 80, pp. 1321–1344, 2017.

[19] T. Jesper Jacobsson et al., "Exploration of the compositional space for mixed lead halogen perovskites for high efficiency solar cells," *Energy & Environmental Science*, vol. 9, no. 5, pp. 1706–1724, 2016.

[20] J. H. Noh et al., "Chemical management for colorful, efficient, and stable inorganic-organic hybrid nanostructured solar cells," *Nano letters*, vol. 13, no. 4, pp. 1764–1769, 2013.

[21] R. Prasanna et al., "Band gap tuning via lattice contraction and octahedral tilting in perovskite materials for photovoltaics," *Journal of the American Chemical Society*, vol. 139, no. 32, pp. 11117–11124, 2017.

[22] J. Im et al., "Antagonism between spin-orbit coupling and steric effects causes anomalous band gap evolution in the perovskite photovoltaic materials $CH_3NH_3Sn_{1-x}Pb_xI_3$," *Journal of Physical Chemistry Letters*, vol. 6, no. 17, pp. 3503–3509, 2015.

[23] F. Hao et al., "Anomalous band gap behavior in mixed sn and pb perovskites enables broadening of absorption spectrum in solar cells," *Journal of the American Chemical Society*, vol. 136, no. 22, pp. 8094–8099, 2014.

[24] A. de Vos et al., "Detailed balance limit of the efficiency of tandem solar cells," *Journal of Physics D: Applied Physics*, vol. 13, no. 5, pp. 839–846, 1980.

[25] Longi, "34.6%! record-breaker longi once again sets a new world efficiency for silicon-perovskite tandem solar cells," https://www.longi.com/en/news/2024-snec-silicon-perovskite-tandem-solar-cells-new-world-efficiency/, 2024 (Accessed: 1/17/2025).

[26] S. Ternes et al., "Correlative in situ multichannel imaging for large-area monitoring of morphology formation in solution-processed perovskite layers," *Solar RRL*, vol. 6, no. 3, p. 2100353, 2022.

[27] D. B. Ritzer et al., “Upscaling of perovskite solar modules: The synergy of fully evaporated layer fabrication and all-laser-scribed interconnections,” *Progress in Photovoltaics*, vol. 30, no. 4, pp. 360–373, 2022.

[28] S. S. Dipta et al., “Encapsulating perovskite solar cells for long-term stability and prevention of lead toxicity,” *Applied Physics Reviews*, vol. 11, no. 2, 2024.

[29] Y. Miao et al., “Green solvent enabled scalable processing of perovskite solar cells with high efficiency,” *Nature Sustainability*, vol. 6, no. 11, pp. 1465–1473, 2023.

[30] Y. Xu et al., “Microencapsulated perovskite crystals via in situ permeation growth from polymer microencapsulation-expansion-contraction strategy: Advancing a record long-term stability beyond 10 000 h for perovskite solar cells,” *Advanced Materials*, vol. 36, no. 18, p. 2313080, 2024.

[31] C. Li et al., “Formability of ABX_3 (X = F, Cl, Br, I) halide perovskites,” *Structural Science, Crystal Engineering and Materials*, vol. 64, no. Pt 6, pp. 702–707, 2008.

[32] W. Travis et al., “On the application of the tolerance factor to inorganic and hybrid halide perovskites: A revised system,” *Chemical science*, vol. 7, no. 7, pp. 4548–4556, 2016.

[33] R. E. Patru et al., “Tetragonal-cubic phase transition and low-field dielectric properties of $CH_3NH_3PbI_3$ crystals,” *Materials*, vol. 14, no. 15, p. 4215, 2021.

[34] M. Saliba et al., “Cesium-containing triple cation perovskite solar cells: Improved stability, reproducibility and high efficiency,” *Energy & Environmental Science*, vol. 9, no. 6, pp. 1989–1997, 2016.

[35] G. E. Eperon et al., “Inorganic caesium lead iodide perovskite solar cells,” *Journal of Materials Chemistry A*, vol. 3, no. 39, pp. 19688–19695, 2015.

[36] P. Brenner et al., "Continuous wave amplified spontaneous emission in phase-stable lead halide perovskites," *Nature Communications*, vol. 10, no. 1, p. 988, 2019.

[37] L. Li et al., "Flexible all-perovskite tandem solar cells approaching 25% efficiency with molecule-bridged hole-selective contact," *Nature Energy*, vol. 7, no. 8, pp. 708–717, 2022.

[38] S. De Wolf et al., "Organometallic halide perovskites: Sharp optical absorption edge and its relation to photovoltaic performance," *Journal of Physical Chemistry Letters*, vol. 5, no. 6, pp. 1035–1039, 2014.

[39] I. Allegro et al., "Distributed feedback lasers by thermal nanoimprint of perovskites using gelatin gratings," *ACS Applied Materials & Interfaces*, vol. 15, no. 6, pp. 8436–8445, 2023.

[40] K. Lin et al., "Perovskite light-emitting diodes with external quantum efficiency exceeding 20%," *Nature*, vol. 562, no. 7726, pp. 245–248, 2018.

[41] V. Sarritzu et al., "Direct or indirect bandgap in hybrid lead halide perovskites?," *Advanced Optical Materials*, vol. 6, no. 10, p. 1701254, 2018.

[42] J. Park et al., "Electronic structure and optical properties of a-$CH_3NH_3PbBr_3$ perovskite single crystal," *Journal of Physical Chemistry Letters*, vol. 6, no. 21, pp. 4304–4308, 2015.

[43] M. A. Green et al., "The emergence of perovskite solar cells," *Nature Photonics*, vol. 8, no. 7, pp. 506–514, 2014.

[44] W. Yin et al., "Unique properties of halide perovskites as possible origins of the superior solar cell performance," *Advanced Materials*, vol. 26, no. 27, pp. 4653–4658, 2014.

[45] J. Chen et al., "Solar cell efficiency exceeding 25% through rb-based perovskitoid scaffold stabilizing the buried perovskite surface," *ACS Energy Letters*, vol. 7, no. 10, pp. 3685–3694, 2022.

[46] C. Luo et al., “Solid-solid chemical bonding featuring targeted defect passivation for efficient perovskite photovoltaics,” *Energy & Environmental Science*, vol. 16, no. 1, pp. 178–189, 2023.

[47] Y. Wu et al., “Stable perovskite solar cells with 25.17% efficiency enabled by improving crystallization and passivating defects synergistically,” *Energy & Environmental Science*, vol. 15, no. 11, pp. 4700–4709, 2022.

[48] X. Liu et al., “Extending the p-conjugated system in spiro-type hole transport material enhances the efficiency and stability of perovskite solar modules,” *Angewandte Chemie International Edition*, vol. 62, no. 29, p. e202304350, 2023.

[49] S. Yu et al., “Homogenized $\mathrm{NiO_x}$ nanoparticles for improved hole transport in inverted perovskite solar cells,” *Science*, vol. 382, no. 6677, pp. 1399–1404, 2023.

[50] Y. Chen et al., “Extended carrier lifetimes and diffusion in hybrid perovskites revealed by hall effect and photoconductivity measurements,” *Nature Communications*, vol. 7, no. 1, p. 12253, 2016.

[51] K. X. Steirer et al., “Defect tolerance in methylammonium lead triiodide perovskite,” *ACS Energy Letters*, vol. 1, no. 2, pp. 360–366, 2016.

[52] J. Kang et al., “High defect tolerance in lead halide perovskite $\mathrm{CsPbBr_3}$,” *Journal of Physical Chemistry Letters*, vol. 8, no. 2, pp. 489–493, 2017.

[53] K. Mertens, “Photovoltaik: Lehrbuch zu Grundlagen, Technologie und Praxis,” *Hanser*, 6th ed., ISBN 978-3-446-47194-8, 2022.

[54] P. Würfel, “Physics of solar cells,” *Wiley*, 3th ed., ISBN 978-3-527-41312-6, 2016.

[55] S. Gharibzadeh et al., “Two birds with one stone: Dual grain-boundary and interface passivation enables >22% efficient inverted

methylammonium-free perovskite solar cells," *Energy & Environmental Science*, vol. 14, no. 11, pp. 5875–5893, 2021.

[56] J. Y. Hyun et al., "Perovskite/silicon tandem solar cells with a V_{oc} of 1784 mV based on an industrially feasible 25 cm^2 TOPCon silicon cell," *ACS Applied Energy Materials*, vol. 5, no. 5, pp. 5449–5456, 2022.

[57] P. Caprioglio et al., "On the relation between the open-circuit voltage and quasi-fermi level splitting in efficient perovskite solar cells," *Advanced Energy Materials*, vol. 9, no. 33, p. 1901631, 2019.

[58] M. Kim et al., "Enhanced electrical properties of Li-salts doped mesoporous TiO_2 in perovskite solar cells," *Joule*, vol. 5, no. 3, pp. 659–672, 2021.

[59] M. Schultes et al., "Sputtered transparent electrodes (IO:H and IZO) with low parasitic near-infrared absorption for perovskite-$Cu(In,Ga)Se_2$ tandem solar cells," *ACS Applied Energy Materials*, vol. 2, no. 11, pp. 7823–7831, 2019.

[60] J. A. Raiford et al., "Atomic layer deposition of vanadium oxide to reduce parasitic absorption and improve stability in n-i-p perovskite solar cells for tandems," *Sustainable Energy & Fuels*, vol. 3, no. 6, pp. 1517–1525, 2019.

[61] N. Tucher et al., "Optical modeling of structured silicon-based tandem solar cells and module stacks," *Optics Express*, vol. 26, no. 18, pp. A761–A768, 2018.

[62] V. Sittinger et al., "Complex refractive indices of Spiro-TTB and C_{60} for optical analysis of perovskite silicon tandem solar cells," *Optics Express*, vol. 30, no. 21, pp. 37957–37970, 2022.

[63] A. Bojar et al., "Optical simulations and optimization of perovskite/CI(G)S tandem solar cells using the transfer matrix method," *Journal of Physics: Energy*, vol. 5, no. 3, p. 035001, 2023.

[64] M. V. Khenkin et al., “Consensus statement for stability assessment and reporting for perovskite photovoltaics based on isos procedures,” *Nature Energy*, vol. 5, no. 1, pp. 35–49, 2020.

[65] Z. Li et al., “Hyperbranched polymer functionalized flexible perovskite solar cells with mechanical robustness and reduced lead leakage,” *Nature Communications*, vol. 14, no. 1, p. 6451, 2023.

[66] F. Cao et al., “Perovskite solar cells with high-efficiency exceeding 25%: A review,” *Energy Materials and Devices*, vol. 2, no. 1, p. 9370018, 2024.

[67] T. Abzieher et al., “From groundwork to efficient solar cells: On the importance of the substrate material in co-evaporated perovskite solar cells,” *Advanced Functional Materials*, vol. 31, no. 42, p. 2104482, 2021.

[68] J. Li et al., “Highly efficient thermally co-evaporated perovskite solar cells and mini-modules,” *Joule*, vol. 4, no. 5, pp. 1035–1053, 2020.

[69] H. Eggers et al., “Inkjet-printed micrometer-thick perovskite solar cells with large columnar grains,” *Advanced Energy Materials*, vol. 10, no. 6, p. 1903184, 2020.

[70] F. Schackmar et al., “Perovskite solar cells with all-inkjet-printed absorber and charge transport layers,” *Advanced Materials Technologies*, vol. 6, no. 2, 2021.

[71] K. Geistert et al., “Controlling thin film morphology formation during gas quenching of slot-die coated perovskite solar modules,” *ACS Applied Materials & Interfaces*, 2023.

[72] K. Xu et al., “Slot-die coated triple-halide perovskites for efficient and scalable perovskite/silicon tandem solar cells,” *ACS Energy Letters*, vol. 7, no. 10, pp. 3600–3611, 2022.

[73] A. S. Subbiah et al., “Enhancing the performance of blade-coated perovskite/silicon tandems via molecular doping and interfacial energy alignment,” *ACS Energy Letters*, vol. 9, no. 2, pp. 727–731, 2024.

[74] B. Chen et al., “Blade-coated perovskites on textured silicon for 26%-efficient monolithic perovskite/silicon tandem solar cells,” *Joule*, vol. 4, no. 4, pp. 850–864, 2020.

[75] J. Warby et al., “Understanding performance limiting interfacial recombination in pin perovskite solar cells,” *Advanced Energy Materials*, vol. 12, no. 12, p. 2103567, 2022.

[76] W. Shockley et al., “Detailed balance limit of efficiency of p-n junction solar cells,” *Journal of Applied Physics*, vol. 32, pp. 510–519, 1961.

[77] Sven. Rühle et al., “Tabulated values of the Shockley-Queisser limit for single junction solar cells,” *Solar Energy*, vol. 130, pp. 139–147, 2016.

[78] T. Tiedje et al., “Limiting efficiency of silicon solar cells,” *IEEE Transactions on Electron Devices*, vol. 31, no. 5, pp. 711–716, 1984.

[79] A. Richter et al., “Reassessment of the limiting efficiency for crystalline silicon solar cells,” *IEEE Journal of Photovoltaics*, vol. 3, no. 4, pp. 1184–1191, 2013.

[80] K. Yoshikawa et al., “Silicon heterojunction solar cell with interdigitated back contacts for a photoconversion efficiency over 26%,” *Nature Energy*, vol. 2, no. 5, pp. 1–8, 2017.

[81] S. V. Boriskina et al., “Exceeding the solar cell Shockley-Queisser limit via thermal up-conversion of low-energy photons,” *Optics Communications*, vol. 314, pp. 71–78, 2014.

[82] T. Trupke et al., “Improving solar cell efficiencies by down-conversion of high-energy photons,” *Journal of Applied Physics*, vol. 92, no. 3, pp. 1668–1674, 2002.

[83] F. Dimroth et al., “Wafer bonded four-junction GaInP/GaAs//-GaInAsP/GaInAs concentrator solar cells with 44.7% efficiency,” *Progress in Photovoltaics*, vol. 22, no. 3, pp. 277–282, 2014.

[84] R. Cariou et al., “III-V-on-silicon solar cells reaching 33% photoconversion efficiency in two-terminal configuration,” *Nature Energy*, vol. 3, no. 4, pp. 326–333, 2018.

[85] R. M. France et al., “Triple-junction solar cells with 39.5% terrestrial and 34.2% space efficiency enabled by thick quantum well superlattices,” *Joule*, vol. 6, no. 5, pp. 1121–1135, 2022.

[86] Z. Zhu et al., “Perovskite tandem solar cells with improved efficiency and stability,” *Journal of Energy Chemistry*, vol. 58, pp. 219–232, 2021.

[87] E. Raza et al., “Review on two-terminal and four-terminal crystalline-silicon/perovskite tandem solar cells; progress, challenges, and future perspectives,” *Energy Reports*, vol. 8, pp. 5820–5851, 2022.

[88] J. P. Mailoa et al., “A 2-terminal perovskite/silicon multijunction solar cell enabled by a silicon tunnel junction,” *Applied Physics Letters*, vol. 106, no. 12, 2015.

[89] E. Köhnen et al., “Highly efficient monolithic perovskite silicon tandem solar cells: Analyzing the influence of current mismatch on device performance,” *Sustainable Energy and Fuels*, vol. 3, no. 8, pp. 1995–2005, 2019.

[90] B. A. Kamino et al., “Low-temperature screen-printed metallization for the scale-up of two-terminal perovskite-silicon tandems,” *ACS Applied Energy Materials*, vol. 2, no. 5, pp. 3815–3821, 2019.

[91] F. Sahli et al., “Improved optics in monolithic perovskite/silicon tandem solar cells with a nanocrystalline silicon recombination junction,” *Advanced Energy Materials*, vol. 8, no. 6, 2018.

[92] P. S. C. Schulze et al., “25.1% high-efficiency monolithic perovskite silicon tandem solar cell with a high bandgap perovskite absorber,” *Solar RRL*, vol. 4, no. 7, p. 2000152, 2020.

[93] J. Werner et al., “Perovskite/silicon tandem solar cells: Marriage of convenience or true love story? - An overview,” *Advanced Materials Interfaces*, vol. 5, no. 1, 2018.

[94] E. Lamanna et al., “Mechanically stacked, two-terminal graphene-based perovskite/silicon tandem solar cell with efficiency over 26%,” *Joule*, vol. 4, no. 4, pp. 865–881, 2020.

[95] G. E. Eperon et al., “Metal halide perovskite tandem and multiple-junction photovoltaics,” *Nature Reviews Chemistry*, vol. 1, no. 12, pp. 1–18, 2017.

[96] M. H. Futscher et al., “Efficiency limit of perovskite/Si tandem solar cells,” *ACS Energy Letters*, vol. 1, no. 4, pp. 863–868, 2016.

[97] N. N. Lal et al., “Perovskite tandem solar cells,” *Advanced Energy Materials*, vol. 7, no. 18, p. 1602761, 2018.

[98] K. Sanglee et al., “Intermediate matching layer for light-induced performance and removable clip-on applications of four-terminal perovskite/silicon heterojunction tandem solar cells,” *Solar Energy Materials and Solar Cells*, vol. 253, p. 112235, 2023.

[99] P. Löper et al., “Organic-inorganic halide perovskite/crystalline silicon four-terminal tandem solar cells,” *Physical Chemistry Chemical Physics*, vol. 17, no. 3, pp. 1619–1629, 2015.

[100] J. Zhou et al., “Mixed tin-lead perovskites with balanced crystallization and oxidation barrier for all-perovskite tandem solar cells,” *Nature Communications*, vol. 15, no. 1, p. 2324, 2024.

[101] Y. Jiang et al., “Optical analysis of perovskite/silicon tandem solar cells,” *Journal of Materials Chemistry C*, vol. 4, no. 24, pp. 5679–5689, 2016.

[102] E. Köhnen et al., “27.9% efficient monolithic perovskite/silicon tandem solar cells on industry compatible bottom cells,” *Solar RRL*, vol. 5, no. 7, p. 2100244, 2021.

[103] J. Tong et al., “Carrier lifetimes of 1 ms in Sn-Pb perovskites enable efficient all-perovskite tandem solar cells,” *Science*, vol. 364, no. 6439, pp. 475–479, 2019.

[104] Y. Yao et al., “Phase-stable wide-bandgap perovskites for four-terminal perovskite/silicon tandem solar cells with over 30% efficiency,” *Small*, vol. 18, no. 38, p. e2203319, 2022.

[105] Y. Xiong et al., “Recent advances in perovskite/Cu(In,Ga)Se_2 tandem solar cells,” *Materials Today Electronics*, vol. 7, p. 100086, 2024.

[106] M. A. Ruiz-Preciado et al., “Monolithic two-terminal perovskite/-CIS tandem solar cells with efficiency approaching 25%,” *ACS Energy Letters*, vol. 7, no. 7, pp. 2273–2281, 2022.

[107] H. Liang et al., “29.9%-efficient, commercially viable perovskite/$CuInSe_2$ thin-film tandem solar cells,” *Joule*, vol. 7, no. 12, pp. 2859–2872, 2023.

[108] BIPM, IEC, IFCC, ILAC, ISO, IUPAC, IUPAP, and OIML, “Evaluation of measurement data — guide to the expression of uncertainty in measurement,” Joint Committee for Guides in Metrology, JCGM 100:2008.

[109] Z. Zhang et al., “Semitransparent perovskite solar cells with an evaporated ultra-thin perovskite absorber,” *Advanced Functional Materials*, p. 2307471, 2023.

[110] T. I. Alanazi et al., “Potassium iodide reduces the stability of triple-cation perovskite solar cells,” *RSC Advances*, vol. 10, no. 66, pp. 40341–40350, 2020.

[111] H. Cheng et al., “Kbf 4 additive for alleviating microstrain, improving crystallinity, and passivating defects in inverted perovskite solar cells,” *Advanced Functional Materials*, vol. 32, no. 36, 2022.

[112] B. Yang et al., “Tightly compacted perovskite laminates on flexible substrates via hot-pressing,” *Applied Sciences*, vol. 10, no. 6, p. 1917, 2020.

[113] J. Xiao et al., “Pressure-assisted $CH_3NH_3PbI_3$ morphology reconstruction to improve the high performance of perovskite solar cells,” *Journal of Materials Chemistry A*, vol. 3, no. 10, pp. 5289–5293, 2015.

[114] W. Kim et al., “Oriented grains with preferred low-angle grain boundaries in halide perovskite films by pressure-induced crystallization,” *Advanced Energy Materials*, vol. 8, no. 10, p. 1702369, 2018.

[115] H. Jung et al., “Adjusted bulk and interfacial properties in highly stable semitransparent perovskite solar cells fabricated by thermocompression bonding between perovskite layers,” *ACS Applied Materials & Interfaces*, vol. 15, no. 26, pp. 31344–31353, 2023.

[116] L. Krückemeier et al., “How to report record open-circuit voltages in lead-halide perovskite solar cells,” *Advanced Energy Materials*, vol. 10, no. 1, p. 1902573, 2020.

[117] F. Fries et al., “Statistical treatment of photoluminescence quantum yield measurements,” *Scientific reports*, vol. 9, no. 1, p. 15638, 2019.

[118] M. Stolterfoht et al., “How to quantify the efficiency potential of neat perovskite films: Perovskite semiconductors with an implied efficiency exceeding 28%,” *Advanced Materials*, vol. 32, no. 17, p. 2000080, 2020.

[119] U. Rau et al., “Efficiency potential of photovoltaic materials and devices unveiled by detailed-balance analysis,” *Physical Review Applied*, vol. 7, no. 4, p. 044016, 2017.

[120] J. Roger et al., “Laminated monolithic perovskite/silicon tandem photovoltaics,” *Advanced Energy Materials*, vol. 12, no. 27, 2022.

[121] Y. Li et al., “Lasing from laminated quasi-2D/3D perovskite planar heterostructures,” *Advanced Functional Materials*, vol. 32, no. 27, p. 2200772, 2022.

[122] Y. J. Donie et al., “A self-assembly method for tunable and scalable nano-stamps: A versatile approach for imprinting nanostructures,” *Advanced Materials Technologies*, vol. 7, no. 6, p. 2101008, 2022.

[123] M. Heydarian, “Laminated perovskite photovoltaics,” Master thesis, Karlsruhe Institute of Technology, LTI, IMT, 2021.

[124] L. K. Schorn, “Development of a novel lamination process for stable perovskite solar cells and future applications in the field of tandem photovoltaics,” Master thesis, Karlsruhe Institute of Technology, LTI, IMT, 2022.

[125] H. Becker et al., “Polymer microfabrication technologies for microfluidic systems,” *Analytical and bioanalytical chemistry*, vol. 390, no. 1, pp. 89–111, 2008.

[126] M. Worgull et al., “Hot embossing of high performance polymers,” *Microsystem Technologies*, vol. 17, no. 4, pp. 585–592, 2011.

[127] M. Worgull et al., “Replication of optical components by hot embossing,” *Proceedings SPIE 7716, Micro-Optics*, p. 771604, 2010.

[128] R. Schmager et al., “Texture of the viola flower for light harvesting in photovoltaics,” *ACS Photonics*, vol. 4, no. 11, pp. 2687–2692, 2017.

[129] A. Roslizar et al., “Hot-embossed microcone-textured fluoropolymer as self-cleaning and anti-reflective photovoltaic module covers,” *Solar Energy Materials and Solar Cells*, vol. 214, p. 110582, 2020.

[130] B. Fritz et al., “Upscaling the fabrication routine of bioreplicated rose petal light harvesting layers for photovoltaic modules,” *Solar Energy*, vol. 201, pp. 666–673, 2020.

[131] O. Bar-On et al., “Micro lasers by scalable lithography of metal-halide perovskites,” *Advanced Materials Technologies*, vol. 3, no. 12, p. 1800212, 2018.

[132] N. Pourdavoud et al., “Room-temperature stimulated emission and lasing in recrystallized cesium lead bromide perovskite thin films,” *Advanced Materials*, vol. 31, no. 39, p. e1903717, 2019.

[133] N. Pourdavoud et al., “Distributed feedback lasers based on $\mathrm{MAPbBr_3}$,” *Advanced Materials Technologies*, vol. 3, no. 4, p. 1700253, 2018.

[134] N. Pourdavoud et al., “Photonic nanostructures patterned by thermal nanoimprint directly into organo-metal halide perovskites,” *Advanced Materials*, vol. 29, no. 12, p. 1605003, 2017.

[135] R. Schmager et al., “Light coupling to quasi-guided modes in nanoimprinted perovskite solar cells,” *Solar Energy Materials and Solar Cells*, vol. 201, p. 110080, 2019.

[136] J. Mao et al., “Novel direct nanopatterning approach to fabricate periodically nanostructured perovskite for optoelectronic applications,” *Advanced Functional Materials*, vol. 27, no. 10, 2017.

[137] H. Wang et al., “Nanoimprinted perovskite nanograting photodetector with improved efficiency,” *ACS Nano*, vol. 10, no. 12, pp. 10921–10928, 2016.

[138] Y. Wang et al., “Diffraction-grated perovskite induced highly efficient solar cells through nanophotonic light trapping,” *Advanced Energy Materials*, vol. 8, no. 12, p. 1702960, 2018.

[139] C. Witt et al., “Impact of pressure and temperature on the compaction dynamics and layer properties of powder-pressed methylammonium lead halide thick films,” *ACS Applied Electronic Materials*, vol. 2, no. 8, pp. 2619–2628, 2020.

[140] S. Shrestha et al., “High-performance direct conversion X-ray detectors based on sintered hybrid lead triiodide perovskite wafers,” *Nature Photonics*, vol. 11, no. 7, pp. 436–440, 2017.

[141] C. Borri et al., “First proof-of-principle of inorganic lead halide perovskites deposition by magnetron-sputtering,” *Nanomaterials*, vol. 10, no. 1, p. 60, 2019.

[142] V. M. Kiyek et al., “Single-source, solvent-free, room temperature deposition of black γ-$CsSnI_3$ films,” *Advanced Materials Interfaces*, vol. 7, no. 11, p. 2000162, 2020.

[143] W. A. Dunlap-Shohl et al., “Interfacial effects during rapid lamination within $MAPbI_3$ thin films and solar cells,” *ACS Applied Energy Materials*, vol. 2, no. 7, pp. 5083–5093, 2019.

[144] B. Ding et al., “Anion exchange-induced crystal engineering via hot-pressing sublimation affording highly efficient and stable perovskite solar cells,” *Solar RRL*, vol. 5, no. 3, p. 2000729, 2021.

[145] O. Y. Gong et al., “High-performing laminated perovskite solar cells by surface engineering of perovskite films,” *Applied Surface Science*, vol. 591, p. 153148, 2022.

[146] L. Tan et al., “Self-encapsulated semi-transparent perovskite solar cells with water-soaked stability and metal-free electrode,” *Organic Electronics*, vol. 48, pp. 308–313, 2017.

[147] C. O. Ramírez Quiroz et al., “Interface molecular engineering for laminated monolithic perovskite/silicon tandem solar cells with 80.4% fill factor,” *Advanced Functional Materials*, vol. 29, no. 40, p. 1901476, 2019.

[148] A. Mayer et al., “Relevance of processing parameters for grain growth of metal halide perovskites with nanoimprint,” *Applied Physics A*, vol. 127, no. 9, pp. 1–18, 2021.

[149] A. Mayer et al., “Upgrading of methylammonium lead halide perovskite layers by thermal imprint,” *Applied Physics A*, vol. 127, no. 4, pp. 1–17, 2021.

[150] S. P. Dunfield et al., “Curtailing perovskite processing limitations via lamination at the perovskite/perovskite interface,” *ACS Energy Letters*, vol. 3, no. 5, pp. 1192–1197, 2018.

[151] A. Tejada et al., “Hybrid perovskite degradation from an optical perspective: A spectroscopic ellipsometry study from the deep ultraviolet to the middle infrared,” *Advanced Optical Materials*, vol. 10, no. 3, 2022.

[152] G. Tumen-Ulzii et al., “Detrimental effect of unreacted PbI_2 on the long-term stability of perovskite solar cells,” *Advanced Materials*, vol. 32, no. 16, p. e1905035, 2020.

[153] M. A. Haque et al., “Processing-performance evolution of perovskite solar cells: From large grain polycrystalline films to single crystals,” *Advanced Energy Materials*, vol. 10, no. 13, p. 1902762, 2020.

[154] S. P. Dunfield et al., “From defects to degradation: A mechanistic understanding of degradation in perovskite solar cell devices and modules,” *Advanced Energy Materials*, vol. 10, no. 26, 2020.

[155] A. Castro-Méndez et al., “The role of grain boundaries in perovskite solar cells,” *Advanced Energy Materials*, vol. 9, no. 38, p. 1901489, 2019.

[156] J. Lee et al., “The role of grain boundaries in perovskite solar cells,” *Materials Today Energy*, vol. 7, pp. 149–160, 2018.

[157] F. Cai et al., “Ionic additive engineering toward high-efficiency perovskite solar cells with reduced grain boundaries and trap density,” *Advanced Functional Materials*, vol. 28, no. 34, p. 1801985, 2018.

[158] M. Kim et al., "Methylammonium chloride induces intermediate phase stabilization for efficient perovskite solar cells," *Joule*, vol. 3, no. 9, pp. 2179–2192, 2019.

[159] Z. Xiao et al., "Solvent annealing of perovskite-induced crystal growth for photovoltaic-device efficiency enhancement," *Advanced Materials*, vol. 26, no. 37, pp. 6503–6509, 2014.

[160] B. Chen et al., "Grain engineering for perovskite/silicon monolithic tandem solar cells with efficiency of 25.4%," *Joule*, vol. 3, no. 1, pp. 177–190, 2019.

[161] X. Ren et al., "Modulating crystal grain size and optoelectronic properties of perovskite films for solar cells by reaction temperature," *Nanoscale*, vol. 8, no. 6, pp. 3816–3822, 2016.

[162] A. M. A. Leguy et al., "Reversible hydration of $CH_3NH_3PbI_3$ in films, single crystals, and solar cells," *Chemistry of Materials*, vol. 27, no. 9, pp. 3397–3407, 2015.

[163] M. Pols et al., "What happens at surfaces and grain boundaries of halide perovskites: Insights from reactive molecular dynamics simulations of $CsPbI_3$," *ACS Applied Materials & Interfaces*, vol. 14, no. 36, pp. 40841–40850, 2022.

[164] T. Han et al., "Mxene-interconnected two-terminal, mechanically-stacked perovskite/silicon tandem solar cell with high efficiency," *Advanced Functional Materials*, 2023.

[165] L. Wang et al., "Annealing engineering in the growth of perovskite grains," *Crystals*, vol. 12, no. 7, p. 894, 2022.

[166] T. Li et al., "Bifacial perovskite solar cells via a rapid lamination process," *ACS Applied Energy Materials*, vol. 3, no. 10, pp. 9493–9497, 2020.

[167] Y. Wang et al., "Pressure-induced phase transformation, reversible amorphization, and anomalous visible light response in organolead

bromide perovskite," *Journal of the American Chemical Society*, vol. 137, no. 34, pp. 11144–11149, 2015.

[168] S. Hsiao et al., "Efficient all-vacuum deposited perovskite solar cells by controlling reagent partial pressure in high vacuum," *Advanced Materials*, vol. 28, no. 32, pp. 7013–7019, 2016.

[169] J. Kong et al., "Perovskite solar cells with enhanced fill factors using polymer-capped solvent annealing," *ACS Applied Energy Materials*, vol. 3, no. 8, pp. 7231–7238, 2020.

[170] B. A. Nejand et al., "Novel solvent-free perovskite deposition in fabrication of normal and inverted architectures of perovskite solar cells," *Scientific reports*, vol. 6, no. 1, p. 33649, 2016.

[171] B. A. Nejand et al., "New scalable cold-roll pressing for post-treatment of perovskite microstructure in perovskite solar cells," *Journal of Physical Chemistry C*, vol. 120, no. 5, pp. 2520–2528, 2016.

[172] M. Rai et al., "Effect of perovskite thickness on electroluminescence and solar cell conversion efficiency," *Journal of Physical Chemistry Letters*, vol. 11, no. 19, pp. 8189–8194, 2020.

[173] J. Wang et al., "Simple solution-processed approach for nanoscale coverage of perovskite on textured silicon surface enabling highly efficient perovskite/Si tandem solar cells," *Energy Technology*, vol. 9, no. 1, p. 2000778, 2021.

[174] M. Jošt et al., "21.6%-efficient monolithic perovskite/Cu(In,Ga)Se_2 tandem solar cells with thin conformal hole transport layers for integration on rough bottom cell surfaces," *ACS Energy Letters*, vol. 4, no. 2, pp. 583–590, 2019.

[175] D. Rueda-Delgado et al., "Solution-processed and evaporated C_{60} interlayers for improved charge transport in perovskite photovoltaics," *Organic Electronics*, vol. 77, p. 105526, 2020.

[176] A. Farag et al., “Evaporated self-assembled monolayer hole transport layers: Lossless interfaces in p-i-n perovskite solar cells,” *Advanced Energy Materials*, vol. 13, no. 8, p. 2203982, 2023.

[177] S. Moghadamzadeh et al., “Triple-cation low-bandgap perovskite thin-films for high-efficiency four-terminal all-perovskite tandem solar cells,” *Journal of Materials Chemistry A*, vol. 8, no. 46, pp. 24608–24619, 2020.

[178] F. Ye et al., “Overcoming C_{60}-induced interfacial recombination in inverted perovskite solar cells by electron-transporting carborane,” *Nature Communications*, vol. 13, no. 1, p. 7454, 2022.

[179] Z. Liu et al., “Reducing perovskite/C_{60} interface losses via sequential interface engineering for efficient perovskite/silicon tandem solar cell,” *Advanced Materials*, vol. 36, no. 8, p. e2308370, 2024.

[180] T. Sherkar et al., “Recombination in perovskite solar cells: Significance of grain boundaries, interface traps, and defect ions,” *ACS Energy Letters*, vol. 2, no. 5, pp. 1214–1222, 2017.

[181] N. Thongprong et al., “Insights into recombination processes from light intensity-dependent open-circuit voltages and ideality factors in planar perovskite solar cells,” *Energy Technology*, vol. 8, no. 5, p. 1901196, 2020.

[182] D. Baumann, “Laminating semi-transparent perovskite solar cells for textured tandem cells,” Master thesis, Karlsruhe Institute of Technology, LTI, IMT, 2022.

[183] M. Saliba et al., “Incorporation of rubidium cations into perovskite solar cells improves photovoltaic performance,” *Science*, vol. 354, no. 6309, pp. 206–209, 2016.

[184] H. Tsai et al., “High-efficiency two-dimensional ruddlesden-popper perovskite solar cells,” *Nature*, vol. 536, no. 7616, pp. 312–316, 2016.

[185] H. Li et al., "Additive engineering to grow micron-sized grains for stable high efficiency perovskite solar cells," *Advanced Science*, vol. 6, no. 18, p. 1901241, 2019.

[186] P. Wu et al., "Mixed cations enabled combined bulk and interfacial passivation for efficient and stable perovskite solar cells," *Nano-Micro Letters*, vol. 15, no. 1, p. 114, 2023.

[187] T. Abzieher et al., "Electron-beam-evaporated nickel oxide hole transport layers for perovskite-based photovoltaics," *Advanced Energy Materials*, vol. 9, no. 12, p. 1802995, 2019.

[188] Q. Jiang et al., "SnO_2: A wonderful electron transport layer for perovskite solar cells," *Small*, vol. 14, no. 31, p. 1801154, 2018.

[189] S. Gharibzadeh et al., "Record open-circuit voltage wide-bandgap perovskite solar cells utilizing 2D/3D perovskite heterostructure," *Advanced Energy Materials*, vol. 9, no. 21, p. 1803699, 2019.

[190] J. Peng et al., "A universal double-side passivation for high open-circuit voltage in perovskite solar cells: Role of carbonyl groups in poly(methyl methacrylate)," *Advanced Energy Materials*, vol. 8, no. 30, p. 1801208, 2018.

[191] K. Liu et al., "Reducing sputter induced stress and damage for efficient perovskite/silicon tandem solar cells," *Journal of Materials Chemistry A*, vol. 10, no. 3, pp. 1343–1349, 2022.

[192] K. Lee et al., "Thickness effects of thermally evaporated C_{60} thin films on regular-type $CH_3NH_3PbI_3$ based solar cells," *Solar Energy Materials and Solar Cells*, vol. 164, pp. 13–18, 2017.

[193] D. Rueda Delgado, "Charge carrier dynamics and interfaces in perovskite solar cells," Dissertation, Karlsruhe Institute of Technology, LTI, 2019.

[194] G. E. Eperon et al., "Neutral color semitransparent microstructured perovskite solar cells," *ACS Nano*, vol. 8, no. 1, pp. 591–598, 2014.

[195] A. Ghaffari et al., “Lamination methods for the fabrication of perovskite and organic photovoltaics,” *Materials horizons*, vol. 9, no. 10, pp. 2473–2495, 2022.

[196] H. Wei et al., “Free-standing flexible carbon electrode for highly efficient hole-conductor-free perovskite solar cells,” *Carbon*, vol. 93, pp. 861–868, 2015.

[197] R. Ishikawa et al., “Perovskite/graphene solar cells without a hole-transport layer,” *ACS Applied Energy Materials*, vol. 2, no. 1, pp. 171–175, 2019.

[198] G. A. Sepalage et al., “Can laminated carbon challenge gold? Toward universal, scalable, and low-cost carbon electrodes for perovskite solar cells,” *Advanced Materials Technologies*, 2021.

[199] H. Zhang et al., “Vacuum-free fabrication of high-performance semitransparent perovskite solar cells via e-glue assisted lamination process,” *Science China Chemistry*, vol. 62, no. 7, pp. 875–882, 2019.

[200] D. Bryant et al., “A transparent conductive adhesive laminate electrode for high-efficiency organic-inorganic lead halide perovskite solar cells,” *Advanced Materials*, vol. 26, no. 44, pp. 7499–7504, 2014.

[201] Z. Li et al., “Laminated carbon nanotube networks for metal electrode-free efficient perovskite solar cells,” *ACS Nano*, vol. 8, no. 7, pp. 6797–6804, 2014.

[202] H. Zhang et al., “Self-adhesive macroporous carbon electrodes for efficient and stable perovskite solar cells,” *Advanced Functional Materials*, vol. 28, no. 39, pp. 1–8, 2018.

[203] I. Yun et al., “Transferable transparent electrodes of liquid metals for bifacial perovskite solar cells and heaters,” *Nano Energy*, vol. 93, no. 106857, 2022.

[204] G. Jeong et al., “Highly efficient self-encapsulated flexible semitransparent perovskite solar cells via bifacial cation exchange,” *ACS Applied Materials & Interfaces*, 2022.

[205] D. Wu et al., “Self-encapsulated wearable perovskite photovoltaics via lamination process and its biomedical application,” *iScience*, vol. 26, no. 7, p. 107248, 2023.

[206] S. K. Yadavalli et al., “Lamination of 21% efficient perovskite solar cells with independent process control of transport layers and interfaces,” *ACS Applied Materials & Interfaces*, vol. 16, no. 13, pp. 16040–16049, 2024.

[207] X. Li et al., “Fully printable organic and perovskite solar cells with transfer-printed flexible electrodes,” *ACS Applied Materials and Interfaces*, vol. 9, no. 22, pp. 18730–18738, 2017.

[208] A. D. Sheikh et al., “Effects of high temperature and thermal cycling on the performance of perovskite solar cells: Acceleration of charge recombination and deterioration of charge extraction,” *ACS Applied Materials & Interfaces*, vol. 9, no. 40, pp. 35018–35029, 2017.

[209] T. Abzieher et al., “Efficient all-evaporated pin-perovskite solar cells: A promising approach toward industrial large-scale fabrication,” *IEEE Journal of Photovoltaics*, vol. 9, no. 5, pp. 1249–1257, 2019.

[210] K. Weiß et al., “Accelerated aging tests vs field performance of PV modules,” *Progess in Energy*, vol. 4, no. 4, p. 042009, 2022.

[211] J. Kim et al., “An effective method of predicting perovskite solar cell lifetime-case study on planar $CH_3NH_3PbI_3$ and $HC(NH_2)_2PbI_3$ perovskite solar cells and hole transfer materials of Spiro-OMeTAD and PTAA,” *Solar Energy Materials and Solar Cells*, vol. 162, pp. 41–46, 2017.

[212] X. Zhao et al., “Accelerated aging of all-inorganic, interface-stabilized perovskite solar cells,” *Science*, vol. 377, no. 6603, pp. 307–310, 2022.

[213] Y. C. Kim et al., “Engineering interface structures between lead halide perovskite and copper phthalocyanine for efficient and stable perovskite solar cells,” *Energy & Environmental Science*, vol. 10, no. 10, pp. 2109–2116, 2017.

[214] N. Arora et al., “Perovskite solar cells with CuSCN hole extraction layers yield stabilized efficiencies greater than 20%,” *Science*, vol. 358, no. 6364, pp. 768–771, 2017.

[215] S. Sajid et al., “Breakthroughs in NiO_x-HTMs towards stable, low-cost and efficient perovskite solar cells,” *Nano Energy*, vol. 51, pp. 408–424, 2018.

[216] J. Tirado et al., “Air-stable n-i-p planar perovskite solar cells using nickel oxide nanocrystals as sole hole-transporting material,” *ACS Applied Energy Materials*, vol. 2, no. 7, pp. 4890–4899, 2019.

[217] B. Gil et al., “Design of SnO_2 electron transport layer in perovskite solar cells to achieve 2000 h stability under 1 Sun illumination and 85 °C,” *Advanced Materials Interfaces*, vol. 10, no. 11, 2023.

[218] K. A. Bush et al., “23.6%-efficient monolithic perovskite/silicon tandem solar cells with improved stability,” *Nature Energy*, vol. 2, no. 4, pp. 1–7, 2017.

[219] B. A. Nejand et al., “New physical deposition approach for low cost inorganic hole transport layer in normal architecture of durable perovskite solar cells,” *ACS Applied Materials & Interfaces*, vol. 7, no. 39, pp. 21807–21818, 2015.

[220] M. Imran et al., “Role of annealing temperature of nickel oxide (NiO_x) as hole transport layer in work function alignment with perovskite,” *Applied Physics A*, vol. 127, no. 2, pp. 1–8, 2021.

[221] P. Wu et al., “Advances in SnO_2 -based perovskite solar cells: From preparation to photovoltaic applications,” *Journal of Materials Chemistry A*, vol. 9, no. 35, pp. 19554–19588, 2021.

[222] Y. Yang et al., “Laminating fabrication of bifacial organic-inorganic perovskite solar cells,” *International Journal of Photoenergy*, vol. 2020, pp. 1–8, 2020.

[223] H. Cheng et al., “Towards cost-efficient and stable perovskite solar cells and modules: Utilization of self-assembled monolayers,” *Materials Chemistry Frontiers*, 2023.

[224] H. Wang et al., “Bifacial, color-tunable semitransparent perovskite solar cells for building-integrated photovoltaics,” *ACS Applied Materials & Interfaces*, vol. 12, no. 1, pp. 484–493, 2020.

[225] J. Werner et al., “Sputtered rear electrode with broadband transparency for perovskite solar cells,” *Solar Energy Materials and Solar Cells*, vol. 141, pp. 407–413, 2015.

[226] M. Najafi et al., “Highly efficient and stable semi-transparent p-i-n planar perovskite solar cells by atmospheric pressure spatial atomic layer deposited ZnO,” *Solar RRL*, vol. 2, no. 10, p. 1800147, 2018.

[227] F. Sahli et al., “Fully textured monolithic perovskite/silicon tandem solar cells with 25.2% power conversion efficiency,” *Nature Materials*, vol. 17, no. 9, pp. 820–826, 2018.

[228] B. Yu et al., “Impermeable atomic layer deposition for sputtering buffer layer in efficient semi-transparent and tandem solar cells via activating unreactive substrate,” *Advanced Materials*, vol. 35, no. 5, p. e2202447, 2023.

[229] S. Lee et al., “Photon recycling in halide perovskite solar cells for higher efficiencies,” *MRS Bulletin*, vol. 45, no. 6, pp. 439–448, 2020.

[230] B. T. Feleki et al., “p-i-n perovskite solar cells on steel substrates,” *ACS Applied Energy Materials*, vol. 5, no. 6, pp. 6709–6715, 2022.

[231] T. He et al., “A tough and high-performance transparent electrode from a scalable and transfer-free method,” *ACS Nano*, vol. 8, no. 5, pp. 4782–4789, 2014.

[232] A. J. Bett et al., “Semi-transparent perovskite solar cells with ITO directly sputtered on Spiro-OMeTAD for tandem applications,” *ACS Applied Materials & Interfaces*, vol. 11, no. 49, pp. 45796–45804, 2019.

[233] P. Tockhorn et al., “Improved quantum efficiency by advanced light management in nanotextured solution-processed perovskite solar cells,” *ACS Photonics*, vol. 7, no. 9, pp. 2589–2600, 2020.

[234] D. Yang et al., “Stable efficiency exceeding 20.6% for inverted perovskite solar cells through polymer-optimized pcbm electron-transport layers,” *Nano letters*, vol. 19, no. 5, pp. 3313–3320, 2019.

[235] K. Zhang et al., “Fullerenes and derivatives as electron transport materials in perovskite solar cells,” *Science China Chemistry*, vol. 60, no. 1, pp. 144–150, 2017.

[236] L. Calió et al., “Hole-transport materials for perovskite solar cells,” *Angewandte Chemie International Edition*, vol. 55, no. 47, pp. 14522–14545, 2016.

[237] J. Correa-Baena et al., “Identifying and suppressing interfacial recombination to achieve high open-circuit voltage in perovskite solar cells,” *Energy & Environmental Science*, vol. 10, no. 5, pp. 1207–1212, 2017.

[238] W. Song et al., “Improving the morphology stability of Spiro-OMeTAD films for enhanced thermal stability of perovskite solar cells,” *ACS Applied Materials & Interfaces*, vol. 13, no. 37, pp. 44294–44301, 2021.

[239] Y. Wang et al., “PTAA as efficient hole transport materials in perovskite solar cells: A review,” *Solar RRL*, vol. 6, no. 8, 2022.

[240] M. Saliba et al., “How to make over 20% efficient perovskite solar cells in regular (n-i-p) and inverted (p-i-n) architectures,” *Chemistry of Materials*, vol. 30, no. 13, pp. 4193–4201, 2018.

[241] H. Lai et al., “High-performance flexible all-perovskite tandem solar cells with reduced V_{oc} -deficit in wide-bandgap subcell,” *Advanced Energy Materials*, vol. 12, no. 45, 2022.

[242] Q. Li et al., “Efficient perovskite solar cells with pressing transferred top metal electrodes,” *Materials Letters*, vol. 301, no. 130244, 2021.

[243] H. Zhang et al., “Laminated high-performance semi-transparent perovsktie solar cells: Enabled by sticky polyethyleminine as glue,” *Organic Electronics*, vol. 100, p. 106352, 2022.

[244] B. Roose et al., “Critical assessment of the use of excess lead iodide in lead halide perovskite solar cells,” *Journal of Physical Chemistry Letters*, vol. 11, no. 16, pp. 6505–6512, 2020.

[245] J. Kim et al., “The role of intrinsic defects in methylammonium lead iodide perovskite,” *Journal of Physical Chemistry Letters*, vol. 5, no. 8, pp. 1312–1317, 2014.

[246] C. W. Jang et al., “Lamination-produced semi-transparent/flexible perovskite solar cells with doped-graphene anode and cathode,” *Journal of Alloys and Compounds*, vol. 775, pp. 905–911, 2019.

[247] N. K. Rana et al., “Defect passivation and fabrication of stable large-area (2.0 cm^2) perovskite solar cells with cost-effective metal contacts,” *ACS Applied Electronic Materials*, vol. 6, no. 5, pp. 3325–3336, 2024.

[248] S. S. Dipta et al., “Highly efficient double-side-passivated perovskite solar cells for reduced degradation and low photovoltage loss,” *Solar Energy Materials and Solar Cells*, vol. 266, p. 112655, 2024.

[249] Y. Yang et al., “High performance carbon-based planar perovskite solar cells by hot-pressing approach,” *Solar Energy Materials and Solar Cells*, vol. 210, no. 110517, 2020.

[250] F. H. Isikgor et al., “Scaling-up perovskite solar cells on hydrophobic surfaces,” *Nano Energy*, vol. 81, p. 105633, 2021.

[251] L. Shi et al., "Gas chromatography-mass spectrometry analyses of encapsulated stable perovskite solar cells," *Science*, vol. 368, no. 6497, 2020.

[252] J. C. Yu et al., "High-performance and stable semi-transparent perovskite solar cells through composition engineering," *Advanced Science*, vol. 9, no. 22, p. e2201487, 2022.

[253] S. Wang et al., "High-performance perovskite solar cells with large grain-size obtained by using the lewis acid-base adduct of thiourea," *Solar RRL*, vol. 2, no. 6, p. 1800034, 2018.

[254] P. Mariani et al., "Low-temperature strain-free encapsulation for perovskite solar cells and modules passing multifaceted accelerated ageing tests," *Nature Communications*, vol. 15, p. 4552, 2024.

[255] X. Lu et al., "Dynamic reversible oxidation-reduction of iodide ions for operationally stable perovskite solar cells under ISOS-L-3 protocol," *Advanced Materials*, vol. 36, no. 25, p. 2400852, 2024.

[256] A. Chauhan et al., "Degradation in perovskite solar cells stored under different environmental conditions," *Journal of Physics D: Applied Physics*, vol. 50, no. 32, p. 325105, 2017.

[257] K. Chatzimanolis et al., "Inverted perovskite solar cells with enhanced lifetime and thermal stability enabled by a metallic tantalum disulfide buffer layer," *Nanoscale Advances*, vol. 3, pp. 3124–3135, 2021.

[258] Q. Jiang et al., "Towards linking lab and field lifetimes of perovskite solar cells," *Nature*, vol. 623, pp. 313–318, 2023.

[259] Y. Han et al., "Degradation observations of encapsulated planar $CH_3NH_3PbI_3$ perovskite solar cells at high temperatures and humidity," *J. Mater. Chem. A*, vol. 3, no. 15, pp. 8139–8147, 2015.

[260] R. A. Kerner et al., "Low threshold voltages electrochemically drive gold migration in halide perovskite devices," *ACS Energy Letters*, vol. 5, no. 11, pp. 3352–3356, 2020.

[261] S. Cacovich et al., “Gold and iodine diffusion in large area perovskite solar cells under illumination,” *Nanoscale*, vol. 9, no. 14, pp. 4700–4706, 2017.

[262] N. N. Shlenskaya et al., “Light-induced reactivity of gold and hybrid perovskite as a new possible degradation mechanism in perovskite solar cells,” *Journal of Materials Chemistry A*, vol. 6, no. 4, pp. 1780–1786, 2018.

[263] C. Besleaga et al., “Iodine migration and degradation of perovskite solar cells enhanced by metallic electrodes,” *Journal of Physical Chemistry Letters*, vol. 7, no. 24, pp. 5168–5175, 2016.

[264] G. A. Sepalage et al., “Can laminated carbon challenge gold? Toward universal, scalable, and low-cost carbon electrodes for perovskite solar cells,” *Advanced Materials Technologies*, vol. 7, no. 6, p. 2101148, 2022.

[265] W. Gaynor et al., “Fully solution-processed inverted polymer solar cells with laminated nanowire electrodes,” *ACS Nano*, vol. 4, no. 1, pp. 30–34, 2010.

[266] C. Shimada et al., “Viscous conductive glue layer in semitransparent polymer-based solar cells fabricated by a lamination process,” *ACS Applied Materials and Interfaces*, vol. 5, no. 21, pp. 11087–11092, 2013.

[267] X. L. Trinh et al., “Fully solution-processed perovskite solar cells fabricated by lamination process with silver nanoparticle film as top electrode,” *Energy Reports*, vol. 6, pp. 1297–1303, 2020.

[268] X. Hu et al., “Air and thermally stable perovskite solar cells with CVD-graphene as the blocking layer,” *Nanoscale*, vol. 9, no. 24, pp. 8274–8280, 2017.

[269] F. Meng et al., “Ultra-low-cost coal-based carbon electrodes with seamless interfacial contact for effective sandwich-structured perovskite solar cells,” *Carbon*, vol. 145, pp. 290–296, 2019.

[270] J. H. Heo et al., “Semitransparent $FAPbI_{3\text{-}x}Br_x$ perovskite solar cells stable under simultaneous damp heat (85 °C/85%) and 1 Sun light soaking,” *Advanced Materials Technologies*, vol. 4, no. 3, 2019.

[271] S. Khatoon et al., “Perovskite solar cell’s efficiency, stability and scalability: A review,” *Materials Science for Energy Technologies*, vol. 6, pp. 437–459, 2023.

[272] Z. Zhang et al., “Size-tunable MoS_2 nanosheets for controlling the crystal morphology and residual stress in sequentially deposited perovskite solar cells with over 22.5% efficiency,” *Journal of Materials Chemistry A*, vol. 10, no. 7, pp. 3605–3617, 2022.

[273] H. Bioki et al., “Improved morphology, structure and optical properties of $CH_3NH_3PbI_3$ film via hq additive in PbI_2 precursor solution for efficient and stable mesoporous perovskite solar cells,” *Synthetic Metals*, vol. 283, 2022.

[274] S. Sidhik et al., “Modulating the grain size, phase and optoelectronic quality of perovskite films with cesium iodide for high-performance solar cells,” *Journal of Materials Chemistry C*, vol. 6, no. 29, pp. 7880–7889, 2018.

[275] D. B. Khadka et al., “Insights into accelerated degradation of perovskite solar cells under continuous illumination driven by thermal stress and interfacial junction,” *ACS Applied Energy Materials*, vol. 4, no. 10, pp. 11121–11132, 2021.

[276] D. R. Ceratti et al., “Self-healing inside $APbBr_3$ halide perovskite crystals,” *Advanced Materials*, vol. 30, no. 10, 2018.

[277] E. J. Juarez-Perez et al., “Photodecomposition and thermal decomposition in methylammonium halide lead perovskites and inferred design principles to increase photovoltaic device stability,” *Journal of Materials Chemistry A*, vol. 6, no. 20, pp. 9604–9612, 2018.

[278] J. Lee et al., “Graphene interfacial diffusion barrier between CuSCN and Au layers for stable perovskite solar cells,” *Carbon*, vol. 157, pp. 731–740, 2020.

[279] P. Docampo et al., “Obviating the requirement for oxygen in SnO_2-based solid-state dye-sensitized solar cells,” *Nanotechnology*, vol. 22, no. 22, p. 225403, 2011.

[280] K. Domanski et al., “Not all that glitters is gold: Metal-migration-induced degradation in perovskite solar cells,” *ACS Nano*, vol. 10, no. 6, pp. 6306–6314, 2016.

[281] K. Aitola et al., “High temperature-stable perovskite solar cell based on low-cost carbon nanotube hole contact,” *Advanced Materials*, vol. 29, no. 17, p. 1606398, 2017.

[282] R. Schmager, U. W. Paetzold, J. Roger, P. Fassl, and T. Abzieher, “Perowskit-basierte mehrfachsolarzelle und verfahren zu ihrer herstellung,” EP 22712309.8, international filing date: 24.02.2022.

[283] Z. J. Yu et al., “Techno-economic viability of silicon-based tandem photovoltaic modules in the United States,” *Nature Energy*, vol. 3, no. 9, pp. 747–753, 2018.

[284] S. E. Sofia et al., “Roadmap for cost-effective, commercially-viable perovskite silicon tandems for the current and future PV market,” *Sustainable Energy and Fuels*, vol. 4, no. 2, pp. 852–862, 2020.

[285] S. Mariotti et al., “Interface engineering for high-performance, triple-halide perovskite-silicon tandem solar cells,” *Science*, vol. 381, no. 6653, pp. 63–69, 2023.

[286] S. Albrecht et al., “Towards optical optimization of planar monolithic perovskite/silicon-heterojunction tandem solar cells,” *Journal of Optics*, vol. 18, no. 6, 2016.

[287] E. Aydin et al., “Ligand-bridged charge extraction and enhanced quantum efficiency enable efficient n-i-p perovskite/silicon tandem

solar cells," *ACSEnergy & Environmental Science*, vol. 14, no. 8, pp. 7804–7810, 2021.

[288] F. Lang et al., "Revealing fundamental efficiency limits of monolithic perovskite/silicon tandem photovoltaics through subcell characterization," *ACS Energy Letters*, vol. 6, p. 43, 2021.

[289] K. A. Bush et al., "Minimizing current and voltage losses to reach 25% efficient monolithic two-terminal perovskite-silicon tandem solar cells," *ACS Energy Letters*, vol. 3, no. 9, pp. 2173–2180, 2018.

[290] C. Battaglia et al., "High-efficiency crystalline silicon solar cells: status and perspectives," *Energy & Environmental Science*, vol. 9, p. 1552, 2016.

[291] I. Y. Choi et al., "Two-terminal mechanical perovskite/silicon tandem solar cells with transparent conductive adhesives," *Nano Energy*, vol. 65, p. 104044, 2019.

[292] E. Alvianto et al., "Sustainable manufacturing of perovskite-CIGS tandem solar cells through lamination with metal-free transparent conductive adhesives," *ACS Energy Letters*, no. 9, p. 2057–2064, 2024.

[293] H. Hu et al., "Laminated two-terminal all-perovskite tandem solar cells with transparent conductive adhesives," *ACS Applied Materials & Interfaces*, vol. 17, no. 5, pp. 4377–4390, 2021.

[294] H. Kanda et al., "Interface optoelectronics engineering for mechanically stacked tandem solar cells based on perovskite and silicon," *ACS Applied Materials and Interfaces*, vol. 8, no. 49, pp. 33553–33561, 2016.

[295] H. Kanda et al., "Facile fabrication method of small-sized crystal silicon solar cells for ubiquitous applications and tandem device with perovskite solar cells," *Materials Today Energy*, vol. 7, pp. 190–198, 2018.

[296] A. Agresti et al., “Highly efficient 2D materials engineered perovskite/Si tandem bifacial cells beyond 29%,” *IEEE Journal of Photovoltaics*, vol. 12, no. 6, pp. 1273–1281, 2022.

[297] W. Zhu et al., “Homogeneous crystallization of MA-free, wide-bandgap perovskite films via self-assembled monolayer capping for laminated silicon/perovskite tandem solar cells,” *Chemical Engineering Journal*, vol. 500, p. 156798, 2024.

[298] K. Aitola et al., “Encapsulation of commercial and emerging solar cells with focus on perovskite solar cells,” *Solar Energy*, vol. 237, pp. 264–283, 2022.

[299] C. Messmer et al., “Optimized front tco and metal grid electrode for module-integrated perovskite-silicon tandem solar cells,” *Progress in Photovoltaics*, vol. 30, no. 4, pp. 374–383, 2022.

[300] N. Shrivastav et al., “Investigations aimed at producing 33% efficient perovskite-silicon tandem solar cells through device simulations,” *RSC Advances*, vol. 11, no. 59, pp. 37366–37374, 2021.

[301] M. Heydarian et al., “Maximizing current density in monolithic perovskite silicon tandem solar cells,” *Solar RRL*, vol. 7, no. 7, 2023.

[302] P. Tockhorn et al., “Nano-optical designs for high-efficiency monolithic perovskite-silicon tandem solar cells,” *Nature Nanotechnology*, vol. 17, no. 11, pp. 1214–1221, 2022.

[303] S. Manzoor et al., “Improved light management in planar silicon and perovskite solar cells using PDMS scattering layer,” *Solar Energy Materials and Solar Cells*, vol. 173, pp. 59–65, 2017.

[304] Y. Hou et al., “Efficient tandem solar cells with solution-processed perovskite on textured crystalline silicon,” *Science*, vol. 367, no. 6482, pp. 1135–1140, 2020.

[305] A. Al-Ashouri et al., “Monolithic perovskite/silicon tandem solar cell with $>$29% efficiency by enhanced hole extraction,” *Science*, vol. 370, no. 6522, pp. 1300–1309, 2020.

[306] M. De Bastiani et al., “Efficient bifacial monolithic perovskite/silicon tandem solar cells via bandgap engineering,” *Nature Energy 2017 2:5*, vol. 6, no. 2, pp. 167–175, 2021.

[307] K. A. Bush et al., “Compositional engineering for efficient wide band gap perovskites with improved stability to photoinduced phase segregation,” *ACS Energy Letters*, vol. 3, no. 2, pp. 428–435, 2018.

[308] F. Gota et al., “Energy yield advantages of three-terminal perovskite-silicon tandem photovoltaics,” *Joule*, vol. 4, no. 11, pp. 2387–2403, 2020.

[309] M. Singh et al., “Comparing optical performance of a wide range of perovskite/silicon tandem architectures under real-world conditions,” *Nanophotonics*, vol. 10, no. 8, pp. 2043–2057, 2021.

[310] M. Stolterfoht et al., “Visualization and suppression of interfacial recombination for high-efficiency large-area pin perovskite solar cells,” *Nature Energy*, vol. 3, no. 10, pp. 847–854, 2018.

[311] D. Menzel et al., “Field effect passivation in perovskite solar cells by a LiF interlayer,” *Advanced Energy Materials*, vol. 12, no. 30, 2022.

[312] D. Saranin et al., “Transition metal carbides (MXenes) for efficient NiO-based inverted perovskite solar cells,” *Nano Energy*, vol. 82, p. 105771, 2021.

[313] Fujifilm, “Prescale - Pressure measurement film,” https://www.fujifilm.com/de/en/business/inspection/measurement-film/prescale (Accessed: 1/17/2025).

[314] Schott AG, “Technical details of AF 32,” https://www.schott.com/en-gr/products/af-32-eco-p1000308/technical-details (Accessed: 1/17/2025).

[315] M. Alexe et al., “Wafer bonding: Applications and technology,” *Springer*, ISBN 978-3-540-21049-8, 2004.

[316] S. Essig, “Entwicklung von GaInP/GaAs/Si-Mehrfachsolarzellen mittels Wafer-Bonding,” Dissertation, Universität Konstanz, 2014.

[317] L. Rakocevic et al., “Loss analysis in perovskite photovoltaic modules,” *Solar RRL*, vol. 3, no. 12, 2019.

[318] E. Y. Choi et al., “Development of moisture-proof polydimethylsiloxane/aluminum oxide film and stability improvement of perovskite solar cells using the film,” *RSC Advances*, vol. 9, no. 21, pp. 11737–11744, 2019.

[319] T. R. Klein et al., “Lamination of transparent conductive adhesives for tandem solar cell applications,” *Journal of Physics D: Applied Physics*, vol. 54, no. 18, p. 184002, 2021.

[320] R. Witteck et al., “Reducing thermal degradation of perovskite solar cells during vacuum lamination by internal diffusion barriers,” *ACS Applied Energy Materials*, vol. 7, no. 22, p. 10750–10757, 2024.

[321] S. Garner et al., “Ultra-slim flexible glass for roll-to-roll electronic device fabrication,” *Applied Physics A*, vol. 116, no. 2, pp. 403–407, 2014.

[322] N. Yasrebi et al., “Optimization of sputtering parameters for the deposition of low resistivity indium tin oxide thin films,” *Acta Metallurgica Sinica (English Letters)*, vol. 27, no. 2, pp. 324–330, 2014.

[323] H. Kanda et al., “Analysis of sputtering damage on I-V curves for perovskite solar cells and simulation with reversed diode model,” *Journal of Physical Chemistry C*, vol. 120, no. 50, pp. 28441–28447, 2016.

[324] E. Aydin et al., “Sputtered transparent electrodes for optoelectronic devices: Induced damage and mitigation strategies,” *Matter*, vol. 4, no. 11, pp. 3549–3584, 2021.

[325] N. M. Ahmed et al., “The effect of post annealing temperature on grain size of indium-tin-oxide for optical and electrical properties improvement,” *Results in Physics*, vol. 13, p. 102159, 2019.

[326] G. C. E. Jost et al., "Reliability aspects of hydrogen-doped indium oxide," *Physica Status Solidi A*, vol. 213, no. 7, pp. 1751–1759, 2016.

[327] T. Koida et al., "Hydrogen-doped In_2O_3 as high-mobility transparent conductive oxide," *Japanese Journal of Applied Physics*, vol. 46, no. 7L, p. L685, 2007.

[328] M. Li et al., "Embedded nickel-mesh transparent electrodes for highly efficient and mechanically stable flexible perovskite photovoltaics: Toward a portable mobile energy source," *Advanced Materials*, vol. 32, no. 38, p. e2003422, 2020.

[329] H. Ji et al., "Novel Ag-mesh transparent hybrid electrodes for highly efficient and mechanically stable flexible perovskite solar cells," *Advanced Materials Interfaces*, vol. 9, no. 16, p. 2200483, 2022.

[330] C. Ongaro et al., "Integration of metal meshes as transparent conducting electrodes into perovskite solar cells," *Advanced Materials Interfaces*, p. 2300923, 2023.

[331] Y. Li et al., "Bandgap tuning strategy by cations and halide ions of lead halide perovskites learned from machine learning," *RSC Advances*, vol. 11, no. 26, pp. 15688–15694, 2021.

[332] R. Santbergen et al., "Minimizing optical losses in monolithic perovskite/c-Si tandem solar cells with a flat top cell," *Optics Express*, vol. 24, no. 18, pp. A1288–99, 2016.

[333] D. T. Grant et al., "Design guidelines for perovskite/silicon 2-terminal tandem solar cells: An optical study," *Optics Express*, vol. 24, no. 22, pp. A1454–A1470, 2016.

[334] S. Altazin et al., "Design of perovskite/crystalline-silicon monolithic tandem solar cells," *Optics Express*, vol. 26, no. 10, pp. A579–A590, 2018.

[335] Z. Peng et al., "Upscaling of perovskite/c-Si tandem solar cells by using industrial adaptable processes," *AIP Conference Proceedings*, vol. 2826, no. 1, p. 090003, 2023.

[336] J. Lin et al., "Dual surface modifications of NiO_x/perovskite interface for enhancement of device stability," *ACS Applied Materials and Interfaces*, vol. 15, no. 20, pp. 24437–24447, 2023.

[337] T. Feeney et al., "Four-terminal perovskite/copper indium gallium selenide tandem solar cells: Unveiling the path to >27% in power conversion efficiency," *Solar RRL*, vol. 6, no. 12, 2022.

[338] B. A. Nejand et al., "Scalable two-terminal all-perovskite tandem solar modules with a 19.1% efficiency," *Nature Energy*, vol. 7, no. 7, pp. 620–630, 2022.

[339] H. Yun et al., "Ethanol-based green-solution processing of a-formamidinium lead triiodide perovskite layers," *Nature Energy*, vol. 7, no. 9, pp. 828–834, 2022.

[340] N. Cheng et al., "A modified two-step sequential spin-coating method for perovskite solar cells using CsI containing organic salts in mixed ethanol/methanol solvent," *Solar Energy Materials and Solar Cells*, vol. 250, p. 112107, 2023.

[341] Q. Yang et al., "Origin of sputter damage during transparent conductive oxide deposition for semitransparent perovskite solar cells," *Journal of Materials Chemistry A*, vol. 12, no. 24, pp. 14816–14827, 2024.

[342] Y. Li et al., "Nanoscale size control of Si pyramid texture for perovskite/Si tandem solar cells enabling solution-based perovskite top-cell fabrication and improved si bottom-cell response," *Advanced Materials Interfaces*, vol. 10, no. 35, p. 2300504, 2024.

[343] Y. Liang et al., "Highly efficient perovskite solar cells with light management of surface antireflection," *Bulletin of the Chemical Society of Japan*, vol. 96, no. 2, pp. 148–155, 2023.

[344] M. Jošt et al., "Perovskite/CIGS tandem solar cells: From certified 24.2% toward 30% and beyond," *ACS Energy Letters*, vol. 7, no. 4, pp. 1298–1307, 2022.

[345] F. Jiang et al., "Metal electrode-free perovskite solar cells with transfer-laminated conducting polymer electrode," *Optics Express*, vol. 23, no. 3, pp. A83–A91, 2015.

[346] P. You et al., "Efficient semitransparent perovskite solar cells with graphene electrodes," *Advanced Materials*, vol. 27, no. 24, pp. 3632–3638, 2015.

[347] L. Bu et al., "Semitransparent fully air processed perovskite solar cells," *ACS Applied Materials and Interfaces*, vol. 7, no. 32, pp. 17776–17781, 2015.

[348] M. Makha et al., "A transparent, solvent-free laminated top electrode for perovskite solar cells," *Science and Technology of Advanced Materials*, vol. 17, no. 1, pp. 260–266, 2016.

[349] J. H. Heo et al., "Efficient organic-inorganic hybrid flexible perovskite solar cells prepared by lamination of polytriarylamine/$CH_3NH_3PbI_3$/anodized Ti metal substrate and graphene/PDMS transparent electrode substrate," *ACS Applied Materials and Interfaces*, vol. 10, no. 37, 2018.

[350] L. Gao et al., "Flexible and highly durable perovskite solar cells with a sandwiched device structure," *ACS Applied Materials and Interfaces*, vol. 11, no. 19, pp. 17475–17481, 2019.

[351] Y. Shao et al., "Insight into the interfacial elastic contact in stacking perovskite solar cells," *Advanced Materials Interfaces*, vol. 6, no. 7, 2019.

[352] L. J. Sutherland et al., "A high-pressure isostatic lamination technique to fabricate versatile carbon electrode-based perovskite solar cells," *Communications Materials*, vol. 5, no. 1, 2024.

[353] G. Huang et al., "Achieving over 20% efficiency in laminated HTM-free carbon electrode perovskite solar cells through in situ interface reconstruction," *Angewandte Chemie International Edition*, p. e202420687, 2024.

Acknowledgements

I want to express my deepest gratitude to everyone who contributed to the realization of this thesis. First, I thank my doctoral advisor, Prof. Dr. Ulrich W. Paetzold, who accompanied me throughout my research. His constant support, wise advice, and enthusiasm for the photovoltaic field have significantly contributed to the success of this work. I would also like to thank Prof. Dr. Hendrik Hölscher for taking on the role of co-advisor.

The Perovskite Taskforce at LTI, organized by Prof. Dr. Ulrich W. Paetzold, was an invaluable scientific and technical support among researchers through fruitful discussions and interdisciplinary insights. Many thanks to the entire group, especially to the co-authors of publications involved in this work: Dr. Tobias Abzieher, Dr. Bahram Abdollahi Nejand, Daniel O. Baumann, Dr. Ahmed Farag, Dr. Paul Fassl, Thomas Feeney, Benjamin Hacene, Dr. Hang Hu, Felix Laufer, Dr. Yang Li, Dr. Mahdi Malekshahi Byranvand, Dr. Somayeh Moghadamzadeh, Dr. Fabian Schackmar, and Dr. Raphael Schmager.

Many thanks to KIT, IMT, and LTI for enabling me to work on my research in suitable conditions. Special thanks to Prof. Dr. Ulrich Lemmer, Prof. Dr. Ulrich W. Paetzold, PD Dr. Matthias Worgull, and Prof. Dr. Bryce Richards for providing the laboratories and equipment necessary for perovskite research from fabrication to characterization.

I also thank Weiyuan Duan, Sun Nan, Dr. Kaining Ding, and Dr. Andreas Lambertz from FZ Jülich for supporting my project on laminated tandems by developing and providing the SHJ solar cells adapted to my research.

Sincere thanks go to Dr. Isabel Allegro, Dr. Simon Ternes, Thomas Feeney, Pirmin Tischler, Julian Petry, Ronja Pappenberger, Daniel O. Baumann, Julian Petermann, Roja Singh, Dr. Helge Eggers, Dr. Paul Fassl, and Daniel Nickel for proofreading this dissertation.

I thank my colleagues Dr. Faranak Sadegh, Dr. Anaghda Sharma, and Dr. Mahmoud Hassan, with whom I collaborated. I acknowledge my privilege of mentoring and supporting the lamination team as they honed their expertise in laminated perovskite photovoltaics.

Many thanks to the master students I was pleased to supervise and work with. Minasadat Heydarian worked with impressive precision and determination, building the basis of the highly efficient devices presented in this thesis. Luisa. K. Schorn demonstrated outstanding meticulousness and efficiency, providing essential insight into the perovskite lamination technology. Daniel O. Baumann challenged fundamental concepts, the key to success in proof-of-concept experiments. Thanks also to Amer Alhomaidi and Hannah Racky, whom I had the pleasure of co-supervising with Dr. Yang Li and Benjamin Hacene.

I want to thank Marc Schneider at IMT for providing invaluable support with the hot-pressing machine. Thanks also to Reza Akbarzadeh Naseri, Christian Kaiser, Felix Geislhöringer, Hans Vögele, and Mario Sütsch from the LTI technical team and workshop. Their expertise and assistance significantly contributed to the efficiency of this project.

My heartfelt thanks go to Daniel Nickel. I feel lucky we pursued this adventure together. I am also sincerely grateful to my Doktorschwestern Isabel Allegro and Roja Singh, as well as Simon Ternes, Thomas Feeney, Julian Petry, Felix Laufer, and Julian Petermann. We certainly had our share of many great times. Your support throughout all the phases of my PhD, which you understand as well as I do, has meant the world to me.

I am profoundly thankful to my friends and family, particularly my sister Cloé and parents Elisabeth and Patrick Roger, for their unconditional support. My brother Paul is also in my thoughts as I reflect on this accomplishment. It is with profound gratitude that I celebrate the completion of this work, marking an important milestone in my personal journey and professional career.

Schriften des Instituts für Mikrostrukturtechnik am Karlsruher Institut für Technologie (KIT)

ISSN 1869-5183

Band 1	Georg Obermaier Research-to-Business Beziehungen: Technologietransfer durch Kommunikation von Werten (Barrieren, Erfolgsfaktoren und Strategien). ISBN 978-3-86644-448-5
Band 2	Thomas Grund Entwicklung von Kunststoff-Mikroventilen im Batch-Verfahren. ISBN 978-3-86644-496-6
Band 3	Sven Schüle Modular adaptive mikrooptische Systeme in Kombination mit Mikroaktoren. ISBN 978-3-86644-529-1
Band 4	Markus Simon Röntgenlinsen mit großer Apertur. ISBN 978-3-86644-530-7
Band 5	K. Phillip Schierjott Miniaturisierte Kapillarelektrophorese zur kontinuierlichen Überwachung von Kationen und Anionen in Prozessströmen. ISBN 978-3-86644-523-9
Band 6	Stephanie Kißling Chemische und elektrochemische Methoden zur Oberflächenbearbeitung von galvanogeformten Nickel-Mikrostrukturen. ISBN 978-3-86644-548-2

Band 7 Friederike J. Gruhl
Oberflächenmodifikation von Surface Acoustic Wave (SAW) Biosensoren für biomedizinische Anwendungen.
ISBN 978-3-86644-543-7

Band 8 Laura Zimmermann
Dreidimensional nanostrukturierte und superhydrophobe mikrofluidische Systeme zur Tröpfchengenerierung und -handhabung.
ISBN 978-3-86644-634-2

Band 9 Martina Reinhardt
Funktionalisierte, polymere Mikrostrukturen für die dreidimensionale Zellkultur.
ISBN 978-3-86644-616-8

Band 10 Mauno Schelb
Integrierte Sensoren mit photonischen Kristallen auf Polymerbasis.
ISBN 978-3-86644-813-1

Band 11 Daniel Auernhammer
Integrierte Lagesensorik für ein adaptives mikrooptisches Ablenksystem.
ISBN 978-3-86644-829-2

Band 12 Nils Z. Danckwardt
Pumpfreier Magnetpartikeltransport in einem Mikroreaktionssystem: Konzeption, Simulation und Machbarkeitsnachweis.
ISBN 978-3-86644-846-9

Band 13 Alexander Kolew
Heißprägen von Verbundfolien für mikrofluidische Anwendungen.
ISBN 978-3-86644-888-9

Die Bände sind unter www.ksp.kit.edu als PDF frei verfügbar oder als Druckausgabe zu bestellen.

Band 14 Marko Brammer
Modulare Optoelektronische Mikrofluidische
Backplane.
ISBN 978-3-86644-920-6

Band 15 Christiane Neumann
Entwicklung einer Plattform zur individuellen Ansteuerung
von Mikroventilen und Aktoren auf der Grundlage eines
Phasenüberganges zum Einsatz in der Mikrofluidik.
ISBN 978-3-86644-975-6

Band 16 Julian Hartbaum
Magnetisches Nanoaktorsystem.
ISBN 978-3-86644-981-7

Band 17 Johannes Kenntner
Herstellung von Gitterstrukturen mit Aspektverhältnis 100 für die
Phasenkontrastbildgebung in einem Talbot-Interferometer.
ISBN 978-3-7315-0016-2

Band 18 Kristina Kreppenhofer
Modular Biomicrofluidics - Mikrofluidikchips im Baukastensystem für Anwendungen aus der Zellbiologie.
ISBN 978-3-7315-0036-0

Band 19 Ansgar Waldbaur
Entwicklung eines maskenlosen Fotolithographiesystems
zum Einsatz im Rapid Prototyping in der Mikrofluidik und
zur gezielten Oberflächenfunktionalisierung.
ISBN 978-3-7315-0119-0

Band 20 Christof Megnin
Formgedächtnis-Mikroventile für eine fluidische Plattform.
ISBN 978-3-7315-0121-3

Band 21 Srinivasa Reddy Yeduru
Development of Microactuators Based on
the Magnetic Shape Memory Effect.
ISBN 978-3-7315-0125-1

Die Bände sind unter www.ksp.kit.edu als PDF frei verfügbar oder als Druckausgabe zu bestellen.

Band 22 Michael Röhrig
Fabrication and Analysis of Bio-Inspired Smart Surfaces.
ISBN 978-3-7315-0163-3

Band 23 Taleieh Rajabi
Entwicklung eines mikrofluidischen Zweikammer-Chipsystems mit integrierter Sensorik für die Anwendung in der Tumorforschung.
ISBN 978-3-7315-0220-3

Band 24 Frieder Märkle
Laserbasierte Verfahren zur Herstellung hochdichter Peptidarrays.
ISBN 978-3-7315-0222-7

Band 25 Tobias Meier
Magnetoresistive and Thermoresistive Scanning Probe Microscopy with Applications in Micro- and Nanotechnology.
ISBN 978-3-7315-0253-1

Band 26 Felix Marschall
Entwicklung eines Röntgenmikroskops für Photonenenergien von 15 keV bis 30 keV.
ISBN 978-3-7315-0263-0

Band 27 Leonardo Pires Carneiro
Development of an Electrochemical Biosensor Platform and a Suitable Low-Impedance Surface Modification Strategy.
ISBN 978-3-7315-0272-2

Band 28 Sebastian Mathias Schillo
Prozessentwicklung für die Automatisierung der Herstellung und Anwendung von hochdichten Peptidmicroarrays.
ISBN 978-3-7315-0274-6

Die Bände sind unter www.ksp.kit.edu als PDF frei verfügbar oder als Druckausgabe zu bestellen.

Band 29 Nicole E. Steidle
Micro- and Nanostructured Microfluidic Devices
for Localized Protein Immobilization and Other
Biomedical Applications.
ISBN 978-3-7315-0297-5

Band 30 Jochen Heneka
Prozessentwicklung eines industrietauglichen Verfahrens
zur Fertigung von vereinzelten LIGA-Mikrobauteilen.
ISBN 978-3-7315-0326-2

Band 31 Seoung-Eun Kim
Konzeption und prototypische Fertigung einer
nicht-invasiven mikrofluidischen Plattform für die
Elektrophysiologie (NIMEP) zur Zellenanlyse.
ISBN 978-3-7315-0378-1

Band 32 Elisabeth Wilhelm
Entwicklung eines mikrofluidischen Brailledisplays.
ISBN 978-3-7315-0385-9

Band 33 Viktor Pinneker
Entwicklung miniaturisierter Aktorsysteme basierend
auf magnetischen Formgedächtnislegierungen.
ISBN 978-3-7315-0500-6

Band 34 Ali Caglar Özen
Novel MRI Technologies for Structural and Functional
Imaging of Tissues with Ultra-short T_2 Values.
ISBN 978-3-7315-0657-7

Band 35 Anne Bäcker
Veränderliche 3D Zellgerüstträger auf Cryogelbasis
zur Kultivierung von Prostatakarzinomzellen.
ISBN 978-3-7315-0676-8

Band 36 Frieder Johannes Koch
X-ray optics made by X-ray lithography:
Process optimization and quality control.
ISBN 978-3-7315-0679-9

Die Bände sind unter www.ksp.kit.edu als PDF frei verfügbar oder als Druckausgabe zu bestellen.

Band 37	Tobias Jörg Schröter Vergrößerung des Sehfeldes der Röntgen-Phasenkontrast-Bildgebung für die klinische Anwendung. ISBN 978-3-7315-0731-4
Band 38	Felix Vüllers Bioinspired Superhydrophobic Nano- and Microstructured Surfaces for Drag Reduction and Optoelectronics. ISBN 978-3-7315-0816-8
Band 39	Frederik Kotz Entwicklung neuer Materialien für die additive Fertigung und das Rapid Prototyping von Glas und Polymethylmethacrylat. ISBN 978-3-7315-0835-9
Band 40	Michael Oldenburg Photon upconversion heterostructures made from surface-anchored metal-organic frameworks. ISBN 978-3-7315-0863-2
Band 41	Elisa Kornemann Entwicklung einer Röntgenzoomlinse. ISBN 978-3-7315-0885-4
Band 42	Hossein Davoodi NMR micro-detectors tailored for multinuclear and electrochemistry lab-on-a-chip applications. ISBN 978-3-7315-1118-2
Band 43	Florian Brüderlin Advanced Elastocaloric Cooling Devices Based on Shape Memory Alloy Films. ISBN 978-3-7315-1065-9
Band 44	Andreas Striegel Werkzeug- und Prozessentwicklung des Roll-to-Roll-Hochdurchsatzverfahrens zur kontinuierlichen, großflächigen Mikrostrukturierung. ISBN 978-3-7315-1106-9

Die Bände sind unter www.ksp.kit.edu als PDF frei verfügbar oder als Druckausgabe zu bestellen.

Band 45 Marlene Kopf
Langzeitstabilität der Innendrücke von Kavernen
benachbarter MEMS-Sensoren auf Siliziumbasis.
ISBN 978-3-7315-1121-2

Band 46 Simon Ternes
In Situ Characterization and Modelling of Drying Dynamics
for Scalable Printing of Hybrid Perovskite Photovoltaics.
ISBN 978-3-7315-1255-4

Band 47 Omar Nassar
Innovative micro-NMR/MRI functionality utilizing
flexible electronics and control systems.
ISBN 978-3-7315-1176-2

Band 48 Joel Joseph
Power Generation by Resonant Self-Actuation.
ISBN 978-3-7315-1327-8

Band 49 Alexander Opolka
Refraktive Multifokusröntgenlinsen und
Hartmann-Shack-Sensoren.
ISBN 978-3-7315-1349-0

Band 50 Xi Chen
Energy Harvesting Based on Bistable Shape
Memory Film Actuation.
ISBN 978-3-7315-1375-9

Band 51 David Benedikt Ritzer
Laserbasierte Verschaltung und Strukturierung
von Perowskit-Solarmodulen.
ISBN 978-3-7315-1387-2

Band 52 Julie Roger
Lamination and recrystallization of perovskite
thin films for photovoltaics.
ISBN 978-3-7315-1450-3

JULIE ROGER

Lamination and recrystallization of perovskite thin films for photovoltaics

Photovoltaics (PV) play a central role in the global transition to renewable energy sources. Among the new concepts being developed, perovskite solar cells have emerged as a particularly promising technology for next generation PV. This work presents an innovative manufacturing process for perovskite-based solar cells using lamination. The devices are processed in two independent half-stacks, which are united in a final step by hot-pressing. This approach contrasts with the conventional method of sequential layer deposition and increases the freedom in the choice of materials, deposition techniques, and solar cell architectures.

Proof-of-concept architectures are presented that are difficult or impossible to fabricate conventionally, with a focus on scalable deposition techniques for the inorganic contact layers. Laminated perovskite solar cells achieve power conversion efficiencies on par with conventional references while exhibiting enhanced long-term stability over a year. The process also appears readily applicable to tandem PV, as showcased by the first prototypes of laminated monolithic perovskite/silicon tandem solar cells with a significant improvement in efficiency. This work thus demonstrates that lamination offers the necessary flexibility in fabrication of perovskite-based PV to directly address the remaining milestones of the technology worldwide – scalability, stability, and efficiency – paving the way toward commercialization.

ISSN 1869-5183
ISBN 978-3-7315-1450-3

Gedruckt auf FSC-zertifiziertem Papier

ISBN 978-3-7315-1450-3
9 783731 514503